Department of Civil and Mechanical Engineering
PhD Thesis

Development and application of phase field models for fracture mechanics-based assessment of fatigue life of offshore wind structures in a corrosive environment

Alireza Golahmar

Development and application of phase field models for fracture mechanics-based assessment of fatigue life of offshore wind structures in a corrosive environment

Alireza Golahmar

Department of Civil and Mechanical Engineering
Technical University of Denmark 2023

Thesis Title:
Development and application of phase field models for fracture mechanics-based assessment of fatigue life of offshore wind structures in a corrosive environment

Author:
Alireza Golahmar

Academic Supervisors:
Professor Christian F. Niordson
Technical University of Denmark

Associate Professor Emilio Martínez-Pañeda
Imperial College London

Associate Professor Brian Nyvang Legarth
Technical University of Denmark

Industrial Supervisors:
Senior Lead Structural Engineer Dariusz Eichler
Vattenfall Vindkraft A/S

Senior Lead Engineer Dr. Thomas von Borstel
Vattenfall Vindkraft A/S

PhD Assessment Committee:
Professor Laura De Lorenzis
ETH, Zurich

Associate Professor Ramin Aghababaei
Aarhus University

Associate Professor Konstantinos Poulios
Technical University of Denmark

PhD Thesis
May 2023

Published by: DTU, Department of Civil and Mechanical Engineering, Koppels Allé, 404, 2800 Kgs. Lyngby Denmark
www.construct.dtu.dk
ISBN: 978-87-7475-757-3
DCAMM Special Report No. S334

Preface

This thesis is submitted to fulfill the requirements for obtaining a PhD degree from Technical University of Denmark (DTU). The PhD project has been funded by Vattenfall Vindkraft A/S and Innovation Fund Denmark (grant 0153-00018B). The research was conducted at the Department of Civil and Mechanical Engineering, Section of Solid Mechanics, during the period from June 2020 to May 2023. The project was supervised by Professor Christian F. Niordson (DTU), Associate Professor Emilio Martínez-Pañeda (Imperial College London), Associate Professor Brian Nyvang Legarth (DTU), Senior Lead Structural Engineer Dariusz Eichler (Vattenfall Vindkraft A/S), and Senior Lead Engineer Dr. Thomas von Borstel (Vattenfall Vindkraft A/S).

Alireza Golahmar
Kgs. Lyngby, May 2023

Abstract

Offshore wind is one of the most sustainable and efficient ways for generating renewable energy. However, operating and maintaining wind turbines in a demanding and costly offshore environment poses significant challenges. Eventually, offshore wind turbines will reach the end of their operational lifespan. The primary factor influencing the lifespan of offshore wind turbines is corrosion fatigue of their foundations, as they endure severe dynamic loads and corrosive seawater conditions. The key question is when failure will happen and how many years they can function effectively. To address this question, this thesis aims to develop novel computational models that encompass multiple scientific disciplines, enabling accurate predictions of the service lifespan of offshore wind turbines.

The proposed modelling framework builds upon recent advancements in the phase field fracture formulations for fatigue damage. It introduces a cyclic degradation of fracture energy, which effectively recovers Paris law behavior and stress-fatigue life (S-N curves). Furthermore, the framework incorporates the impact of a harsh environment using a mechanistic, implicitly multi-scale approach that accounts for the degradation of fracture energy due to the hydrogen content. Our study demonstrates that the presented coupled deformation-diffusion-damage model allows accurate prediction of fatigue crack nucleation and growth across a wide range of loading scenarios and specimen geometries. Notably, the model successfully captures the concept of transition flaw size, a fundamental aspect of engineering standards and fracture mechanics-based design.

By comparing the numerical simulations with experimental data, it is evident that the model reliably predicts fatigue lives, endurance limits, and accounts for the influence of stress concentration factors and load ratios, without requiring fitting procedures. Furthermore, the model establishes a connection between S-N curves and Paris law behavior, facilitating the prediction of fatigue crack growth in brittle materials using stress-fatigue life data and vice versa. This versatile modelling framework also offers a valuable tool for assessing the influence of the environment on the Paris law and S-N curve parameters. This enables optimization of design and maintenance strategies through the utilization of *Virtual Testing* and *Digital Twins* concepts, as well as facilitates efficient planning of targeted experimental campaigns.

Resumé (in Danish)

Havvindmøller er en af de mest bæredygtige og effektive måder at generere vedvarende energi på. Imidlertid udgør drift og vedligeholdelse af vindmøller i krævende og omkostningsfulde offshore-miljø betydelige udfordringer. Levetiden for havvindmøller er begrænset af korrosionsudmattelse af deres fundamenter, da de udsættes for store dynamiske belastninger og korrosive forhold i havvandet, og bestemmelse af levetiden er derfor af afgørende betydning. I denne afhandling udvikles nye beregningsmodeller, baseret på flere videnskabelige discipliner, og de muliggør præcise forudsigelser af levetiden for havvindmøller.

Den udviklede model bygger på nylige fremskridt inden for fasefeltsbrudformulering for udmattelse af metaller. Den introducerer en cyklisk degradering af brudenergien, der effektivt modellerer Paris-lov opførsel og spændingsudmattelse (S-N kurver). Derudover inkorporerer modellen påvirkningen af et barskt miljø ved hjælp af en mekanistisk, implicit multi-tilgang, der tager højde for degradering af brudenergien på grund af hydrogen. Modellen viser, at den koblede deformation-diffusion-skademodel muliggør præcise forudsigelser af udmattelsesrevndannelse og vækst over et bredt spektrum af belastningsscenarier og prøvegeometrier.

Ved at sammenligne de numeriske simuleringer med eksperimentelle data bliver det vist, at modellen pålideligt forudsiger udmattelsesliv, og at den tager højde for indflydelsen af spændingskoncentrationer og belastningsforhold uden brug af fitting- parametre. Derudover etablerer modellen en forbindelse mellem S-N kurver og Paris-lov opførsel, hvilket letter forudsigelsen af udmattelsesrevner i sprøde materialer. Den udviklede model udgør et alsidigt metodegrundlag af miljøets indflydelse på udmattelsesopførslen, on den muliggør optimering af design- og vedligeholdelsesstrategier gennem anvendelse af *Virtuel Testning* og *Digitale Tvillinger*, der kan lede til effektiv planlægning af målrettede eksperimentelle kampagner.

Acknowledgements

I would like to express my sincere gratitude to Prof. Christian F. Niordson, whose unwavering support, infinite patience, constant backing, and friendship have been instrumental in the success of this thesis. I am deeply appreciative of the assistance and encouraging remarks from all the faculty members, administrative staff, and laboratory technicians of the Section of Solid Mechanics at the Technical University of Denmark. I am particularly grateful to Associate Prof. Brian Nyvang Legarth for always making himself available and Prof. Ann Bettina Richelsen for being an inspiring role model. I am also thankful for the feedback and advice provided by Associate Prof. Konstantinos Poulios. The collaborative and supportive working environment, fostered by my young colleagues, has been truly remarkable, and I extend my heartfelt thanks to all of them for their indispensable contributions.

During my research visit to Imperial College London, I had the privilege to learn from brilliant scientists, and their priceless guidance deserves special recognition. The kindness and professionalism displayed by the members of the Mechanics of Infrastructure Materials Lab will always be cherished. Among the numerous friendships I formed, I want to highlight my deep appreciation for my host, Associate Prof. Emilio Martínez-Pañeda, who has been an exceptional scientific mentor. The invaluable guidance, unwavering support, and boundless patience provided by him have played a crucial role in the achievement of this thesis.

I am indebted to the energy company Vattenfall Vindkraft A/S for their collaboration on my PhD project. I extend my gratitude to Dariusz Eichler and Dr. Thomas von Borstel for their highly valuable input and guidance, which have significantly contributed to the success of this thesis. The enriching discussions with my colleagues at the Department of Offshore Wind Foundation have also played a vital role in enhancing my technical skills. I had the privilege of learning from all of them, and I eagerly anticipate our continued collaboration in the future. Furthermore, I am grateful for the interactions I had with numerous academics and engineers during scientific events and joint industrial projects throughout my three-year PhD journey. Their valuable advice and encouraging remarks are deeply appreciated.

Finally, I would like to extend a special acknowledgment to my beloved family and dearest friends. The unwavering encouragement from my parents and brother has been an invaluable source of strength for me.

Publications

The following publications are part of this thesis:

[P1] A. Golahmar, C. F. Niordson, and E. Martínez-Pañeda. A phase field model for high-cycle fatigue: Total-life analysis. International Journal of Fatigue 170 (2023), p. 107558.

[P2] P. K. Kristensen, A. Golahmar, E. Martínez-Pañeda, and C. F. Niordson. Accelerated high-cycle phase field fatigue predictions. European Journal of Mechanics / A Solids 100 (2023), p. 104991.

[P3] A. Golahmar, C. F. Niordson, and E. Martínez-Pañeda. A phase field model for fatigue crack growth analysis. To be submitted.

[P4] A. Golahmar, P. K. Kristensen, C. F. Niordson, and E. Martínez-Pañeda. A phase field model for hydrogen-assisted fatigue. International Journal of Fatigue 154 (2022), p. 106521.

Contents

1 Introduction

1.1 Motivation

Climate change is a critical global challenge that requires urgent action, and transitioning to alternative sources of energy is crucial in achieving this. Renewable energy sources, such as wind power, offer a sustainable solution, with low carbon footprints and minimal impact on the environment. Offshore wind energy, in particular, has become a flagship strategy for many companies, including Vattenfall, in their pursuit of climate neutrality. At present, wind turbines have a lifetime of approximately 25 years, and thus there is still room for further development in their life-cycle management. The main factor influencing the lifetime of offshore wind turbines is the corrosion fatigue of their support structures, as they are exposed to high dynamic loads and harsh seawater environments. Accurate predictions of fatigue lifetime are necessary to ensure the safe operation of the structures during their operational life and potentially beyond.

Given that current engineering practices in offshore wind structures are largely reliant on empirical methods, there is a pressing need to develop multi-physics computational models that can reliably predict their service life. Such scientific advances will pave the way for the first generation of physically-based life assessment models, which will be integrated into fitness-for-service practices. This will allow for *Virtual Testing* and *Digital Twins* in the wind energy sector, potentially impacting material selection and inspection planning. The model predictions will be essential for extending the service life of structures that are approaching the end of their service life. Any extension of their lifespan or availability for re-powering will lead to increased revenue from energy production, enabling the wind industry to invest more in renewable energy and move closer to the global goal of becoming fossil-free.

1.2 Fatigue

The term ”fatigue failure” pertains to the repeated application of macroscopic loads or displacements at stress levels significantly lower than the quasi-static strength of the material. The fatigue process can typically be divided into two stages: (i) crack initiation and (ii) crack growth. In the initiation stage, irreversible/permanent microscopic degradation phenomena such as micro-voids form in the material at micro-heterogeneities, leading to the subsequent formation of micro-cracks [1]. The initiation stage is inherently stochastic and governed by the micro-structural arrangement of the material. With continued load application, damage accumulates in the material, and the micro-cracks eventually coalesce to form dominant fatigue (macro-) cracks. One or more of these macro-cracks propagate through the material, initially in a stable manner, until they become unstable and cause the complete failure of the component.

Typically, the fatigue resistance of a material is expressed as the number of cycles it can withstand before failure. This can be determined through classical empirical techniques, fracture mechanics-based methodologies, or material models that take into account fatigue damage. Classical empirical techniques rely on fitting data from a significant number of experimental tests. A seminal contribution to this field was made by Wöhler [2], who introduced the stress-life or S-N curve approach, which is widely used today. A typical S-N curve is a graphical representation, mathematically described by, e.g., the Basquin

power law [3], that relates the constant applied stress (or strain) amplitude of a cyclic load to the maximum number of cycles a component can withstand before failure. Fatigue life analyses are generally classified into two distinct regimes. The first is referred to as high-cycle fatigue (HCF), where the material is subjected to low cyclic stress amplitudes and primarily behaves elastically. Failure in this regime typically requires a large number of cycles (often more than 10^6 cycles). This method has gained popularity in applications that involve low-amplitude cyclic stresses, such as offshore wind turbines that are subjected to mechanical loads originating from wind and sea waves. The second scenario involves, on the other hand, applied stresses that are significant enough to induce plastic deformation, resulting in failure within a much smaller number of cycles, often fewer than 10^4 cycles. This regime is referred to as low-cycle fatigue (LCF). Stress-life methods are of limited use due to their empirical nature, which makes it challenging to generalize them to a wide range of materials, geometries, and loading conditions.

Fracture mechanics-based approaches commonly employ the Paris law, which was proposed by Paris and Erdogan [4] to characterize the stable growth of a fatigue crack. This law introduces a power function that relates the stress intensity factor range to the rate of fatigue crack growth on a bi-logarithmic scale. The parameters of this function are experimentally calibrated to represent both material-specific properties and the test environment. This relationship is, however, only applicable within the Paris regime, which is characterized by stable crack growth. It cannot replicate the regimes of crack nucleation and failure, which are known as the slow and fast crack growth regimes, respectively. To address its limitation, the Paris law has undergone continuous improvement and extension. This has culminated in the form of the widely used NASGRO equation [5], which is capable of reproducing many fundamental aspects of fatigue behavior, including the nucleation, growth, and failure phases.

In the realm of computational fracture mechanics, numerical methods that incorporate fatigue into constitutive material models are frequently used. The Cohesive Zone Model (CZM) is one of the most commonly employed approaches, relying on representative traction-separation laws to determine damage evolution under fatigue loading [6, 7]. Despite its usefulness, CZM-based analyses necessitate explicit resolution of the near-tip strain fields at every load cycle to determine the actual accumulation of the crack opening. Additionally, CZM has limitations in predicting complex crack paths, as the propagation path must be known in advance. Another approach is the Extended Finite Element Method (XFEM), first introduced by Belytschko and co-workers [8, 9], which uses local enrichment of standard finite element shape functions. The method can be applied to determine the stress intensity factor range values required for Paris law formulation [10–12]. When using XFEM, it is essential to trace the crack propagation path, which can be challenging to handle in complex cracking situations. This includes the initiation, growth, branching, and merging of cracks, particularly for non-planar crack surfaces in 3D cases.

An alternative to these methods is Continuum Damage Mechanics (CDM) modelling of fatigue damage [13, 14]. CDM is founded on thermodynamic micro-mechanical models that link the nucleation and growth of micro-structural defects to macroscopic state variables. Several damage evolution models have been developed to simulate fatigue crack growth in the context of low- and high-cycle fatigue loading [15, 16]. However, one of the main challenges associated with CDM-based models is the selection of an appropriate material constitutive law that accurately captures both the plastic behavior of the material and the evolution of damage.

1.3 Phase field fracture and fatigue

Phase field fracture model has emerged as a widely used variational approach for investigating complex cracking phenomena. The model relies on the fundamental thermodynamic framework proposed by Griffith [17], which postulates that a crack will grow when the material's critical energy release rate is exceeded. Francfort and Marigo [18] integrated Griffith's energy balance into variational formulations by including the surface energy, dissipated by the creation of a crack, in the material's total energy potential. Bourdin et al. [19, 20] proposed to regularise the resulting functional by introducing a scalar damage variable, later known as phase field, which interpolates smoothly between an intact and a broken state of the material.

Since its inception, the phase field fracture model has gained significant popularity, mainly due to its ability to accurately capture complex cracking features, such as initiation of cracks from multiple locations or the merging of various defects, in arbitrary geometries and dimensions, without the need for any ad hoc criteria. Considerable attention has been given to enhancing solution schemes [21–23] and discretization strategies [24, 25], which have played a crucial role in driving the model's wider adoption. Given that the model is based on sound mathematical principles and is straightforward to implement and customize, it has been widely employed in various applications, including ductile damage [26–29], dynamic fracture [30–34], mixed-mode fracture [35], Herzian indentation fracture [36], interface fracture [37], composites delamination [38–42], fracture in shells [43], ceramics [44, 45], elastomers [46], shape memory alloys [47], functionally graded materials [48, 49], thermal shocks [50], Lithium ion batteries [51–53], and hydrogen embrittlement [54–57] among many others; see Ref. [58] for an overview.

In recent years, attempts have been made to integrate fatigue damage into the phase field fracture models. Lo et al. [59] proposed a method of adding a viscous term to the conventional phase field model for brittle material, along with a modified J-integral, to generate a fatigue crack growth behaviour that follows the Paris law. Typically, an extra variable representing the fatigue history is added to the model. The definition of this variable often involves a dissipative term in the microforce balance of the phase field [60–62], which enhances crack growth, or as a fatigue degradation function that effectively lowers the material's fracture toughness [47, 63–67]. As a result, an extra equation is included to charactrize the evolution of the fatigue history variable. Boldrini et al. [60] formulated this equation using thermodynamic principles, whereas Loew et al. [61] suggested one based on micro-crack growth behaviour. Seiler et al. [65] employed the local strain approach to include plasticity using Neuber's rule, and Schreiber et al. [62] utilized Miner's rule to describe the fatigue damage evolution. Alessi et al. [63] proposed the use of the accumulated strain during the loading phase of each cycle as the driving force for fatigue damage. According to [63], the authors in [47, 64, 68–71] accumulated the tensile portions of the strain energy density (elastoplastic energy density in [70, 71]) during the loading (unloading in [69]) phases only.

1.4 Hydrogen embrittlement

Engineering failures frequently arise as a result of the interplay between environmental factors and mechanical loading, with hydrogen embrittlement standing out as one of the most significant environmental effects. The detrimental impact of hydrogen on the mechanical properties of metallic materials has been known for more than a century [72]. This phenomenon, often characterized by sub-critical cracking, not only poses a threat to the viability of hydrogen as a future energy carrier but also constrains the application of modern steels in existing energy infrastructures. There is a wealth of documented evidence that

highlights the occurrence of catastrophic failure resulting from hydrogen embrittlement in various industrial components exposed to gases and aqueous electrolytes, including but not limited to pressure vessels, pipelines, and offshore structures. It is important to note that hydrogen embrittlement can manifest even in the absence of apparent corrosion indications and after long periods of service, leading to unexpected and premature failure of components. Given that prevailing engineering methods are primarily empirical, it is crucial to develop models that can simulate hydrogen-induced degradation and replicate the microstructure-dependent mechanical response on a scale that is relevant to engineering applications.

One critical characteristic of hydrogen atoms is their small size compared to iron and other metallic atoms, which enables them to diffuse through the metal lattice even at low temperatures. There are two primary ways in which hydrogen can enter a metal: by being absorbed from hydrogen-containing gas, or through electrochemical reactions that occur on the metal's surface, such as corrosion. During the latter process, Volmer reactions can result in hydrogen atoms being adsorbed onto the surface of the metal, some of which may then diffuse into the metal lattice [73]. The process by which hydrogen is absorbed into metals involves a complex interplay of surface kinetics and thermodynamics, which falls outside the scope of this thesis. Upon entering a metal, hydrogen atoms diffuse rapidly through its crystal lattice and are accumulated in regions with high hydrostatic stress, indicating lattice dilatation and facilitating mass transport. The hydrogen atoms have a tendency to accumulate at expanded sites within the lattice due to their greater affinity for these sites. Microstructural features are a crucial determinant not only of the overall diffusion rates within the lattice structure but also of the trapping behavior of hydrogen within the material. Microstructural defects, such as dislocations, grain boundaries, vacancies/voids, carbides and interfaces, can all serve as hydrogen traps [74]. In 1970, Oriani [75] introduced a thermodynamically balanced model that describes how hydrogen is distributed between normal interstitial lattice sites (NILS) and traps.

Identifying the fundamental mechanisms of hydrogen embrittlement has proven to be a challenging task due to the intricate interplay between hydrogen and microstructural characteristics, coupled with the wide range of investigated hydrogen-metal systems. The literature proposes two primary atomistic mechanisms that account for hydrogen embrittlement in steels; see Refs. [76, 77] for an overview. According to the Hydrogen Enhanced Decohesion (HEDE) mechanism, the accumulation of hydrogen atoms at the fracture process zone leads to a reduction in fracture resistance by decreasing the cohesive energy of the material [75, 78]. In contrast, the Hydrogen Enhanced Localised Plasticity (HELP) mechanism suggests that hydrogen accumulates around dislocations, leading to a reduction in the size and width of the dislocations, which in turn lowers the Peierls stress [79]. This results in the softening of the solid material. The HEDE mechanism is commonly recognized as the primary mechanism in modern steels, as it is capable of accurately capturing the key experimental observations in hydrogen environments [80].

The field of computational modeling for hydrogen-assisted fractures has undergone significant advancements in recent years. A range of methods have been introduced to effectively capture the initiation and propagation of hydrogen-assisted cracks, including weakest-link methods [81, 82], dislocation-based approaches [83, 84], CZM-based methods [85–87], gradient damage models [56], and phase field fracture formulations [54, 55, 57, 88, 89]. Despite the extensive research on modeling in the context of static/monotonic fracture, the study of fatigue has rarely been explored with computational tools. The presence of hydrogen can affect the cyclic behavior of materials [90, 91], increase the likelihood of crack initiation [92, 93], and significantly accelerate the growth of fatigue cracks

[94, 95]. To accurately estimate the reduction in fatigue life caused by hydrogen, several factors that augment the rate of fatigue crack growth must be taken into account, such as the concentration of hydrogen, the material's susceptibility to embrittlement, hydrogen diffusivity, and loading frequency and amplitude. Nevertheless, due to the complex and computationally intensive nature of assessing fatigue damage, the impact of hydrogen on fatigue crack growth rates has primarily been investigated through experimentation, with only a handful of works involving numerical analysis [96, 97].

1.5 Thesis outline

This thesis is comprised of four scientific publications [P1, P2, P3, P4] developed during the PhD program. The main body of the thesis is structured as follows: Chapter 2 presents the theoretical framework of the phase field fracture model, including its extension to fatigue damage. Chapter 3 explores the impact of hydrogen embrittlement. Chapter 4 details the numerical scheme and its implementation in the finite element software Abaqus. Chapter 5 summarizes the numerical examples and their experimental verification conducted throughout the publications. Finally, Chapter 6 concludes the thesis and provides insight into future work and opportunities.

1.6 A note on notation

Thought this thesis, the notation used is as follows: Scalars are denoted by lightface italic letters, such as ϕ, vectors by bold letters, such as $\mathbf{u}$, and second- or higher-order tensors by bold italic letters, such as $\boldsymbol{\sigma}$. The inner product of two tensors is denoted by vertically stacked dots, such as $\boldsymbol{\sigma} : \boldsymbol{\varepsilon}$. The gradient of a quantity $\square$ is represented by $\nabla\square$, the divergence by $\nabla \cdot \square$, and the Laplacian by $\Delta\square$.

2 Phase field fracture

In this chapter, a comprehensive overview is presented on the fundamental principles of phase field fracture theory, including its extension to fatigue damage. The framework is established by utilizing the energetic principles of rate-independent systems, which are represented through an energy balance and a dissipation inequality. The framework also makes certain assumptions, such as small strains, negligible inertial effects, gradual loading/unloading over time, and isothermal conditions. The formulation presented in this chapter describes the response of a solid body that occupies an arbitrary volume denoted by $\Omega \subset \mathbb{R}^{\delta}$ $(\delta \in [1, 2, 3])$, with an external boundary given by $\partial\Omega \subset \mathbb{R}^{\delta-1}$, and an outward unit normal vector represented by $\mathbf{n}$.

2.1 Field variables and kinematics

The primary variables are defined as the displacement field $\mathbf{u}$ and the damage phase field ϕ. Under the assumption of small deformations, the strain tensor $\boldsymbol{\varepsilon}$ is expressed as follows:

$$\boldsymbol{\varepsilon} = \frac{1}{2}\left(\nabla^{\mathsf{T}}\mathbf{u} + \nabla\mathbf{u}\right) \tag{2.1}$$

The initiation and growth of cracks are characterized by utilizing an auxiliary phase field variable. The use of a phase field variable, for implicitly tracking interfaces, has demonstrated to be effective in addressing a diverse range of interfacial problems, including metallic corrosion [98] and microstructural evolution [99]. Within the framework of fracture mechanics, the phase field variable can be viewed as a damage variable $\phi \in [0; 1]$. It must increase monotonically ($\dot{\phi} \geqslant 0$) and serves to describe the extent of damage, with a value of $\phi = 1$ indicating a crack and $\phi = 0$ representing undamaged material points. The smooth and continuous property of the phase field variable ϕ allows for the representation of discrete cracks in a diffused or smeared manner (see Fig. 2.1). The extent of this smearing is regulated by a phase field length scale parameter denoted by ℓ. This approach is computationally advantageous since it allows for the modeling of cracks as smooth transitions, which eliminates the need for explicit tracking of discrete cracks. Additionally, it provides an effective means of approximating the fracture energy over a discontinuous surface Γ, as described in [20].

$$\Psi^s = \int_{\Gamma} G_c \,\mathrm{d}S \approx \int_{\Omega} G_c \gamma_\ell(\phi, \nabla\phi)\,\mathrm{d}V\,, \qquad \text{for} \quad \ell \to 0^+\,, \tag{2.2}$$

where G_c represents the material toughness or critical energy release rate, and γ_ℓ denotes the crack surface density functional. The crack surface density functional accounts for the energy dissipation associated with the creation of new crack surfaces, while the material toughness reflects the resistance of a material to fracture propagation. The rate-independent description of fracture can now be extended to account for time and history-dependent scenarios. To accomplish this, a cumulative history variable denoted by $\bar{\alpha}$ is introduced, which satisfies $\dot{\bar{\alpha}} \geqslant 0$ at the current time τ. Additionally, a fatigue degradation function $f(\bar{\alpha})$ is included to account for the effect of cyclic loading on fracture behavior. With these additions, the fracture energy can be reformulated as follows:

$$\Psi^s = \int_0^t \int_{\Omega} f(\bar{\alpha}(\tau))\, G_c\, \dot{\gamma}_\ell(\phi, \nabla\phi)\,\mathrm{d}V\mathrm{d}\tau \tag{2.3}$$

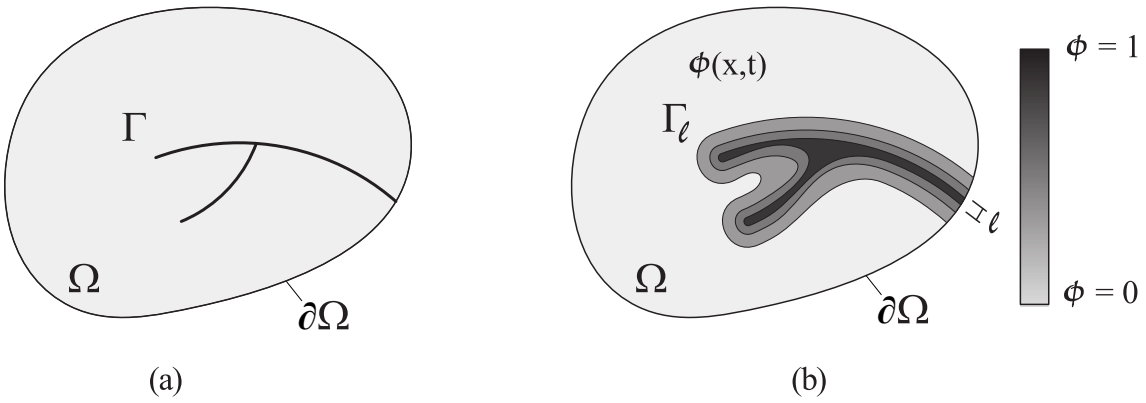

Figure 2.1: Schematic representation of a continuum body Ω with (a) an actual crack surface Γ and (b) a diffused crack surface represented by phase field $\Gamma_\ell(\phi)$. Source: Adapted from [54].

2.2 Principle of virtual power. Balance of forces

In order to obtain the balance equations for the coupled problem, the principle of virtual power is applied. The external surface of the body is divided into two parts, $\partial\Omega_u$ and $\partial\Omega_h$, with respect to the displacement field **u**. The first part, $\partial\Omega_u$, corresponds to the region where the displacement is prescribed by Dirichlet-type boundary conditions. The second part, $\partial\Omega_h$, corresponds to the region where the traction **h** is prescribed by Neumann-type boundary conditions. In addition to these boundary conditions, a body force field per unit volume **b** can also be specified. For the phase field ϕ, a Dirichlet-type boundary condition can be imposed at Γ, which represents a crack surface embedded in the continuum body. Furthermore, a phase field fracture microtraction $\mathfrak{f}$ can be specified on $\partial\Omega_\mathfrak{f}$. As a result, the external and internal virtual powers can be expressed as follows:

$$\begin{aligned}\dot{\mathcal{W}}_{\text{ext}} &= \int_{\partial\Omega} \left\{ \mathbf{h}\cdot\dot{\mathbf{u}} + \mathfrak{f}\dot{\phi} \right\} \mathrm{d}S + \int_{\Omega} \mathbf{b}\cdot\dot{\mathbf{u}}\,\mathrm{d}V \\ \dot{\mathcal{W}}_{\text{int}} &= \int_{\Omega} \left\{ \boldsymbol{\sigma} : \nabla\dot{\mathbf{u}} + \omega\dot{\phi} + \boldsymbol{\xi}\cdot\nabla\dot{\phi} \right\} \mathrm{d}V\end{aligned} \tag{2.4}$$

where $\boldsymbol{\sigma}$ denotes the Cauchy stress tensor which is work conjugate to the elastic strains ε. Similarly, ω and $\boldsymbol{\xi}$ represent the micro-stress quantities that are work conjugate to the phase field ϕ and its gradient $\nabla\phi$, respectively. Applying the fundamental lemma of calculus of variations and Gauss' divergence theorem to the internal virtual power (2.4b) renders

$$\dot{\mathcal{W}}_{\text{int}} = \int_{\partial\Omega} \left\{ (\boldsymbol{\sigma}\cdot\mathbf{n})\cdot\dot{\mathbf{u}} + (\xi\cdot\mathbf{n})\,\dot{\phi} \right\} \mathrm{d}S - \int_{\Omega} \left\{ (\nabla\cdot\boldsymbol{\sigma})\cdot\dot{\mathbf{u}} + (\nabla\cdot\boldsymbol{\xi} - \omega)\,\dot{\phi} \right\} \mathrm{d}V \tag{2.5}$$

Applying the principle of virtual power ($\dot{\mathcal{W}}\text{int} - \dot{\mathcal{W}}\text{ext} = 0$), we can derive a set of local force balances in Ω by requiring the second integral of (2.5) to vanish for all kinematically admissible variations of the virtual quantities,

$$\begin{aligned}\nabla\cdot\boldsymbol{\sigma} + \mathbf{b} &= \mathbf{0} \\ \nabla\cdot\boldsymbol{\xi} - \omega &= 0\end{aligned} \tag{2.6}$$

Since the first integral of (2.5) represents a portion of the external virtual work (2.4b), we can derive the corresponding set of boundary conditions on $\partial\Omega$

$$\begin{aligned} \mathbf{h} &= \boldsymbol{\sigma} \cdot \mathbf{n} \\ \mathfrak{f} &= \boldsymbol{\xi} \cdot \mathbf{n} \end{aligned} \tag{2.7}$$

2.3 Free-energy imbalance

The first two laws of thermodynamics can be combined by considering the Helmholtz free energy per unit volume $\psi(\boldsymbol{\varepsilon}, \phi, \nabla\phi)$ and the external work $\mathcal{W}_{\text{ext}}$, such that

$$\int_\Omega \dot{\psi}\, \mathrm{d}V - \int_{\partial\Omega} \dot{\mathcal{W}}_{\text{ext}}\, \mathrm{d}S \leqslant 0 \tag{2.8}$$

which is commonly known as the Clausius–Duhem inequality. Given (2.4b), the local free-energy inequality reads

$$\int_\Omega \dot{\psi}\, \mathrm{d}V - \int_{\partial\Omega} \left\{ \mathbf{h} \cdot \dot{\mathbf{u}} + \mathfrak{f}\dot{\phi} \right\} \mathrm{d}S - \int_\Omega \mathbf{b} \cdot \dot{\mathbf{u}}\, \mathrm{d}V \leqslant 0 \tag{2.9}$$

By plugging in Eq. (2.7) and utilizing the divergence theorem, we can reformulate the local free-energy inequality as follows:

$$\int_\Omega \dot{\psi}\, \mathrm{d}V - \int_\Omega \left\{ \left[(\nabla \cdot \boldsymbol{\sigma}) \cdot \dot{\mathbf{u}} + \boldsymbol{\sigma} : \nabla\dot{\mathbf{u}} \right] + \left[(\nabla \cdot \boldsymbol{\xi})\, \dot{\phi} + \boldsymbol{\xi} \cdot \nabla\dot{\phi} \right] \right\} \mathrm{d}V \leqslant 0 \tag{2.10}$$

which by inserting Eq. (2.6) reads

$$\int_\Omega \dot{\psi}\, \mathrm{d}V - \int_\Omega \left\{ \boldsymbol{\sigma} : \nabla\dot{\mathbf{u}} + \omega\dot{\phi} + \boldsymbol{\xi} \cdot \nabla\dot{\phi} \right\} \mathrm{d}V \leqslant 0 \tag{2.11}$$

Since Eq. (2.11) should hold for any arbitrary domain, it must also be satisfied locally,

$$\left(\boldsymbol{\sigma} - \frac{\partial\psi}{\partial\boldsymbol{\varepsilon}} \right) : \dot{\boldsymbol{\varepsilon}} + \left(\omega - \frac{\partial\psi}{\partial\phi} \right) \dot{\phi} + \left(\xi - \frac{\partial\psi}{\partial\nabla\phi} \right) \cdot \nabla\dot{\phi} \geqslant 0 \tag{2.12}$$

for which we introduce a free energy function ψ as the sum of the elastic strain energy density ψ^e and the fracture surface energy density ψ^s, such that

$$\psi(\boldsymbol{\varepsilon}, \phi, \nabla\phi \,|\, \bar{\alpha}) = \psi^e(\boldsymbol{\varepsilon}, \phi) + \psi^s(\phi, \nabla\phi \,|\, \bar{\alpha}) \tag{2.13}$$

2.4 Constitutive theory

Building on the definition of free energy (2.13), we will now establish a constitutive theory that accounts for the coupling between the deformation, fracture, and fatigue behavior.

2.4.1 Elasticity

We define the strain energy density ψ^e as a function of the strains $\boldsymbol{\varepsilon}$, the isotropic linear elastic stiffness tensor $\boldsymbol{\mathcal{L}}_0$, and a phase field degradation function $g(\phi)$, which will be introduced shortly. Therefore, we have:

$$\psi^e(\boldsymbol{\varepsilon}, \phi) = g(\phi)\psi_0^e(\boldsymbol{\varepsilon}) \quad \text{with} \quad \psi_0^e(\boldsymbol{\varepsilon}) = \frac{1}{2}\boldsymbol{\varepsilon}^{\mathsf{T}} : \boldsymbol{\mathcal{L}}_0 : \boldsymbol{\varepsilon} \tag{2.14}$$

Here, ψ_0^e represents the strain energy density for an isotropic solid that is undamaged. With this in mind, we can obtain the Cauchy stress tensor $\boldsymbol{\sigma}$ as follows:

$$\boldsymbol{\sigma} = \frac{\partial\psi}{\partial\boldsymbol{\varepsilon}} = g(\phi)\boldsymbol{\mathcal{L}}_0 : \boldsymbol{\varepsilon} \tag{2.15}$$

It's worth noting that the phase field variable affects the material's stiffness, as is commonly observed in CDM-based models.

2.4.2 Fracture surface energy

We will now define the fracture surface energy density ψ^s in accordance with Eq. (2.3). Specifically, this surface energy density is a function of the phase field damage ϕ, its gradient $\nabla\phi$, and a fatigue degradation function $f(\bar{\alpha})$, which will be introduced later. The definition of ψ^s can be expressed as follows:

$$\psi^s(\phi, \nabla\phi \,|\, \bar{\alpha}) = f(\bar{\alpha})\, G_c\, \gamma_\ell(\phi, \nabla\phi) \tag{2.16}$$

where the crack surface density functional γ_ℓ is given by:

$$\gamma_\ell(\phi, \nabla\phi) = \frac{1}{4c_w}\left(\frac{w(\phi)}{\ell} + \ell|\nabla\phi|^2\right) \quad \text{with} \quad c_w = \int_0^1 \sqrt{w(\zeta)}\,\mathrm{d}\zeta \tag{2.17}$$

Here, $w(\phi)$ is the geometric crack function, which will be defined shortly, and c_w is a scaling factor.

2.4.3 Strain energy decomposition

The original phase field fracture model predicts analogous responses under tension and compression. This implies that crack propagation is equally affected by tensile and compressive stresses, and owing to the isotropic degradation of material stiffness, the crack surfaces can overlap without sustaining any compressive forces. To prevent the initiation and growth of cracks during compression, it is suggested to decompose the strain energy density into tensile (active) and compressive (inactive) components,

$$\psi^e(\boldsymbol{\varepsilon}, \phi) = g(\phi)\, \psi_0^+(\boldsymbol{\varepsilon}) + \psi_0^-(\boldsymbol{\varepsilon}) \tag{2.18}$$

where the degradation resulting from the phase field evolution impacts only the tensile (active) portion of the strain energy density. There are several decomposition splits that have been proposed in the literature. In this thesis, we will adopt several widely used formulations. The isotropic model, also known as No-split, which was first introduced in [19], involves the degradation of the entire strain energy density, as given in Eq. (2.14). As a consequence, fracture propagation can occur even in compressed regions, leading to crack trajectories that are physically unrealistic [100]. This limits the isotropic model to cases involving monotonic tensile loading. To address the limitations of the isotropic model, the volumetric/deviatoric split was proposed in [100]. With this formulation, the degradation function affects only the energy density associated with the positive volumetric part and the deviatoric part of the strain tensor. The corresponding expression is given as follows:

$$\begin{aligned} \psi_0^+(\boldsymbol{\varepsilon}) &= \frac{1}{2}\left(\lambda + \tfrac{2}{3}Q\right)\langle \mathrm{tr}(\boldsymbol{\varepsilon})\rangle_+^2 + Q\,(\boldsymbol{\varepsilon}' : \boldsymbol{\varepsilon}') \\ \psi_0^-(\boldsymbol{\varepsilon}) &= \frac{1}{2}\left(\lambda + \tfrac{2}{3}Q\right)\langle \mathrm{tr}(\boldsymbol{\varepsilon})\rangle_-^2 \end{aligned} \quad \text{with} \quad \boldsymbol{\varepsilon}' = \boldsymbol{\varepsilon} - \frac{1}{3}\,\mathrm{tr}(\boldsymbol{\varepsilon})\boldsymbol{I} \tag{2.19}$$

Here, λ and Q are the Lamé constants for isotropic materials, and $\mathbf{I}$ represents the identity matrix. Additionally, $\pm$ denotes the plus-minus sign, and $\langle\Box\rangle$ refers to the Macaulay brackets, $\langle\Box\rangle_\pm := \frac{1}{2}(\Box \pm |\Box|)$, to select either the positive or negative portion of the argument. The next formulation we consider is the spectral split, which was proposed in [21]. It distinguishes between the degraded and undegraded components of the strain energy density using the spectral decomposition of the strain tensor,

$$\psi_0^\pm(\boldsymbol{\varepsilon}) = \frac{1}{2}\lambda\langle \mathrm{tr}(\boldsymbol{\varepsilon})\rangle_\pm^2 + Q\,\mathrm{tr}\left(\boldsymbol{\varepsilon}_\pm^2\right) \quad \text{with} \quad \boldsymbol{\varepsilon}_\pm = \sum_{i=1}^{3} \langle \varepsilon_i\rangle_\pm\, \mathbf{n}_i \otimes \mathbf{n}_i \tag{2.20}$$

Here, the strain tensor is expressed in terms of the principal strains $\{\varepsilon_i\}_{i=1}^3$ and their corresponding principal directions $\{\mathbf{n}_i\}_{i=1}^3$. The difference between the decomposition splits (2.20) and (2.19) is apparent when all three principal strains are negative, as discussed in [30]. In such a situation, the deviatoric strain energy portion of Eq. (2.19) will still degrade, causing the phase field variable to evolve in the affected areas. The final approach is the No-tension split, first proposed in [101]. It only degrades the energy associated with the positive-definite symmetric part of the strain tensor leaving the negative-definite symmetric part undegraded. This formulation is capable of capturing the behavior of masonry-like brittle and quasi-brittle materials [102], which tend to develop cracks parallel to the axial direction under uniaxial compression. The procedures for defining 3D strain states are outlined in [59], while the energy split is given by:

$$\psi_0^{\pm}(\boldsymbol{\varepsilon}) = \frac{1}{2}\lambda\,\mathrm{tr}^2(\boldsymbol{\varepsilon}_{\pm}) + Q\,\mathrm{tr}\left(\boldsymbol{\varepsilon}_{\pm}^2\right) \qquad \text{with} \qquad \boldsymbol{\varepsilon}_{\pm} = \mathrm{sym}_{\pm}(\boldsymbol{\varepsilon}) \tag{2.21}$$

Here, $\mathrm{sym}_{\pm}(\boldsymbol{\varepsilon})$ denotes the positive- or negative-definite symmetric portion of the strain tensor. It should be highlighted that due to the strain energy decomposition, the stress-strain relationship becomes highly non-linear

$$\boldsymbol{\sigma} = g(\phi)\,\frac{\partial \psi_0^{+}(\boldsymbol{\varepsilon})}{\partial \boldsymbol{\varepsilon}} + \frac{\partial \psi_0^{-}(\boldsymbol{\varepsilon})}{\partial \boldsymbol{\varepsilon}} \tag{2.22}$$

which often necessitates a significantly greater computational effort when compared to the isotropic formulation. To address this issue, Ambati et al. [103] proposed a *hybrid* formulation that combines the strengths of both the isotropic and decomposition split models. By doing so, they were able to significantly reduce the computational cost while still accurately capturing the material behavior. The primary idea underlying the hybrid formulation involves applying decomposition exclusively to the phase field evolution equation (2.6b) while maintaining the linear momentum balance equation (2.6a) derived from the isotropic model. As a result, crack propagation is primarily driven by the tensile (active) component of the strain energy, whereas the stiffness degradation caused by the phase field evolution occurs isotropically, but only when the stress state is primarily tensile.

2.4.4 Irreversibility condition

Damage represents an irreversible process, and therefore, the phase field evolution law must satisfy the condition $\dot{\phi} \geqslant 0$. In accordance with Miehe et al. [22], we introduce a history variable field $\mathcal{H}$ for a given time t,

$$\mathcal{H} = \max_{\tau \in [0,t]} \psi_0^{+}(\boldsymbol{\varepsilon}(x,\tau))\,, \tag{2.23}$$

that complies with the Karush-Kuhn-Tucker (KKT) conditions for both loading and unloading phases,

$$\psi_0^{+} - \mathcal{H} \leqslant 0\,, \qquad \dot{\mathcal{H}} \geqslant 0\,, \qquad \dot{\mathcal{H}}(\psi_0^{+} - \mathcal{H}) = 0 \tag{2.24}$$

Despite its practicality and potential to facilitate the convergence of phase field solution, the history variable method has faced substantial criticism [36, 104] due to its potential impact on crack initiation from non-sharp defects, as well as its violation of variational consistency. However, the latter concern is not significant in this context since the fatigue extension of the phase field does not follow variational consistency in its current form. Alternative methods for enforcing irreversibility have also been suggested, including penalty-based approaches [105, 106], Lagrange multiplier methods [107], and crack-sets [19, 108]. For an in-depth discussion and comparative studies, refer to Ref. [106]. In this thesis, we utilize the crack-set approach in combination with the history variable

method. This involves adding nodes to a set with a Dirichlet-type boundary condition of $\phi = 1$, based on the phase field variable surpassing a specified threshold (in this case: 0.95). We have observed that this approach appears to alleviate certain convergence problems that arise at the initial crack tip following a certain degree of crack propagation in high-cycle fatigue simulations.

2.4.5 Phase field micro-force variables

We now derive the phase field micro-stress quantities ω and $\boldsymbol{\xi}$. Initially, by considering Eqs. (2.14), (2.16), and (2.23), we obtain the total free energy density of the solid (Eq. (2.13) as follows:

$$\psi(\boldsymbol{\varepsilon}, \phi, \nabla\phi \,|\, \bar{\alpha}) = g(\phi)\mathcal{H} + f(\bar{\alpha})\frac{G_c}{4c_w}\left(\frac{w(\phi)}{\ell} + \ell|\nabla\phi|^2\right) \tag{2.25}$$

As a result, the micro-stress variables ω and $\boldsymbol{\xi}$ can be easily determined as

$$\omega = \frac{\partial\psi}{\partial\phi} = g'(\phi)\mathcal{H} + f(\bar{\alpha})\frac{G_c}{4c_w\ell}w'(\phi) \qquad \boldsymbol{\xi} = \frac{\partial\psi}{\partial\nabla\phi} = f(\bar{\alpha})\frac{G_c\ell}{2c_w}\nabla\phi \tag{2.26}$$

By incorporating these constitutive relations into the phase field balance equation (2.6b), we obtain the strong form of the phase field damage evolution under fatigue loading,

$$\frac{G_c f(\bar{\alpha})}{2c_w}\left(\frac{w'(\phi)}{2\ell} - \ell\nabla^2\phi\right) - \frac{G_c\ell}{2c_w}\nabla\phi\nabla f(\bar{\alpha}) + g'(\phi)\mathcal{H} = 0 \tag{2.27}$$

2.4.6 Degradation and dissipation functions

First, we set out to establish the phase field degradation function $g(\phi)$, which controls the degradation of the elastic strain energy as damage progresses, and it must fulfill the following requirements:

$$g(0) = 1, \qquad g(1) = 0, \qquad g'(\phi) \leqslant 0 \qquad \text{for} \quad 0 \leqslant \phi \leqslant 1 \tag{2.28}$$

Here, the first two conditions serve as limits for the intact and completely fractured states, while the final condition guarantees the convergence of $\partial\psi/\partial\phi$ to a final value in the fully fractured state. In this thesis, we utilize the extensively applied quadratic degradation function:

$$g(\phi) = (1-\phi)^2 \tag{2.29}$$

Furthermore, we establish the damage dissipation function $w(\phi)$, which governs the energy dissipation resulting from the creation of a new crack, and it must satisfy the following conditions:

$$w(0) = 0, \qquad w(1) = w_1 > 0, \qquad w'(\phi) \geqslant 0 \qquad \text{for} \quad 0 \leqslant \phi \leqslant 1 \tag{2.30}$$

To achieve this, we employ two of the arguably most prominent phase field damage models found in the literature, known as the `AT1` [109] and `AT2` [20] models. Both models are grounded in the Ambrosio and Tortorelli (AT) [110] regularization approach, which is inspired by the image segmentation study conducted by Mumford and Shah [111]. The particular choice of $w(\phi) = \phi^2, (c_w = 1/2)$ results in the `AT2` formulation, whereas $w(\phi) = \phi, (c_w = 2/3)$ leads to the `AT1` model. The latter encompasses a purely linear and elastic strain-stress response before the initiation of damage, in contrast to the `AT2` scenario, where $w'(0) = 0$. By incorporating these specific choice into the generalized strong

form of the phase field damage evolution (2.27), we obtain the following particularised strong forms, excluding fatigue behavior:

$$\begin{aligned} \frac{3G_c}{8\ell}\left(1-2\ell^2\Delta\phi\right)-2(1-\phi)\mathcal{H}=0 \qquad &(\texttt{AT1}) \\ \frac{G_c}{\ell}\left(\phi-\ell^2\Delta\phi\right)-2(1-\phi)\mathcal{H}=0 \qquad &(\texttt{AT2}) \end{aligned} \tag{2.31}$$

A key characteristic of the AT2 model is its natural confinement within the range of 0 to 1. Consequently, there is no requirement for supplementary measures to ensure adherence to these boundaries. On the other hand, the AT1 model does not intrinsically impose a lower bound on the phase field variable, causing the phase field to gravitate towards negative infinity as the strain approaches 0. To address this situation, it is necessary to define a fracture driving force threshold, $\mathcal{H}_{\text{min}}$, for the AT1 model, which guarantees that the history field in equation (2.23) results in [112]:

$$\mathcal{H}=\max\left\{\max_{\tau\in[0,t]}\psi_0^+(\boldsymbol{\varepsilon}(\mathbf{x},\tau)),\,\mathcal{H}_{\text{min}}\right\} \quad \text{with} \quad \mathcal{H}_{\text{min}}=\frac{3G_c}{16\ell} \tag{2.32}$$

Here, $\mathcal{H}_{\text{min}}$ represents the minimum threshold strain energy, which is derived from the homogeneous solution of Eq. (2.31a) when $\Delta\phi=0$. This occurs precisely at the onset of damage, when $\phi=0$. Recently, Molnár et al. [107] demonstrated that in certain cases, this minimum value might result in underestimating the fracture resistance. As an alternative, they proposed a method utilizing Lagrange multipliers, which was integrated into Abaqus to ensure both a lower bound and irreversibility for the phase field.

We will now consider the uniform/homogeneous solution to Eq. (2.31) with the aim of obtaining a more comprehensive understanding of the phase field length scale ℓ. Consequently, within a one-dimensional context, a sample characterized by Young's modulus E and exposed to a uniaxial monotonic tensile stress $\sigma=g\left(\phi\right)E\varepsilon$ will exhibit a homogeneous stress solution that attains its peak at the subsequent critical strength and strain:

$$\texttt{AT1}:\ \sigma_c=\sqrt{\frac{3EG_c}{8\ell}},\ \ \varepsilon_c=\sqrt{\frac{3G_c}{8\ell E}}, \qquad \texttt{AT2}:\ \sigma_c=\frac{3}{16}\sqrt{\frac{EG_c}{3\ell}},\ \ \varepsilon_c=\sqrt{\frac{G_c}{3\ell E}} \tag{2.33}$$

In this case, ℓ is demonstrated to be more than just a regularization parameter, as it also functions as a material property that specifies the material's strength. This capability allows phase field models to predict crack initiation and naturally account for the transition flaw size effect as demonstrated in [108, 113]. Essentially, phase field models excel at capturing both strength-dominated failures (related to short cracks) and toughness-dominated fractures (associated with long crack), as well as the seamless transition between these two criteria. However, the fact that the critical stress is determined by the phase field length scale can sometimes be problematic. The required size of the length scale relative to the problem's geometry might lead to an unrealistic critical stress, or conversely, as noted in [114]. To tackle these difficulties and separate the critical stress from phase field length scale, Sargado et al. [115] introduced a new set of degradation functions that maintain the linear elastic response before fracture occurs. At the same time, various researchers [116–118] have proposed combining phase field fracture models with cohesive zone models to create a more comprehensive approach. Other alternative phase field models suggested in the literature include those utilizing Ginzburg-Landau formulations [119], which are typically used in phase transition studies, or higher-order phase field models [24], which are known for their superior convergence properties. However, the latter approach necessitates a high degree of continuity in the discretization procedure, which has impeded its extensive implementation.

2.4.7 Fatigue damage

Phase field fatigue models have demonstrated their ability to capture the initiation and propagation of fatigue cracks, and inherently reproduce key features like the Wöhler curve or Paris law behavior [64]. Nonetheless, to accurately represent behaviors commonly observed in experimental data and extensively incorporated into fatigue design standards, current models require further refinement. Within the scope of total-life assessments, it is essential to define appropriate model or material parameters capable of capturing: (i) the S-N curve slope, (ii) the material's endurance limit, and (iii) the effect of load ratio. Therefore, our objective is to create a framework that integrates these additional modeling features, and demonstrate its capacity to replicate experimental findings while inherently accounting for stress concentration factors (e.g., estimating the fatigue life of a notched sample based on a smooth S-N curve).

First, in line with [63], the damage caused by cyclic loading is represented through the introduction of a fatigue degradation function $f(\bar{\alpha})$, which efficiently lowers the material's toughness based on the fatigue history accumulated in the solid. The fatigue degradation functions suggested in the literature [64, 69] are considered in this thesis:

$$
\begin{aligned}
f_0(\bar{\alpha}) &= \left(1 - \frac{\bar{\alpha} - \bar{\alpha}_0}{\bar{\alpha} + \bar{\alpha}_0}\right)^2 \qquad \text{for } \bar{\alpha} \in [\bar{\alpha}_0,\, \infty] \text{ (otherwise } f_0(\bar{\alpha}) = 1) \\
f_1(\bar{\alpha}) &= \left(1 - \frac{\bar{\alpha}}{\bar{\alpha} + \bar{\alpha}_0}\right)^2 \qquad \text{for } \bar{\alpha} \in [0,\, +\infty] \\
f_2(\bar{\alpha}) &= \left(1 - \frac{\bar{\alpha}}{\bar{\alpha}_0}\right)^2 \qquad \text{for } \bar{\alpha} \in [0,\, \bar{\alpha}_0] \\
f_3(\bar{\alpha}) &= \left(1 - \kappa \log \frac{\bar{\alpha}}{\bar{\alpha}_0}\right)^2 \qquad \text{for } \bar{\alpha} \in [\bar{\alpha}_0,\, \bar{\alpha}_0 10^{1/\kappa}] \text{ (otherwise } f_3(\bar{\alpha}) = 1)
\end{aligned}
\tag{2.34}
$$

Here, $\bar{\alpha}_0$ is intended to be a material parameter calibrated using experimental data. For the case of f_3, κ is an additional material parameter that controls its slope. As depicted in Fig. 2.2, the primary distinction among f_0, f_1, f_2, and f_3 is that both f_0 and f_1 yield asymptotically decreasing values, whereas f_2 and f_3 reach zero for a specific finite value of $\bar{\alpha}$. In addition, f_0 and f_3 introduce an initial threshold branch where the material toughness is not influenced by fatigue as the value of $\bar{\alpha}$ progressively increases. Furthermore, the fatigue history variable $\bar{\alpha}$ ought to represent the accumulation of any quantity α that characterizes the material's cyclic history. In accordance with Carrara et al. [64], we retain the model's energetic essence and utilize the tensile (active) portion of the elastic strain energy density, as defined in Section 2.4.3, to serve as the fatigue history variable,

$$
\alpha = g(\phi)\psi_0^+(\boldsymbol{\varepsilon}) \tag{2.35}
$$

Here, the use of the *degraded* strain energy density guarantees that the crack tip singularity will not impact its value. Subsequently, the evolution of the fatigue history variable $\bar{\alpha}$ can be described within the time discretization as follows:

$$
\bar{\alpha}_{t+\Delta t} = \bar{\alpha}_t + \int_t^{t+\Delta t} \dot{\bar{\alpha}}\, \mathrm{d}\tau = \bar{\alpha}_t + \Delta\bar{\alpha} \tag{2.36}
$$

A crucial element in the development of phase field fatigue models hinges on the determination of $\Delta\bar{\alpha}$, which represents the method used to account for fatigue damage accumulation. In [64], fatigue damage accumulation is taken into consideration solely during the

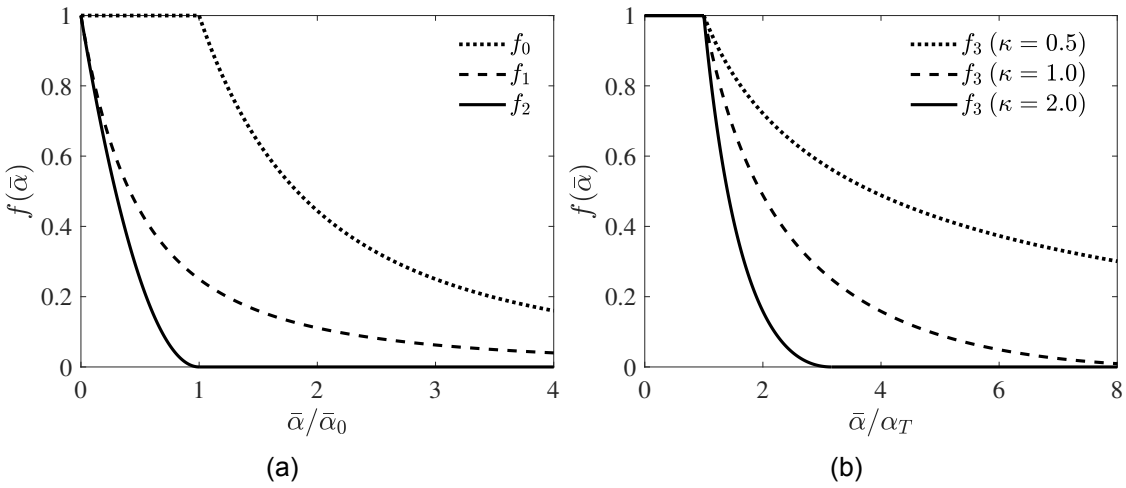

Figure 2.2: Evolution of the fatigue degradation functions, see Eq. (2.34).

loading portion of the cycle, which negatively impacts the monotonic loading scenarios. To rectify this problem, Seles et al. [69] proposed accounting for fatigue damage accumulation exclusively during the unloading phase. Nevertheless, our observations indicate that this could lead to an unrealistic growth in the fatigue history variable in regions behind the crack tip due to localized unloading at those areas. In this thesis, we recommend considering fatigue damage accumulation only during a single reversal per cycle (from peak to valley, as illustrated in Fig. 2.3), thereby avoiding any adverse effects on monotonic loading scenarios. The updated accumulation approach has great significance as it allows for a substantial reduction in computational costs by enabling the accurate representation of $\bar{\alpha}$ accumulation with just one increment per cycle. For loading cases with constant amplitude, internal increments within a cycle can be substituted by applying a constant load with the maximum amplitude value as its magnitude. As demonstrated in Fig. 2.3, the fatigue history variable's maximum and minimum values, labeled as α_{max} and α_{min}, can be assessed at the peak and valley of the cycle during a single reversal. Expanding on our fatigue accumulation approach, we move forward to establish a model represented by $\Delta\bar{\alpha}$, which takes into account (i) the S-N curve slope, (ii) the material's endurance limit, and (iii) the influence of the stress ratio. This all-encompassing formula

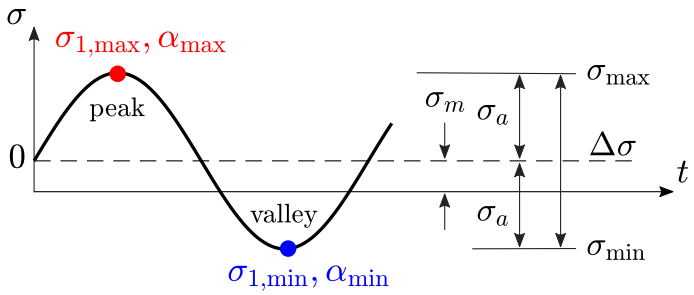

Figure 2.3: Constant amplitude cyclic stressing and definitions of the main variables. The red dot (peak) shows the location where $\sigma_{1,\text{max}}$ and α_{max} are calculated, where the blue dot (valley) shows the instant at which $\sigma_{1,\text{min}}$ and α_{min} are determined. Adapted from [P1].

is expressed as follows:

$$\Delta\bar{\alpha} = \left(\frac{\alpha_{\max}}{\alpha_n}\right)^n \left(\frac{1-R}{2}\right)^{2\eta n} H\left(\max_{\tau\in[0,t]} \alpha_{\max}\left(\frac{1-R}{2}\right)^{2\eta} - \alpha_e\right) \tag{2.37}$$

and each of its elements is described below. Here, one should note that $\Delta\bar{\alpha}$ is defined as a dimensionless quantity.

Slope of the S-N curve. To grant the model the necessary adaptability to align with any S-N curve slope, we introduce a material parameter, the exponent n, along with an extra term, $(\alpha_{\max}/\alpha_n)^n$. A normalization parameter, α_n, is required for maintaining dimensional coherence. We choose $\alpha_n = 1/2\sigma_c\varepsilon_c$, which is derived from the critical stresses and strains provided in Eq. (2.33).

Endurance Limit. To incorporate a material endurance limit into the model, we introduce a fatigue threshold variable, α_e, which represents the point below which cyclic damage does not take place. This is employed in conjunction with the Heaviside function $H(\square)$, which equals one for positive arguments and zero otherwise. The value of α_e can be approximated using the material's fatigue/endurance limit σ_e, which is the stress level below which a material can endure an infinite number of repeated load cycles without exhibiting failure, as $\alpha_e = \sigma_e^2/(2E)$.

Stress Ratio. The stress or load ratio is known to have a considerable impact on fatigue behavior and can be defined as $R = \sigma_{1,\min}/\sigma_{1,\max}$, where $\sigma_{1,\max}$ and $\sigma_{1,\min}$ represent the maximum and minimum principal stresses within each cycle, respectively (refer to Fig. 2.3). For proportional loading, as seen in all analyses within this thesis, this definition does not pose any confusion. However, when dealing with non-proportional loading, it becomes essential to accurately define the values. A suitable approach could involve determining the direction, $\boldsymbol{n}_1$, based on the maximum principal value, and then assessing both the maximum and minimum stresses along that direction. It should be emphasized that R is not an input to the model; rather, it is a material point quantity that can be assessed upon the completion of each cycle. In order to incorporate R into our fatigue accumulation approach, we draw inspiration from conventional mean stress relationships/theories. Specifically, the Walker mean stress relationship [120] has been extensively employed to enhance Basquin-type laws in order to accommodate non-zero mean stresses. The expression for this relationship is as follows:

$$\sigma_{ar} = \sigma_{\max}\left(\frac{1-R}{2}\right)^{\eta}, \qquad \text{for } (\sigma_{\max} > 0) \tag{2.38}$$

In this context, σ_{ar} represents the equivalent stress amplitude, which is defined as the stress amplitude causing the same degree of material damage under cyclic loading with a zero mean stress ($\sigma_m = 0$). The material constant η, ranging from 0 to 1, is introduced to characterize the material's susceptibility to mean stress. The Walker equation simplifies to the prevalent Smith-Watson-Topper (SWT) relationship [121], for $\eta = 0.5$. When sufficient data is accessible for calibrating η, the Walker equation exhibits excellent consistency with experimental findings [122]. As demonstrated in Eq. (2.37), our proposed model incorporates terms inspired by Walker's approach to accommodate the impact of load ratio.

3 Hydrogen embrittlement

In this chapter, we explore the essential concepts related to hydrogen embrittlement and its impact on the fracturing of solids. The transport of hydrogen to the fracture process zone is based on a synergistic deformation-diffusion mechanism, which is influenced by chemical potential gradients. This mechanism extends Fick's law for mass diffusion and ultimately affects the subsequent cracking process. The cracking behavior is governed by a hydrogen-sensitive surface energy deterioration law, which is founded on rigorous first-principles calculations.

3.1 Kinematics

Let C denote the number of hydrogen atoms measured in moles per unit volume. When hydrogen enters the metal, it occupies both normal interstitial lattice sites (NILS) and microstructural trapping sites that are linked to internal imperfections, like voids and dislocations. In this thesis, we only consider the concentration of hydrogen within the lattice sites. The variation in hydrogen concentration over time, represented as $\dot{C} = \mathrm{d}C/\mathrm{d}t$, is due to the diffusion of hydrogen across the outer boundary $\partial\Omega$, with an outward normal $\mathbf{n}$, as follows:

$$\int_{\Omega} \dot{C}\,\mathrm{d}V + \int_{\partial\Omega} \mathbf{J}\cdot\mathbf{n}\,\mathrm{d}S = 0 \tag{3.1}$$

where $\mathbf{J}$ represents the hydrogen flux, measured as the number of hydrogen atoms in moles per unit area per unit time. By applying Gauss' divergence theorem, the local balance equation for the hydrogen transport in Ω is obtained as

$$\dot{C} + \nabla\cdot\mathbf{J} = 0 \tag{3.2}$$

along with the concentration flux $q = -\mathbf{J}\cdot\mathbf{n}$, which serves as a boundary condition on $\partial\Omega$. Hence, the outer boundary of the body is divided into two parts, $\partial\Omega_C$ and $\partial\Omega_q$. The first part, $\partial\Omega_C$, corresponds to the region where the hydrogen concentration C is prescribed by Dirichlet-type boundary conditions. The second part, $\partial\Omega_q$, corresponds to the region where the hydrogen flux $\mathbf{J}$ is dictated by Neumann-type boundary conditions. The hydrogen diffusion is driven by the gradient of the chemical potential, $\nabla\mu$, which is linked to the hydrogen flux through the linear Onsager relation [123], as follows:

$$\mathbf{J} = -\frac{DC}{\mathcal{R}T}\nabla\mu \tag{3.3}$$

where $\mathcal{R} = 8.314\,\mathrm{J/(mol\,K)}$ is the gas constant, T is the absolute temperature, and D denotes the diffusivity coefficient, which is assumed to be unaffected by variations in the stress state.

3.2 Hydrogen-dependent surface energy

As previously discussed in Section 1.4, the significant reduction in fracture resistance observed in metals subjected to hydrogen is encapsulated by drawing upon atomistic insights. The hydrogen enhanced decohesion (HEDE) mechanism postulates that the accumulation of hydrogen atoms within the crystal lattice weakens the bond energy between metal atoms. Numerous investigations employing Density Functional Theory (DFT) have been carried out to explore the decohesion of fracture surfaces while altering hydrogen coverage (refer to, e.g., [124–126] and the cited references). As mentioned in Refs.

[54, 85], DFT computations of surface energy sensitivity in relation to hydrogen coverage demonstrate a linear trend, with the slope dependent on the specific material system being studied. Alvaro et al. [125], for instance, calculated the change in surface energy due to the presence of hydrogen atoms at $\Sigma 3$ and $\Sigma 5$ grain boundaries in nickel. Their findings, presented as normalized surface energy $\gamma(\theta)/\gamma(0)$ are illustrated in Fig. 3.1 as a function of hydrogen coverage θ, accompanied by a linear fit to the dataset. Consequently, a quantum mechanically guided degradation law can be established as follows:

$$\frac{\gamma(\theta)}{\gamma(0)} = 1 - \chi\theta \tag{3.4}$$

where, χ represents the damage coefficient that quantifies the hydrogen-induced reduction of fracture energy. Likewise, χ can be approximated for other materials by fitting DFT calculations. In their study, Jiang and Carter [124] estimated values of 0.89 and 0.67 for iron and aluminum, respectively. Considering the connection between the critical energy release rate and the surface energy, given by $G_c = 2\gamma$, it is possible to alternatively express the dependence of the critical energy release rate on hydrogen coverage as follows:

$$\frac{G_c(\theta)}{G_c(0)} = 1 - \chi\theta \tag{3.5}$$

where $G_c(0)$ denotes the critical energy release rate in an inert environment. Ultimately, the Langmuir-McLean isotherm can be employed to calculate the hydrogen coverage θ at decohering interfaces from the bulk concentration, in accordance with thermodynamic equilibrium, as expressed below:

$$\theta = \frac{C}{C + \exp\left(\frac{-\Delta g_b^0}{\mathcal{R}T}\right)} \tag{3.6}$$

Here, Δg_b^0 signifies the interface binding energy. Assuming that intergranular cracking takes place in the presence of hydrogen, a value of Δg_b^0 =30 kJ/mol is consistently applied throughout this thesis to represent hydrogen trapped at grain boundaries [85, 97].

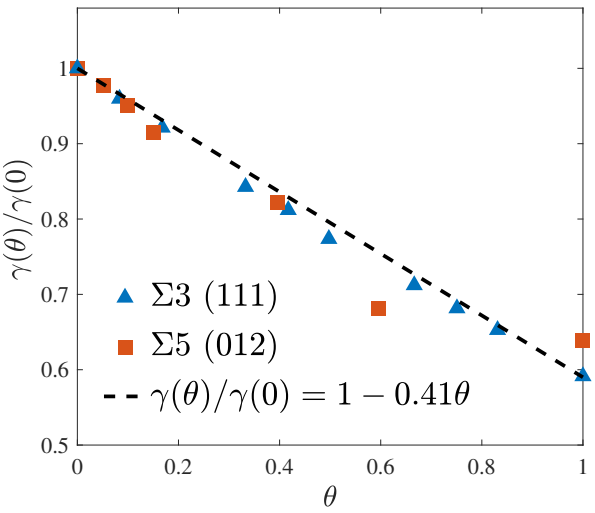

Figure 3.1: Impact of hydrogen on nickel's surface energy. Linear fitting of DFT computations by Alvaro et al. [125] for $\Sigma 3$ and $\Sigma 5$ grain boundaries. *Source*: Adapted from [54].

Consequently, the current framework accounts for the influence of microstructural trapping sites on fracture and can include their impact on mass transport using an effective diffusivity coefficient. The particular choices made here are grounded in the assumption that hydrogen-induced cracking is driven by an interface decohesion mechanism. Nevertheless, it is important to highlight that the phase field formulation developed for hydrogen-assisted fatigue is versatile, as it can be adjusted to incorporate various phenomenological or mechanistic interpretations by selecting appropriate hydrogen degradation functions $f_C = G_c(C)/G_c(0)$.

3.3 Stress-driven hydrogen transport couple with phase field fracture

We now proceed to couple the hydrogen diffusion problem with the mechanical-phase field problem, as outlined in Section 2. Recalling the Clausius–Duhem inequality (2.9) and accounting for the flux of energy carried into the body through its out boundary by the diffusing species, the local free-energy inequality (2.10) renders

$$\int_\Omega \dot{\psi}\,\mathrm{d}V - \int_{\partial\Omega} \left\{ \mathbf{h}\cdot\dot{\mathbf{u}} + \mathfrak{f}\dot{\phi} \right\} \mathrm{d}S - \int_\Omega \mathbf{b}\cdot\dot{\mathbf{u}}\,\mathrm{d}V - \int_{\partial\Omega} q\,\mu \leqslant 0 \tag{3.7}$$

Utilizing the divergence theorem and considering Eqs. (2.7) and (3.2) along with their corresponding set of boundary conditions, the local free-energy imbalance reads

$$\left(\boldsymbol{\sigma} - \frac{\partial\psi}{\partial\boldsymbol{\varepsilon}}\right) : \dot{\boldsymbol{\varepsilon}} + \left(\omega - \frac{\partial\psi}{\partial\phi}\right)\dot{\phi} + \left(\xi - \frac{\partial\psi}{\partial\nabla\phi}\right)\cdot\nabla\dot{\phi} + \left(\mu - \frac{\partial\psi}{\partial C}\right)\dot{C} - \mathbf{J}\cdot\nabla\mu \geqslant 0 \tag{3.8}$$

for which the free energy function ψ, which previously introduced in Section 2.3, is now altered to account for the effect of hydrogen, including the hydrogen-chemical energy density ψ^C, as follows:

$$\begin{aligned}\psi(\boldsymbol{\varepsilon},\phi,\nabla\phi,C\,|\,\bar{\alpha}) = &\underbrace{g(\phi)\left(\psi_0^e - K\bar{V}_H\left(C-C^0\right)\mathrm{tr}\,\boldsymbol{\varepsilon}\right)}_{\psi^e} \\ &+ \underbrace{f(\bar{\alpha})f_C(C)\frac{G_c}{4c_w}\left(\frac{w(\phi)}{\ell} + \ell|\nabla\phi|^2\right)}_{\psi^s} \\ &+ \underbrace{\mu^0 C + \mathcal{R}TN\big(\theta\,\ln(\theta) + (1-\theta)\,\ln(1-\theta)\big)}_{\psi^C}\end{aligned} \tag{3.9}$$

where μ^0 and C^0 represent the reference chemical potential and hydrogen concentration, respectively, while N denotes the number of interstitial lattice sites with a lattice site occupancy $\theta = C/N$. The material's bulk modulus is denoted by $K = \lambda + 2/3Q$, and the hydrogen's partial molar volume, denoted by $\bar{V}_H$, has a value of $\bar{V}_H = 2000\,\mathrm{mm}^3/\mathrm{mol}$ for iron-based materials. The elastic strain energy density ψ^e, discussed in Section 2.4.1, has been adapted to account for the influence of hydrogen, as described by Di Leo et al. [127]. This updated formulation is now referred to as the chemo-elastic strain energy density. The fracture energy ψ^s remains in accordance with the definition provided in Section 2.4.2. However, the material toughness now depends on the hydrogen content, as it is influenced by the hydrogen degradation function $f_C(C)$. In accordance with the revised free energy density definition (3.9), we will present our constitutive choices that consider

the interplay among deformation, fatigue fracture, and hydrogen diffusion. Concerning deformation, the Cauchy stress tensor $\boldsymbol{\sigma}$ is now determined as:

$$\boldsymbol{\sigma} = \frac{\partial \psi}{\partial \boldsymbol{\varepsilon}} = g(\phi)\left(\boldsymbol{\mathcal{L}}_0 : \boldsymbol{\varepsilon} - K\bar{V}_H\left(C - C^0\right)\boldsymbol{I}\right) \tag{3.10}$$

The second term, accounting for lattice dilation, is generally regarded as having a negligible influence on hydrogen embrittlement phenomena, as indicated by Hirth [128]. Consequently, it is omitted from consideration. In the context of phase field fracture, the microstress variables ω and $\boldsymbol{\zeta}$, as derived in Section 2.4.5, have been modified to incorporate the influence of hydrogen:

$$\omega = \frac{\partial \psi}{\partial \phi} = g'(\phi)\mathcal{H} + f(\bar{\alpha})\frac{G_c(C)}{4c_w\ell}w'(\phi) \qquad \boldsymbol{\xi} = \frac{\partial \psi}{\partial \nabla\phi} = f(\bar{\alpha})\frac{G_c(C)\ell}{2c_w}\nabla\phi \tag{3.11}$$

To complete our constitutive theory, we present the relevant relations for hydrogen transport. Consistent with equations (3.8) to (3.9), the chemical potential of hydrogen in lattice sites is derived as follows:

$$\mu = \frac{\partial \psi}{\partial C} = \mu^0 + \mathcal{R}T\ln\left(\frac{\theta}{1-\theta}\right) - \bar{V}_H\sigma_H + f(\bar{\alpha})\frac{\mathrm{d}G_c(C)}{\mathrm{d}\theta}\frac{\mathrm{d}\theta}{\mathrm{d}C}\frac{1}{4c_w}\left(\frac{w(\phi)}{\ell} + \ell|\nabla\phi|^2\right) \tag{3.12}$$

which includes a hydrostatic stress σ_H-dependent term to account for the impact of volumetric strains on driving diffusion [129]. The last term, which enhances hydrogen transport from damaged regions to intact regions by lowering the chemical potential, is neglected and instead a penalty-based *moving* chemical boundary condition is implemented to enable the aqueous solution to immediately occupy the space created with crack advance [130] (see section 4.4 for details regarding implementation). It should be noted that this is only relevant to experiments where the specimen is continuously exposed to a hydrogenous environment, as opposed to the tests where hydrogen has been dissolved within the material prior to loading and not during the tests. By substituting the chemical potential equation (3.12) into the Onsager relation (3.3), we can determine the hydrogen flux **J** as follows:

$$\mathbf{J} = -\frac{DC}{(1-\theta)}\left(\frac{\nabla C}{C} - \frac{\nabla N}{N}\right) + \frac{DC}{\mathcal{R}T}\bar{V}_H\nabla\sigma_H \tag{3.13}$$

Assuming low occupancy ($\theta \ll 1$) and a constant concentration of lattice sites ($\nabla N = 0$), we arrive at the following equation for the hydrogen flux:

$$\mathbf{J} = -D\nabla C + \frac{DC}{\mathcal{R}T}\bar{V}_H\nabla\sigma_H \tag{3.14}$$

From Eq. (3.12) or Eq. (3.14), it is clear that hydrostatic tensile stresses decrease the chemical potential (or increase the hydrogen flux), which in turn leading to enhanced hydrogen solubility as a result of lattice dilation. This process attracts hydrogen towards regions experiencing high volumetric strains, like crack tips. In addition, the idea presented can be applied to the transportation of hydrogen in a lattice or in a diffusible form, depending on the value assigned to the hydrogen diffusivity coefficient D. The effect of trap density evolution, such as in dislocation trapping sites, is not considered here for simplicity, but it can be included by following Isfandbod and Martínez-Pañeda [131].

3.4 Governing equations for coupled problem

By incorporating the constitutive choices (3.11) and (3.14) into Eqs. (2.6b) and (3.2), respectively, and assuming a small concentration gradient at the interface [54], we can

obtain updated strong forms of the phase field damage evolution and the hydrogen diffusion problem. As a result, the coupled deformation-diffusion-phase field problem can be summarized by its strong forms:

$$\begin{aligned} \nabla \cdot \big(g(\phi)\boldsymbol{\mathcal{L}}_0 : \boldsymbol{\varepsilon}\big) + \mathbf{b} &= \mathbf{0} \\ \frac{G_c(C) f(\bar{\alpha})}{2c_w}\left(\frac{w'(\phi)}{2\ell} - \ell\nabla^2\phi\right) - \frac{G_c(C)\ell}{2c_w}\nabla\phi\nabla f(\bar{\alpha}) + g'(\phi)\mathcal{H} &= 0 \\ \dot{C} - D\nabla^2 C + \nabla\cdot\left(\frac{DC}{\mathcal{R}T}\bar{V}_H\nabla\sigma_H\right) &= 0 \end{aligned} \tag{3.15}$$

where the physical elements of the problem are interdependent and interact in a sequential manner. Initially, mechanical deformation generates a stress field that affects the transport of hydrogen. The hydrostatic stress gradient is particularly significant, as demonstrated in equation (3.15c). Subsequently, mass transport causes the accumulation of hydrogen at the fracture process zone, which leads to a decrease in the critical energy release rate and affects fracture resistance. This, in turn, influences the phase field evolution, as stated in equation (3.15b). Finally, the hydrogen-sensitive phase field variable reduces stiffness via a phase field degradation function, which is reflected in the linear momentum balance equation (3.15a).

4 Numerical implementation

This section outlines the numerical implementation of the coupled deformation-diffusion-phase field problem within the framework of the finite element method. The solution strategies for the resulting system of equations are explained, along with the fatigue acceleration techniques developed in this thesis. To incorporate *moving* chemical boundary conditions, a penalty approach is employed, allowing the diffusion-environment interface to evolve in accordance with the phase field crack. The models are implemented in Abaqus, a commercial finite element software, using user element (UEL) subroutines, which allow the user to define tangent stiffness matrices and right-hand side vectors through the use of FORTRAN code. A separate implementation is also carried out in Julia, utilizing the open-source finite element package Ferrite.jl. To promote collaboration and further advancements, the majority of the codes are made publicly accessible for other researchers to benefit from.

4.1 Weak form

For finite element (FE) analysis, directly solving a system of partial differential equations (PDEs) in their strong forms can be challenging, as they necessitate exact solutions to boundary value problems within a specific domain, potentially leading to high computational costs or infeasibility. Conversely, weak forms of these equations only mandate the fulfillment of specific integral conditions rather than exact point-wise ones, simplifying numerical solutions and making them more appropriate for FE analysis. We begin by multiplying the governing balance equations in their strong forms (3.15) by a set of appropriate "test" functions and integrating them across an arbitrary domain. Subsequently, by utilizing the divergence theorem and implementing the relevant boundary conditions, the weak forms of the displacement, phase field and hydrogen transport problems read

$$
\begin{aligned}
&\int_\Omega \Big\{ \big[g(\phi)+k\big]\boldsymbol{\sigma}_0 : \nabla\delta\mathbf{u} - \mathbf{b}\cdot\delta\mathbf{u} \Big\}\,\mathrm{d}V - \int_{\partial\Omega_h} \mathbf{h}\cdot\delta\mathbf{u}\,\mathrm{d}S = 0 \\
&\int_\Omega \left\{ g'(\phi)\delta\phi\,\mathcal{H} + f(\bar{\alpha})\frac{G_c}{4c_w}\left(\frac{w'(\phi)\delta\phi}{\ell} + 2\ell\nabla\phi\cdot\nabla\delta\phi\right)\right\}\mathrm{d}V - \int_{\partial\Omega_\mathfrak{f}} \mathfrak{f}\,\delta\phi\,\mathrm{d}S = 0 \\
&\int_\Omega \left\{ \dot{C}\,\delta C + D\nabla C\cdot\nabla\delta C - g(\phi)\frac{DC}{\mathcal{R}T}\bar{V}_H\nabla\sigma_H\cdot\nabla\delta C \right\}\mathrm{d}V - \int_{\partial\Omega_q} q\,\delta C\,\mathrm{d}S = 0
\end{aligned}
\tag{4.1}
$$

where $\boldsymbol{\sigma}_0$ represents the undamaged Cauchy stress tensor, and k denotes a small positive parameter to maintain the system of FE equations well-conditioned when $\phi = 1$; a value of $k = 10^{-7}$ is consistently adopted throughout this thesis. To enhance clarity and readability, we have excluded the concentration term C from the argument of G_c in this chapter.

4.2 Finite element discretization

Utilizing Voigt notation and assuming a plane strain condition, the primary variables of the coupled problem - displacement, phase field and hydrogen concentration - are discretized based on their nodal values $\mathbf{u}_i = \{u_x, u_y\}_i^\mathsf{T}$, ϕ_i and C_i at node i, as follows:

$$
\mathbf{u} = \sum_{i=1}^{m} \boldsymbol{N}_i^u \mathbf{u}_i\,, \qquad \phi = \sum_{i=1}^{m} N_i\phi_i\,, \qquad C = \sum_{i=1}^{m} N_i C_i \tag{4.2}
$$

where m denotes the total number of nodes for each element, while N_i represents the shape functions associated with node i, and $\boldsymbol{N}_i^u$ refers to the shape function matrix, which is a diagonal matrix containing N_i in its diagonal elements. Consequently, the related gradient quantities can be discretized in the following manner:

$$\boldsymbol{\varepsilon} = \sum_{i=1}^{m} \boldsymbol{B}_i^u \mathbf{u}_i \,, \qquad \nabla\phi = \sum_{i=1}^{m} \mathbf{B}_i \phi_i \,, \qquad \nabla C = \sum_{i=1}^{m} \mathbf{B}_i C_i \tag{4.3}$$

where $\boldsymbol{B}_i^u$ denotes the strain-displacement matrix, while $\mathbf{B}_i$ represents a vector that comprises the spatial derivatives of the shape functions. The expressions for the strain-displacement matrix, spatial derivative vector, and shape function matrix are as follows:

$$\boldsymbol{B}_i^u = \begin{bmatrix} \partial N_i/\partial x & 0 \\ 0 & \partial N_i/\partial y \\ \partial N_i/\partial y & \partial N_i/\partial x \end{bmatrix}, \qquad \mathbf{B}_i = \begin{bmatrix} \partial N_i/\partial x \\ \partial N_i/\partial y \end{bmatrix}, \qquad \boldsymbol{N}_i^u = \begin{bmatrix} N_i & 0 \\ 0 & N_i \end{bmatrix} \tag{4.4}$$

where the nonzero entries of $\boldsymbol{B}_i^u$ are partial derivatives of the shape functions with respect to x and y. Additionally, the virtual quantities $\delta\mathbf{u}$, $\delta\phi$ and δC along with their derivatives, can also be discretized in a similar manner:

$$\begin{aligned} \delta\mathbf{u} &= \sum_{i=1}^{m} \boldsymbol{N}_i^u \delta\mathbf{u}_i \,, & \delta\phi &= \sum_{i=1}^{m} N_i \delta\phi_i \,, & \delta C &= \sum_{i=1}^{m} N_i \delta C_i \\ \delta\boldsymbol{\varepsilon} &= \sum_{i=1}^{m} \boldsymbol{B}_i^u \delta\mathbf{u}_i \,, & \nabla\delta\phi &= \sum_{i=1}^{m} \mathbf{B}_i \delta\phi_i \,, & \nabla\delta C &= \sum_{i=1}^{m} \mathbf{B}_i \delta C_i \end{aligned} \tag{4.5}$$

4.3 Residuals and stiffness matrices

Now, making use of the finite element discretization outlined in (4.2) and (4.3) and considering that (4.1) must hold for any kinematically admissible variations of the virtual quantities $\delta\square$, the corresponding residuals are derived as

$$\begin{aligned} \mathbf{r}_i^u &= \int_\Omega \big[g(\phi) + k\big] (\boldsymbol{B}_i^u)^\mathsf{T} \boldsymbol{\sigma_0} \,\mathrm{d}V - \int_\Omega (\boldsymbol{N}_i^u)^\mathsf{T} \mathbf{b} \,\mathrm{d}V - \int_{\partial\Omega_h} (\boldsymbol{N}_i^u)^\mathsf{T} \mathbf{h} \,\mathrm{d}S \\ r_i^\phi &= \int_\Omega \left\{ g'(\phi) N_i \,\mathcal{H} + f(\bar{\alpha}) \frac{G_c}{4c_w} \left(\frac{w'(\phi)}{\ell} N_i + 2\ell (\mathbf{B}_i)^\mathsf{T} \nabla\phi \right) \right\} \mathrm{d}V - \int_{\partial\Omega_\mathfrak{f}} N_i \,\mathfrak{f} \,\mathrm{d}S \\ r_i^C &= \int_\Omega \left\{ N_i \,\dot{C} + (\mathbf{B}_i)^\mathsf{T} D \nabla C - g(\phi) (\mathbf{B}_i)^\mathsf{T} \frac{DC}{\mathcal{R}T} \bar{V}_H \nabla\sigma_H \right\} \mathrm{d}V - \int_{\partial\Omega_q} N_i \, q \,\mathrm{d}S \end{aligned} \tag{4.6}$$

To obtain the consistent tangent stiffness matrices, one can differentiate the residuals with respect to the nodal variables, as follows:

$$\begin{aligned} \boldsymbol{K}_{ij}^u &= \frac{\partial \mathbf{r}_i^u}{\partial \mathbf{u}_j} = \int_\Omega \big[g(\phi) + k\big] (\boldsymbol{B}_i^u)^\mathsf{T} \boldsymbol{\mathcal{L}}_0 \, \boldsymbol{B}_j^u \,\mathrm{d}V \\ \boldsymbol{K}_{ij}^\phi &= \frac{\partial r_i^\phi}{\partial \phi_j} = \int_\Omega \left\{ \left(g''(\phi) \,\mathcal{H} + f(\bar{\alpha}) \frac{G_c}{4c_w \ell} w''(\phi) \right) N_i N_j + f(\bar{\alpha}) \frac{G_c \ell}{2c_w} (\mathbf{B}_i)^\mathsf{T} \mathbf{B}_j \right\} \mathrm{d}V \\ \boldsymbol{K}_{ij}^C &= \frac{\partial r_i^C}{\partial C_j} = \int_\Omega \left\{ \frac{N_i N_j}{\mathrm{d}t} + (\mathbf{B}_i)^\mathsf{T} D \, \mathbf{B}_i - g(\phi) (\mathbf{B}_i)^\mathsf{T} \frac{D N_j}{\mathcal{R}T} \bar{V}_H \nabla\sigma_H \right\} \mathrm{d}V \end{aligned} \tag{4.7}$$

In order to estimate the time derivatives of the nodal hydrogen concentration $\dot{C} = \mathrm{d}C/\mathrm{d}t$, we utilize the discretization described in Eq. (4.2), following a similar interpolation as employed for C. The computation of the hydrostatic stress gradient $\nabla\sigma_H$ is carried out by employing the derivatives of the shape functions in conjunction with the hydrostatic stress values at the integration points.

4.4 Moving chemical boundary conditions

In an in-situ charging experiment where the sample is constantly subjected to a hydrogen environment, the key aspect to understand the hydrogen-assisted fracture lies in capturing the mechanisms driving hydrogen transport through a growing crack. A suitable method for this analysis involves assuming that the environment, whether it is in the form of gaseous hydrogen or an aqueous electrolyte, will instantly fill the space created as the crack progresses. Moreover, hydrogen typically saturates surface sites, given that the free energy at these locations is lower than within the lattice [132]. This essentially implies that hydrogen is expected to be present on the surface, supplied either by the surrounding environment or the lattice itself. As a result, the hydrogen concentration value associated with the environment, C_{env}, should be assigned to the newly created surface or boundary caused by crack propagation. We utilize a penalty-based method [130, 133] in this thesis to appropriately enforce the hydrogen concentration within the affected regions. Consequently, an additional term is added to the chemical residual (4.6c), which is expressed as follows:

$$\int_{\Omega} k_p \, N_i \left(C - C_{\text{env}}\right) \langle 2\phi - 1 \rangle_+ \, \mathrm{d}V \tag{4.8}$$

where the variables C and C_{env} represent quantities at the integration point, and the term $\langle \square \rangle_+$ refers to the Macaulay brackets. The effect of introducing this additional term on the diffusivity matrix (4.7c) can be represented as follows:

$$\int_{\Omega} k_p \, N_i N_j \langle 2\phi - 1 \rangle_+ \, \mathrm{d}V \tag{4.9}$$

The penalty method is employed to incrementally increase the hydrogen concentration in regions with significant damage (where $\phi > 0.5$). A high penalty factor value k_p guaranties that the concentration in fully damaged areas ($\phi = 1$) matches the environmental concentration C_{env}, without impeding convergence. Throughout this thesis, a consistent value of $k_p = 10^6$ is used.

4.5 Solution schemes

Considering the following linearized system of equations,

$$\begin{Bmatrix} \mathbf{u} \\ \boldsymbol{\phi} \\ \mathbf{c} \end{Bmatrix}_{t+\Delta t} = \begin{Bmatrix} \mathbf{u} \\ \boldsymbol{\phi} \\ \mathbf{c} \end{Bmatrix}_{t} - \begin{bmatrix} \boldsymbol{K}^u & 0 & 0 \\ 0 & \boldsymbol{K}^\phi & 0 \\ 0 & 0 & \boldsymbol{K}^C \end{bmatrix}_t^{-1} \begin{Bmatrix} \mathbf{r}^u \\ \mathbf{r}^\phi \\ \mathbf{r}^C \end{Bmatrix}_t \tag{4.10}$$

we can employ an incremental-iterative scheme combined with the *Newton-Raphson* method to determine the solutions where $\mathbf{r}^u = \mathbf{0}$, $\mathbf{r}^\phi = \mathbf{0}$ and $\mathbf{r}^C = \mathbf{0}$, given the nonlinearity of the residuals (4.6). Two solution strategies are generally utilized for solving the deformation-phase field problem in phase field fracture without hydrogen: the *monolithic* scheme and the *staggered* scheme. The monolithic scheme solves the equations for the displacement and the phase field at the same time, while the staggered scheme solves them sequentially. Both methods have their pros and cons, and the choice depends on the application and desired level of accuracy and efficiency.

4.5.1 Monolithic solution scheme

There has been significant focus on developing effective strategies for solving the fully coupled problem of deformation and phase field fracture. The total potential energy of the system, which includes both the stored bulk and fracture surface energies, exhibits non-convexity with respect to the primary variables: displacement **u** and phase field ϕ. The non-convex nature of the problem poses challenges for convergence and stability in *monolithic* solution schemes, that solve for **u** and ϕ simultaneously, as standard *Newton-Raphson* methods may fail to achieve convergence. To address these limitations, various numerical techniques have been employed, including specialized line search algorithms [23], generalized dissipation-based path following solvers [134], Schwarz preconditioned inexact Newton's methods [135], error-oriented newton method [136] and modified Newton methods [137]. In this thesis, [P1,P3], we utilize an efficient quasi-Newton monolithic solution scheme that relies on the Broyden-Fletcher-Goldfarb-Shannon (BFGS) algorithm [138, 139].

The BFGS algorithm is a widely-used technique for solving nonlinear optimization problems [140–142]. In the context of phase field fracture, this method is used to iteratively update the solutions for u and ϕ until they reach a state of convergence. Unlike the Newton method, which recalculates the stiffness matrix entirely, or the modified Newton method, which leaves it unchanged, the BFGS algorithm updates the stiffness matrix in a simple manner after each iteration. Furthermore, for symmetric stiffness matrices, the update to the approximate stiffness matrix can be directly applied to its inverse [143]. This approach retains symmetry and positive definiteness, if such properties were present in the original matrix. The approach has several advantages, such as being computationally efficient and robust, which is crucial for minimizing the cost of cycle-by-cycle fatigue simulations, especially for problems with a large number of degrees of freedom. However, it may require careful tuning of the BFGS parameters and can be sensitive to the initial guess for the tangent stiffness matrix. In general, it is necessary for the initial guess to be a symmetric and positive definite matrix, which makes it unsuitable for problems involving hydrogen, as this often results in an asymmetric stiffness matrix. For a more detailed discussion on numerical implementation in Abaqus, convergence criteria, and comparative studies with other solution schemes, the reader is referred to Refs. [35, 138, 139].

4.5.2 Staggered solution scheme

A widely adopted method for addressing the deformation-phase field problem involves concentrating on one primary variable at a time. By doing this, the system's total potential energy becomes convex with respect to the other primary variable. As a result, the equations for **u** and ϕ can be solved separately as *staggered* fields with sequential coupling. It allows for the independent assessment of convergence for both **u** and ϕ at the end of each increment. Often referred to as a one-pass or single-iteration alternating minimization (AM) algorithm, this approach has gained considerable popularity in the field [22, 88, 144]. Although effective, the method is computationally demanding and no longer unconditionally stable [23, 145]. To ensure accuracy and prevent deviation from the equilibrium solution, a time increment sensitivity study is necessary, which involves using very small load steps.

To overcome these limitations, multi-pass algorithms have been proposed that derive opposing field values based on the previous iteration instead of from the increment. This method enables the implementation of an appropriate stopping criterion, which determines when to stop alternating between the two fields (see Algorithm 1). Consequently, the accuracy of the equilibrium solution no longer depends on the careful choice of increment sizes. Moreover, this approach accommodates larger time increments by utilizing

multiple iterations per increment, especially when addressing substantial crack growth, as opposed to the single-iteration strategy [54]. There are various stopping criteria that can be employed, such as the energy-based criterion developed by Ambati et al. and detailed in [103], or the residual-based method utilized by Seleš et al. in Abaqus, as discussed in [69]. In this thesis [P4], we adopt the latter approach and showcase how increment insensitivity can significantly affect fatigue analyses, as detailed in Section 5. Furthermore, due to the asymmetrical stiffness matrix associated with the hydrogen diffusion problem, we found it impractical to use the BFGS quasi-Newton algorithm in this particular scenario. In this thesis, we set the stopping criterion for the required tolerance of the residual norm to $\texttt{TOL} = 10^{-5}$, which is the recommended value in [69].

Algorithm 1 Mutli-pass alternate minimization (AM) algorithm

Increment $n+1$
Initialize: $\phi_0 = \phi_n$, $\mathbf{u}_0 = \mathbf{u}_n$, $k = 0$
while $||\mathbf{r}^{\phi}(\mathbf{u}_{k+1}, \phi_{k+1})||_{\infty} \leq \texttt{TOL}$ **do**
  Solve ϕ_{k+1} with $\mathbf{u}_k$ in $\boldsymbol{K}^{\phi}\boldsymbol{\phi}_{k+1} = \mathbf{r}^{\phi}(\mathbf{u}_k)$
  Solve $\mathbf{u}_{k+1}$ with ϕ_{k+1} in $\boldsymbol{K}^{u}\mathbf{u}_{k+1} = \mathbf{r}^{u}(\phi_{k+1})$
  $k \leftarrow 1$
end while
$\phi_{n+1} = \phi_k$, $\mathbf{u}_{n+1} = \mathbf{u}_k$

4.6 Accelerated fatigue computations

Besides the high computational cost resulting from the non-convexity nature of the balance equations, phase field fracture models require fine meshes to resolve phase field length scales [113], further adding to the inefficiency. Significant efforts have been devoted to improve discretization strategies, such as adaptive mesh refinement techniques [146–149], specialized element formulations [150], and the integration of finite element and finite volume methods [151]. Although various improvements for solution schemes have been suggested, as described in Section 4.5.1, the high computational cost of phase field fracture poses a major challenge to cycle-by-cycle fatigue simulations and restricts the analysis of high-cycle fatigue. One commonly used method to reduce the costs of high-cycle fatigue simulations is to employ *cycle jump* strategies, which involves extrapolating the cycle-by-cycle solution to skip the calculation of multiple load cycles [152]. In their work on phase field fatigue, Loew et al. [61] implemented a similar strategy by locally extrapolating the fatigue history variable.

In [P3], we present innovative techniques to accelerate cycle-by-cycle phase field fatigue simulations. We propose two complementary approaches that significantly improve computational performance while not interfering with existing cycle jump strategies, which can also be included to further boost efficiency. One approach is to modify the method of accumulating fatigue damage. As explained earlier in Section 2, our proposal is to accumulate fatigue effects only during one reversal per cycle. This means that for cases where the load amplitude remains constant, the internal increments within a cycle are substituted with a constant load, referred to as the Constant Load Accumulation (CLA) strategy. This method is particularly effective for high-cycle fatigue situations, where the material exhibits mainly linear elastic behavior. It's important to note that some loading scenarios, such as non-proportional loading, may necessitate multiple internal increments within each load cycle. The method provides a critical advantage by enabling the incorporation of multiple load cycles $\mathcal{N} > 1$ within a single increment, significantly improving computational efficiency without compromising accuracy (as discussed in Section 3). For this purpose, Eq.

(2.36) that updates the accumulated fatigue history variable $\bar{\alpha}$ can be readily modified to:

$$\bar{\alpha}_{t+\mathcal{N}\Delta t} = \bar{\alpha}_t + \mathcal{N}\Delta\bar{\alpha} \tag{4.11}$$

Another approach to accelerate cycle-by-cycle fatigue simulations is by modifying the multi-pass staggered solution schemes, described in Section 4.5.2. The modification involves storing the tangent stiffness matrices in factorized form rather than updating them in each load increment. With this change, subsequent increments or iterations can be solved at a much lower computational cost. This approach, referred to as Modified Newton (MN) strategy, is particularly useful in high-cycle fatigue situations where there are small variations in the overall system, and consequently in the solution variables, between each load increment. The first acceleration strategy can be easily implemented in both Abaqus and Julia. On the other hand, the second strategy can only be implemented in Julia since Abaqus does not allow access to the global solution strategy from user subroutines.

5 Results

This chapter presents a comprehensive overview of the results obtained and their experimental validation throughout this thesis [P1, P2, P3, P4]. The modeling capabilities of the proposed phase field fatigue model is investigated in Section 5.1 through total-life analyses. Furthermore, the robustness and efficiency of the proposed acceleration strategies are explored in Section 5.2. To further assess the model's performance, we conduct fatigue crack growth analyses in Section 5.3. Finally, the predictive capabilities of the model in the presence of a corrosive environment are outlined in Section 5.4.

5.1 Total-life analysis

This section presents the outcomes of numerical experiments carried out to assess the performance of the phase field fatigue model proposed in this thesis [P1]. We first aim to gain a better understanding of the model characteristics by analyzing the response of a smooth bar under uniaxial cyclic loading (Section 5.1.1). A parametric study is performed to investigate the impact of the fatigue model/material parameters on the S-N curves. We then compare the model predictions with S-N curves derived from fatigue experiments on both smooth and notched cylindrical bars (Section 5.1.2). Throughout this section, unless otherwise stated, we utilize the `AT1` model, the $f_2(\bar{\alpha})$ fatigue degradation function (2.34), the No-tension split (2.21), and the quasi-Newton monolithic solution scheme (Section 4.5.1).

5.1.1 Smooth bar subjected to uniaxial tension-compression loading

To begin with, the model's characteristics are understood by examining a smooth bar that is exposed to uniaxial cyclic loading, with a load ratio of $R = -1$. The problem can be solved in a semi-analytic way by analyzing the homogeneous solution to Eq. (2.27). The remote stress (or strain) is assumed to have a piece-wise cyclic linear variation. Even though the numerical studies are focused on constant amplitude loading, it is important to note that the model can handle any type of loading history and account for load sequence effects.

Overview of material behaviour

In Fig. 5.1, the changes in elastic strain energy density and its tensile (active) and compressive (inactive) parts are demonstrated. The No-tension split is the only one that accurately divides the strain energy density to eliminate the compressive part during tension and the tensile part during compression, unlike the other splits. The performance of the No-tension split is further emphasized in Fig. 5.2, which shows the cyclic variation of the fatigue history variable $\bar{\alpha}$. This figure shows that the accumulation of fatigue effects only occurs during the peak-to-valley portion of each cycle, and that the rate of growth of $\bar{\alpha}$ decreases as the power exponent n increases.

In addition, simulations using the `AT2` phase field model were conducted with remote stress and strain amplitudes to compare load- as well as displacement-controlled numerical experiments and gain insights into the evolution of the model's behavior. Fig 5.3 illustrates the material's stress-strain response as well as relevant variable changes ($\bar{\alpha}, \phi$, cyclic stress/strain) as the number of cycles N progresses. In Fig. 5.3b, it can be observed that the phase field variable evolves slowly at the beginning and then rapidly increases towards the end when the strain reaches the critical strain value of ε_c in the case of load-controlled loading. However, in displacement-controlled loading, the phase field variable approaches the upper limit of $\phi \to 1$ asymptotically, as seen in Fig. 5.3d).

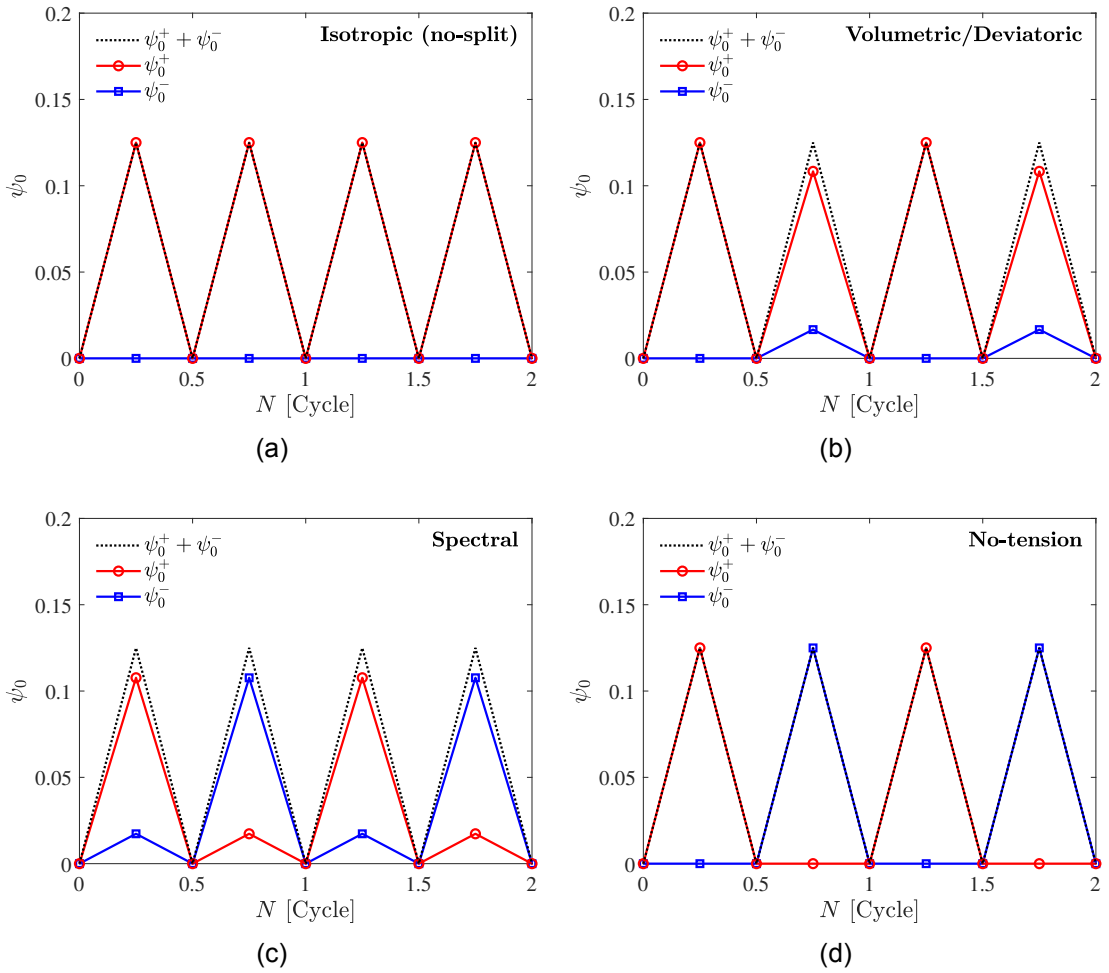

Figure 5.1: Impact of strain energy density decomposition on fatigue driving force $\alpha = g(\phi)\psi_0^+$; tensile ψ_0^+ and compressive ψ_0^- portions for a symmetric uniaxial tension–compression loading ($R = -1$) considering the (a) Isotropic, (b) Volumetric/deviatoric, (c) Spectral, and (d) No-tension splits. Adapted from [P1].

Therefore, in displacement-control conditions, a failure threshold of $\phi = 0.95$ needs to be set. The time variation of ϕ affects the cyclic evolution of the fatigue history variable $\bar{\alpha}$ as well as the cyclic stress. This is due to the phase field degradation function (2.29), which appears in the definitions of both $\boldsymbol{\sigma}$ (2.15) and α (2.35).

To gain further insight, we investigated the effect of the phase field damage models (`AT1` versus `AT2`) and the load amplitudes which resulted in cyclic stresses below and above the assumed material endurance limit. The cyclic loading was stopped after 220 cycles, and a uniaxial monotonic load was applied. The results are illustrated in Fig. 5.4. When the stresses are below the endurance limit, the fatigue does not affect the monotonic response or critical strength (strain) of the bar, as shown in Fig. 5.4a. However, when the load amplitude exceeds the endurance limit, as depicted in Fig. 5.4b, the critical strength and strain of the bar significantly decreases in the monotonic response. This is observed for both `AT1` and `AT2` models, with the former exhibiting a more significant effect.

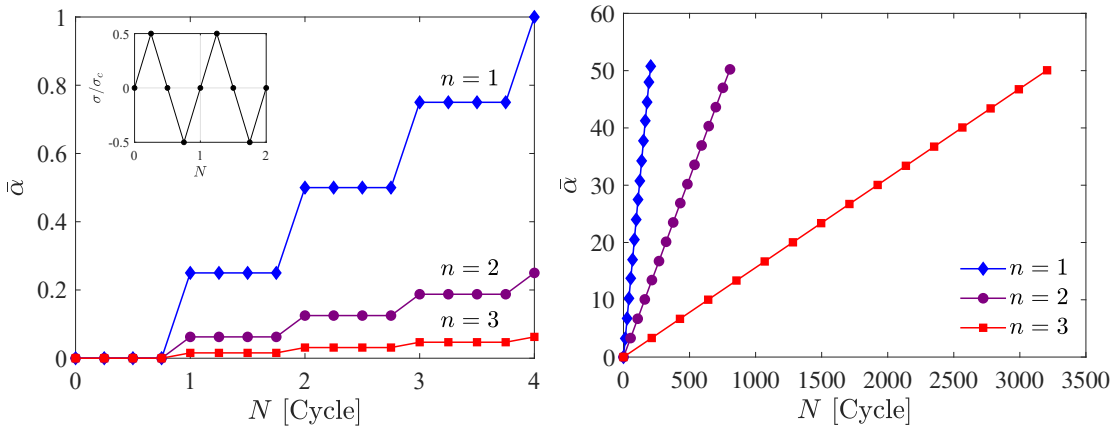

Figure 5.2: Cyclic variation of the fatigue history variable $\bar{\alpha}$ for different power exponent n values: (a) close-up of the initial cycles, illustrating that the No-tension split suitably accumulates damage within a single half-cycle per cycle, and (b) evolution across multiple cycles, demonstrating the impact of the power exponent. Adapted from [P1].

Parametric study

A parametric investigation is performed to examine how the fatigue model/material parameters affect the results. Fig. 5.5a and Fig. 5.5b illustrate the outcomes of the calculations assessing the sensitivity to $\bar{\alpha}_0$ and α_e in terms of the S-N curves, which show the relationship between the applied stress amplitude and the number of cycles to failure. The study employs the `AT1` model, and the stress amplitude is normalised by the material strength. The arrows indicate the fatigue runout phenomenon, where the samples do not fail within the test's duration. The results shown in Fig. 5.5a indicate that higher values of $\bar{\alpha}_0$ are associated with longer fatigue life, which aligns with what was anticipated. In addition, Fig. 5.5b illustrates that lowering the threshold parameter α_e causes a reduction in the stress amplitude at which fatigue life is considered infinite (the endurance limit). The slope of the S-N curves remains relatively unchanged for both $\bar{\alpha}_0$ and α_e, despite variations in their respective values.

The investigation into the role of the power exponent n concludes the parametric study. The results, shown in Fig. 5.6a, exhibit a clear correlation between the magnitude of n and the S-N curves. A higher value of n results in fatigue responses that are more susceptible to variations in the stress amplitude. Thus, n adds modeling flexibility to capture the slope m^* of the S-N curve for any material. As demonstrated in Fig. 5.6b, a linear relationship exists between n and m. Based on this finding, Table 5.1 lists the coefficients of this linear relationship (5.1) for different phase field models and fatigue degradation functions,

$$n = \mathcal{C}_1 m + \mathcal{C}_2 \tag{5.1}$$

where $m = -(m^*)^{-1}$. Moreover, it is important to observe that at higher stress amplitudes, the S-N curve exhibits a non-linear trend, which indicates a failure mechanism driven by static rather than fatigue damage, as previously discussed by Carrara et al. [64].

Load ratio effect

The proposed model will be tested to determine if it can accurately capture the impact of mean stress on S-N curve behavior. This will be achieved by examining two load-controlled scenarios. The first scenario involves varying the stress ratio R while main-

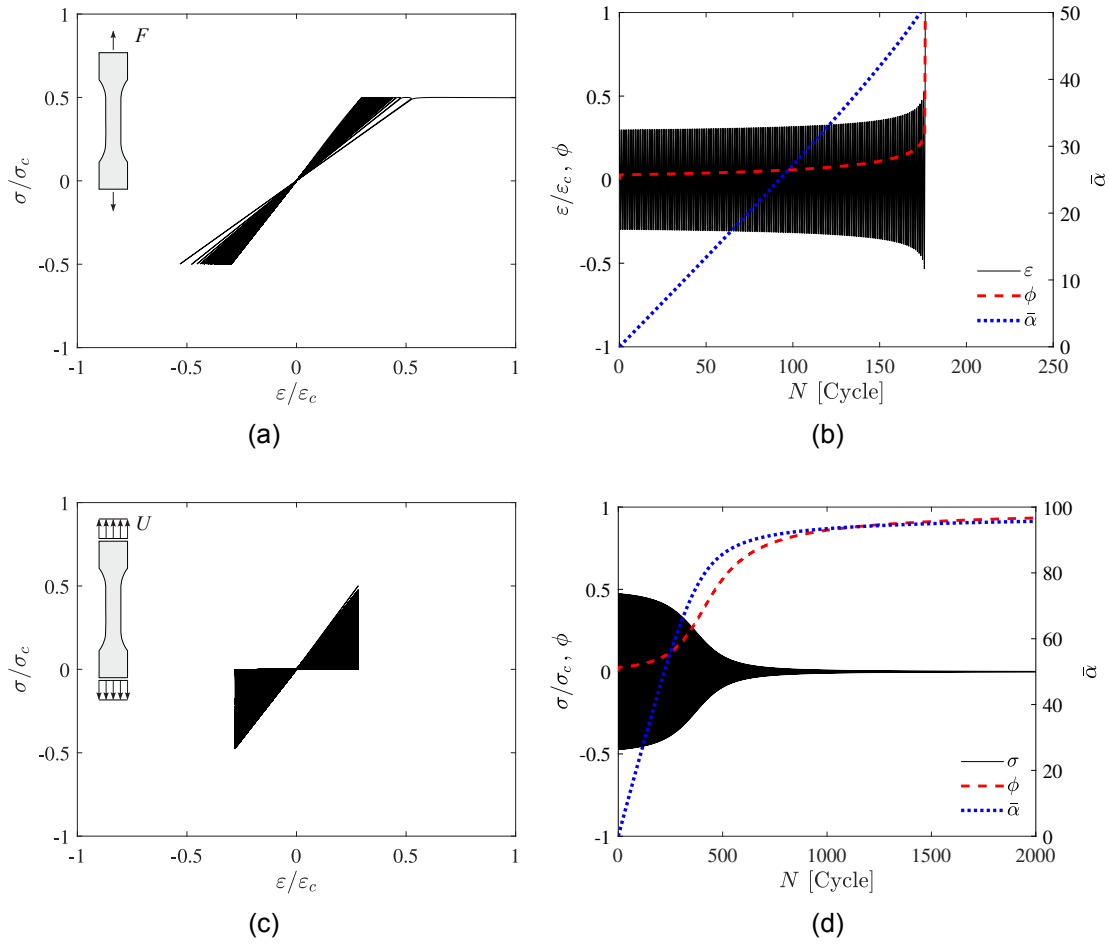

Figure 5.3: Material's and model's behaviour under load-controlled, (a) and (b), and displacement-controlled, (c) and (d), cases. Stress-strain curves are depicted in (a) and (c), while (b) and (d) illustrate the changes of relevant variables ($\bar{\alpha}$, ϕ, cyclic stress/strain) according to cycle number N. Adapted from [P1].

	f_0		f_1		f_2	
	$\mathcal{C}_1$	$\mathcal{C}_2$	$\mathcal{C}_1$	$\mathcal{C}_2$	$\mathcal{C}_1$	$\mathcal{C}_2$
AT1	0.50	-0.56	0.50	-0.63	0.50	-0.13
AT2	0.50	-0.55	0.49	-0.61	0.49	-0.12

Table 5.1: Linear relationship coefficients between the power exponent n and the S-N slope, as described in Eq. (5.1). Adapted from [P1].

taining a fixed stress amplitude σ_a. The second scenario involves varying the stress ratio R while maintaining a fixed maximum stress σ_{max}. The given situations are of particular interest due to the discrepancies in experimental findings regarding the relationship between R and the number of cycles. Experiments with a constant σ_a have demonstrated an extended fatigue life when R is reduced; conversely, this is not the case for tests with a fixed σ_{max} [122, 153]. The results are presented in Fig. 5.7, which also includes a subplot showing the applied loading conditions. It is evident that the fatigue life and the endurance limit are affected by the load ratio R for both loading scenarios. In the case of fixed stress amplitude shown in Fig. 5.7a, it can be seen that the fatigue life reduces

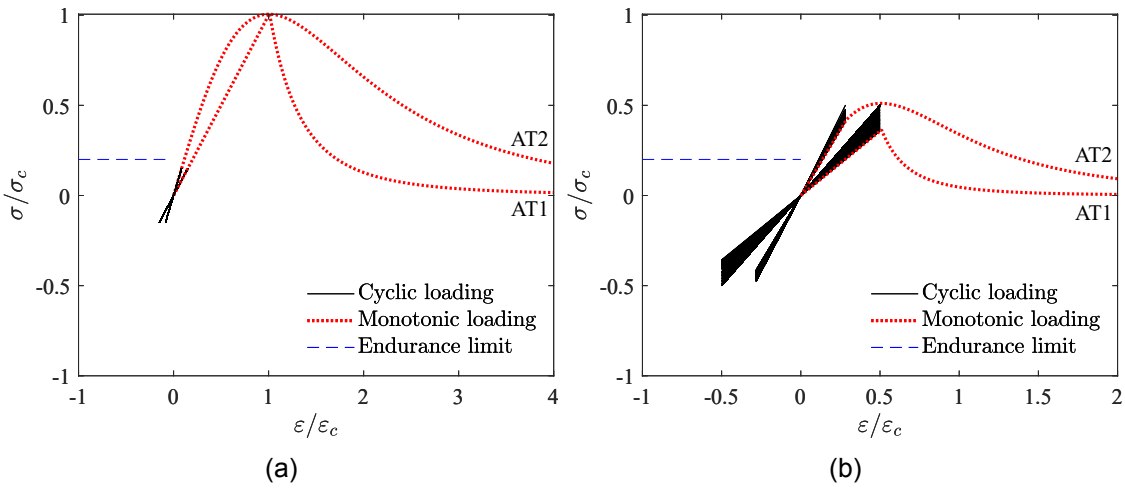

Figure 5.4: Uniaxial cyclic and monotonic response for `AT1` and `AT2` damage models, considering various initial remote strain amplitudes. The cycle count leads to almost coinciding curves (black areas). Adapted from [P1].

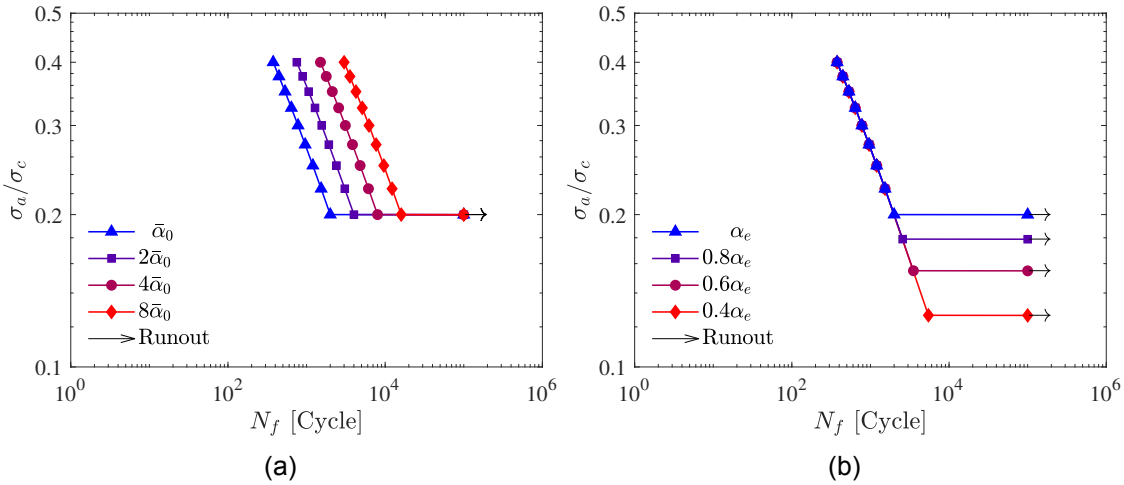

Figure 5.5: Parametric investigation. Sensitivity of the S-N curve with respect to: (a) the fatigue model parameter $\bar{\alpha}_0$, and (b) the threshold parameter α_e. Adapted from [P1].

significantly as the load ratio R increases for a given σ_a, which aligns with experimental findings [122]. In addition, it is noticeable that the S-N curve deviates from linearity and shows a significant decrease in the fatigue life at higher load ratios. This behaviour can be clarified by considering that, for higher load ratios, the maximum cyclic stress level depicted in the subplot approaches the critical strength of the material σ_c, which implies that the failure is primarily due to static damage rather than fatigue (refer to Fig. 5.6a). Moving on to the results for the constant σ_{max} scenario shown in Fig. 5.7b, the trend is different from the constant σ_a case and matches experimental findings (see Ref. [153] and the experimental comparison provided below). Specifically, the fatigue lives increase as the load ratio R increases. This demonstrates that the proposed model is effective in capturing the dependence of the sensitivity to load ratio R under both constant stress amplitude and constant maximum stress scenarios.

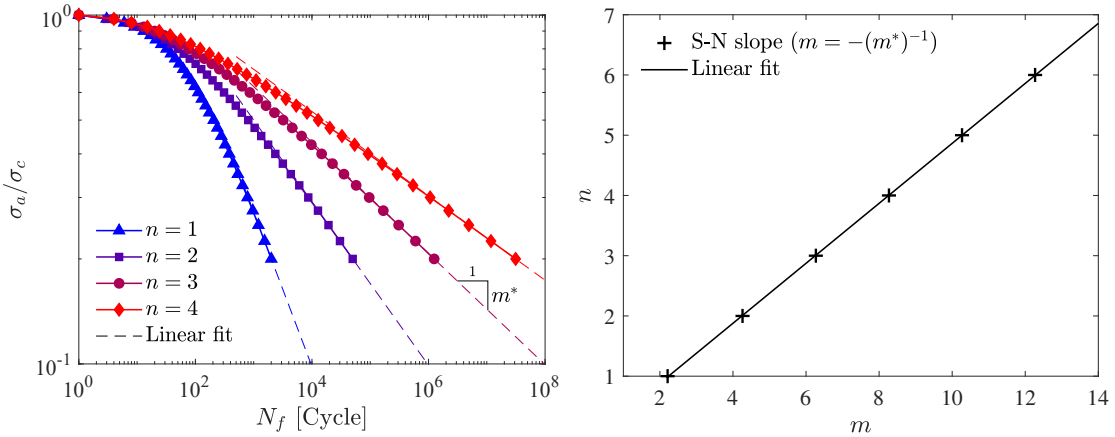

(a) (b)

Figure 5.6: Parametric investigation. Examining the impact of the power exponent n on (a) the S-N curve characteristics and (b) the linear relationship with the S-N slope. Adapted from [P1].

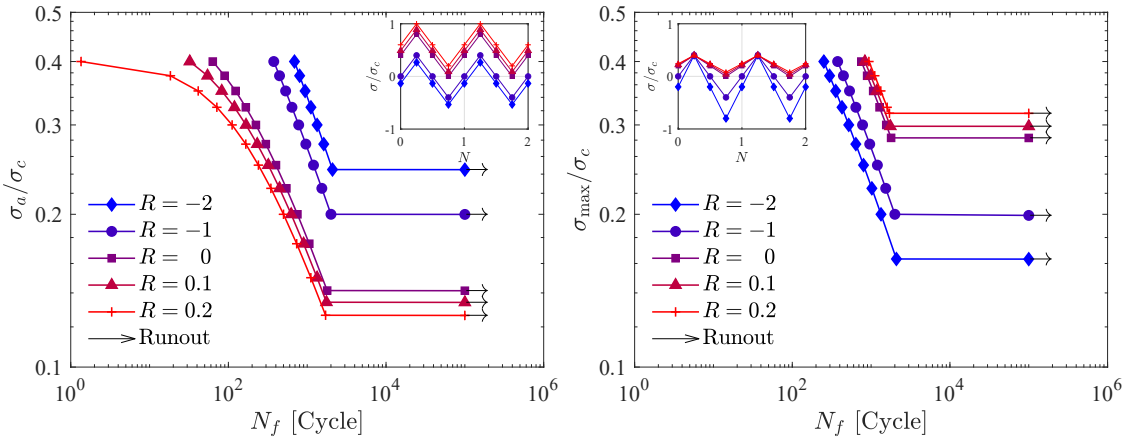

(a) (b)

Figure 5.7: Influence of load ratio R, predictions obtained using (a) a constant stress amplitude σ_a, and (b) a constant maximum stress $\sigma_{\max}$. The subplots shows the applied loading scenarios. Adapted from [P1].

5.1.2 Comparison with experimental S-N curves

Moving forward, we will evaluate the model predictions by comparing them with S-N curves derived from fatigue experiments conducted on cylindrical bars subjected to uniaxial tension-compression, with consideration given to both smooth and notched samples. The experimental data used in this analysis are sourced from Ref. [153] and involve two steel types: AISI 4340 steel, which possesses a tensile strength of 1,793 MPa, and 300M steel, which has a tensile strength of 2,000 MPa. The experiments were conducted under constant maximum stress amplitudes and different stress ratios R, in a laboratory environment exposed to ambient air. During the experiment, the samples were loaded with a piece-wise linear cyclic force, and the load ratio was set to $R = -1$. To determine the endurance limit, the S-N curve was used by finding the stress level below which the material is expected to have infinite life. The parameters n and $\bar{\alpha}_0$ are linked to the slope and intercept of the S-N curve when plotted on a logarithmic scale. By estimating n and

$\bar{\alpha}_0$ based on unnotched samples subjected to fully-reversed cyclic loading, the model can predict the effects of other factors, such as notch radius or sensitivity to loading ratio, without requiring additional fitting. One can use semi-analytical methods to obtain results for the unnotched samples by considering the homogeneous solution to Eq. (2.27). On the other hand, for the notched samples, finite element calculations are employed, and axial symmetry is utilized to consider only one planar section of the samples. Moreover, since the samples exhibit vertical symmetry, as shown in Fig. 5.8, only the upper half of the domain is modelled. The finite element domain is discretised using bilinear quadrilateral axisymmetric elements with full integration. In order to guarantee the proper resolution of the fracture process zone, the mesh is refined in the region leading up to the notch tip.

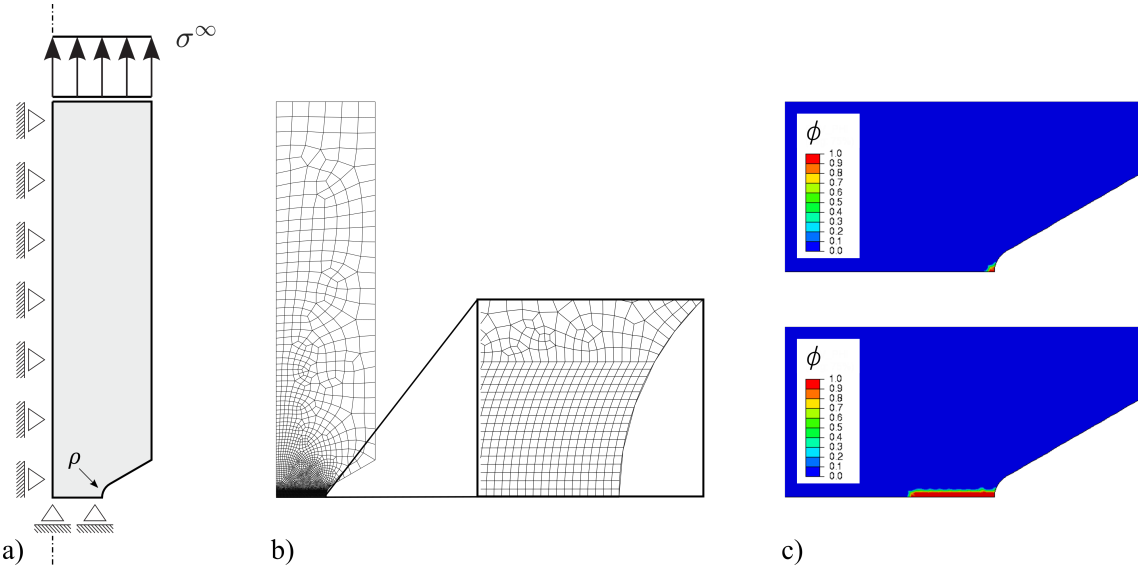

Figure 5.8: Cylindrical bar with a $60°$ V-groove notch: (a) geometry and boundary conditions, (b) finite element mesh, featuring an in-depth look at the mesh near the notch's edge, and (c) exemplary phase field contours that illustrate crack onset and propagation, until the critical failure point, for 300M steel. Adapted from [P1].

The findings, derived from experiments and numerical simulations, are presented in Fig. 5.9. The results show that the predicted *Virtual* S-N curves align well with the measured data. Both the experimental and simulation outcomes exhibit a considerable susceptibility to the notch radius, as decreasing the radius reduces the fatigue life. This effect is due to the fact that smaller radii lead to greater stress concentrations at the notch tip, which cause the fatigue crack to initiate earlier, as anticipated. Additionally, it is noteworthy that the correlation between the 300M steel experiments and simulations is less accurate when the notch radius is smaller ($K_t = 5$). This is because the experimental S-N curve shows a change in slope which could be attributed to plastic phenomena, specifically the reverse yielding effect [154]. Finally, the AISI 4340 experiments reveal that the model effectively incorporates the impact of stress concentrations on the endurance limit. In summary, the model has showcased its capability to predict the fatigue lives and endurance limit of specimens with various notches (stress concentrators), without necessitating any adjustment.

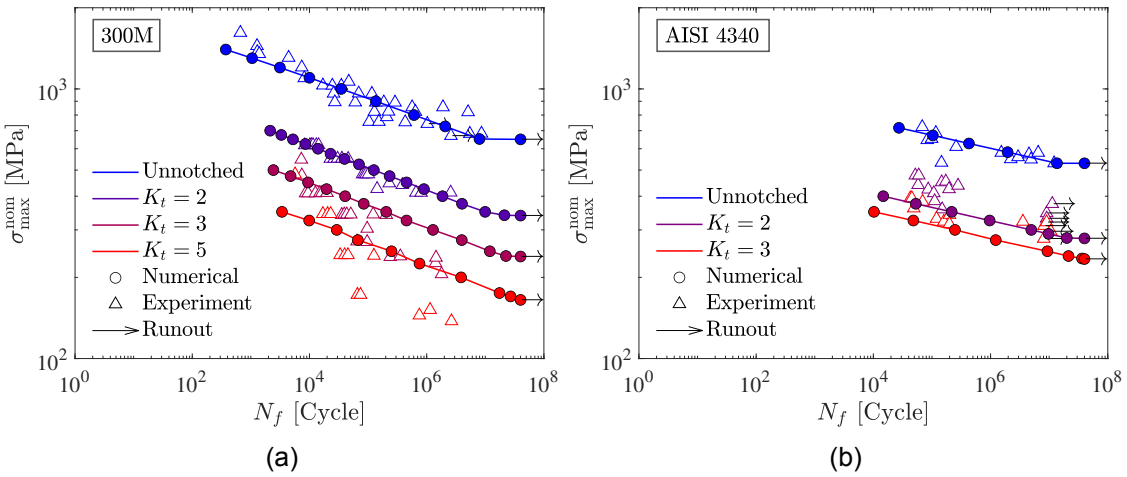

Figure 5.9: Experimental validation. *Virtual* and experimental [153] S-N curves derived from smooth and notched cylindrical bars for two steel varieties: (a) 300M, and (b) AISI 4340. The model demonstrates its capability to capture the impact of stress concentration factors on shortened fatigue life. Adapted from [P1].

Expanding on the previous 300M findings, we utilize the model to delve deeper into the material's fatigue characteristic. In Fig. 5.10a, we depict the relationship between the number of cycles leading up to initiation and failure, and the maximum nominal stress $\sigma_{\text{max}}^{\text{nom}}$ and stress concentration factor K_t. The findings demonstrated that discrepancies between crack initiation and ultimate failure escalate as the notch becomes sharper due to the intensified localization of strain, stress, and damage. In addition, we explore the relationship between different length scales by modifying the phase field length scale parameter ℓ, while keeping the notch radius ρ constant (refer to Fig. 5.10b). Particularly, we select a value of ℓ that is twice as large ($2\ell = 0.63$ mm). The findings indicate that an increase in ℓ results in a decrease in fatigue resistance. This outcome aligns with expectations because an increase in ℓ causes a reduction in material strength, leading to

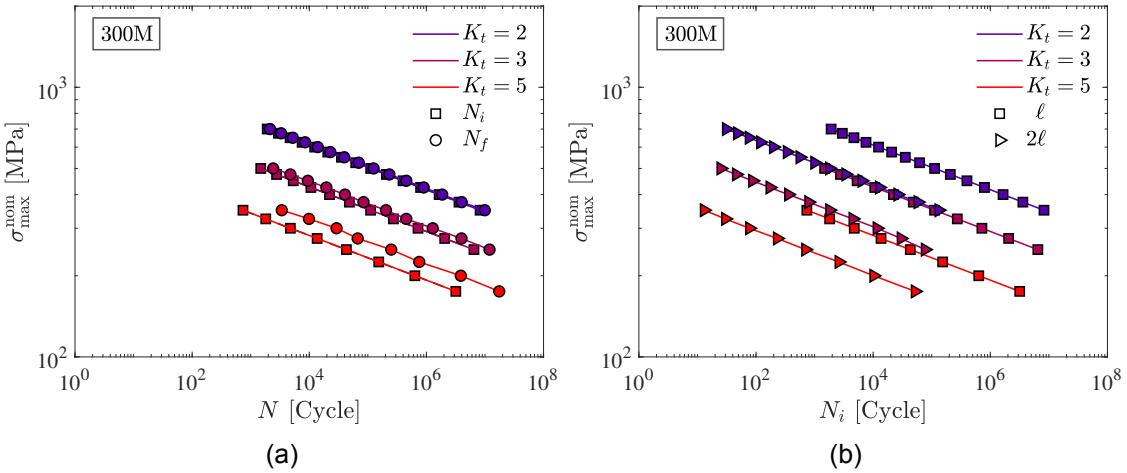

Figure 5.10: Predicted S-N curve characteristics for notched cylindrical bars: (a) comparison of crack initiation cycles N_i with failure cycles N_f, and (b) the relationship between phase field length scale ℓ and notch radius ρ. These results are based on 300M steel parameters. Adapted from [P1].

a shorter time for crack nucleation as explained in Eq. (2.33). It is worth noting that the values of ℓ tested are comparable to the notch radius. Nonetheless, the results obtained do not exhibit a proportional relationship with ℓ/ρ. This indicates the involvement of other length scales in the problem. For instance, the results for $K_t = 2$ and 2ℓ versus $K_t = 3$ and ℓ demonstrate similar outcomes despite the values of ρ/ℓ being different (1.168 and 1.613, respectively). Thus, to fully understand the connection between the various length scales involved in the problem, it may be necessary to conduct a comprehensive dimensional analysis.

In conclusion, we verify the accuracy of the load ratio effect predictions made by our model through experiments conducted on two types of steel, namely 300M and AISI 4340. We used the same model parameters as before, and the numerical predictions are presented alongside the experimental data in Fig. 5.11. Both the numerical and experimental results reveal that, when $\sigma^{\infty}_{\text{max}}$ is held constant, increasing the load ratio R leads to an increase in the number of cycles to failure N_f. Additionally, our model provides good quantitative agreement with the experimental data for both 300M and AISI 4340, indicating that it can accurately capture the mean stress effect. However, we did observe some differences in the case of 300M and $R = -2$, where the samples were compressed for most of their fatigue lives, leading to noticeable experimental scatter.

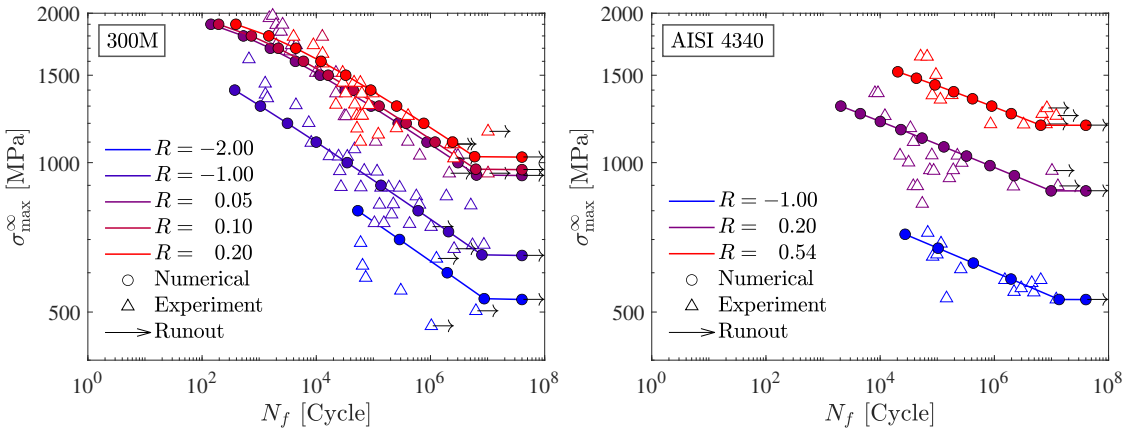

(a) (b)

Figure 5.11: Experimental validation. S-N curves derived from numerical simulations and experimental data [153] for smooth cylindrical bars subjected to different load ratios R, featuring two steel variants: (a) 300M, and (b) AISI 4340. The model demonstrates its capacity to predict how load ratio influences the material's fatigue resistance. Adapted from [P1].

5.2 Accelerated fatigue computations

This section presents the results of numerical experiments conducted to evaluate the performance of two new acceleration strategies proposed in this thesis [P1, P2]. First, our solution strategies are validated against a reference solution scheme by studying the growth of fatigue cracks in a square plate (Section 5.2.1). The goal of our study in Section 5.2.2 is to compare complex crack trajectories obtained using various strain energy decomposition splits. To achieve this, we analyze the initiation and growth of fatigue cracks in an asymmetric three-point bending specimen that includes multiple holes. Section 5.2.3 showcases the robustness of the model and its capability to simulate fatigue cracks in large scale 3D geometries. Throughout this section, unless otherwise stated, we utilize the AT2 model, the $f_0(\bar{\alpha})$ fatigue degradation function (2.34), the No-tension split (2.21), and the Modified Newton (MN) solution algorithm (Section 4.6).

5.2.1 Cracked square plate

The benchmark of the phase field fracture community has become the study of a square plate with an initial crack that is subjected to uniaxial loading. The loading conditions and dimensions of the plate (in mm) are shown in Fig. 5.12a, which can also be found in Refs. [64, 139]. The plate undergoes a cyclic remote displacement that is piece-wise linear, with a load ratio of $R = 0$ and a maximum amplitude of $\bar{u}_{\text{max}} = 0.0002$ mm. The cyclic loading is repeated for 120,000 cycles. The initial crack is set up by imposing a Dirichlet condition on the phase field. To ensure a uniform crack width, the Dirichlet boundary condition is enforced on two rows of elements. A mesh consisting of approximately 32,000 bilinear quadrilateral elements with full integration is used to discretise the computational domain. In order to accurately resolve the fracture process zone, the mesh is refined in the area where the crack propagates. The study was divided into four different scenarios.

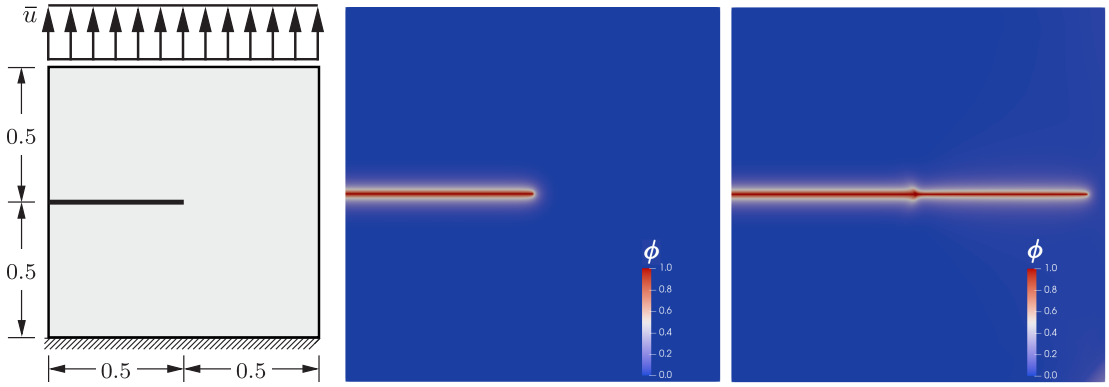

(a) (b) (c)

Figure 5.12: Cracked square plate. (a) geometry (with dimensions in mm) and loading conditions, (b) initial phase field crack contour, and (c) fatigue crack propagation after 120,000 load cycles. Adapted from [P2].

The first scenario was considered as the baseline condition, where the standard fatigue accumulation [64] was used, including four internal increments within a cycle (tensile loading, unloading, compressive loading and unloading). The multi-pass staggered algorithm from Algorithm 1 was used for obtaining results in this scenario, and no acceleration strategies proposed in this thesis were included. In the second scenario, the Modified Newton (MN) strategy was used to simulate fatigue crack growth. In the third scenario, only the Constant Load Acceleration (CLA) strategy was employed. Finally, the fourth scenario involved using both the MN and CLA schemes together. All computations were carried out

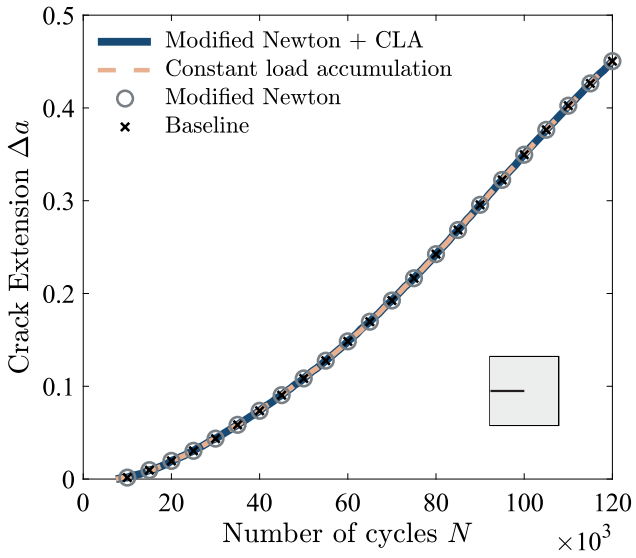

Figure 5.13: Cracked square plate. Fatigue crack extension versus number of load cycles. The graph shows the results obtained using the reference (baseline) conditions, as well as the two acceleration strategies proposed here (Modified Newton, MN; Constant load accumulation, CLA), both separately and together. Adapted from [P2].

on a single core of a CPU model Xeon E5-2650 v4. Figure 5.13 depicts the finite element results in terms of crack extension Δa (measured in mm) versus number of load cycles N. The distance between the initial crack tip and the farthest material point where the phase field value ϕ reaches 0.95 is used to calculate crack extension here. When compared to the baseline, the data indicate that the acceleration strategies had no significant effect on crack extension. The performance of different acceleration strategies is compared in Table 5.2 using various measures. The first measure is the actual computational time in hours, but it should be noted that individual time values may not provide a precise measure of performance despite efforts to minimize noise by using identical CPU types and avoiding parallel computing. A more reliable measure is the total number of matrix factorizations, which includes both the displacement and damage subproblems. The table also shows the total number of iterations used for both the phase field and displacement subproblems. The findings demonstrate that employing the CLA acceleration strategy can considerably reduce the computational time by minimizing the required number of load increments, which also leads to fewer iterations and factorizations. On the other hand, the MN strategy involves a trade-off between a decrease in matrix factorizations and an increase in required iterations, particularly for the displacement subproblem. Here, using the MN strategy results in approximately 100 times fewer matrix factorizations than

Solutions strategy	MN + CLA	CLA	MN	Baseline
Computational time [hr]	13.0	32.7	40.1	96.5
Matrix factorizations	1 191	120 032	2 379	240 032
Total iterations ϕ	120 205	120 032	240 114	240 032
Total iterations **u**	276 812	120 032	973 678	240 032

Table 5.2: Cracked square plate. Comparison of the reference (baseline) solution with the two acceleration strategies proposed here (Modified Newton, MN; Constant load accumulation, CLA), both separately and together. Adapted from [P2].

the baseline, at the cost of only four times more iterations required for the displacement subproblem. It is essential to highlight that the iterations needed for the displacement subproblem are inexpensive when using the MN strategy as they only require reconstructing the residuals and effortlessly determining the solution with the preexisting factorized tangent stiffness matrix. The findings demonstrate that both accumulation strategies can yield significant performance improvements either separately or combined, without compromising accuracy. Furthermore, these approaches are compatible with current cycle jump techniques, as outlined in [61, 69].

In conclusion, we explore the impact of including multiple load cycles per increment (referred to as "cycle-jumping") on both the accuracy and efficiency of the computational process. Although a minor degree of error is expected to occur due to the discrete sampling of the cyclic load history, when $\mathcal{N} > 1$ in Eq. (4.11), our findings demonstrate that this error is insignificant. To test this, we conduct simulations for the square plate under different maximum remote displacement values of $\bar{u}_{\text{max}} = 0.00020$ mm and 0.00016 mm with 120,000 and 240,000 repeated load cycles, respectively, utilizing the enhanced CLA strategy in combination with the MN algorithm. Figure 5.14 presents the results obtained for various values of $\mathcal{N}$ (ranging from 1 to 32). One can notice that the overall error is negligible, as the differences between the final fatigue crack extension and the baseline value of $\mathcal{N} = 1$ are consistently below 3% (see Table 5.3). Additionally, for a fixed value of $\mathcal{N}$, the deviation in predicted fatigue crack extension at the end of the total number of load cycles diminishes as this number increases. Thus, for high-cycle fatigue scenarios, where millions of load cycles may occur, a large value of $\mathcal{N}$ can be utilized with negligible error. The results in Table 5.3 indicate that computational times do not increase linearly with $\mathcal{N}$, but they do exhibit a consistent decrease within the range studied. Compared to the reference (baseline) scenarios presented in Table 5.2, utilizing the MN algorithm in conjunction with the enhanced CLA strategy with e.g. $\mathcal{N} = 16$ resulted in a 32-fold increase in computational speed.

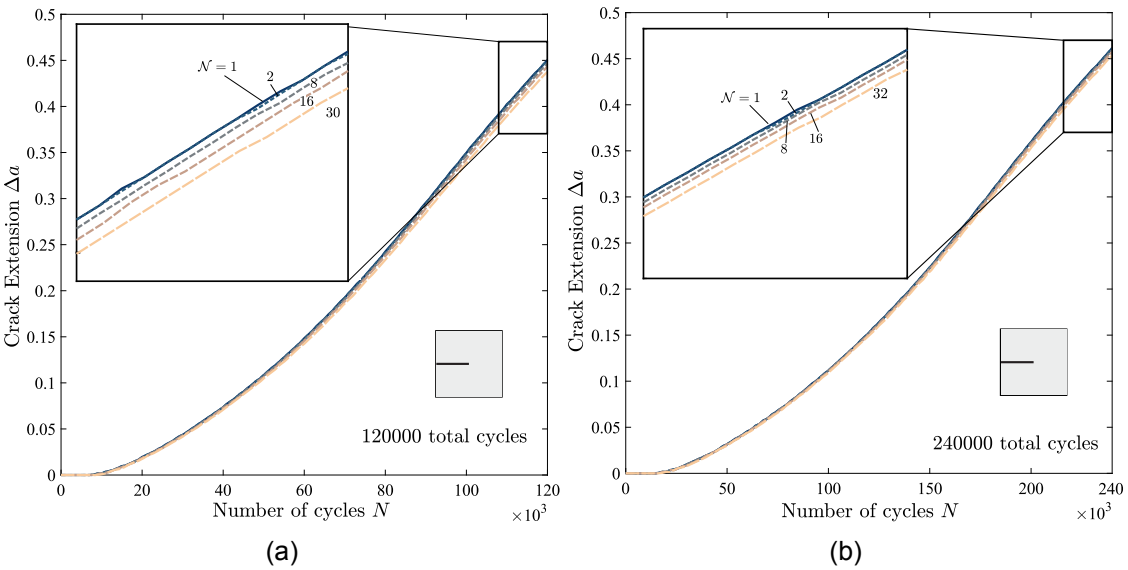

Figure 5.14: Cracked square plate. Fatigue crack extension versus number of load cycles for various values of $\mathcal{N}$ (number of multiple load cycles per increment), utilizing both the MN and CLA acceleration strategies, and repeated load of (b) 120,000 cycles, and (c) 240,000 cycles. Adapted from [P2].

$\mathcal{N}$	1	2	8	16	30
Computational time [hr]	13.0	9.3	5.3	3.0	1.3
Matrix factorizations	1 191	609	293	297	293
Total iterations ϕ	120 205	60 312	15 634	8 271	4 778
Total iterations **u**	276 812	227 920	127 541	70 568	40 896
Crack extension deviation [%]	-	0.19	-0.89	-1.51	-2.85

Table 5.3: Cracked square plate. Impact of including multiple load cycles per increment ($\mathcal{N} > 1$). The results obtained for the case of 120,000 repeated load cycles, utilizing both the MN and CLA acceleration strategies. Adapted from [P2].

5.2.2 Asymmetric three point bending

The second case study focuses on utilizing fatigue acceleration strategies for a more complex boundary problem involving mixed-mode cracking. As illustrated in Fig. 5.15, a rectangular beam containing multiple holes is subjected to three-point bending cyclic loads. The problem includes an initial crack embedded asymmetrically to the loading pins and holes. This benchmark boundary value problem has previously been studied under static/monotonic loading conditions (e.g., Refs. [155, 156]). The beam is subjected to a cyclic remote displacement for 120,000 load cycles under a load ratio of $R = 0$, which is the standard practice for three-point bending fatigue tests. The computational domain is discretised using approximately 128,000 bilinear quadrilateral elements with full integration. To efficiently capture the fatigue history, both the MN and CLA strategies are employed in tandem. The simulations are performed using various strain energy density

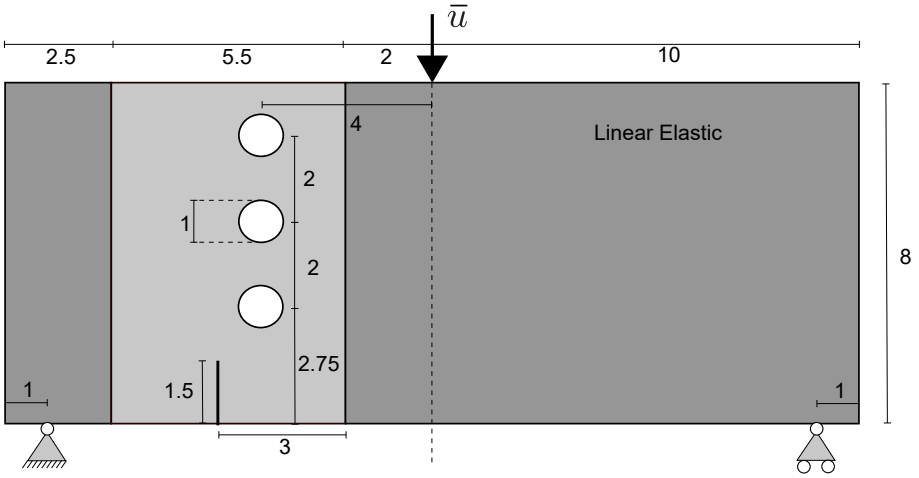

Figure 5.15: Asymmetric three-point bending. Geometry and loading conditions (with dimensions in mm). Only the light gray area undergoes fatigue damage. Adapted from [P2].

decomposition, detailed in Section 2.4.3, to account for differences in fatigue crack growth predictions. Fig. 5.16 shows the crack trajectories obtained at the end of the analysis. It is observed that the crack propagation path is different under cyclic loading compared to static loading; see e.g. Refs. [155, 156]. The reason for this discrepancy is due to the accumulation of fatigue around the holes, which causes the initiation of new secondary cracks before the primary crack intersects with the holes. By incorporating the material's endurance limit into the analysis, it may be possible to eliminate secondary cracks and restore the crack propagation path observed during static loading. According to Table 5.4, it appears that the proposed solution scheme offers significant performance improvements.

This is particularly evident in the reduction of matrix factorizations needed, while only a slight increase in the number of iterations required for the displacement subproblem is observed. It is important to highlight that when using the MN algorithm, the no-tension split demands the longest computational time, but it is still over five times faster compared to using a conventional Newton method without a CLA scheme. Without these acceleration strategies, it can be anticipated that computational time is almost independent of the decomposition split, as only one iteration per field per increment is necessary, even in the most advanced scenario. Therefore, the acceleration is approximately nine times faster for the isotropic and volumetric/deviatoric splits.

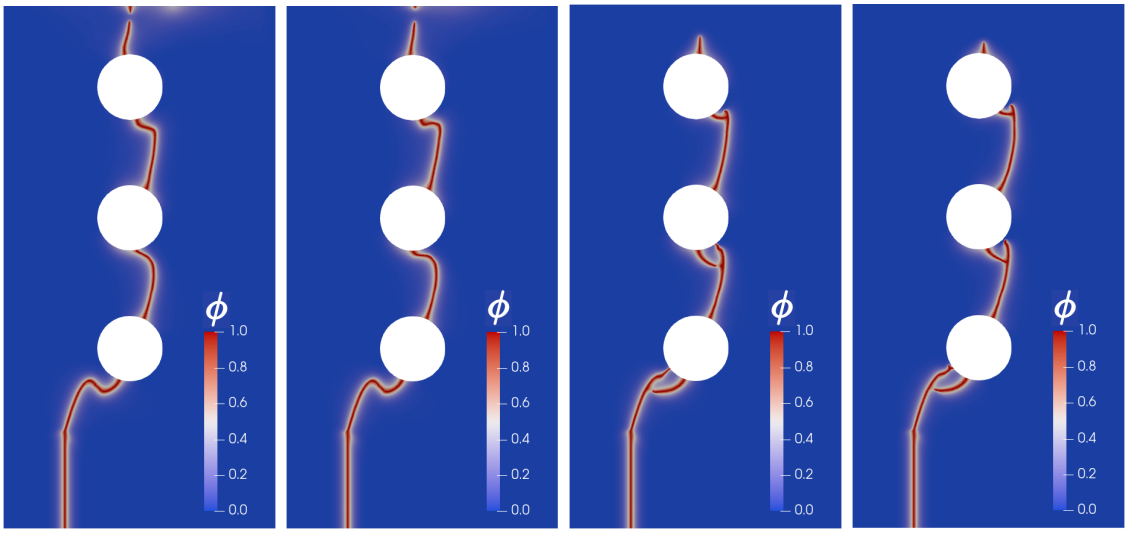

(a) Isotropic (b) Vol./dev. (c) Spectral (d) No-tension

Figure 5.16: Asymmetric three-point bending. Contours of phase field crack after 90,000 load cycles utilizing various strain energy density decomposition. Adapted from [P2].

Strain decomposition	Isotropic	Vol./dev.	Spectral	No-tension	No-tension*
Computational time [hr]	44.9	44.4	60.3	75.5	399.0
Matrix factorizations	1 249	1 278	1 341	1 295	180 130
Total iterations ϕ	91 355	91 400	91 742	91 624	180 130
Total iterations **u**	314 292	328 948	400 795	426 645	180 130

Table 5.4: Asymmetric three-point bending. Impact of strain energy density decomposition on computational performance, utilizing both the MN and CLA acceleration strategies. *Without acceleration strategies. Adapted from [P2].

5.2.3 3D beam under tension with a tilted edge crack

For our final case study, we consider a three-dimensional beam that contains an edge crack positioned at a 45° angle with respect to the beam's cross section, as depicted in Fig. 5.17. The beam is subjected to a uniaxial cyclic displacement on both sides for a total of 600,000 load cycles with a load ratio of $R = 0$. The computational domain is discretised using approximately 196,000 linear tetrahedral elements with full integration. The mesh is refined in the vicinity of the crack. We use both the MN and CLA schemes (with $\mathcal{N} = 4$ load cycles per increment) in combination to effectively capture the fatigue history.

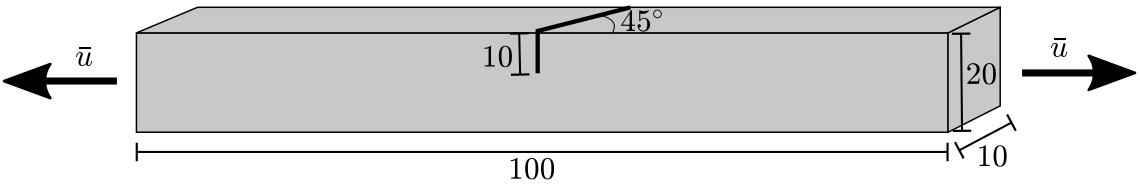

Figure 5.17: 3D beam under uniaxial cyclic tensile load containing a tilted edge crack. Geometry and loading conditions (with dimensions in mm). Adapted from [P2].

The resulting phase field contours, which demonstrate the fatigue crack growth trajectory, are presented in Fig. 5.18. As expected, the crack gradually rotates to align itself perpendicular to the maximum principal stress direction as it grows. The proposed methods greatly speed up the computation, reducing the total number of increments required to capture 600,000 load cycles to only 150,000, while performing 2,978 matrix factorizations. This is a considerable improvement compared to the baseline case, where 1,200,000 increments, matrix factorizations, and iterations would be required. The two acceleration schemes proposed here result in a total of approximately 172,000 iterations for the displacement subproblem and 160,000 for the phase field subproblem. This reduces the number of matrix factorizations by a factor of over 400, which is the main factor affecting computational time for such large problems. For problems with millions of cycles, a higher number of load cycles per increment $\mathcal{N}$ can be used for even higher computational efficiency without compromising accuracy. With these acceleration schemes, phase field fatigue is demonstrated to be a powerful tool for predicting complex fatigue crack growth in 3D over hundreds of thousands of load cycles.

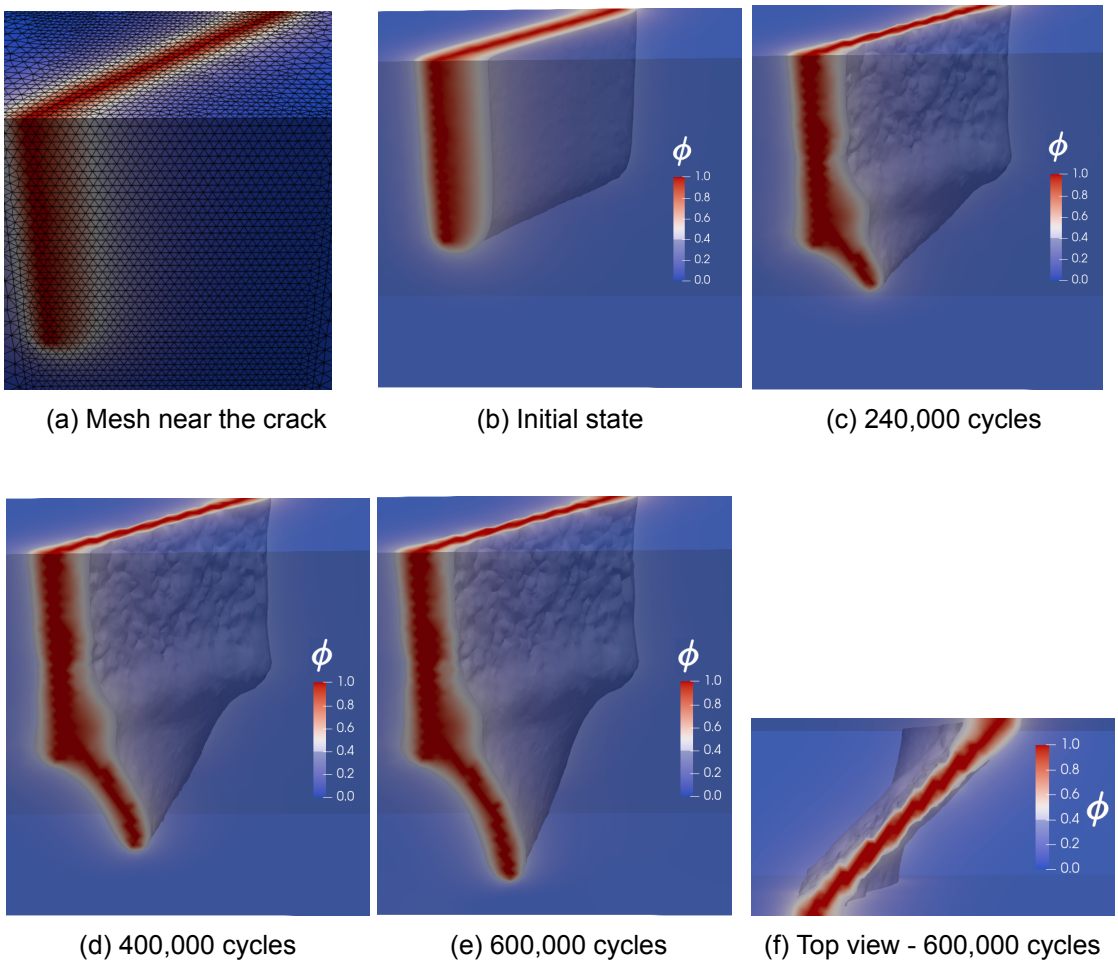

(a) Mesh near the crack (b) Initial state (c) 240,000 cycles

(d) 400,000 cycles (e) 600,000 cycles (f) Top view - 600,000 cycles

Figure 5.18: 3D beam under uniaxial cyclic tensile load containing a tilted edge crack. Phase field contours at various stages of fatigue. As the crack grows, it gradually reorients itself to become perpendicular to the maximum principal stress direction. Adapted from [P2].

5.3 Fatigue crack growth analysis

This section presents the results of numerical experiments conducted to further assess the performance of the phase field fatigue model proposed in this thesis [P1]. First, a boundary layer formulation is employed to gain insights into fatigue crack growth (FCG) under small-scale yielding conditions (Section 5.3.1). Through a parametric study, the influence of fatigue model/material parameters on FCG rate curves is investigated, establishing a correlation between S-N and FCG rate curves. The model's predictions are then compared to experimental data obtained from compact tension (CT) tests (Section 5.3.2). Furthermore, the model's ability to capture the concept of transition flaw size is explored by analyzing a finite plate with an internal crack of varying length (Section 5.3.3). Finally, the model's predictions are verified against experimental data on curvilinear crack path trajectories obtained from single edge notched polystyrene samples (Section 5.3.4). Throughout this section, unless otherwise stated, we utilize the `AT1` model, the $f_1(\bar{\alpha})$ fatigue degradation function (2.34), the No-tension split (2.21), the quasi-Newton monolithic solution scheme (Section 4.5.1), and the enhanced CLA solution strategy (Section 5.2).

5.3.1 Boundary Layer model

First, we investigate the fatigue crack growth behaviour under small scale yielding conditions. To achieve this, we employ a boundary layer formulation that utilizes a circular region of a body containing a crack. The model prescribes a remote K_I field, which is applied only to the upper half of the domain due to symmetry, as shown in Fig. 5.19. The remote K_I field is elastic and is generated by prescribing the displacements of the outer region nodes according to the Williams expansion [157]. The displacements of the nodes in the polar coordinate system (r, θ) centered at the crack tip are described by their horizontal and vertical components, respectively

$$
\begin{aligned}
u_x(r,\theta) &= K_I \frac{1+\nu}{E}\sqrt{\frac{r}{2\pi}}\cos\left(\frac{\theta}{2}\right)\left[3-4\nu-\cos\left(\theta\right)\right] \\
u_y(r,\theta) &= K_I \frac{1+\nu}{E}\sqrt{\frac{r}{2\pi}}\sin\left(\frac{\theta}{2}\right)\left[3-4\nu-\cos\left(\theta\right)\right]
\end{aligned}
\tag{5.2}
$$

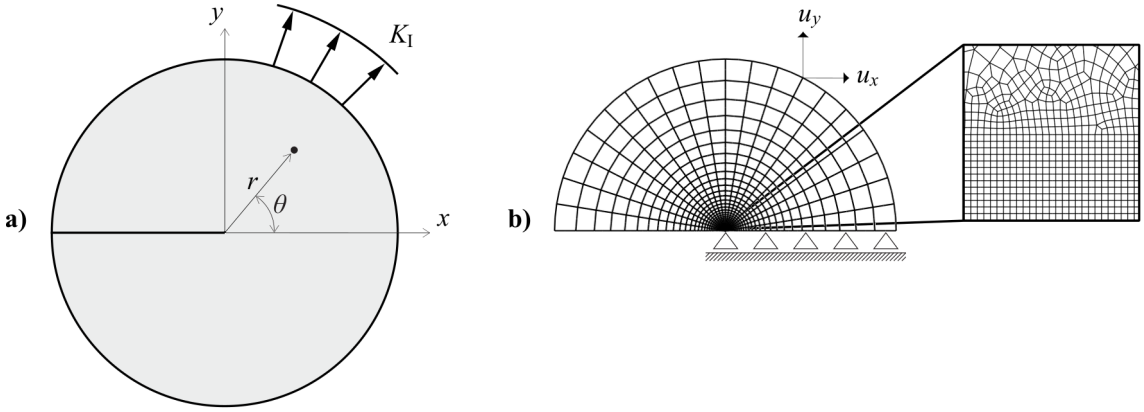

Figure 5.19: Boundary layer model. (a) Geometry and loading conditions, and (b) finite element mesh, featuring an in-depth look at the mesh near the crack tip. Adapted from [P3].

where the stress intensity factor is defined as a sinusoidal function for the application of cyclic loads

$$K_{\mathsf{I}} = K_{\mathsf{m}} + \frac{\Delta K}{2} \sin\left(2\pi f\, t\right) \quad \text{with} \quad K_{\mathsf{m}} = \frac{\Delta K}{2} + \frac{R\,\Delta K}{1-R} \tag{5.3}$$

where f represents the frequency of the load, t the time of the test, K_{m} the mean value of the load, $\Delta K = K_{\mathsf{max}} - K_{\mathsf{min}}$ the range of the load, and $R = K_{\mathsf{min}}/K_{\mathsf{max}}$ the load ratio. The circular area is discretised using 4,572 bilinear quadrilateral plane strain elements with full integration, and the mesh is refined in the area where the crack propagates. We can establish a reference stress intensity factor K_0 and a fracture process zone length L_f, as defined by [108, 113]:

$$K_0 = \sqrt{\frac{G_c E}{(1-\nu^2)}} \quad \text{and} \quad L_f = \frac{G_c\left(1-\nu^2\right)}{E} \tag{5.4}$$

Parametric study

First, a parametric investigation is conducted to examine the influence of fatigue material/model parameters, introduced in Section 2.4.7. The study begins by analyzing the role of the power exponent n. Fig. 5.20a illustrates the results in terms of normalized fatigue crack extension versus the number of load cycles. These computations are performed for a load range of $\Delta K/K_0 = 0.1$. It can be observed that, for a given number of cycles, higher values of the power exponent lead to shorter fatigue crack extensions. As shown in Fig. 5.20a, a linear fit can be applied to the curves to determine the slope, representing the crack growth rates. Fig. 5.20b presents fatigue crack growth rates, FCGR, obtained for different stress intensity factor ranges ΔK and power exponent values n, plotted on a logarithmic scale. The results demonstrate a linear behavior within the Paris region, where crack growth remains stable. Beyond this region, the crack growth rate increases significantly, indicating unstable crack growth. Interestingly, the results reveal a clear relationship between the magnitude of n and the slope of the curves m in the Paris region. A higher value of n leads to FCGRs that are more sensitive to variations in the stress intensity factor range. Similar to the S-N curve shown in Fig. 5.6a, the power exponent n

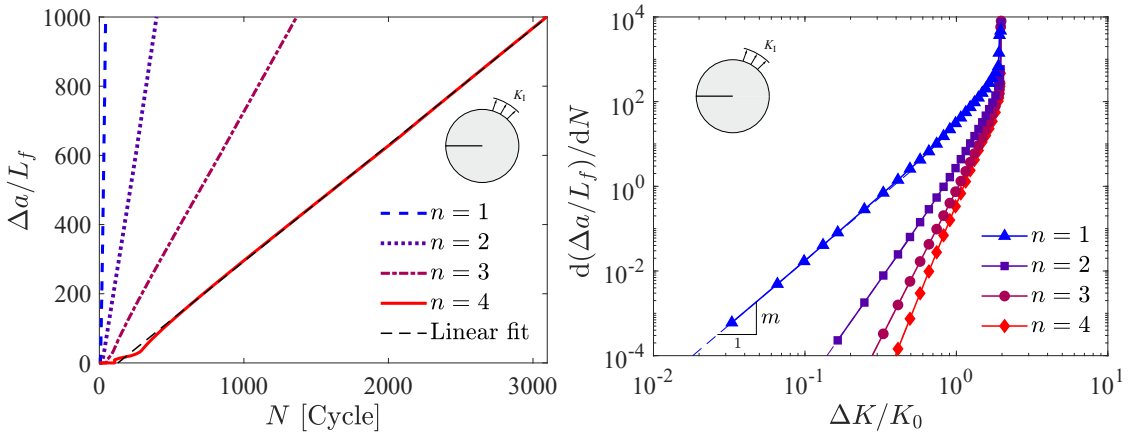

Figure 5.20: Boundary layer model. Examining the impact of the power exponent n on (a) crack extension (b) the fatigue crack growth rate curve with every data point representing a finite elements simulation. Adapted from [P3].

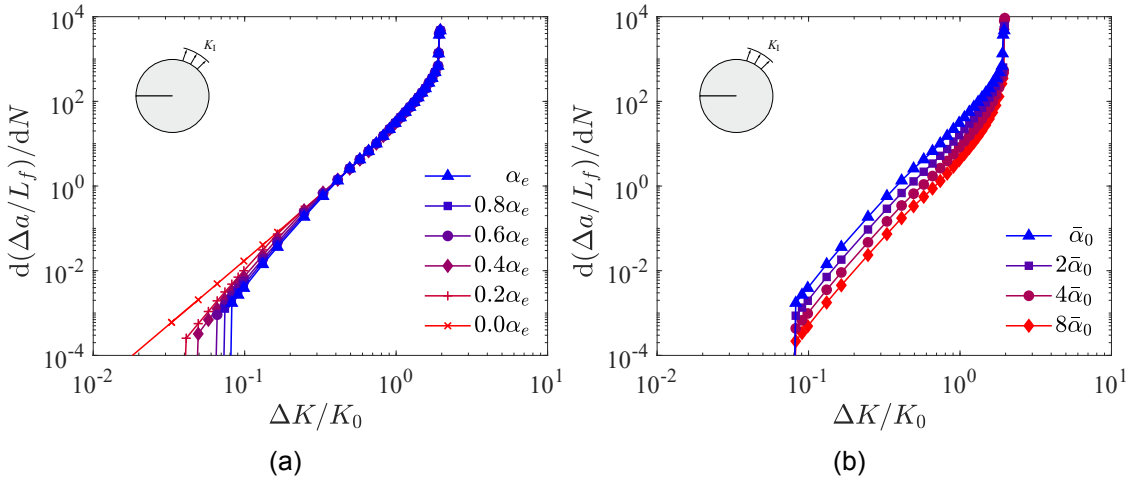

Figure 5.21: Boundary later model. Sensitivity of the fatigue crack growth rate curve with respect to: (a) the threshold parameter α_e, and (b) the fatigue model parameter $\bar{\alpha}_0$. Adapted from [P3].

offers modeling flexibility to accurately capture the slope m of the Paris curve for different materials. Furthermore, we will later demonstrate the ability of our model to establish a connection between the S-N and FCGR curves. It is crucial to note that altering the power exponent n does not have an impact on the ultimate fracture, as all the curves converge at the material's critical stress intensity factor K_{Ic}. Figs. 5.21a and 5.21b illustrate the results of the sensitivity analysis, evaluating the impact of α_e and $\bar{\alpha}_0$ on the FCGR curves. The results shown in Fig. 5.21a demonstrate that reducing the threshold parameter α_e, as defined in Eq. (2.37), to incorporate a material stress endurance limit, leads to a decrease in the size of the nucleation/threshold region. This decrease is quantified by a reduction in the material's threshold stress intensity factor K_{th}, which indicates a relatively low or negligible crack growth rate. In addition, as depicted in Fig. 5.21b, high values of $\bar{\alpha}_0$ correspond to elevated FCGRs within the Paris region, while having no significant impact on the other two regions. It is important to highlight that the slopes of the curves in the Paris region remain relatively consistent for both α_e and $\bar{\alpha}_0$, regardless of variations in

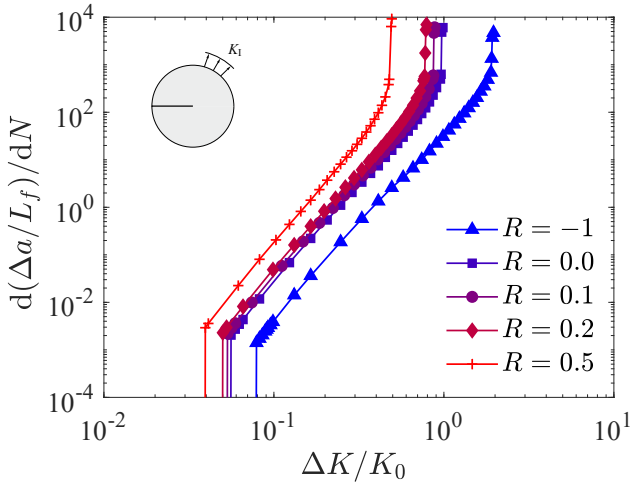

Figure 5.22: Boundary layer model. Influence of the load ratio R on the fatigue crack growth rate curve. Adapted from [P3].

their respective values. Finally, we conclude our parametric study by investigating the influence of the load ratio effect on the behavior of the FCGR curve in our model. The results shown in Fig. 5.22 demonstrate a significant impact of the load ratio R on all three regions of the FCGR curves. Consistent with experimental observations [5, 153], we observe a substantial increase in FCGR for a given ΔK as the load ratio R increases. Moreover, the critical stress intensity factor K_{Ic} and the threshold stress intensity factor K_{th} of the material both decrease with an increase in R. This decrease can be attributed to the higher load ratios leading to an increase in the maximum value of the applied cyclic load, denoted as $K_{\mathsf{max}} = \Delta K/(1-R)$.

A link between S-N curve and Paris law

We proceed to investigate how our model can link the S-N and Paris approaches for brittle solids. Initially, we perform uniaxial fatigue simulations on a smooth bar. The problem can be addressed semi-analytically by examining the homogeneous solution to Eq. (2.27). The bar undergoes a fully-reversed cyclic remote stress variation. We consider three values for the power exponent: $n = 1, 2$, and 3, resulting in S-N slope values of $-1/m \simeq 3$, 5, and 7, respectively (refer to Eq. (5.1) and Table 5.1). The S-N curve slope and its intercept with the $\log N$ (or $\log \sigma$) axis correspond to the fatigue parameters n and $\bar{\alpha}_0$, as explained in detail in [P1]. For our analysis, we introduce a hypothetical S-N curve, which intercepts with the $\log \sigma$ axis at the material strength σ_c value, as provided by Eq. (2.33). Therefore, by considering $n = 1$ and a data set ($\sigma^{\infty}_{\mathsf{max}}/\sigma_c = 1/3$) from our hypothetical S-N curve, we estimate a value of $\bar{\alpha}_0 = 3/2$. The outcomes are displayed in Fig. 5.23a, expressed as the (normalized) remote stress amplitude versus the number of load cycles to failure, utilizing a log-log plot. The computed S-N curves demonstrate linear behavior and follow a Basquin relationship [158],

$$\frac{\sigma_{\mathsf{max}}}{\sigma_c} = (N)^{-\frac{1}{m}} \,, \tag{5.5}$$

with all the curves converge at the material strength value on the $\log \sigma$ axis. We then perform fatigue crack growth simulations using our boundary layer formulation, adopting the same fatigue material/model parameters as those in our smooth bar. Fig. 5.23b displays the numerical outcomes alongside the analytical results derived from a Paris relationship [158],

$$\frac{\mathsf{d}a}{\mathsf{d}N} = \mathcal{C}\left(\frac{K_I}{K_{Ic}}\right)^m \quad \text{with} \quad \mathcal{C} = \left(\frac{m}{m-2}\right) r_c \quad \text{and} \quad r_c = \frac{1}{2\pi}\left(\frac{K_{Ic}}{\sigma_c}\right)^2 \,, \tag{5.6}$$

where the Paris pre-factor $\mathcal{C}$ and the exponent m are both associated with the S-N curve parameters, given in Eq. (5.5). Our findings highlight a strong correlation between two key fatigue phenomena. The exponents of the Basquin law and the Paris law are interconnected, with the latter being the inverse of the former. The computed FCGR curves exhibit a linear trend, with the fitted curves providing Paris pre-factor values that align remarkably well with the analytical results [158]. This discovery suggests that it is feasible to predict the fatigue crack growth behavior of a brittle solid using stress-life data, and vice versa. By introducing our phase field fatigue model, we can combine these normally independently treated phenomena. This has the potential to streamline analysis and design methodologies, while also reducing the amount of testing needed for fatigue damage characterization of brittle materials.

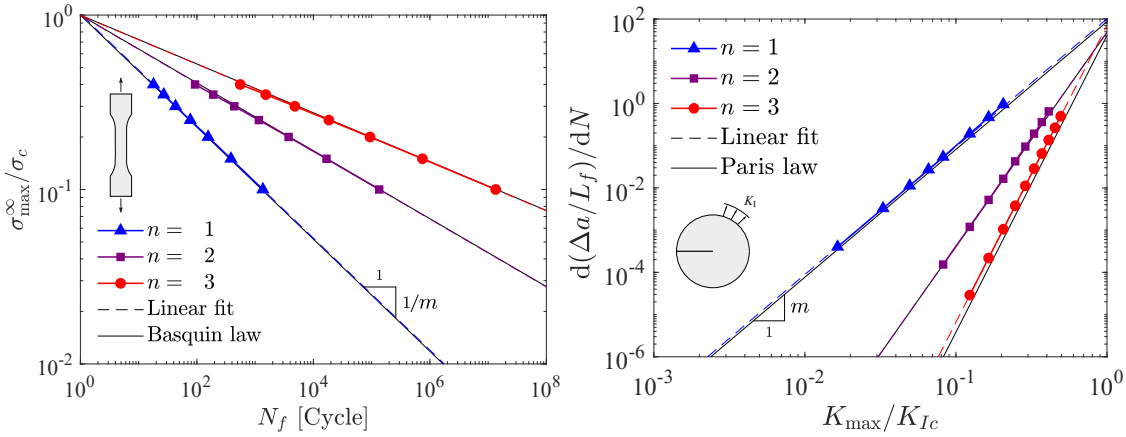

Figure 5.23: A link between key fatigue phenomena: (a) S-N curve and (b) Paris law. Results have been obtained for $R = -1$ and $\alpha_e = 0$. Adapted from [P3].

5.3.2 Fatigue crack growth in a Compact-Tension specimen

To further verify the ability of the proposed model to accurately predict fatigue crack growth (FCG) rates, we employ the widely recognized compact tension (CT) test. The CT test configuration, as shown in Fig. 5.24, aligns with the experimental setup described by Mehmanparast et al. [159]. The FCG experiments were carried out as part of the SLIC (Structural Life-cycle Industry Collaboration) joint industry project, aimed at enhancing our understanding of fatigue in butt-welded thick steel plates - a critical component in the manufacturing of foundations for offshore wind turbines. The material selected for the FCG tests is S355G8+M (EN-10225:1) structural steel, which is commonly used in offshore monopiles due to its excellent weldability and ability to withstand the harsh offshore environment. Our analysis focuses specifically on the experimental data obtained from the parent material, also referred to as the base metal (BM), under an inert environment. We perform a series of numerical simulations on one-half of the domain, taking advantage of its symmetry. The samples undergo cyclic load variations with the maximum load $P_{\max}$ and the load ratio R (see Table 5.5). The computational domains consist of approximately 15,750 - 17,000 bilinear quadrilateral plane strain elements with full integration. The mesh is refined in the region where the crack propagates.

Test ID	W [mm]	B [mm]	a_0 [mm]	$P_{\max}$ [kN]	R
A1	49.9	16.0	16.5	9.0	0.1
A2	49.9	16.0	14.8	6.7	0.1
B1	50.0	15.9	14.7	10.0	0.1
B2	50.0	15.9	14.5	10.0	0.1

Table 5.5: Compact tension (CT) test dimensions and loading conditions. Adapted from [P3].

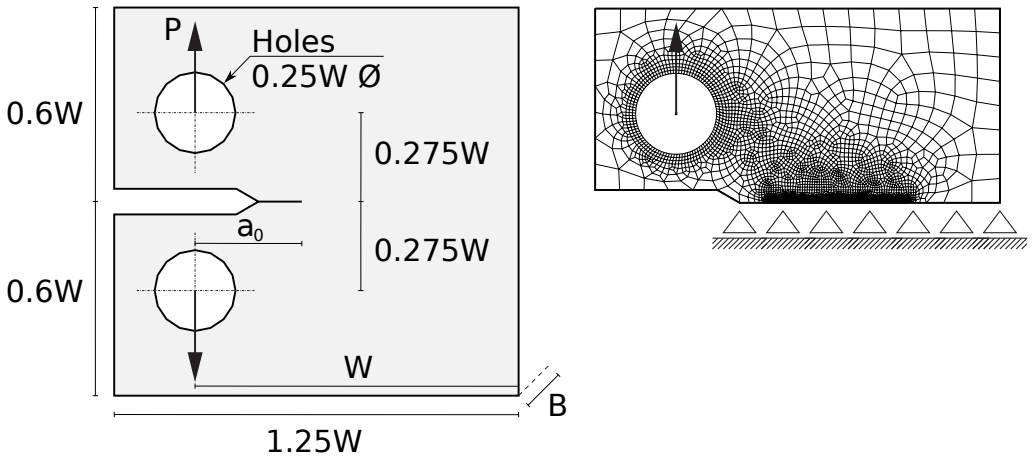

Figure 5.24: Compact tension (CT) test. Geometry, boundary conditions and finite element mesh. Adapted from [P3].

Under the assumptions of LEFM, the change in stress intensity factor can be determined by [160]

$$\Delta K = \frac{\Delta P}{B\sqrt{W}} \frac{(2+\beta)}{(1-\beta)^{3/2}} \left(0.886 + 4.64\beta - 13.32\beta^2 + 14.72\beta^3 - 5.6\beta^4\right) \tag{5.7}$$

with $\beta = a/W$. The fatigue parameters $n = 1$ and $\bar{\alpha}_0 = 89.2$ are estimated from the design S-N curve for structural steels, based on the slope, intercept, and fatigue limit, as provided in the DNV-GL standard [161]. Our analysis is specifically focused on category C[1], which pertains to non-welded classifications in an inert environment. The S-N curve for this category is characterized by a slope of $m = 3.0$, an intercept of 12.592 (on the log N axis), and a fatigue limit of $\sigma_e = 73.10$ MPa. It is crucial to emphasize that the S-N curve obtained from laboratory fatigue experiments conducted on smooth/polished samples of S355 steel demonstrates a higher value of m, as reported in Refs. [162, 163].

The experimental and numerical results are presented in Fig. 5.25 on a logarithmic scale, depicting the fatigue crack growth (FCG) rates ($\mathrm{d}a/\mathrm{d}N$) as a function of the stress intensity factor range ΔK. To calculate the FCG rates, a 7-point incremental polynomial technique, as recommended by the ASTM standard [164], was used. Additionally, the graph illustrates the Paris law relationships suggested by the BS7910 standard [165], which include both the simplified and two-stage models. It can be seen that the *Virtual* FCG rate curves predicted are in good agreement with the measured data. Both experiments and simulations show linear behavior in the Paris regime. The data indicates that in the given stress intensity factor range, the initial portion of FCG data points align with or fall below the 2-stage law suggested by BS7910. However, the subsequent portion of data points falls within the range of the simplified and 2-stage laws, leaning towards the simplified law. This observation implies that, for the given stress intensity factor range, the simplified Paris-law suggested by BS7910 offers a conservative assessment of the FCG behaviour in an inert environment. Building on the findings of Mehmanparast et al. [159], it is important to note an apparent variation in the FCG behavior between the samples A1 and A2 from Test Centre A, as well as B1 and B2 from Test Centre B. This difference is particularly pronounced in the initial stages of the FCG experiments. Such variability could likely be traced back to intrinsic differences in material properties, a factor that may significantly influence the early-stage FCG behavior of these samples.

[1]Manually gas cut material or material with machine gas cut edges with shallow and regular drag lines.

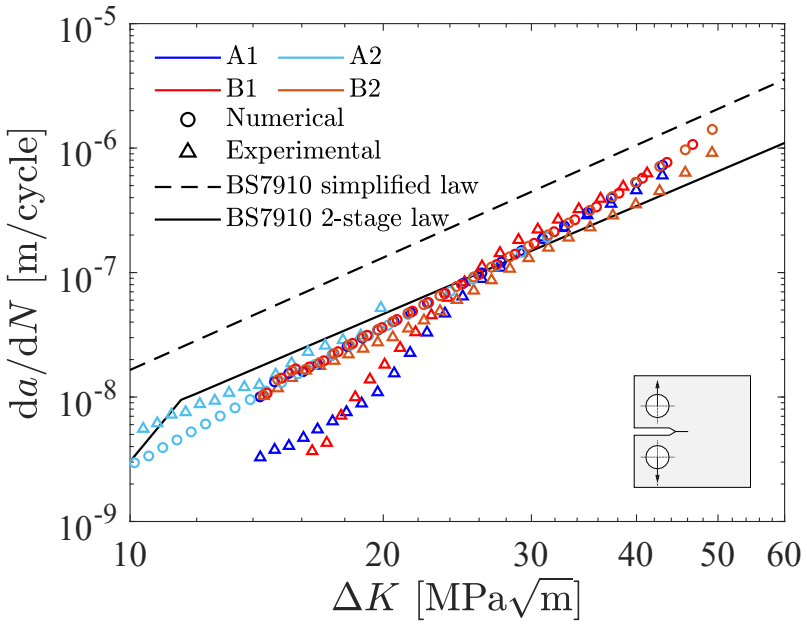

Figure 5.25: Numerical and experimental fatigue crack growth rate (FCGR) curves obtained form compact tension (CT) specimen for a base material (BM) in an inert environment. The graph showcases the simplified and two-stage trends recommend in BS7910 standard [165]. Adapted from [P3].

5.3.3 Size effects and the transition flaw size

We now investigate the ability of our model in capturing the interplay between material and structural size effects. As mentioned in Section 2.4.6, the inclusion of a finite length scale ℓ^+ in the phase field models yields a critical stress that is proportional to $1/\sqrt{\ell}$. This critical stress is not present in Griffith's formulation or linear elastic fracture mechanics (LEFM), making ℓ a significant material property. The inclusion of a positive, constant ℓ is motivated by the limitations of Griffith's theory in capturing well-established size effects. One such crucial size effect is the transition flaw size concept: If a crack is smaller than the critical flaw size, it will not propagate, and failure will occur at the material strength (or at the yield strength σ_y in the case of plastic design). In this context, we aim to demonstrate the natural emergence of the transition flaw size concept from our phase field model, considering both monotonic and cyclic loading scenarios. To achieve this, we investigate a pre-existing

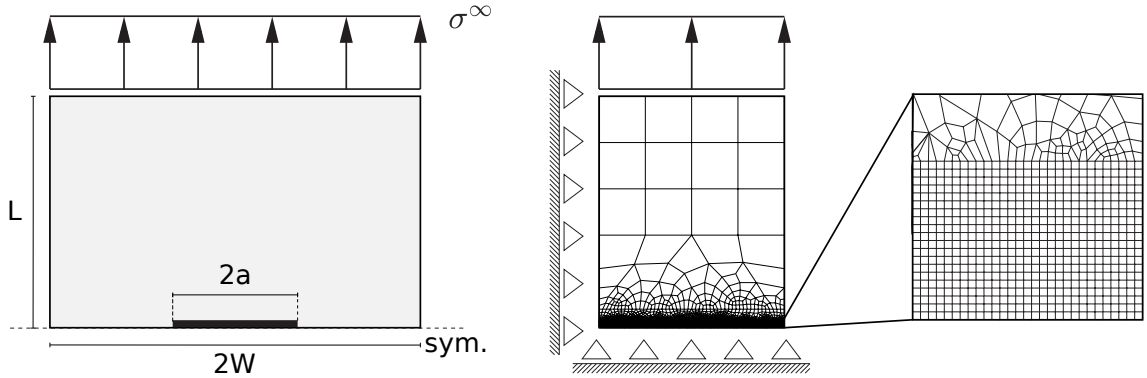

Figure 5.26: Internal crack in a finite plate with uniform remote stress loading. Geometry, boundary conditions and finite element mesh. Adapted from [P3].

crack with finite length in a plate of finite width, where the plate dimensions are set as $L = 4W = 4$ mm (see Fig. 5.26). This benchmark boundary value problem has previously been studied under static/monotonic loading conditions in Ref. [108]. We conduct a series of numerical simulations on a quarter of the domain, utilizing symmetry, with the initial crack half-length a varying from $0.002W$ to $0.512W$. To apply the loading, a fully-reversed cyclic remote stress variation is imposed on the upper edge of the plate. The plate is discretized using 12,302 bilinear quadrilateral plane stress elements with full integration. Under the assumptions of LEFM, the critical load at which the crack propagates can be determined by [160]

$$\sigma^{\infty} = \frac{1}{Y}\sqrt{\frac{EG}{\pi a}} \qquad \text{with} \qquad Y = \left(\sec\frac{\pi a}{2W}\right)^{1/2}\left[1 - 0.025\left(\frac{a}{W}\right)^2 + 0.06\left(\frac{a}{W}\right)^4\right] \tag{5.8}$$

The results obtained are shown in Fig. 5.27, in terms of the remote stress amplitude versus the crack half-length, also known as Kitagawa-Takahashi diagram. The graph showcases several key criteria, including the strength failure criterion $\sigma = \sigma_c$ (referred to as plastic failure when $\sigma_c = \sigma_y$), the Griffith (LEFM) criterion $G = G_c$, and the endurance stress limit $\sigma = \sigma_e$. The stress amplitude is normalized based on the material strength, as described in Eq. (2.33). The model's ability to connect stress and toughness criteria for both static and fatigue fracture is evident. It demonstrates a strong agreement with the Griffith criterion when analyzing larger cracks, while smoothly transitioning to a strength-driven failure as the crack size decreases below the critical flaw size. For finite life, data points can be added at constant number of cycles (e.g. 10^2 and 10^4 cycles), with the upper limit representing static failure while the lower limit signifying infinite life (non-propagating cracks). For infinite life, we have fitted a curve ($G = G_{th}$) to the results obtained in the toughness-driven region. This allows us to estimate a transition flow size associated with fatigue at the intersection of the curves for G_{th} and σ_e (i.e. $a/W \approx 0.007$). It is crucial to highlight that the estimated flaw size in this case is smaller than its static counterpart ($a/W \approx 0.020$). Moreover, this size decreases as the number of load cycles increases, bridging the gap between these two limiting values.

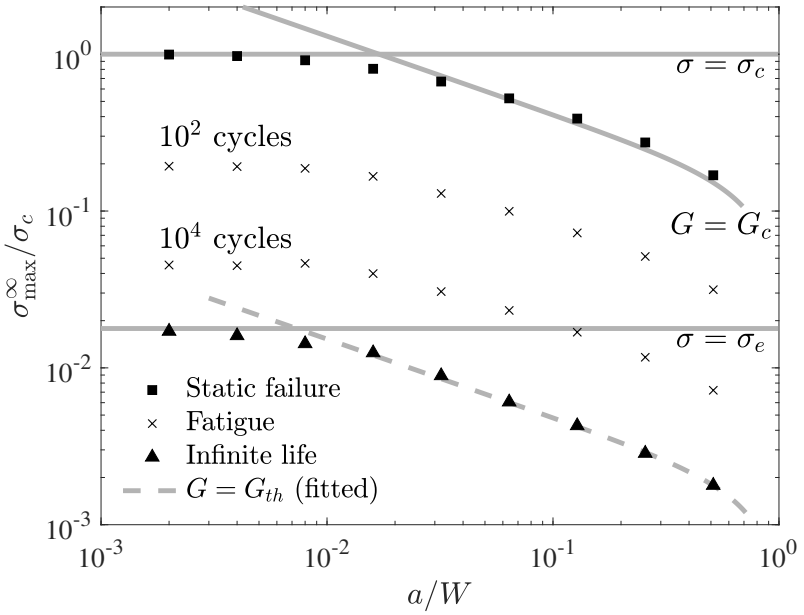

Figure 5.27: Transition flaw size analysis: Kitagawa-Takahashi diagram. Adapted from [P3].

5.3.4 Curvilinear crack growth prediction

We now verify the predictive capabilities of our model in determining the trajectories of curvilinear crack paths formed under heterogeneous (mixed-mode) stress conditions. Understanding the mechanics behind crack path curving and kinking is crucial for developing future material compositions that can effectively deflect crack propagation. These experiments were originally conducted by Chudnovsky et al. [166] on single-edge notched polystyrene samples. The dimensions of these samples, in mm, are presented in Fig. 5.28. In each sample, a circular hole is positioned at varying distances ($d_c = 2.5$, 3.5, 4.5, and 5.5 mm) from the center of the hole to the expected crack trajectory. This experimental setup enables the study of the interaction between the hole (acting as a stress raiser) and an oncoming crack. Ref. [166] states that crack propagation in the tested material involves the creation of a specific damage zone. This zone is marked by the formation of crazes, which demonstrates the mechanical aspect of the process. Notably, the size of the damage zone is significantly smaller than the geometric parameter of the problem, specifically the hole diameter. The influence of a hole on the stress field extends to a distance on the order of its diameter. Thus, a hole located ahead of the crack tip is expected to cause a deviation in the crack path near the hole. A summary of the experimental data obtained can be found in the work of Rubinstein [167]. Simulations are conducted with remote stress and strain amplitudes (with a load ratio of $R = 0.1$) to compare load- as well as displacement-controlled numerical experiments. The computational domain consists of 223,838 bilinear quadrilateral plane strain elements with full integration. To ensure an accurate representation of the fracture process zone, the mesh is refined in the anticipated crack propagation area.

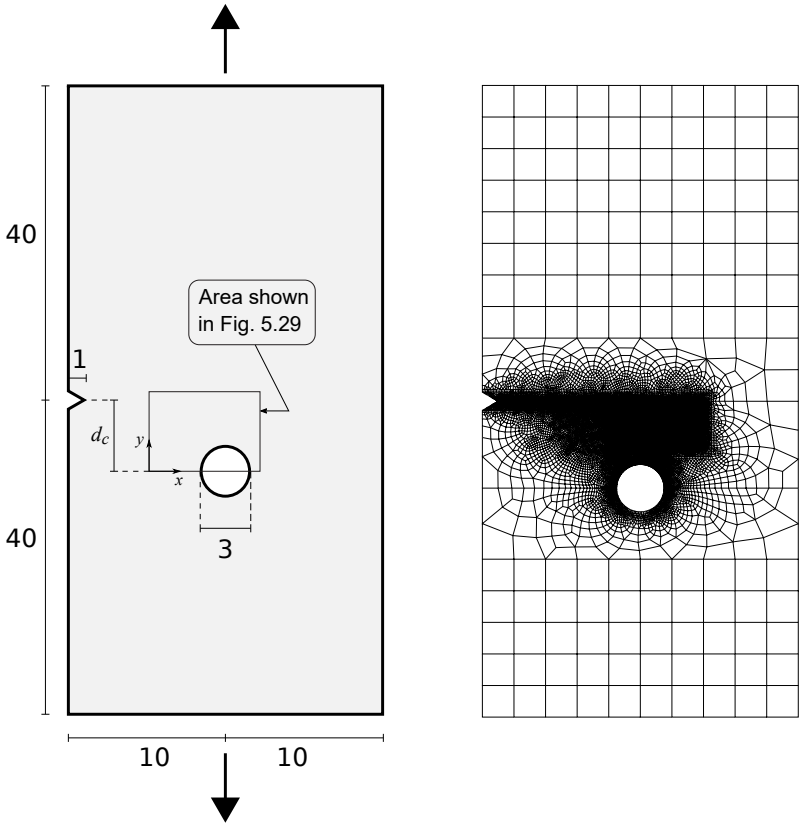

Figure 5.28: Notched rectangular plate containing a hole. Geometry (with dimensions in mm), loading conditions and finite element mesh. d_c is the distance from the center of the hole to the expected crack path. Adapted from [P3].

The results derived from our analysis are illustrated in Fig. 5.29. This figure presents four experimental crack paths and their associated numerical predictions, which have been normalized by the hole radius, within the effective region (refer to Fig. 5.28). Our findings indicate that the model accurately captures the effect of the hole on the approaching crack. As the vertical distance between the hole and the notch decreases, the hole's influence becomes more pronounced. This leads to a rotation of the damage/active zone and a subsequent transformation in its shape. Three distinct scenarios of crack interaction with a hole have been identified based on these observations: (i) crack attraction ($y/r = 1.67$), (ii) both attraction and repulsion ($y/r = 2.33$ and 3.00), and finally, (iii) scenarios where the hole has no noticeable impact on the crack path. It is important to underscore that the integration of the material's endurance limit into the analysis has successfully mitigated the initial accumulation of fatigue around the holes. This strategic incorporation prevents the emergence of new secondary cracks before the primary crack comes into contact with the holes. In conclusion, the model's prediction of the crack path aligns substantially with the experimental results, indicating its validity and effectiveness.

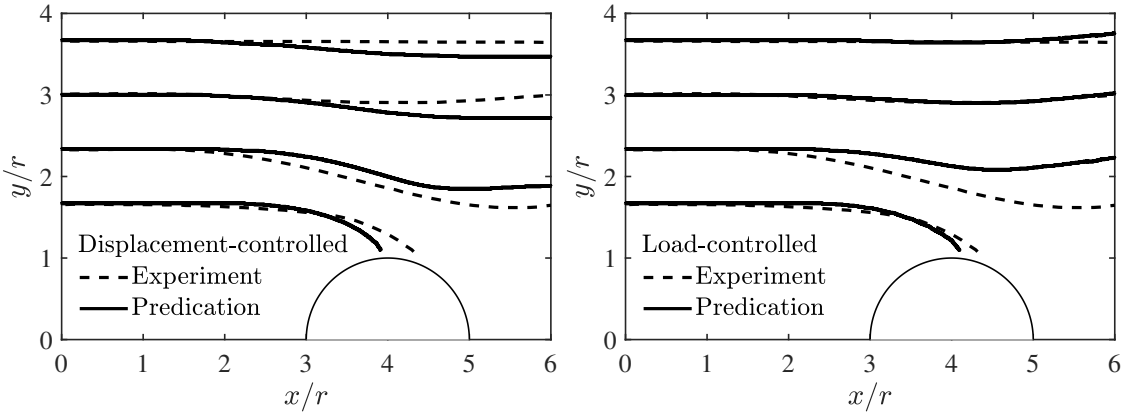

Figure 5.29: Numerical and experimental crack path trajectories obtained from single edge notched polystyrene samples: (a) load-controlled, and (b) displacement-controlled cyclic tests. Adapted from [P3].

5.4 Environmentally-assisted fatigue

The hydrogen-assisted fatigue model proposed in this thesis [P4] is demonstrated to have strong predictive capabilities through a series of numerical experiments. These experiments are outlined in the following sections. In Section 5.4.1, the accuracy of our numerical implementation is validated without the presence of hydrogen. Furthermore, this section shows how the model can accurately account for the role of hydrogen in accelerating crack propagation rates. In Section 5.4.2, a boundary layer formulation is utilized to gain a deeper understanding of hydrogen-assisted fatigue crack growth under assumptions of small-scale yielding. Section 5.4.3 investigates the fatigue behavior of notched samples, predicting *Virtual* S-N curves for different hydrogenous environments. Finally, in Section 5.4.4, the model's predictions are compared to fatigue experiments conducted on smooth dog-bone specimens that were exposed to either air or high-pressure hydrogen gas. Throughout this section, unless otherwise stated, we utilize the `AT2` model, the $f_0(\bar{\alpha})$ fatigue degradation function (2.34), the volumetric-deviatoric split (2.19), and the residual-based staggered solution scheme (Section 4.5.2).

5.4.1 Cracked square plate

Initially, we validate our model in the absence of hydrogen. To achieve this, we return to our cracked square plate, presented in Section 5.2.1 (see Fig. 5.12). The plate undergoes a cyclic remote displacement that is piece-wise linear, with a load ratio of $R = -1$. A mesh consisting of 27,410 quadratic quadrilateral elements with reduced integration is used to discretise the domain. The outcomes are shown in Fig. 5.30 and depict the relationship between crack extension Δa (measured in mm) and the number of cycles N, based on three options of the strain energy density decomposition. The computations are compared to the predictions of Carrara et al. [64] and Kristensen and Martínez-Pañeda [139], demonstrating good agreement. Especially, Kristensen and Martínez-Pañeda's quasi-Newton monolithic implementation agrees well, while Carrara et al.'s work utilizes an energy-based criterion to ensure the staggered solution scheme iterates until reaching the monolithic solution [103]. The literature indicates that if the isotropic (no-split) model is used, higher fatigue crack propagation rates are anticipated since both tension and compression portions of a load cycle contribute to damage (see also Fig. 5.1a).

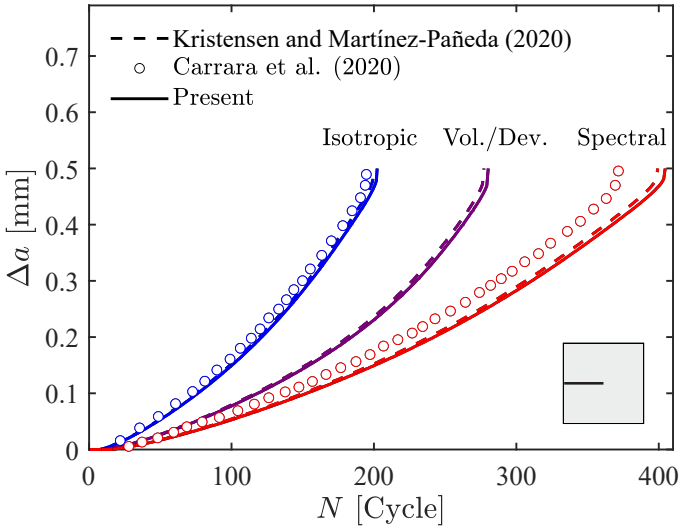

Figure 5.30: Cracked square plate. Fatigue crack extension versus number of load cycles in an inert setting: Comparison with findings from Kristensen and Martínez-Pañeda [139] as well as Carrara et al. [64]. Adapted from [P4].

Furthermore, the model's residual-based solution scheme is evaluated by comparing its performance with the one-pass (single-iteration) staggered algorithm using the isotropic model. As shown in Fig. 5.31, the results reveal that the one-pass algorithm requires a significant number of increments per cycle to converge towards the residual-based scheme. This number of increments per cycle leads to a high computational effort, which renders the one-pass algorithm unsuitable for fatigue simulations. It is worth noting that the residual-based scheme is identical to the solution obtained using the quasi-Newton monolithic scheme [139]. However, the latter approach proved to be unfeasible for solving the system of equations that incorporates the hydrogen diffusion problem due to the presence of an asymmetrical stiffness matrix.

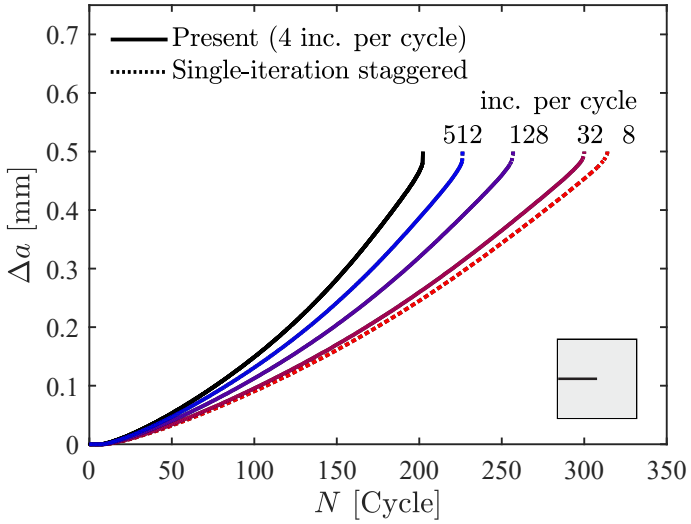

Figure 5.31: Cracked square plate. Fatigue crack extension versus number of load cycles in an inert setting: Analysis of the residual-based method versus the single-iteration (one-pass) staggered approach.

Subsequently, the plate is placed in a hydrogen-rich environment at ambient temperature. The plate is assumed to have been pre-charged and continuously exposed to the hydrogen environment during the experiment. As a result, an initial condition is assigned with a uniform distribution of hydrogen, where the hydrogen concentration at time zero is constant and equal to the environmental hydrogen concentration, denoted by $C_0 = C_{\text{env}}$ for all material points along the plate. At all outer surfaces of the plate, including the initial crack, a constant hydrogen concentration $C(t) = C_{\text{env}}$ is maintained. The results, depicted in Fig. 5.32 for three hydrogen environments, indicate that fatigue crack propagation rates increase as the environmental hydrogen concentration increases, which is consistent with previous studies, e.g., [168, 169]. While assuming a constant hydrogen concentration at the crack faces may simplify calculations, it is more accurate to utilize generalized Neumann-type boundary conditions [130, 170] or hydrostatic stress-dependent Dirichlet boundary conditions [83, 127, 171].

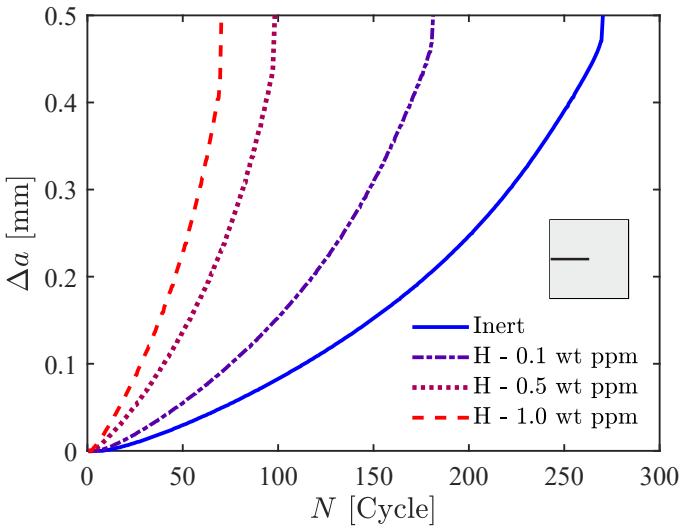

Figure 5.32: Cracked square plate. Fatigue crack extension versus number of load cycles for different environmental hydrogen concentrations. Adapted from [P4].

5.4.2 Boundary layer model

Next, we investigate the effect of hydrogen on fatigue behaviour under assumptions of small scale yielding. To achieve this, we return to our boundary layer model, presented in Section 5.3.1 (see Fig. 5.19). To accurately capture the sinusoidal load history, each load cycle is divided into a minimum of 20 internal time increments. The computational domain is discretised using 4,572 quadratic quadrilateral elements with reduced integration. In an inert environment, a reference stress intensity factor K_0 and a fracture process zone length L_f are defined in Eq. (5.4). First, we consider a stationary crack in a solid material that is initially charged with hydrogen at a uniform concentration of C_0, and is being subjected to a sinusoidal cyclic load with a load ratio of $R = 0$. As time passes, the distribution of hydrogen at the tip of the crack changes. To quantify this change, we can use dimensionless groups that are defined by the Buckingham Π theorem,

$$\frac{C}{C_0} = \mathcal{F}\left(\frac{fL_0^2}{D}, \quad \frac{tD}{L_0^2}, \quad \frac{E\bar{V}_H}{\mathcal{R}T}\right) \tag{5.9}$$

Dimensional analysis yields the length parameter $L_0 = (K_{\mathsf{m}}/E)^2$, which provides a measure of the crack tip quantities. Two dimensionless groups, the normalised frequency $\bar{f} = \dfrac{fL_0^2}{D}$ and the normalised time $\bar{t} = \dfrac{tD}{L_0^2}$, aim to measure the influence of test and diffusion times. Hydrogen diffusion is partly influenced by hydrostatic stress gradients, as described in Eq. (3.14), causing hydrogen atoms to diffuse into regions with high volumetric strains. In steady-state conditions, the hydrogen concentration can be determined as:

$$C = C_0 \exp\left(\frac{\bar{V}_H \sigma_H}{\mathcal{R}T}\right). \tag{5.10}$$

The distribution of hydrogen near the crack tip varies during the application of the cyclic load. Fig. 5.33 illustrates the obtained results at three stages (maximum, mean, and minimum) of the initial load cycle for an effectively low frequency, mimicking steady-state conditions. The concentration of hydrogen is expected to increase with applied load, and it reaches its peak value at the crack tip, where hydrostatic stress is largest. Furthermore,

for a zero value of the hydrostatic stress at $K_{\text{min}} = 0$, the hydrogen concentration remains constant, as anticipated.

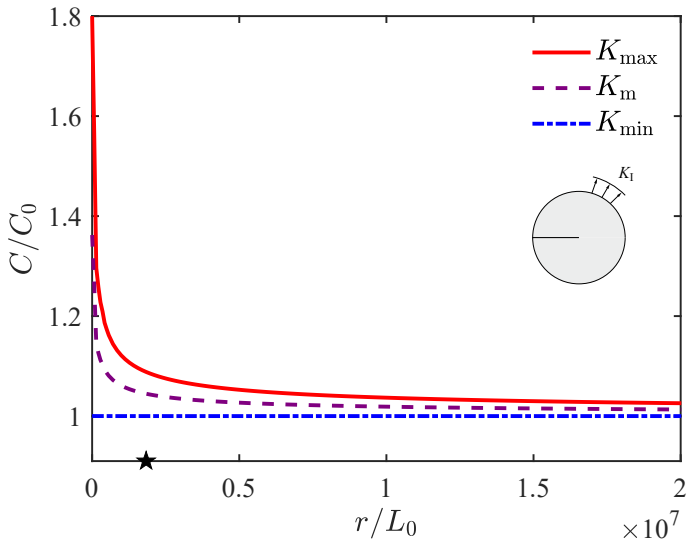

Figure 5.33: Boundary layer model. Hydrogen concentration near a stationary crack tip during three stages of the initial loading cycle. The results are obtained under steady-state conditions and a load ratio $R = 0$. Adapted from [P4].

Let us now examine the situation of transient conditions and investigate how the loading frequency and diffusion time interact. In Fig. 5.34, we see a graph of the hydrogen concentration ahead of the crack tip over time. The point being examined is marked by a star in Fig. 5.33. The results indicate that the maximum hydrogen content near the crack tip is significantly influenced by the loading frequency, regardless of the test duration. In cases where the hydrogen diffusivity is high compared to the load cycle's duration (low f), the amplitude of the hydrogen concentration aligns with that of the hydrostatic stress, similar to the steady-state scenario (5.10). However, at high frequencies, unloading initiates prior to the hydrogen distribution reaching a steady-state solution, resulting in a lower maximum value of C during the experiment compared to lower frequencies. At the highest frequency ($f = 10^3$ Hz), the hydrogen concentration does not exhibit any oscillations. Instead, it stabilizes at a constant value which is approximately 5% lower than the maximum hydrogen concentration obtained at low frequencies.

Our investigation focuses now on how the interplay between diffusion time and frequency affects the rates at which fatigue cracks grow. The graph presented in Fig. 5.35 illustrates the relationship between (normalized) fatigue crack extension and the number of load cycles, with respect to the hydrogen concentration present in the environment C_{env}. The simulations were conducted on a pre-charged solid with an initial hydrogen concentration of $C(t = 0) = C_{\text{env}}$, and which was subsequently exposed to a hydrogenous environment throughout the testing process ($C(t) = C_{\text{env}}$ at the outer boundaries). The results depicted in Fig. 5.35 demonstrate that the model successfully predicts the expected patterns: for a given number of load cycles, higher hydrogen concentrations correspond to greater fatigue crack extension. The linear portion of the curve can be used to determine the slope (i.e., crack propagation rates) by applying a linear fit, as shown in Fig. 5.35.

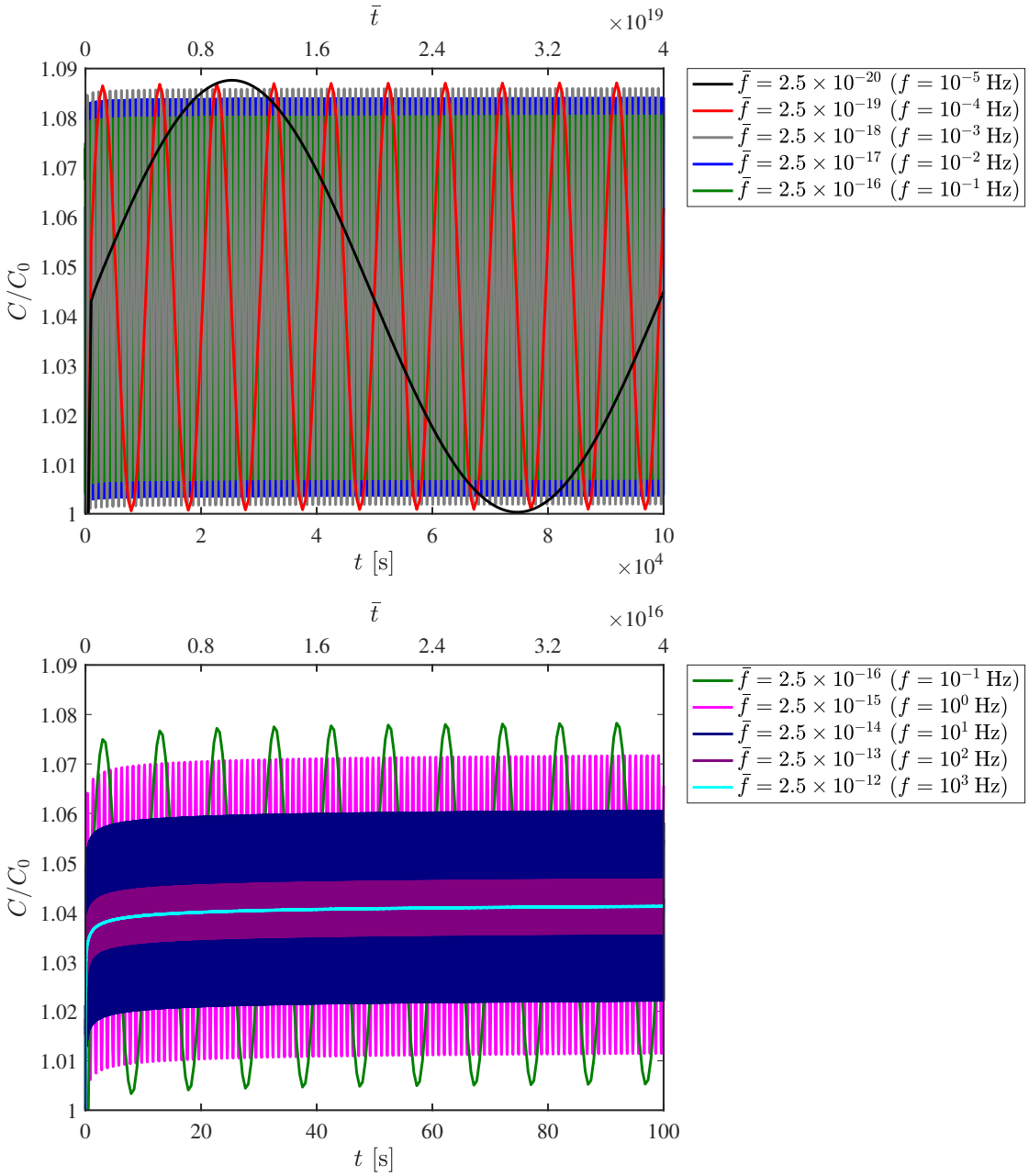

Figure 5.34: Boundary layer model. Temporal hydrogen concentration at a point near a stationary crack tip, considering different loading frequencies and an $R = 0$ load ratio. Adapted from [P4].

Fig. 5.36 depicts the fatigue crack growth rates obtained for varying hydrogen concentrations and different values of ΔK, using a log-log graph. As expected, the computed curves exhibit linear behavior in the Paris region, where cracks grow steadily. By utilizing the Paris equation $\mathrm{d}a/\mathrm{d}N = \mathcal{C}\Delta K^m$, we observe that the value of $\mathcal{C}$ increases with increasing hydrogen content, supporting the experimental observations. The exponent m, however, seems to be less influenced by the environment, with a value of approximately 3.2, which is consistent with the range of metals in inert environments that has been reported previously [172]. In addition, the sensitivity of fatigue crack growth rates to frequency is demonstrated in Fig. 5.37. The model reproduces a commonly observed trend in experimental results, where the effect of hydrogen on the fatigue behavior of met-

als falls into two categories: (i) fast tests (high f) where hydrogen does not have sufficient time to accumulate in the fracture process zone, resulting in reduced likelihood of embrittlement, and (ii) slow tests (low f) where hydrogen diffuses into high hydrostatic stress regions, leading to increased embrittlement. The model is capable of effectively predicting the gradual transition between these two categories.

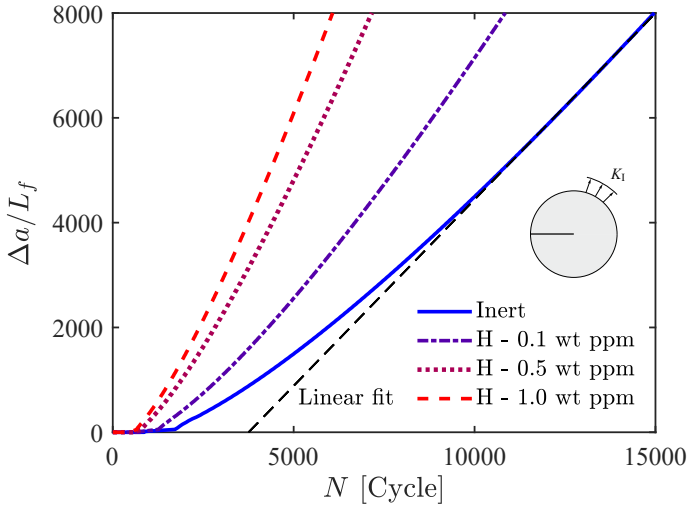

Figure 5.35: Boundary Layer Model: Fatigue Crack extension versus number of load cycles for varying hydrogen concentrations with $\Delta K/K_0 = 0.08$, $R = 0.1$, and $f = 1$ Hz. Adapted from [P4].

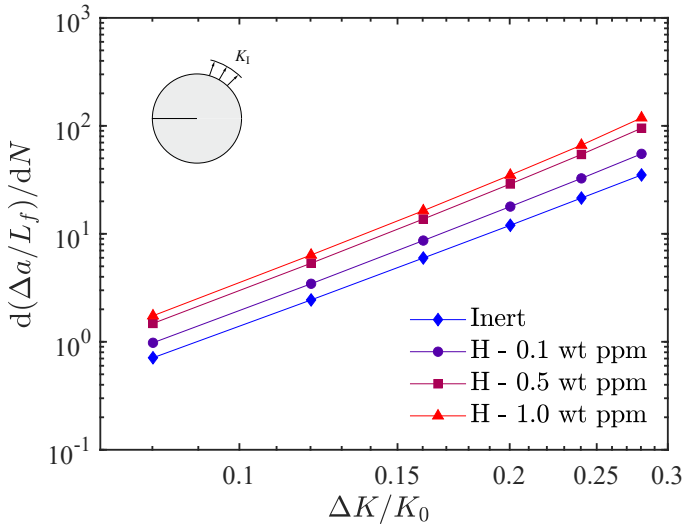

Figure 5.36: Boundary layer model. Paris law response: Fatigue crack growth rate against loading range for varying hydrogen concentrations with $R = 0.1$ and $f = 1$ Hz. Adapted from [P4].

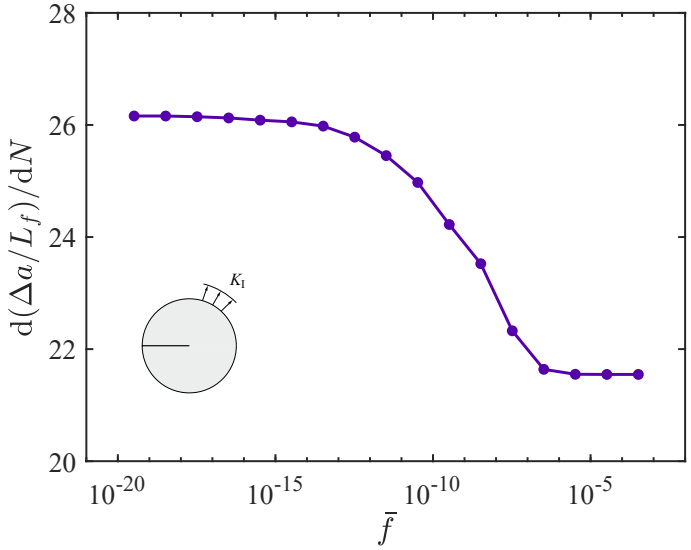

Figure 5.37: Boundary layer model. Visualizing frequency domains: Fatigue crack growth rate against normalised frequency with $\Delta K/K_0 = 0.24$, $R = 0$ and $C_0 = C_{\mathsf{env}} = 0.1$ wt ppm. Adapted from [P4].

5.4.3 Notched cylindrical bar

Now, we investigate the growth of fatigue cracks in samples with non-sharp defects. A cylindrical bar with a notch on its outer surface (as depicted in Fig. 5.38a) is considered. A section of the bar is modeled using axisymmetric conditions, and the finite element model includes 17,003 quadratic quadrilateral axisymmetric elements with reduced integration. The mesh is refined near the notch tip. The bar is pre-charged and then subjected to cyclic loading by applying a piece-wise linear remote displacement with a load ratio of $R = 0$. To create a realistic environment, the outer surfaces of the bar, including the notch

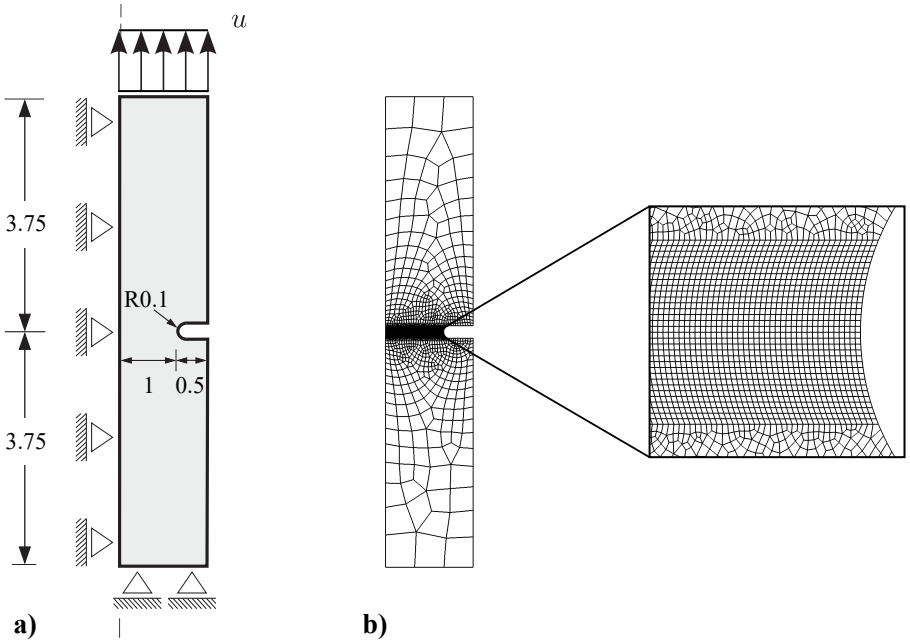

Figure 5.38: Notched cylindrical bar. (a) Geometry and loading conditions (with dimensions in mm), and (b) finite element mesh, featuring an in-depth look at the mesh near the notch's edge. Adapted from [P4].

faces, are kept in contact with the hydrogenous environment throughout the testing process. Fig. 5.39 illustrates the outcomes of the numerical experiment. The data is presented in S-N curves, which depict the alternating remote stress against the number of load cycles until failure. The data pertains to three environments, and the stresses are normalized using the material's critical strength, as described in Eq. (2.33). The results indicate that as hydrogen concentrations increase, fatigue lives become shorter for a given stress amplitude. Moreover, as stress amplitude decreases, the number of load cycles to failure increases, in all cases, and the slope of the S-N curve appears to be unaffected by the hydrogen environment.

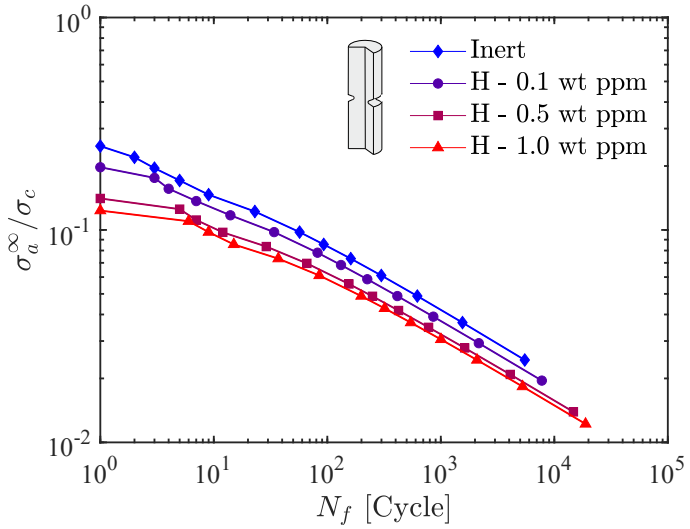

Figure 5.39: Notched cylindrical bar. *Virtual* S-N curves: Remote stress amplitude against number of load cycles to failure for varying hydrogen concentrations. Adapted from [P4].

To accurately predict fatigue crack propagation in harsh environments, it is crucial to have appropriate boundary conditions. To enforce chemical boundary conditions that move with the crack, we utilize a penalty approach as described in Section 4.4. This approach effectively captures the exposure of newly created crack faces to the environment. Fig. 5.40 depicts this concept through phase field and hydrogen concentration contours, which show that the concentration in the damaged regions becomes equivalent to C_{env} as the crack propagates. It is important to note that these contours relate to $\sigma^\infty = \sigma_{\text{min}} = 0$, which means that hydrostatic stress has no impact on hydrogen concentration.

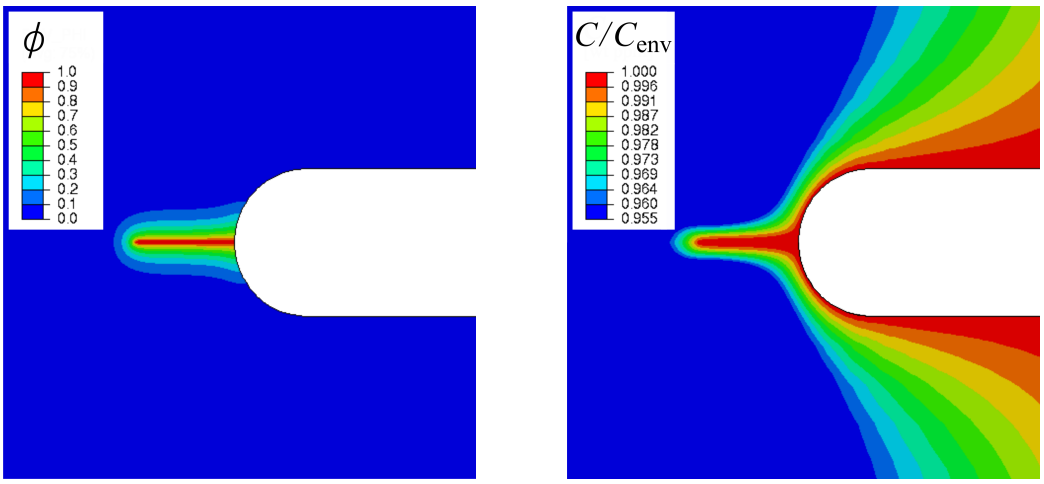

(a) (b)

Figure 5.40: Notched cylindrical bar. *Moving* chemical boundary conditions with a propagating fatigue crack: (a) phase field and (b) hydrogen concentration contours ahead of the notch tip (zoomed-in-view) after 700 load cycles, displayed at $u = u_{\text{min}} = 0$. Adapted from [P4].

5.4.4 Comparison with experimental S-N curves

In conclusion, we have compared the model's predictions to the S-N curves derived from fatigue experiments conducted by Matsunaga et al. [173] on smooth dog-bone specimens of two types of steel. The first type of steel is a Cr-Mo steel (JIS-SCM435), which has a tensile strength of 840 MPa, while the second type is a carbon steel (JIS-SM490B) with a tensile strength of 530 MPa. The experiments were conducted under uniaxial cyclic loading with a load ratio of $R = -1$, both in ambient air and in hydrogen gas with a high pressure of 115 MPa. The problem can be solved in a semi-analytic way by analyzing the homogeneous solution to Eq. (2.27). The remote stress is assumed to have a piecewise cyclic linear variation. We utilize the logarithmic fatigue degradation function $f_3(\bar{\alpha})$ in Eq. (2.34) along with the spectral decomposition split (2.20). The fatigue parameters $\bar{\alpha}_0$ and κ are selected to obtain the best match with the air experiments. The hydrogen concentration can be related to the H_2 pressure by Sievert's law, which expresses the concentration as a function of the solubility S and the fugacity f_{H_2}:

$$C = S\sqrt{f_{H_2}} \quad \text{with} \quad S = S_0 \exp\left(\frac{-E_s}{\mathcal{R}T}\right), \tag{5.11}$$

where E_s represents an activation energy. Ref. [174] provides information on the values of S_0 and E_s for comparable steel types. The Abel-Noble equation can be used to establish a relationship between the fugacity and hydrogen pressure p:

$$f_{H_2} = p \exp\left(\frac{pb}{\mathcal{R}T}\right) \tag{5.12}$$

Here, the Abel-Noble parameter has been set to $b = 15.84$ cm^3/mol, which results in a value of $f_{H_2} = 242.9$ MPa. The hydrogen concentrations for JIS-SCM435 and JIS-SM490B are calculated as 0.00577 wt ppm and 0.04042 wt ppm, respectively. It is important to consider the impact of hydrostatic stress on solubility, so we use Eq. (5.10) to adjust the hydrogen concentration and determine the final amount of hydrogen absorbed.

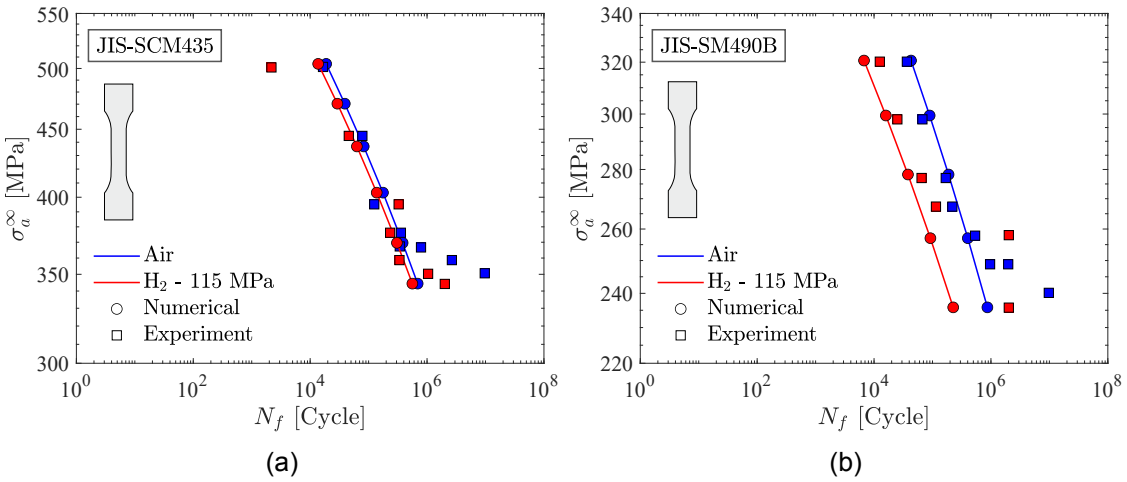

Figure 5.41: Comparative S-N curves for smooth specimens: Current numerical and experimental results from [173] in air and under 115 MPa hydrogen pressure. Two materials analyzed: (a) JIS-SCM435, a Cr-Mo steel steel, and (b) JIS-SM490B, a carbon steel. Adapted from [P4].

The results of the experiments and simulations are depicted in Fig. 5.41. Although the experiments show some inherent scatter, the *Virtual* S-N curves generated from the simulations match well with the measured data. The JIS-SM490B steel exhibits higher susceptibility to hydrogen due to its higher solubility, resulting in a reduction of the number of load cycles to failure by nearly ten-fold in both experiments and simulations. However, it is noteworthy that the level of agreement between simulations and experiments is not as satisfactory when it comes to low stress amplitudes, especially in air. This is mainly due to the absence of a fatigue endurance threshold in the current analysis.

6 Conclusions

A novel multi-physics chemo-mechanics framework to assess environmentally-assisted fatigue by means of phase field fracture models has been developed. Fracture and fatigue cracking are predicted by using an energy-based criterion that relies on the thermodynamics of fracture. The influence of hydrogen environment is taken into account by incorporating a first-principles degradation law for the fracture surface energy. The presented modelling framework incorporates the two primary phase field damage models (`AT1` and `AT2`), various fatigue degradation functions, and novel damage accumulation strategies that substantially accelerate numerical simulations and account for (i) the S-N curve slope, (ii) the material's endurance limit, and (iii) the influence of the stress ratio. The model couples deformation, diffusion, and fatigue crack growth, capturing the influence of the hydrostatic stress on solubility. The theoretical framework has been successfully implemented, in the context of the finite element method, validated, and used to address several boundary value problems of particular interest. The following key findings are highlighted:

- *Virtual* S-N curves are generated for different environments, stress ratios, and samples with both smooth and notched surfaces.
- The sensitivity of fatigue life to stress raisers, such as notches, is effectively captured by the model. It demonstrates that as stress concentration increases, both fatigue life and endurance limit decrease.
- The influence of the stress ratio on the fatigue response is adequately accounted for. Consistent with experimental findings, the model predicts that reducing the stress ratio R for a constant stress amplitude σ_a leads to increased fatigue life and endurance limit. Conversely, when the maximum stress σ_{max} is fixed, the model predicts the opposite effect - the fatigue life and endurance limit decrease.
- The model accurately identifies and distinguishes three specific regions in the process of fatigue crack growth: the threshold region (characterized by minimal or no crack growth), the Paris region (associated with stable and consistent growth), and the fracture region (marked by rapid and extensive crack propagation).
- The model establishes a strong link between two fundamental fatigue phenomena, revealing an interconnected relationship between the exponents of the Basquin law (S-N curves) and the Paris law.
- The model effectively captures the complex interaction between material and structural size effects by reconciling stress and toughness criteria for static and fatigue fracture analyses. The findings demonstrate a notable alignment with the Griffith criterion when examining larger cracks, while seamlessly transitioning to a strength-based failure mechanism as the crack size decreases below the critical flaw size.
- The distribution of hydrogen at the crack tip is highly sensitive to both the loading frequency f and the hydrogen diffusivity coefficient D. When the loading frequency is sufficiently high, the hydrogen concentration shows a consistent increase over time, reaching a saturation value without exhibiting cyclic oscillations.
- The model effectively captures the impact of hydrogen concentration on the rate of fatigue crack growth, allowing for a quantification of the influence of hydrogen on the Paris law coefficient.

- By mapping the sensitivity of crack growth rates to loading frequency, two distinct limit states are identified: the fast test (high f) and the slow test (low f). These findings align with experimental observations and the model predicts a seamless transition between them.
- The model demonstrates strong alignment with a diverse range of datasets derived from laboratory experiments. These datasets encompass a variety of materials and testing conditions, including: (i) fatigue lives and endurance limit data of 300M and AISI 4340 steels tested under inert environments, (ii) fatigue crack growth rate data of S355G8+M steel tested under inert environments, (iii) fatigue lives data of Cr-Mo and carbon steels exposed to hydrogen environments, and (iv) data on curvilinear crack path trajectories obtained from single edge notched polystyrene samples.
- The acceleration strategies presented enable predicting complex 3D cracking trajectories in high cycle fatigue while maintaining accuracy. As a result, phase field fatigue models are empowered to provide predictions that are directly applicable to engineering practices at relevant scales.

6.1 Application and future work

It is expected that the work developed during the present PhD thesis will lay the groundwork for the first generation of physically-based life assessment models, which will be incorporated into fitness-for-service practices. The development of computational tools that can accurately predict corrosion fatigue failures in materials and environments relevant to offshore wind energy would facilitate informed end-of-life decision-making, optimise material selection and reduce operation and maintenance (O&M) costs (e.g., through strategic inspection planning). The modelling framework presented offers a platform for effectively predicting the service life of components subjected to high-cycle fatigue and hydrogen embrittlement. To further enhance its capabilities, there are several potential directions for future research and development, including:

- Investigation of low- and mid-cycle fatigue and cyclic plasticity effects [154].
- Investigation of a universal link between S-N curve (Basquin law) and Paris law, including both brittle and ductile materials [175–177].
- Study of the effects of weldments, including weld geometry, welding quality/process, microstructural variations in the weld region (base material, heat affected zone, and fusion zone), residual stresses, and post-weld treatments, on fatigue life [178].
- Analysis of crack closure effects, including oxide, roughness, and plasticity induced crack closures [1].
- Examination of the effect of surface roughness induced by corrosion or resulting from machining [179].
- Investigation into the influence of multiple trapping sites on the diffusion of hydrogen atoms into the solid phase (cathodic reactions) [97, 180].
- Study of the evolution of the aqueous electrolyte–metal interface due to material dissolution in pitting corrosion or stress corrosion cracking (anodic reactions) [98].
- Exploration of the diffusion of oxygen and molten salt, which govern the corrosion kinetics.
- Evaluation of sensitivity to the environment (pH, chloride concentration) and the (transient) electrochemical-diffusion interface [181, 182].

Bibliography

[1] S. Suresh. *Fatigue of Materials*. 2nd. Cambridge University Press, 1998.

[2] A. Wöhler. *Über die festigkeitsversuche mit eisen und stahl*. Ernst & Korn, 1870.

[3] O. H. Basquin. “The exponential law of endurance tests”. In: *Proc ASTM*. Vol. 10. 1910, pp. 625–630.

[4] P. Paris and F. Erdogan. “A critical analysis of crack propagation laws”. In: *Journal of Basic Engineering* 85 (1963), pp. 528–533.

[5] S. R. Mettu et al. “NASGRO 3.0 - A: software for analyzing aging aircraft”. In: 1999, pp. 792–801.

[6] K. L. Roe and T. Siegmund. “An irreversible cohesive zone model for interface fatigue crack growth simulation”. In: *Engineering Fracture Mechanics* 70 (2003), pp. 209–232.

[7] O. Nguyen et al. “A cohesive model of fatigue crack growth”. In: *International Journal of Fracture* 110 (2001), pp. 351–369.

[8] N. Moës, J. Dolbow, and T. Belytschko. “A finite element method for crack growth without remeshing”. In: *International Journal for Numerical Methods in Engineering* 46 (1999), pp. 131–150.

[9] A. Gravouil, N. Moës, and T. Belytschko. “Non-planar 3D crack growth by the extended finite element and level sets-Part II: Level set update”. In: *International Journal for Numerical Methods in Engineering* 53 (2002), pp. 2569–2586.

[10] F. Rabold and M. Kuna. “Automated Finite Element Simulation of Fatigue Crack Growth in Three-dimensional Structures with the Software System ProCrack”. In: *Procedia Materials Science* 3 (2014), pp. 1099–1104.

[11] K. Rege and H. G. Lemu. “A review of fatigue crack propagation modelling techniques using FEM and XFEM”. In: *IOP Conference Series: Materials Science and Engineering* 276 (2017), p. 12027.

[12] R. Branco, F. V. Antunes, and J. D. Costa. “A review on 3D-FE adaptive remeshing techniques for crack growth modelling”. In: *Engineering Fracture Mechanics* 141 (2015), pp. 170–195.

[13] J. L. Chaboche. “Constitutive equations for cyclic plasticity and cyclic viscoplasticity”. In: *International Journal of Plasticity* 5 (1989), pp. 247–302.

[14] J Lemaitre and J L Chaboche. *Mechanics of solid materials*. 1st. Cambridge University Press, 1990.

[15] F. Hamon et al. “A damage model for fatigue crack propagation from moderate to high Δk levels”. In: *Fatigue and Fracture of Engineering Materials and Structures* 35 (2012), pp. 160–172.

[16] S. K. Kim et al. “Estimation of Fatigue Crack Growth Rate for 7% Nickel Steel under Room and Cryogenic Temperatures Using Damage-Coupled Finite Element Analysis”. In: *Metals* 5 (2015), pp. 603–627.

[17] A. A. Griffith. “The Phenomena of Rupture and Flow in Solids”. In: *Philosophical Transactions of the Royal Society A: Mathematical, Physical and Engineering Sciences* 221 (1921), pp. 163–198.

[18] G. A. Francfort and J. J. Marigo. “Revisiting brittle fracture as an energy minimization problem”. In: *Journal of the Mechanics and Physics of Solids* 46 (1998), pp. 1319–1342.

[19] B. Bourdin, G. A. Francfort, and J. J. Marigo. “Numerical experiments in revisited brittle fracture”. In: *Journal of the Mechanics and Physics of Solids* 48 (2000), pp. 797–826.
[20] B. Bourdin, G. A. Francfort, and J. J. Marigo. “The Variational Approach to Fracture”. In: *Journal of Elasticity* 91 (2008), pp. 5–148.
[21] C. Miehe, F. Welshinger, and M. Hofacker. “Thermodynamically consistent phase-field models of fracture: Variational principles and multi-field FE implementations”. In: *International Journal for Numerical Methods in Engineering* 83 (2010), pp. 1273–1311.
[22] C. Miehe, M. Hofacker, and F. Welschinger. “A phase field model for rate-independent crack propagation: Robust algorithmic implementation based on operator splits”. In: *Computer Methods in Applied Mechanics and Engineering* 199 (2010), pp. 2765–2778.
[23] T. Gerasimov and L. De Lorenzis. “A line search assisted monolithic approach for phase-field computing of brittle fracture”. In: *Computer Methods in Applied Mechanics and Engineering* 312 (2016), pp. 276–303.
[24] M. J. Borden et al. “A higher-order phase-field model for brittle fracture: Formulation and analysis within the isogeometric analysis framework”. In: *Computer Methods in Applied Mechanics and Engineering* 273 (2014), pp. 100–118.
[25] D. Schillinger, M. J. Borden, and H. K. Stolarski. “Isogeometric collocation for phase-field fracture models”. In: *Computer Methods in Applied Mechanics and Engineering* 284 (2015), pp. 583–610.
[26] M. Ambati, T. Gerasimov, and L. De Lorenzis. “Phase-field modeling of ductile fracture”. In: *Computational Mechanics* 55 (2015), pp. 1017–1040.
[27] M. J. Borden et al. “A phase-field formulation for fracture in ductile materials: Finite deformation balance law derivation, plastic degradation, and stress triaxiality effects”. In: *Computer Methods in Applied Mechanics and Engineering* 312 (2016), pp. 130–166.
[28] C. Miehe, F. Aldakheel, and A. Raina. “Phase field modeling of ductile fracture at finite strains: A variational gradient-extended plasticity-damage theory”. In: *International Journal of Plasticity* 84 (2016), pp. 1–32.
[29] R. Alessi et al. *Comparison of Phase-Field Models of Fracture Coupled with Plasticity*. Ed. by E de Souza- Neto M Chiumenti E. Oñate D. Peric. 2018.
[30] M. J. Borden et al. “A phase-field description of dynamic brittle fracture”. In: *Computer Methods in Applied Mechanics and Engineering* 217-220 (2012), pp. 77–95.
[31] A. Schlüter et al. “Phase field approximation of dynamic brittle fracture”. In: *Computational Mechanics* 54 (2014).
[32] S. Zhou, T Rabczuk, and X. Zhuang. “Phase field modeling of quasi-static and dynamic crack propagation: COMSOL implementation and case studies”. In: *Advances in Engineering Software* 122 (2018), pp. 31–49.
[33] R. J. M. Geelen et al. “A phase-field formulation for dynamic cohesive fracture”. In: *Computer Methods in Applied Mechanics and Engineering* 348 (2019), pp. 680–711.
[34] G. Molnár et al. “An open-source Abaqus implementation of the phase-field method to study the effect of plasticity on the instantaneous fracture toughness in dynamic crack propagation”. In: *Computer Methods in Applied Mechanics and Engineering* 365 (2020), p. 113004.
[35] J. Y. Wu, Y. Huang, and V. P. Nguyen. “Three-dimensional phase-field modeling of mode I + II / III failure in solids”. In: *Computer Methods in Applied Mechanics and Engineering* 373 (2021), p. 113537.

[36] M. Strobl and Th. Seelig. “Phase field modeling of Hertzian indentation fracture”. In: *Journal of the Mechanics and Physics of Solids* 143 (2020), p. 104026.
[37] T. T. Nguyen et al. “A phase-field method for computational modeling of interfacial damage interacting with crack propagation in realistic microstructures obtained by microtomography”. In: *Computer Methods in Applied Mechanics and Engineering* 312 (2016).
[38] J. Reinoso et al. “Strength prediction of notched thin ply laminates using finite fracture mechanics and the phase field approach”. In: *Composites Science and Technology* 150 (2017), pp. 205–216.
[39] V. Carollo, J. Reinoso, and M. Paggi. “A 3D finite strain model for intralayer and interlayer crack simulation coupling the phase field approach and cohesive zone model”. In: *Composite Structures* 182 (2017), pp. 636–651.
[40] R. Alessi and F. Freddi. “Failure and complex crack patterns in hybrid laminates: A phase-field approach”. In: *Composites Part B: Engineering* 179 (2019), p. 107256.
[41] T. K. Mandal, V. P. Nguyen, and J. Y. Wu. “A length scale insensitive anisotropic phase field fracture model for hyperelastic composites”. In: *International Journal of Mechanical Sciences* 188 (2020), p. 105941.
[42] A. Quintanas-Corominas et al. “A phase field approach enhanced with a cohesive zone model for modeling delamination induced by matrix cracking”. In: *Computer Methods in Applied Mechanics and Engineering* 358 (2020), p. 112618.
[43] J. Reinoso, M. Paggi, and C. Linder. “Phase field modeling of brittle fracture for enhanced assumed strain shells at large deformations: formulation and finite element implementation”. In: *Computational Mechanics* 59 (2017), pp. 981–1001.
[44] V. Carollo, J. Reinoso, and M. Paggi. “Modeling complex crack paths in ceramic laminates: A novel variational framework combining the phase field method of fracture and the cohesive zone model”. In: *Journal of the European Ceramic Society* 38 (2018), pp. 2994–3003.
[45] W. Li and K. Shirvan. “Multiphysics phase-field modeling of quasi-static cracking in urania ceramic nuclear fuel”. In: *Ceramics International* 47 (2021), pp. 793–810.
[46] A. Kumar, G. A. Francfort, and O. Lopez-Pamies. “Fracture and healing of elastomers: A phase-transition theory and numerical implementation”. In: *Journal of the Mechanics and Physics of Solids* 112 (2018), pp. 523–551.
[47] M. Simoes and E. Martínez-Pañeda. “Phase field modelling of fracture and fatigue in Shape Memory Alloys”. In: *Computer Methods in Applied Mechanics and Engineering* 373 (2021), p. 113504.
[48] Hirshikesh et al. “Phase field modelling of crack propagation in functionally graded materials”. In: *Composites Part B: Engineering* 169 (2019).
[49] P. K. A. V. Kumar et al. “Phase field modeling of fracture in Functionally Graded Materials: G -convergence and mechanical insight on the effect of grading”. In: *Thin-Walled Structures* 159 (2021), p. 107234.
[50] B. Bourdin et al. “Morphogenesis and propagation of complex cracks induced by thermal shocks”. In: *Physical Review Letters* 112 (2014), p. 014301.
[51] Y. Zhao et al. “Phase-field study of electrochemical reactions at exterior and interior interfaces in Li-ion battery electrode particles”. In: *Computer Methods in Applied Mechanics and Engineering* 312 (2016).
[52] M. Klinsmann et al. “Modeling crack growth during Li insertion in storage particles using a fracture phase field approach”. In: *Journal of the Mechanics and Physics of Solids* 92 (2016), pp. 313–344.

[53] A. Mesgarnejad and A. Karma. “Phase field modeling of chemomechanical fracture of intercalation electrodes: Role of charging rate and dimensionality”. In: *Journal of the Mechanics and Physics of Solids* 132 (2019).
[54] E. Martínez-Pañeda, A. Golahmar, and C. F. Niordson. “A phase field formulation for hydrogen assisted cracking”. In: *Computer Methods in Applied Mechanics and Engineering* 342 (2018), pp. 742–761.
[55] F. P. Duda et al. “A phase-field model for solute-assisted brittle fracture in elastic-plastic solids”. In: *International Journal of Plasticity* 102 (2018), pp. 16–40.
[56] L. Anand, Y. Mao, and B. Talamini. “On modeling fracture of ferritic steels due to hydrogen embrittlement”. In: *Journal of the Mechanics and Physics of Solids* 122 (2019), pp. 280–314.
[57] J.-Y. Wu, T K Mandal, and V P Nguyen. “A phase-field regularized cohesive zone model for hydrogen assisted cracking”. In: *Computer Methods in Applied Mechanics and Engineering* 358 (2020), p. 112614.
[58] J. Y. Wu et al. “Phase-field modelling of fracture”. In: *Advances in Applied Mechanics* 53 (2020), pp. 1–183.
[59] Y. S. Lo et al. “A phase-field model for fatigue crack growth”. In: *Journal of the Mechanics and Physics of Solids* 132 (2019), p. 103684.
[60] J. L. Boldrini et al. “A non-isothermal thermodynamically consistent phase field framework for structural damage and fatigue”. In: *Computer Methods in Applied Mechanics and Engineering* 312 (2016), pp. 395–427.
[61] P. J. Loew, B. Peters, and L. A. A. Beex. “Fatigue phase-field damage modeling of rubber using viscous dissipation: Crack nucleation and propagation”. In: *Mechanics of Materials* 142 (2020), p. 103282.
[62] C. Schreiber et al. “A phase field modeling approach of cyclic fatigue crack growth”. In: *International Journal of Fracture* 225 (2020).
[63] R. Alessi, S. Vidoli, and L. De Lorenzis. “A phenomenological approach to fatigue with a variational phase-field model: The one-dimensional case”. In: *Engineering Fracture Mechanics* 190 (2018), pp. 53–73.
[64] P. Carrara et al. “A framework to model the fatigue behavior of brittle materials based on a variational phase-field approach”. In: *Computer Methods in Applied Mechanics and Engineering* 361 (2020), p. 112731.
[65] M. Seiler et al. “An efficient phase-field model for fatigue fracture in ductile materials”. In: *Engineering Fracture Mechanics* 224 (2020).
[66] M. Simoes et al. “Modelling fatigue crack growth in shape memory alloys”. In: *Fatigue & Fracture of Engineering Materials & Structures* 45 (2022), pp. 1243–1257.
[67] W. Ai, B. Wu, and E. Martínez-Pañeda. “A coupled phase field formulation for modelling fatigue cracking in lithium-ion battery electrode particles”. In: *Journal of Power Sources* 544 (2022), p. 231805.
[68] M. M. Hasan and T. Baxevanis. “A phase-field model for low-cycle fatigue of brittle materials”. In: *International Journal of Fatigue* 150 (2021), p. 106297.
[69] K. Seleš et al. “A general phase-field model for fatigue failure in brittle and ductile solids”. In: *Computational Mechanics* 67 (2021).
[70] J. Ulloa et al. “Phase-field modeling of fatigue coupled to cyclic plasticity in an energetic formulation”. In: *Computer Methods in Applied Mechanics and Engineering* 373 (2021), p. 113473.
[71] Z. Khalil, A. Y. Elghazouli, and E. Martínez-Pañeda. “A generalised phase field model for fatigue crack growth in elastic–plastic solids with an efficient monolithic solver”. In: *Computer Methods in Applied Mechanics and Engineering* 388 (2022), p. 114286.

[72] W. H. Johnson. “On some remarkable changes produced in iron and steel by the action of hydrogen and acids”. In: *Proceedings of the Royal Society of London* 23 (1875), pp. 168–179.
[73] T. Hageman and Emilio Martínez-Pañeda. “An electro-chemo-mechanical framework for predicting hydrogen uptake in metals due to aqueous electrolytes”. In: *Corrosion Science* 208 (2022).
[74] X. Li et al. *Review of Hydrogen Embrittlement in Metals: Hydrogen Diffusion, Hydrogen Characterization, Hydrogen Embrittlement Mechanism and Prevention*. 2020.
[75] R. A. Oriani. “A mechanistic theory of hydrogen embrittlement of steels”. In: *Berichte der Bunsengesellschaft für physikalische Chemie* 76 (1972), pp. 848–857.
[76] M. Dadfarnia et al. “Recent advances on hydrogen embrittlement of structural materials”. In: *International Journal of Fracture* 196 (2015).
[77] I. M. Robertson et al. “Hydrogen Embrittlement Understood”. In: *Metallurgical and Materials Transactions B* 46 (2015), pp. 1085–1103.
[78] A. R. Troiano. “Embrittlement by hydrogen and other interstitials”. In: *Metal Progress* 77 (1960), pp. 112–117.
[79] H. K. Birnbaum and P. Sofronis. “Hydrogen-enhanced localized plasticity - a mechanism for hydrogen-related fracture”. In: *Materials Science and Engineering A* 176 (1994), pp. 191–202.
[80] R. P. Gangloff. “Hydrogen assisted cracking of high strength alloys”. In: *Comprehensive Structural Integrity* 6 (2003), pp. 31–101.
[81] P. Novak et al. “A statistical, physical-based, micro-mechanical model of hydrogen-induced intergranular fracture in steel”. In: *Journal of the Mechanics and Physics of Solids* 58 (2010), pp. 206–226.
[82] C. Ayas, V. S. Deshpande, and N. A. Fleck. “A fracture criterion for the notch strength of high strength steels in the presence of hydrogen”. In: *Journal of the Mechanics and Physics of Solids* 63 (2014), pp. 80–93.
[83] E. Martínez-Pañeda et al. “Strain gradient plasticity modeling of hydrogen diffusion to the crack tip”. In: *International Journal of Hydrogen Energy* 41 (2016), pp. 10265–10274.
[84] J. T. Burns et al. “Measurement and Modeling of Hydrogen Environment-Assisted Cracking in a Ni-Cu-Al-Ti Superalloy”. In: *Metallurgical and Materials Transactions A: Physical Metallurgy and Materials Science* 47 (2016), pp. 990–997.
[85] S. Serebrinsky, E. A. Carter, and M. Ortiz. “A quantum-mechanically informed continuum model of hydrogen embrittlement”. In: *Journal of the Mechanics and Physics of Solids* 52 (2004), pp. 2403–2430.
[86] H. Yu et al. “Continuum level simulation of the grain size and misorientation effects on hydrogen embrittlement in nickel”. In: *Engineering Failure Analysis* 81 (2017), pp. 79–93.
[87] E. Elmukashfi, E. Tarleton, and A. C. F. Cocks. “A modelling framework for coupled hydrogen diffusion and mechanical behaviour of engineering components”. In: *Computational Mechanics* 66 (2020), pp. 189–220.
[88] P. K. Kristensen, C. F. Niordson, and E. Martínez-Pañeda. “A phase field model for elastic-gradient-plastic solids undergoing hydrogen embrittlement”. In: *Journal of the Mechanics and Physics of Solids* 143 (2020), p. 104093.
[89] C. Cui, R. Ma, and E. Martínez-Pañeda. “A generalised, multi-phase-field theory for dissolution-driven stress corrosion cracking and hydrogen embrittlement”. In: *Journal of the Mechanics and Physics of Solids* 166 (2022).

[90] G. M. Castelluccio, C. B. Geller, and D. L. McDowell. “A rationale for modeling hydrogen effects on plastic deformation across scales in FCC metals”. In: *International Journal of Plasticity* 111 (2018), pp. 72–84.
[91] Z. S. Hosseini et al. “Modeling the Hydrogen Effect on the Constitutive Response of a Low Carbon Steel in Cyclic Loading”. In: *Journal of Applied Mechanics, Transactions ASME* 88 (2021), pp. 1–14.
[92] K. A. Esaklul, A. G. Wright, and W. W. Gerberich. “The effect of hydrogen induced surface asperities on fatigue crack closure in ultrahigh strength steel”. In: *Scripta Metallurgica* 17 (1983), pp. 1073–1078.
[93] K. A. Esaklul and W. W. Gerberich. “On the influence of internal hydrogen on fatigue thresholds of HSLA steel”. In: *Scripta Metallurgica* 17 (1983), pp. 1079–1082.
[94] R. Fernández-Sousa, C. Betegón, and E. Martínez-Pañeda. “Analysis of the influence of microstructural traps on hydrogen assisted fatigue”. In: *Acta Materialia* 199 (2020), pp. 253–263.
[95] T. Shinko et al. “Controlling factors and mechanisms of fatigue crack growth influenced by high pressure of gaseous hydrogen in a commercially pure iron”. In: *Theoretical and Applied Fracture Mechanics* 112 (2021), p. 102885.
[96] C. Moriconi, G. Hénaff, and D. Halm. “Cohesive zone modeling of fatigue crack propagation assisted by gaseous hydrogen in metals”. In: *International Journal of Fatigue* 68 (2014), pp. 56–66.
[97] S. del Busto, C. Betegón, and E. Martínez-Pañeda. “A cohesive zone framework for environmentally assisted fatigue”. In: *Engineering Fracture Mechanics* 185 (2017), pp. 210–226.
[98] C. Cui, R. Ma, and E. Martínez-Pañeda. “A phase field formulation for dissolution-driven stress corrosion cracking”. In: *Journal of the Mechanics and Physics of Solids* 147 (2021), p. 104254.
[99] N. Provatas and K. Elder. *Phase-Field Methods in Materials Science and Engineering*. John Wiley & Sons, 2011.
[100] H. Amor, J. J. Marigo, and C. Maurini. “Regularized formulation of the variational brittle fracture with unilateral contact: Numerical experiments”. In: *Journal of the Mechanics and Physics of Solids* 57 (2009), pp. 1209–1229.
[101] F. Freddi and G. Royer-Carfagni. “Regularized variational theories of fracture: A unified approach”. In: *Journal of the Mechanics and Physics of Solids* 58 (2010), pp. 1154–1174.
[102] F. Freddi and G. Royer-Carfagni. “Variational fracture mechanics to model compressive splitting of masonry-like materials”. In: *Annals of Solid and Structural Mechanics* 2 (2011), pp. 57–67.
[103] M. Ambati, T. Gerasimov, and L. De Lorenzis. “A review on phase-field models of brittle fracture and a new fast hybrid formulation”. In: *Computational Mechanics* 55 (2015), pp. 383–405.
[104] T. Linse et al. “A convergence study of phase-field models for brittle fracture”. In: *Engineering Fracture Mechanics* 184 (2017), pp. 307–318.
[105] M. F. Wheeler, T. Wick, and W. Wollner. “An augmented-Lagrangian method for the phase-field approach for pressurized fractures”. In: *Computer Methods in Applied Mechanics and Engineering* 271 (2014), pp. 69–85.
[106] T. Gerasimov and L. De Lorenzis. “On penalization in variational phase-field models of brittle fracture”. In: *Computer Methods in Applied Mechanics and Engineering* 354 (2019), pp. 990–1026.
[107] G. Molnár et al. “Thermodynamically consistent linear-gradient damage model in Abaqus”. In: *Engineering Fracture Mechanics* 266 (2022), p. 108390.

[108] E Tanné et al. “Crack nucleation in variational phase-field models of brittle fracture”. In: *Journal of the Mechanics and Physics of Solids* 110 (2018), pp. 80–99.
[109] K. Pham et al. “Gradient damage models and their use to approximate brittle fracture”. In: *International Journal of Damage Mechanics* 20 (2011), pp. 618–652.
[110] L. Ambrosio and V. M. Tortorelli. “Approximation of functionals depending on jumps by elliptic functionals via gamma-convergence”. In: *Communications on Pure and Applied Mathematics* 43 (1991), pp. 999–1036.
[111] D. Mumford and J. Shah. “Optimal approximations by piecewise smooth functions and associated variational problems”. In: *Communications on Pure and Applied Mathematics* 42 (1989), pp. 577–685.
[112] J. Y. Wu and Y. Huang. “Comprehensive implementations of phase-field damage models in Abaqus”. In: *Theoretical and Applied Fracture Mechanics* 106 (2020).
[113] P. K. Kristensen, C. F. Niordson, and E. Martínez-Pañeda. “An assessment of phase field fracture: crack initiation and growth”. In: *Philosophical Transactions of the Royal Society A: Mathematical, Physical and Engineering Sciences* 379 (2021), p. 20210021.
[114] A. Kumar et al. “Revisiting nucleation in the phase-Field approach to brittle fracture”. In: *Journal of the Mechanics and Physics of Solids* 142 (2020), p. 104027.
[115] J. M. Sargado et al. “High-accuracy phase-field models for brittle fracture based on a new family of degradation functions”. In: *Journal of the Mechanics and Physics of Solids* 111 (2018), pp. 458–489.
[116] F. Freddi and F. Iurlano. “Numerical insight of a variational smeared approach to cohesive fracture”. In: *Journal of the Mechanics and Physics of Solids* 98 (2017), pp. 156–171.
[117] J. Y. Wu. “A unified phase-field theory for the mechanics of damage and quasi-brittle failure”. In: *Journal of the Mechanics and Physics of Solids* 103 (2017), pp. 72–99.
[118] J. Y. Wu and V. P. Nguyen. “A length scale insensitive phase-field damage model for brittle fracture”. In: *Journal of the Mechanics and Physics of Solids* 119 (2018), pp. 20–42.
[119] A. Karma, D. A. Kessler, and H. Levine. “Phase-field model of mode III dynamic fracture”. In: *Physical Review Letters* 87 (2001), pp. 45501–1–45501–4.
[120] K. Walker. “The Effect of Stress Ratio During Crack Propagation and Fatigue for 2024-T3 and 7075-T6 Aluminum, Effects of Environment and Complex Load History on Fatigue Life”. In: *ASTM STP 462* (1970).
[121] K. N. Smith, P. Watson, and T. H. Topper. “Stress- strain function for the fatigue of metals”. In: *Journal of Material, ASTM* 5 (1970), pp. 767–778.
[122] N. E. Dowling, C. A. Calhoun, and A. Arcari. “Mean stress effects in stress-life fatigue and the Walker equation”. In: *Fatigue and Fracture of Engineering Materials and Structures* 32 (2009), pp. 163–179.
[123] R. Kirchheim. *Solid solutions of hydrogen in complex materials*. Ed. by H Ehrenreich and F Spaepen. 2004.
[124] D. E. Jiang and E. A. Carter. “Diffusion of interstitial hydrogen into and through bcc Fe from first principles”. In: *Physical Review B - Condensed Matter and Materials Physics* 70 (2004), pp. 1–9.
[125] A. Alvaro et al. “Hydrogen embrittlement in nickel, visited by first principles modeling, cohesive zone simulation and nanomechanical testing”. In: *International Journal of Hydrogen Energy* 40 (2015), pp. 16892–16900.
[126] A. Tehranchi et al. “Hydrogen-vacancy-dislocation interactions in α-Fe”. In: *Modelling and Simulation in Materials Science and Engineering* 25 (2017), p. 25001.

[127] C. V. Di Leo and L. Anand. “Hydrogen in metals: A coupled theory for species diffusion and large elastic-plastic deformations”. In: *International Journal of Plasticity* 43 (2013), pp. 42–69.
[128] J. P. Hirth. “Effects of hydrogen on the properties of iron and steel”. In: *Metallurgical Transactions A* 11 (1980), pp. 861–890.
[129] P. Sofronis and R. M. McMeeking. “Numerical analysis of hydrogen transport near a blunting crack tip”. In: *Journal of the Mechanics and Physics of Solids* 37 (1989), pp. 317–350.
[130] E. Martínez-Pañeda et al. “On the suitability of slow strain rate tensile testing for assessing hydrogen embrittlement susceptibility”. In: *Corrosion Science* 163 (2020).
[131] M. Isfandbod and E. Martínez-Pañeda. “A mechanism-based multi-trap phase field model for hydrogen assisted fracture”. In: *International Journal of Plasticity* 144 (2021), p. 103044.
[132] S. S. Shishvan, G. Csányi, and V. S. Deshpande. “Hydrogen induced fast-fracture”. In: *Journal of the Mechanics and Physics of Solids* 134 (2020), p. 103740.
[133] Y. Renard and K. Poulios. “GetFEM: Automated FE modeling of multiphysics problems based on a generic weak form language”. In: *ACM Transactions on Mathematical Software (TOMS)* 47 (2020), pp. 1–31.
[134] E. Börjesson, J. J. C. Remmers, and M. Fagerström. “A generalised path-following solver for robust analysis of material failure”. In: *Computational Mechanics* 70 (2022).
[135] A. Kopaničáková, H. Kothari, and R. Krause. “Nonlinear field-split preconditioners for solving monolithic phase-field models of brittle fracture”. In: *Computer Methods in Applied Mechanics and Engineering* 403 (2023).
[136] T. Wick. “An error-oriented newton/inexact augmented Lagrangian approach for fully monolithic phase-field fracture propagation”. In: *SIAM Journal on Scientific Computing* 39 (2017), B589–B617.
[137] T. Wick. “Modified Newton methods for solving fully monolithic phase-field quasi-static brittle fracture propagation”. In: *Computer Methods in Applied Mechanics and Engineering* 325 (2017), pp. 577–611.
[138] J. Y. Wu, Y. Huang, and V. P. Nguyen. “On the BFGS monolithic algorithm for the unified phase field damage theory”. In: *Computer Methods in Applied Mechanics and Engineering* 360 (2020), p. 112704.
[139] P. K. Kristensen and E. Martínez-Pañeda. “Phase field fracture modelling using quasi-Newton methods and a new adaptive step scheme”. In: *Theoretical and Applied Fracture Mechanics* 107 (2020), p. 102446.
[140] D. H. Li and M. Fukushima. “A modified BFGS method and its global convergence in nonconvex minimization”. In: *Journal of Computational and Applied Mathematics* 129 (2001), pp. 15–35.
[141] D. H. Li and M. Fukushima. “On the global convergence of the BFGS method for nonconvex unconstrained optimization problems”. In: *SIAM Journal on Optimization* 11 (2001), pp. 1054–1064.
[142] A. S. Lewis and M. L. Overton. “Nonsmooth optimization via quasi-Newton methods”. In: *Mathematical Programming* 141 (2013), pp. 135–163.
[143] H. Matthies and G. Strang. “The solution of nonlinear finite element equations”. In: *International Journal for Numerical Methods in Engineering* 14 (1979), pp. 1613–1626.
[144] M. Hofacker and C. Miehe. “Continuum phase field modeling of dynamic fracture: variational principles and staggered FE implementation”. In: *International journal of fracture* 178 (2012), pp. 113–129.

[145] N. Singh et al. “A fracture-controlled path-following technique for phase-field modeling of brittle fracture”. In: *Finite Elements in Analysis and Design* 113 (2016), pp. 14–29.
[146] T. Heister, M. F. Wheeler, and T. Wick. “A primal-dual active set method and predictor-corrector mesh adaptivity for computing fracture propagation using a phase-field approach”. In: *Computer Methods in Applied Mechanics and Engineering* 290 (2015), pp. 466–495.
[147] M. Klinsmann et al. “An assessment of the phase field formulation for crack growth”. In: *Computer Methods in Applied Mechanics and Engineering* 294 (2015), pp. 313–330.
[148] F. Freddi and L. Mingazzi. “Mesh refinement procedures for the phase field approach to brittle fracture”. In: *Computer Methods in Applied Mechanics and Engineering* 388 (2022), p. 114214.
[149] F. Freddi and L. Mingazzi. “Adaptive mesh refinement for the phase field method: A FEniCS implementation”. In: *Applications in Engineering Science* 14 (2023), p. 100127.
[150] D. Olesch et al. “Adaptive numerical integration of exponential finite elements for a phase field fracture model”. In: *Computational Mechanics* 67 (2021), pp. 811–821.
[151] J. M. Sargado et al. “A combined finite element–finite volume framework for phase-field fracture”. In: *Computer Methods in Applied Mechanics and Engineering* 373 (2021), p. 113474.
[152] D. Cojocaru and A. M. Karlsson. “A simple numerical method of cycle jumps for cyclically loaded structures”. In: *International Journal of Fatigue* 28 (2006), pp. 1677–1689.
[153] MIL-HDBK-5H. *Military Handbook: Metallic Materials and Elements for Aerospace Vehicle Structures*. U.S. Department of Defense, 1998.
[154] R. C. McClung. “Crack closure and plastic zone sizes in fatigue”. In: *Fatigue & Fracture of Engineering Materials & Structures* 14.4 (1991), pp. 455–468.
[155] G. Molnár and A. Gravouil. “2D and 3D Abaqus implementation of a robust staggered phase-field solution for modeling brittle fracture”. In: *Finite Elements in Analysis and Design* 130 (2017), pp. 27–38.
[156] T. K. Mandal, V. P. Nguyen, and J. Y. Wu. “Length scale and mesh bias sensitivity of phase-field models for brittle and cohesive fracture”. In: *Engineering Fracture Mechanics* 217 (2019), p. 106532.
[157] M. L. Williams. “On the stress distribution at the base of a stationary crack”. In: *Journal of Applied Mechanics* 24 (1957), pp. 109–114.
[158] J. Andersons, M. Hojo, and S. Ochiai. “Model of delamination propagation in brittle-matrix composites under cyclic loading”. In: *Journal of reinforced plastics and composites* 20.5 (2001), pp. 431–450.
[159] A. Mehmanparast, F. Brennan, and I. Tavares. “Fatigue crack growth rates for offshore wind monopile weldments in air and seawater: SLIC inter-laboratory test results”. In: *Materials and Design* 114 (2017), pp. 494–504.
[160] H. Tada, P. C. Paris, and G. R. Irwin. “The stress analysis of cracks”. In: *Handbook, Del Research Corporation* 34.1973 (1973).
[161] GL DNV, GL Group, et al. “Recommended Practice DNVGL-RP-C203-Fatigue Design of Offshore Steel Structures”. In: *Høvik: DNV GL AS* (2016).
[162] A. M. P. de Jesus et al. “A comparison of the fatigue behavior between S355 and S690 steel grades”. In: *Journal of constructional steel research* 79 (2012), pp. 140–150.

[163] V. Milovanović et al. “A Comparison Study of Fatigue Behavior of S355J2+ N, S690QL and X37CrMoV5-1 Steel”. In: *Metals* 12.7 (2022), p. 1199.
[164] American Society for Testing, Materials. Committee E08 on Fatigue, and Fracture. “Standard test method for measurement of fatigue crack growth rates”. In: American Society of Testing Materials. 2008.
[165] British Standards Institution. *Guide on methods for assessing the acceptability of flaws in metallic structures*. British Standard Institution London, UK, 1999.
[166] A. Chudnovsky, K. Chaoui, and A. Moet. “Curvilinear crack layer propagation”. In: *Journal of materials science letters* 6.9 (1987), pp. 1033–1038.
[167] A. A. Rubinstein. “Mechanics of the crack path formation”. In: *International Journal of Fracture* 47 (1991), pp. 291–305.
[168] R. P. Gangloff. *Corrosion fatigue crack propagation in metals*. Tech. rep. NASA 19900015089, 1990, pp. 1–194.
[169] R. P. Gangloff and B. P. Somerday. *Gaseous Hydrogen Embrittlement of Materials in Energy Technologies*. Cambridge: Woodhead Publishing Limited, 2012, p. 520.
[170] A. Turnbull, D. H. Ferriss, and H. Anzai. “Modelling of the hydrogen distribution at a crack tip”. In: *Materials Science and Engineering A* 206.1 (1996), pp. 1–13.
[171] A. Díaz, J. M. Alegre, and I. I. Cuesta. “Coupled hydrogen diffusion simulation using a heat transfer analogy”. In: *International Journal of Mechanical Sciences* 115-116 (2016), pp. 360–369.
[172] T. L. Anderson. *Fracture Mechanics. Fundamentals and Applications*. 3rd. Boca Raton: CRC Press, Taylor & Francis, 2005.
[173] H. Matsunaga et al. “Slow strain rate tensile and fatigue properties of Cr-Mo and carbon steels in a 115 MPa hydrogen gas atmosphere”. In: *International Journal of Hydrogen Energy* 40.16 (2015), pp. 5739–5748.
[174] C. San Marchi and B. P. Somerday. *Technical Reference for Hydrogen Compatibility of Materials*. Tech. rep. SANDIA National Labs, 2012.
[175] N. A. Fleck, K. J. Kang, and M. F. Ashby. “Overview no. 112: The cyclic properties of engineering materials”. In: *Acta Metallurgica et Materialia* 42.2 (1994), pp. 365–381.
[176] N. Pugno et al. “A generalized Paris’ law for fatigue crack growth”. In: *Journal of the Mechanics and Physics of Solids* 54.7 (2006), pp. 1333–1349.
[177] M. Ciavarella and F. Monno. “On the possible generalizations of the Kitagawa–Takahashi diagram and of the El Haddad equation to finite life”. In: *International Journal of Fatigue* 28.12 (2006), pp. 1826–1837.
[178] M. Madia et al. “The IBESS model – Elements, realisation and validation”. In: *Engineering Fracture Mechanics* 198 (2018), pp. 171–208.
[179] D. Arola and C. L. Williams. “Estimating the fatigue stress concentration factor of machined surfaces”. In: *International Journal of Fatigue* 24.9 (2002), pp. 923–930.
[180] M. Dadfarnia, P. Sofronis, and T. Neeraj. “Hydrogen interaction with multiple traps: can it be used to mitigate embrittlement?” In: *International Journal of Hydrogen Energy* 36.16 (2011), pp. 10141–10148.
[181] A. Turnbull. “Review of the electrochemical conditions in cracks with particular reference to corrosion fatigue of structural steels in sea water”. In: *Reviews in Coating and Corrosion* 5 (1982), pp. 43–171.
[182] A. Turnbull. “Modeling of the chemistry and electrochemistry in cracks - a review”. In: *Corrosion* 57.2 (2001), pp. 175–189.

Publications

[P1]

A. Golahmar, C. F. Niordson, and E. Martínez-Pañeda. A phase field model for high-cycle fatigue: Total-life analysis. International Journal of Fatigue 170 (2023), p. 107558.

International Journal of Fatigue 170 (2023) 107558

Contents lists available at ScienceDirect

International Journal of Fatigue

journal homepage: www.elsevier.com/locate/ijfatigue

A phase field model for high-cycle fatigue: Total-life analysis

Alireza Golahmar [a,b], Christian F. Niordson [a], Emilio Martínez-Pañeda [b,*]

[a] Department of Mechanical Engineering, Technical University of Denmark, DK-2800 Kgs. Lyngby, Denmark
[b] Department of Civil and Environmental Engineering, Imperial College London, London SW7 2AZ, UK

ARTICLE INFO

Keywords:
Phase field
Finite element method
Fatigue
S–N curves
Total-life analysis

ABSTRACT

We present a generalised phase field formulation for predicting high-cycle fatigue in metals. Different fatigue degradation functions are presented, together with new damage accumulation strategies, to account for (i) a typical S–N curve slope, (ii) the fatigue endurance limit, and (iii) the mean stress effect. The numerical implementation exploits an efficient quasi-Newton monolithic solution strategy and *Virtual* S–N curves are computed for both smooth and notched samples. The comparison with experiments reveals that the model can accurately predict fatigue lives and endurance limits, as well as naturally capture the influence of the stress concentration factor and the load ratio.

1. Introduction

The fracture of materials subjected to fatigue loading is arguably the main failure mechanism of engineering components, accounting for (up to) 90% of all structural failures [1]. Due to its complexity, the development of numerical methods capable of predicting fatigue cracking is of great utility and has been a prominent research field for several decades. Generally, the evolution of fatigue damage can be divided into two stages: (i) crack nucleation and (ii) crack growth. In the initiation stage, permanent microscopic degradation phenomena such as micro-voids and, subsequently, micro-cracks are formed in the material. These micro-cracks start growing and eventually coalesce, leading to the formation of dominant fatigue (macro-) cracks. One or more of those macro-cracks will then propagate, first in a stable manner, and finally unstably leading to the complete failure of the component.

Fatigue design is commonly based on classical empirical methods which involve data fitting of a large number of experimental tests [2]. Such methods estimate the fatigue life as a function of the cyclic stress (or strain) range, where the fatigue life is defined as the number of cycles (N_f) or reversals ($2N_f$) to failure. A pioneering work in this area is that of Wöhler [3], which is commonly referred to as the stress-life or S–N curve approach. In general, fatigue life analyses are divided into two limiting cases. One is denoted as high-cycle fatigue (HCF), a regime where the material is exposed to low cyclic stress amplitudes, behaving mainly in an elastic manner and requiring a large number of cycles to fail (often up to 10^6 cycles). This approach has become popular in applications involving low-amplitude cyclic stresses such as offshore wind structures exposed to alternating mechanical loads caused by the wind and sea waves. A second scenario is that where the applied stresses are large enough to cause plastic deformations and thus a much lower number of cycles are needed to see failure; 10^4 cycles or fewer, a regime referred to as low-cycle fatigue (LCF). Due to their empirical nature, stress-life methods have limited applicability and can be barely generalised to arbitrary materials, geometries and loading conditions.

Variational phase field fracture models can provide a mechanistic computational framework to predict low- and high- cycle fatigue, overcoming the challenges of empirical methods. The model is based upon Griffith's thermodynamical framework [4], whereby a crack would grow if the energy released by the solid exceeds its critical value, the material toughness. Francfort and Marigo [5] presented a variational formulation for Griffith's energy balance, and Bourdin et al. [6] introduced a scalar phase field variable to regularise the resulting functional and obtain computational predictions of crack evolution as an exchange between stored and fracture energy. Since its early development, the phase field fracture method has been gaining increasing attention and its use has been extended to numerous applications, including ductile damage [7–9], dynamic fracture [10–12], composites delamination [13–15], fracture of functionally graded materials [16,17], and hydrogen-assisted cracking [18–20], among many others; see Refs. [21,22] for an overview.

Recently, efforts have been made to incorporate fatigue damage into variational phase field fracture methods. Lo et al. [23] introduced a viscous term into the standard phase field model for brittle fracture, combined with a modified J-integral, to generate Paris-law type fatigue crack growth behaviour. More commonly, an additional variable

* Corresponding author.
E-mail address: e.martinez-paneda@imperial.ac.uk (E. Martínez-Pañeda).

https://doi.org/10.1016/j.ijfatigue.2023.107558
Received 21 December 2022; Received in revised form 29 January 2023; Accepted 1 February 2023
Available online 3 February 2023

describing the fatigue history is introduced. This variable has been defined either as a dissipative term to the microforce balance of the phase field [24–26], to effectively reduce crack growth resistance, or as a fatigue degradation function that reduces the material toughness [27–32]. Accordingly, an additional equation is introduced to describe the evolution/accumulation of the fatigue history variable. Boldrini et al. [24] derived this additional equation from thermodynamic principles while Loew et al. [25] proposed an equation based on micro-crack growth. Seiler et al. [29] applied a local strain approach to empirically incorporate plasticity via Neuber's rule, while Schreiber et al. [26] employed Miner's rule to govern the evolution of fatigue damage. Alessi and co-workers [27] proposed describing the evolution of fatigue damage as a function of the accumulated strain during the loading stage of each cycle. Following [27], the authors of [28,30,33–37] accumulated the tensile (non-compressive) parts of the strain energy density (elastoplastic energy density in [36,37]) only during the loading (unloading in [35]) stages.

In this work, we present a generalised formulation for modelling the fatigue behaviour of metallic materials. We restrict our attention to high-cycle fatigue (HCF) analysis and build our formulation upon the variational phase field approach for fatigue proposed by Alessi et al. [27] and Carrara et al. [28]. New accumulation strategies for the evolution of fatigue damage are proposed, so as to capture the typical S–N curve slope, the fatigue endurance limit and the mean stress effect (load/stress ratio). The framework encompasses the two most widely used phase field fracture models, the so-called `AT1` [38] and `AT2` [6]. Importantly, the numerical implementation makes use of a quasi-Newton monolithic solution scheme [39,40], which is essential to minimise the cost of cycle-by-cycle fatigue simulations. Moreover, the new accumulation strategy presented further accelerates computations since, as described below, it enables solving the coupled system of iterations only once per loading cycle.

The theoretical elements of the new generalised phase field fatigue framework presented are first described in Section 2. Then, in Section 3, details of the numerical implementation are provided. The results obtained are given in Section 4. Several boundary value problems have been addressed to investigate the performance of the proposed modelling framework. First, the response of a homogeneous bar under uniaxial cyclic/monotonic loading is thoroughly studied to showcase the influence of the different material/model parameters introduced. In addition, the failure of a notched cylindrical bar is predicted for different load ratios and notch radii, and predictions are compared with fatigue experiments (S–N curves) on two types of steel; AISI 4340 and 300M. Finally, the manuscript ends with concluding remarks in Section 5.

2. A phase field model for fatigue damage

The formulation presented in this section refers to the response of an elastic solid body occupying the volume $\Omega \subset \mathbb{R}^{\delta}$ ($\delta \in [1,2,3]$) having the external surface $\partial\Omega \subset \mathbb{R}^{\delta-1}$ with the outward unit normal $\mathbf{n}$. We first define the field variables of the model (Section 2.1), then derive the balance of forces using the principle of virtual power (Section 2.2), proceed to formulate the local free-energy imbalance under isothermal conditions (Section 2.3), and finally particularise our theory to suitable constitutive choices for the deformation, fracture and fatigue behaviour of the solid (Section 2.4).

2.1. Field variables and kinematics

The primary field variables are the displacement field vector $\mathbf{u}$ and the damage phase field ϕ. Assuming small deformations, the strain tensor $\boldsymbol{\varepsilon}$ is given by

$$\boldsymbol{\varepsilon} = \frac{1}{2}\left(\nabla^{\mathsf{T}}\mathbf{u} + \nabla\mathbf{u}\right) \tag{1}$$

The nucleation and growth of fatigue cracks are described by using a smooth continuous scalar phase field $\phi \in [0;1]$. The use of an auxiliary phase field variable to implicitly track interfaces has proven to be a very compelling computational approach for numerous interfacial problems, such as microstructural evolution [41] and metallic corrosion [42]. In the context of fracture mechanics, the phase field variable resembles a damage variable; it must grow monotonically $\dot{\phi} \geq 0$ and describes the degree of damage, with $\phi = 1$ denoting a crack and $\phi = 0$ corresponding to intact material points. Since ϕ is smooth and continuous, discrete cracks are represented in a diffuse fashion, with the smearing of cracks being controlled by a phase field length scale ℓ. The aim of this diffuse representation is to introduce, over a discontinuous surface Γ, the following approximation of the fracture energy [6]:

$$\Psi^{s} = \int_{\Gamma} G_c \,\mathrm{d}S \approx \int_{\Omega} G_c \gamma_{\ell}(\phi, \nabla\phi)\,\mathrm{d}V \qquad \text{for} \quad \ell \to 0^{+} \tag{2}$$

where γ_{ℓ} is the so-called crack surface density functional and G_c denotes the critical Griffith-type energy release rate, or material toughness. We extend this rate-independent description of fracture to accommodate time and history dependent problems. Thus, for a cumulative history variable $\bar{\alpha}$, which fulfils $\dot{\bar{\alpha}} \geq 0$ for a current time τ, and a fatigue degradation function $f(\bar{\alpha})$, the fracture energy can be re-formulated as follows

$$\Psi^{s} = \int_{0}^{t}\int_{\Omega} f(\bar{\alpha}(\tau))\, G_c\, \dot{\gamma}_{\ell}(\phi, \nabla\phi)\,\mathrm{d}V\,\mathrm{d}\tau \tag{3}$$

2.2. Principle of virtual power. Balance of forces

The balance equations for the coupled problem are now derived using the principle of virtual power. With respect to the displacement $\mathbf{u}$, the external surface of the body is decomposed into a part $\partial\Omega_u$, where the displacement is prescribed by Dirichlet-type boundary conditions, and a part $\partial\Omega_h$, where the traction $\mathbf{h}$ is prescribed by Neumann-type boundary conditions. A body force field per unit volume $\mathbf{b}$ can also be prescribed. With respect to the phase field ϕ, a Dirichlet-type boundary condition can be prescribed at Γ, a given crack surface inside the solid body. Additionally, a phase field fracture microtraction f can be prescribed on $\partial\Omega_f$. Accordingly, the external and internal virtual powers read

$$\begin{aligned} \dot{\mathcal{W}}_{\text{ext}} &= \int_{\partial\Omega}\left\{\mathbf{h}\cdot\dot{\mathbf{u}} + f\dot{\phi}\right\}\mathrm{d}S + \int_{\Omega}\mathbf{b}\cdot\dot{\mathbf{u}}\,\mathrm{d}V \\ \dot{\mathcal{W}}_{\text{int}} &= \int_{\Omega}\left\{\boldsymbol{\sigma} : \nabla\dot{\mathbf{u}} + \omega\dot{\phi} + \boldsymbol{\xi}\cdot\nabla\dot{\phi}\right\}\mathrm{d}V \end{aligned} \tag{4}$$

where $\boldsymbol{\sigma}$ is the Cauchy stress tensor work conjugate to the elastic strains $\boldsymbol{\varepsilon}$, and ω and $\boldsymbol{\xi}$ are the microstress quantities work conjugate to the phase field ϕ and its gradient $\nabla\phi$, respectively. Eq. (4) must hold for an arbitrary domain Ω and for any kinematically admissible variations of the virtual quantities. Thus, by application of the Gauss divergence theorem and the fundamental lemma of calculus of variations, the local force balances (in Ω) are given by

$$\begin{aligned} \nabla\cdot\boldsymbol{\sigma} + \mathbf{b} &= \mathbf{0} \\ \nabla\cdot\boldsymbol{\xi} - \omega &= 0 \end{aligned} \tag{5}$$

along with the following natural boundary conditions (on $\partial\Omega$)

$$\begin{aligned} \mathbf{h} &= \boldsymbol{\sigma}\cdot\mathbf{n} \\ f &= \boldsymbol{\xi}\cdot\mathbf{n} \end{aligned} \tag{6}$$

2.3. Free-energy imbalance

The first and second law of thermodynamics can be expressed through the Helmholtz free energy per unit volume $\psi(\boldsymbol{\varepsilon}, \phi, \nabla\phi)$ and the external work $\mathcal{W}_{\text{ext}}$,

$$\int_{\Omega}\dot{\psi}\,\mathrm{d}V - \int_{\partial\Omega}\dot{\mathcal{W}}_{\text{ext}}\,\mathrm{d}S \leq 0 \tag{7}$$

which is generally referred to as Clausius–Duhem inequality. Inserting Eqs. (5)–(6) and applying the divergence theorem, the local free-energy inequality can be rewritten as

$$\int_{\Omega} \dot{\psi}\, \mathrm{d}V - \int_{\Omega} \left\{ \boldsymbol{\sigma} : \nabla \dot{\mathbf{u}} + \omega \dot{\phi} + \boldsymbol{\xi} \cdot \nabla \dot{\phi} \right\} \mathrm{d}V \leq 0 \tag{8}$$

which must hold for any arbitrary volume and, thus, must also hold in a local fashion,

$$\left(\boldsymbol{\sigma} - \frac{\partial \psi}{\partial \boldsymbol{\varepsilon}} \right) : \dot{\boldsymbol{\varepsilon}} + \left(\omega - \frac{\partial \psi}{\partial \phi} \right) \dot{\phi} + \left(\boldsymbol{\xi} - \frac{\partial \psi}{\partial \nabla \phi} \right) \cdot \nabla \dot{\phi} \geq 0 \tag{9}$$

for which a free energy function ψ is proposed as the sum of the elastic strain energy density of the solid ψ^e and the fracture surface energy density ψ^s, such that:

$$\psi(\boldsymbol{\varepsilon}, \phi, \nabla\phi \mid \bar{\alpha}) = \psi^e(\boldsymbol{\varepsilon}, \phi) + \psi^s(\phi, \nabla\phi \mid \bar{\alpha}) \tag{10}$$

2.4. Constitutive theory

Consistent with the free energy definition (10), we proceed now to develop a constitutive theory that couples the deformation, fracture and fatigue behaviour of the solid.

2.4.1. Elasticity

The strain energy density ψ^e is defined as a function of the elastic strains $\boldsymbol{\varepsilon}$, the isotropic linear elastic stiffness tensor $\boldsymbol{\mathcal{L}}_0$ and a phase field degradation function $g(\phi)$, to be defined. Hence,

$$\psi^e(\boldsymbol{\varepsilon}, \phi) = g(\phi)\psi_0^e(\boldsymbol{\varepsilon}) \qquad \text{with} \qquad \psi_0^e(\boldsymbol{\varepsilon}) = \frac{1}{2}\boldsymbol{\varepsilon}^{\mathsf{T}} : \boldsymbol{\mathcal{L}}_0 : \boldsymbol{\varepsilon} \tag{11}$$

where ψ_0^e denotes the strain energy density for an undamaged isotropic solid. Accordingly, the Cauchy stress tensor $\boldsymbol{\sigma}$ can now be derived as

$$\boldsymbol{\sigma} = \frac{\partial \psi}{\partial \boldsymbol{\varepsilon}} = g(\phi)\boldsymbol{\mathcal{L}}_0 : \boldsymbol{\varepsilon}\,, \tag{12}$$

emphasising how the phase field order parameter reduces the stiffness of the solid, as in continuum damage mechanics approaches.

2.4.2. Fracture surface energy

The surface energy density of a fractured solid ψ^s, in agreement with (3), is defined as a function of the phase field damage ϕ, its gradient $\nabla\phi$ and a fatigue degradation function $f(\bar{\alpha})$, to be defined,

$$\psi^s(\phi, \nabla\phi \mid \bar{\alpha}) = f(\bar{\alpha})\, G_c\, \gamma_\ell(\phi, \nabla\phi) \tag{13}$$

in which the crack surface density functional γ_ℓ is expressed as

$$\gamma_\ell(\phi, \nabla\phi) = \frac{1}{4c_w}\left(\frac{w(\phi)}{\ell} + \ell |\nabla\phi|^2 \right) \qquad \text{with} \qquad c_w = \int_0^1 \sqrt{w(\zeta)}\mathrm{d}\zeta \tag{14}$$

where $w(\phi)$ is the geometric crack function, to be defined, and c_w is a scaling constant.

2.4.3. Strain energy decomposition

To prevent the nucleation and growth of cracks under compression, the strain energy density can be decomposed into active (tensile) and inactive (compressive) parts,

$$\psi^e(\boldsymbol{\varepsilon}, \phi) = g(\phi)\, \psi_0^+(\boldsymbol{\varepsilon}) + \psi_0^-(\boldsymbol{\varepsilon}) \tag{15}$$

where we follow the *hybrid* formulation proposed by Ambati et al. [43] in applying the decomposition only to the phase field evolution equation. Among the multiple decomposition splits proposed in the literature, the present work adopts the following choices:

(i) `Spectral tension-compression` split by Miehe et al. [44]:

$$\psi_0^{\pm}(\boldsymbol{\varepsilon}) = \frac{1}{2}\lambda \langle \mathrm{tr}(\boldsymbol{\varepsilon}) \rangle_{\pm}^2 + \mu\, \mathrm{tr}\left(\boldsymbol{\varepsilon}_{\pm}^2 \right) \qquad \text{with} \qquad \boldsymbol{\varepsilon}_{\pm} = \sum_{i=1}^{3} \langle \varepsilon_i \rangle_{\pm}\, \boldsymbol{n}_i \otimes \mathbf{n}_i \tag{16}$$

(ii) `No-tension` split by Freddi et al. [45] (see also [23] for 3D strain states):

$$\psi_0^{\pm}(\boldsymbol{\varepsilon}) = \frac{1}{2}\lambda\, \mathrm{tr}^2(\boldsymbol{\varepsilon}_{\pm}) + \mu\, \mathrm{tr}\left(\boldsymbol{\varepsilon}_{\pm}^2 \right) \qquad \text{with} \qquad \boldsymbol{\varepsilon}_{\pm} = \mathrm{sym}_{\pm}(\boldsymbol{\varepsilon}) \tag{17}$$

(iii) `Volumetric-deviatoric` split by Amor et al. [46]:

$$\begin{aligned} \psi_0^+(\boldsymbol{\varepsilon}) &= \frac{1}{2}\left(\lambda + \tfrac{2}{3}\mu \right) \langle \mathrm{tr}(\boldsymbol{\varepsilon}) \rangle_+^2 + \mu \left(\boldsymbol{\varepsilon}^{\mathrm{dev}} : \boldsymbol{\varepsilon}^{\mathrm{dev}} \right) \\ \psi_0^-(\boldsymbol{\varepsilon}) &= \frac{1}{2}\left(\lambda + \tfrac{2}{3}\mu \right) \langle \mathrm{tr}(\boldsymbol{\varepsilon}) \rangle_-^2 \\ \text{with } \boldsymbol{\varepsilon}^{\mathrm{dev}} &= \boldsymbol{\varepsilon} - \tfrac{1}{3}\,\mathrm{tr}(\boldsymbol{\varepsilon})\mathbf{I} \end{aligned} \tag{18}$$

where λ and μ are the Lamé constants for an isotropic material and $\mathbf{I}$ is the identity matrix. Also, $\pm$ is the plus–minus sign and $\langle \square \rangle$ are the Macaulay brackets, such that $\langle \square \rangle_{\pm} := \frac{1}{2}(\square \pm |\square|)$, and $\mathrm{sym}_{\pm}(\boldsymbol{\varepsilon})$ is the positive/negative-definite symmetric part of the strain tensor. For the case of `Spectral` and `No-tension` splits, the infinitesimal strain tensor is given in terms of the principal strains $\{\varepsilon_i\}_{i=1}^3$ and principal strain directions $\{\mathbf{n}_i\}_{i=1}^3$.

2.4.4. Irreversibility condition

Damage is an irreversible process and, as a consequence, the phase field evolution law must fulfil the condition $\dot{\phi} \geq 0$. To this end, we follow Miehe et al. [47] and define a history variable field $\mathcal{H}$ for a current time t,

$$\mathcal{H} = \max_{\tau \in [0,t]} \psi_0^+(\boldsymbol{\varepsilon}(\mathbf{x}, \tau))\,, \tag{19}$$

which satisfies the Karush–Kuhn–Tucker (KKT) conditions for both loading and unloading stages,

$$\psi_0^+ - \mathcal{H} \leq 0\,, \qquad \dot{\mathcal{H}} \geq 0\,, \qquad \dot{\mathcal{H}}(\psi_0^+ - \mathcal{H}) = 0 \tag{20}$$

2.4.5. Phase field fracture

We proceed to derive the phase field micro-stress quantities ω and $\boldsymbol{\xi}$. First, considering, (11), (13) and (19), the total free energy density of the solid (10) renders

$$\psi(\boldsymbol{\varepsilon}, \phi, \nabla\phi \mid \bar{\alpha}) = g(\phi)\mathcal{H} + f(\bar{\alpha})\frac{G_c}{4c_w}\left(\frac{w(\phi)}{\ell} + \ell |\nabla\phi|^2 \right) \tag{21}$$

Accordingly, the micro-stress variables ω and $\boldsymbol{\xi}$ can readily be derived as

$$\omega = \frac{\partial \psi}{\partial \phi} = g'(\phi)\mathcal{H} + f(\bar{\alpha})\frac{G_c}{4c_w \ell} w'(\phi)\,, \qquad \boldsymbol{\xi} = \frac{\partial \psi}{\partial \nabla\phi} = f(\bar{\alpha})\frac{G_c \ell}{2c_w}\nabla\phi \tag{22}$$

Inserting these constitutive relations in the phase field local balance (5)b yields the strong form of the evolution of the crack phase field under fatigue loading,

$$\frac{G_c f(\bar{\alpha})}{2c_w}\left(\frac{w'(\phi)}{2\ell} - \ell\nabla^2\phi \right) - \frac{G_c \ell}{2c_w}\nabla\phi\nabla f(\bar{\alpha}) + g'(\phi)\mathcal{H} = 0 \tag{23}$$

2.4.6. Degradation and dissipation functions

First, we proceed to define the phase field degradation function $g(\phi)$, which governs the degradation of the stored elastic energy due to damage evolution, and must satisfy

$$g(0) = 1, \qquad g(1) = 0, \qquad g'(\phi) \leq 0 \qquad \text{for} \quad 0 \leq \phi \leq 1 \tag{24}$$

where the first two constraints are the limits for the fully intact and fully broken states while the last constraint ensures convergence of $\partial\psi/\partial\phi$ to a final value for the fully broken state. To this end, we adopt the widely used quadratic degradation function

$$g(\phi) = (1 - \phi)^2 \tag{25}$$

In addition, we define the damage dissipation function $w(\phi)$, which rules the energy dissipation due to the formation of a new crack, and must fulfil

$$w(0) = 0, \qquad w(1) = w_1 > 0, \qquad w'(\phi) \geqslant 0 \qquad \text{for} \quad 0 \leq \phi \leq 1 \tag{26}$$

for which we adopt what are arguably the two most widely used models in the literature, the so-called `AT1` [38] and `AT2` [6] phase field models. The specific choice $w(\phi) = \phi^2$ ($c_w = 1/2$) renders the `AT2` model while $w(\phi) = \phi$ ($c_w = 2/3$) corresponds to the `AT1` formulation. The latter introduces a purely elastic response prior to the onset of

damage, unlike the AT2 case, where $w'(0) = 0$. As a result, a damage driving force threshold $\mathcal{H}_{\min}$ should be defined for the AT1 model, such that the history field (19) yields

$$\mathcal{H} = \max\left\{ \max_{\tau\in[0,t]} \psi_0^+(\boldsymbol{\varepsilon}(\mathbf{x},\tau)),\ \mathcal{H}_{\min} \right\} \quad \text{with} \quad \mathcal{H}_{\min} = \frac{3G_c}{16\ell} \tag{27}$$

Considering the homogeneous solution to (23) provides further insight into the role of the phase field length scale ℓ. Thus, in a 1D setting, for a sample with Young's modulus E, subjected to a uniaxial monotonic stress $\sigma = g(\phi)\, E\varepsilon$; the homogeneous solution for the stress reaches a maximum at the following critical strength and strain,

$$\begin{aligned} &\text{AT1}: \ \sigma_c = \sqrt{\frac{3EG_c}{8\ell}}, \quad \varepsilon_c = \sqrt{\frac{3G_c}{8\ell E}} \\ &\text{AT2}: \ \sigma_c = \frac{3}{16}\sqrt{\frac{EG_c}{3\ell}}, \quad \varepsilon_c = \sqrt{\frac{G_c}{3\ell E}} \end{aligned} \tag{28}$$

where ℓ is shown to be not only a regularising parameter but also a material property that defines the material strength. This enables phase field models to predict crack nucleation and naturally recover the transition flaw size effect [22,48]; i.e., capturing both toughness-dominated failures (for long cracks) and strength-dominated failures (short cracks).

2.4.7. Fatigue damage

Phase field fatigue models have proven to be capable of capturing the nucleation and growth of fatigue cracks, and can naturally recover key features such as the Wöhler curve or Paris law behaviour [28]. However, existing models need to be enhanced to be able to capture behaviour frequently observed in experiments and widely embedded in fatigue design standards. In the context of total-life analyses, this includes the definition of suitable model/material parameters that enables capturing: (i) the slope of the S–N curve, (ii) the endurance limit of the material, and (iii) the load ratio effect. Thus, our work aims at developing a framework that can incorporate those additional modelling capabilities, and at showcasing the ability of this framework to reproduce experimental data and naturally capture the role of stress concentration factors (e.g., predicting the life of a notched component from a smooth S–N curve).

First, following [27], the damage resulting from the application of cyclic loads is captured by introducing a fatigue degradation function $f(\bar{\alpha})$, which effectively degrades the material toughness as a function of the fatigue history experienced by the solid. The following fatigue degradation functions, proposed in the literature [28,35], are considered here

$$\begin{aligned} f_0(\bar{\alpha}) &= \left(1 - \frac{\bar{\alpha} - \bar{\alpha}_0}{\bar{\alpha} + \bar{\alpha}_0}\right)^2 && \text{for} \ \ \bar{\alpha} \in \left[\bar{\alpha}_0, \infty\right] \ \ (\text{otherwise } f_0(\bar{\alpha}) = 1) \\ f_1(\bar{\alpha}) &= \left(1 - \frac{\bar{\alpha}}{\bar{\alpha} + \bar{\alpha}_0}\right)^2 && \text{for} \ \ \bar{\alpha} \in [0, +\infty] \\ f_2(\bar{\alpha}) &= \left(1 - \frac{\bar{\alpha}}{\bar{\alpha}_0}\right)^2 && \text{for} \ \ \bar{\alpha} \in \left[0, \bar{\alpha}_0\right] \end{aligned} \tag{29}$$

where $\bar{\alpha}_0$ is meant to be a material parameter to be calibrated with experiments. As shown in Fig. 1, the main difference between them is that f_0 and f_1 deliver an asymptotically vanishing value while f_2 vanishes for a finite value of $\bar{\alpha}$. In addition, f_0 provides an initial threshold branch where material toughness remains unaffected by fatigue as the value of $\bar{\alpha}$ increases.

In addition, the fatigue history variable $\bar{\alpha}$ should describe the accumulation of any quantity α that can describe the cyclic history of the material. We follow Carrara et al. [28] in maintaining the energetic nature of the model and thus use the active part of the stored elastic energy density, defined in Section 2.4.3, as the fatigue history variable, i.e.

$$\alpha = g(\phi)\psi_0^+(\boldsymbol{\varepsilon}) \tag{30}$$

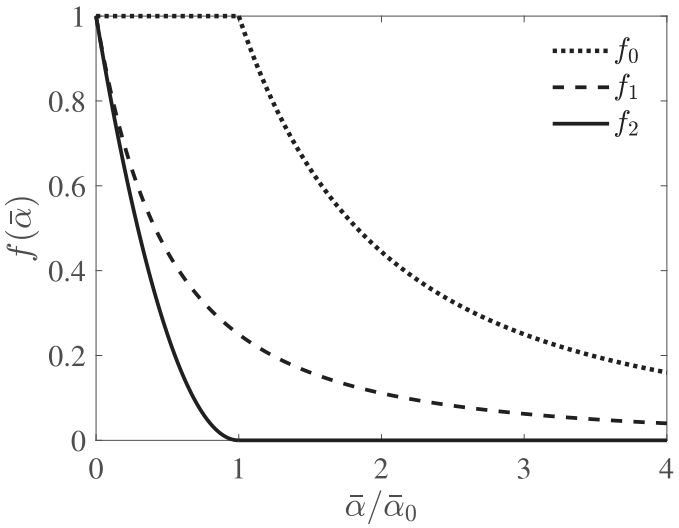

Fig. 1. Evolution of the three fatigue degradation functions considered, see Eq. (29).

Note that the adoption of the *degraded* strain energy density ensures that the quantity is not affected by the crack tip singularity. Accordingly, the evolution of the fatigue history variable $\bar{\alpha}$, within the time discretisation, is given by

$$\bar{\alpha}_{t+\Delta t} = \bar{\alpha}_t + \int_t^{t+\Delta t} \dot{\bar{\alpha}}\, \mathrm{d}\tau = \bar{\alpha}_t + \Delta\bar{\alpha} \tag{31}$$

A key aspect in developing a constitutive phase field fatigue model lies in the definition of $\Delta\bar{\alpha}$; the approach employed to account for the accumulation of fatigue damage. In Ref. [28], the accumulation of fatigue damage is considered only during the loading part of the cycle, which undesirably affects the proportional (monotonic) loading case. To address this issue, Seles et al. [35] considered the accumulation of fatigue effects only during the unloading stage. However, we have observed that this might result in an unrealistic increase of the fatigue history variable in areas behind the crack tip as a result of localised unloading in those material points. Here, we suggest accumulating fatigue effects only during one reversal per cycle (peak to valley, see Fig. 2), thus not affecting the monotonic loading cases. Most importantly, the new accumulation strategy enables us to achieve very significant reductions in computational cost as it allows us to accurately describe the accumulation of $\bar{\alpha}$ by using only one increment per cycle. Thus, for constant amplitude cases, internal increments within a cycle are instead replaced by the application of a constant (representative) load with the maximum value of the amplitude as its magnitude. As shown in Fig. 2, the maximum and minimum values of the fatigue history variable are respectively denoted as $\alpha_{\max}$ and $\alpha_{\min}$, and can be estimated at the cycle peak and the valley during one reversal.

Building upon our fatigue accumulation strategy, we proceed to define $\Delta\bar{\alpha}$ to present a model that accounts for (i) the slope of the S–N curve, (ii) the endurance limit, and (iii) the effect of the stress ratio. This generalised expression reads:

$$\Delta\bar{\alpha} = \left(\frac{\alpha_{\max}}{\alpha_n}\right)^n \left(\frac{1-R}{2}\right)^{2\kappa n} H\left(\max_{\tau\in[0,t]} \alpha_{\max}\left(\frac{1-R}{2}\right)^{2\kappa} - \alpha_e\right) \tag{32}$$

and each of its elements is described below. Here, one should note that $\Delta\bar{\alpha}$ is defined as a dimensionless quantity. A comparison with some of the main existing phase field fatigue models is provided in Appendix A.

S–N curve slope. We add a material parameter, the exponent n, and an additional term, $(\alpha_{\max}/\alpha_n)^n$, to endow the model with the flexibility needed to match the slope of any S–N curve. Here, a normalisation

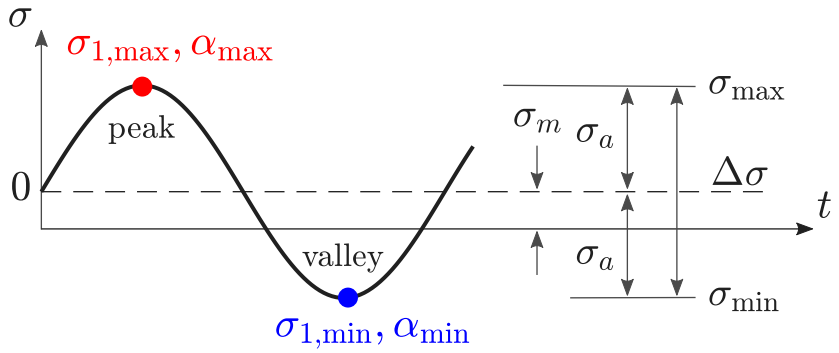

Fig. 2. Constant amplitude cyclic stressing and definitions of the main variables. The red dot (peak) shows the location where $\sigma^{\mathrm{I}}_{\max}$ and $\alpha_{\max}$ are calculated, where the blue dot (valley) shows the instant at which $\sigma^{\mathrm{I}}_{\min}$ and $\alpha_{\min}$ are determined.

parameter α_n is needed to achieve dimensional consistency. We adopt $\alpha_n = 1/2\sigma_c\varepsilon_c$, based on the critical stresses and strains given in Eq. (28).

Endurance limit. A fatigue threshold variable α_e is introduced to endow the model with a material endurance limit, below which cyclic damage does not occur. This is used in combination with the Heaviside function $H(\square)$, which equals one for positive arguments and zero for negative ones. The magnitude of α_e can be estimated from the material endurance stress σ_e as $\alpha_e = \sigma_e^2/(2E)$.

Stress ratio. Fatigue behaviour is known to exhibit significant sensitivity to the stress ratio, which can be defined as $R = \sigma_{1,\min}/\sigma_{1,\max}$, where $\sigma_{1,\min}$ and $\sigma_{1,\max}$ respectively denote the minimum and maximum principal stresses within each cycle (see Fig. 2). In the case of proportional loading, which is the case for all analyses in the present paper, this does not lead to ambiguity. However, for non-proportional loading care must be taken to define the values properly. A suitable choice may be to choose the direction, $\boldsymbol{n}_1$, according to the maximum principle value, and evaluate both the maximum and the minimum normal stresses in this direction. It should be noted that R is not an input to the model but a material point quantity that can be estimated at the end of each cycle. To introduce R into the accumulation of the fatigue history variable, we take inspiration from classical mean stress relationships. In particular, the Walker mean stress relationship [49] has been widely used to enrich Basquin-type laws to account for non-zero mean stresses; this relationship reads,

$$\sigma_{ar} = \sigma_{\max}\left(\frac{1-R}{2}\right)^{\kappa} \qquad \text{for} \quad (\sigma_{\max} > 0) \tag{33}$$

where σ_{ar} is the equivalent stress amplitude when the mean stress is $\sigma_m = 0$, $\sigma_{\max}$ is the maximum stress within each cycle, and $\kappa \in [0,1]$ is a material constant, describing the measure of the material's sensitivity to mean stress. For $\kappa = 0.5$, the Walker equation reduces to the well-known Smith–Watson–Topper (SWT) relationship [50]. As shown in Eq. (32), our model employs Walker-based terms to capture the load ratio effect. Other approaches, involving the use of sign functions (see Appendix A), did not provide a good agreement with experiments.

3. Numerical implementation

Details of the numerical implementation are provided here, starting with the finite element discretisation (Section 3.1), followed by the formulation of the residuals and the stiffness matrices (Section 3.2).

3.1. Finite element discretisation

The finite element (FE) method is used to solve the coupled problem. Making use of Voigt notation, the primary kinematic variables of the coupled problem are discretised in terms of their nodal values $\mathbf{u}_i = \{u_x, u_y, u_z\}_i^{\intercal}$ and ϕ_i at node i as

$$\mathbf{u} = \sum_{i=1}^{m} \mathbf{N}_i \mathbf{u}_i \qquad \text{and} \qquad \phi = \sum_{i=1}^{m} N_i \phi_i \tag{34}$$

where m is the total number of nodes per element, N_i the shape functions associated with node i, and $\mathbf{N}_i$ the shape function matrix, a diagonal matrix with N_i in the diagonal terms. Accordingly, the corresponding gradient quantities can be discretised as

$$\boldsymbol{\varepsilon} = \sum_{i=1}^{m} \mathbf{B}_i^u \mathbf{u}_i \qquad \text{and} \qquad \nabla\phi = \sum_{i=1}^{m} \mathbf{B}_i \phi_i \tag{35}$$

where $\mathbf{B}_i^{\mathbf{u}}$ denotes the standard strain–displacement matrices and $\mathbf{B}_i$ is a vector containing the spatial derivatives of the shape functions.

3.2. Residuals and stiffness matrices

We now proceed to formulate the weak form of the coupled problem. Considering the principle of virtual power (4) and the constitutive choices described in Section 2.4, the weak forms of the displacement and phase field problems read

$$\begin{aligned} &\int_\Omega \left\{ \big[g(\phi)+k\big]\boldsymbol{\sigma}_0 : \nabla\dot{\mathbf{u}} - \mathbf{b}\cdot\dot{\mathbf{u}} \right\} \mathrm{d}V - \int_{\partial\Omega_h} \mathbf{h}\cdot\dot{\mathbf{u}}\,\mathrm{d}S = 0 \\ &\int_\Omega \left\{ g'(\phi)\dot{\phi}\,\mathcal{H} + f(\bar{\alpha})\frac{G_c}{4c_w}\left(\frac{w'(\phi)\dot{\phi}}{\ell} + 2\ell\nabla\phi\cdot\nabla\dot{\phi}\right) \right\} \mathrm{d}V \\ &\quad - \int_{\partial\Omega_f} f\,\dot{\phi}\,\mathrm{d}S = 0 \end{aligned} \tag{36}$$

where $\boldsymbol{\sigma}_0$ is the Cauchy stress tensor of the undamaged solid and k is a small and positive constant used to avoid ill-conditioning of the system of equations when $\phi = 1$; in this work $k = 10^{-7}$. Now, making use of the finite element discretisation outlined in (34) and (35) and considering that (36) must hold for any kinematically admissible variations of the virtual quantities $\dot{\square}$, the corresponding residuals are derived as

$$\begin{aligned} \mathbf{r}_i^u &= \int_\Omega \big[g(\phi)+k\big](\mathbf{B}_i^u)^{\intercal}\boldsymbol{\sigma}_0\,\mathrm{d}V - \int_\Omega (\mathbf{N}_i)^{\intercal}\mathbf{b}\,\mathrm{d}V - \int_{\partial\Omega_h} (\mathbf{N}_i)^{\intercal}\mathbf{h}\,\mathrm{d}S \\ r_i^\phi &= \int_\Omega \left\{ g'(\phi)N_i\,\mathcal{H} + f(\bar{\alpha})\frac{G_c}{4c_w}\left(\frac{w'(\phi)}{\ell}N_i + 2\ell(\mathbf{B}_i)^{\intercal}\nabla\phi\right) \right\} \mathrm{d}V \\ &\quad - \int_{\partial\Omega_f} N_i\,f\,\mathrm{d}S \end{aligned} \tag{37}$$

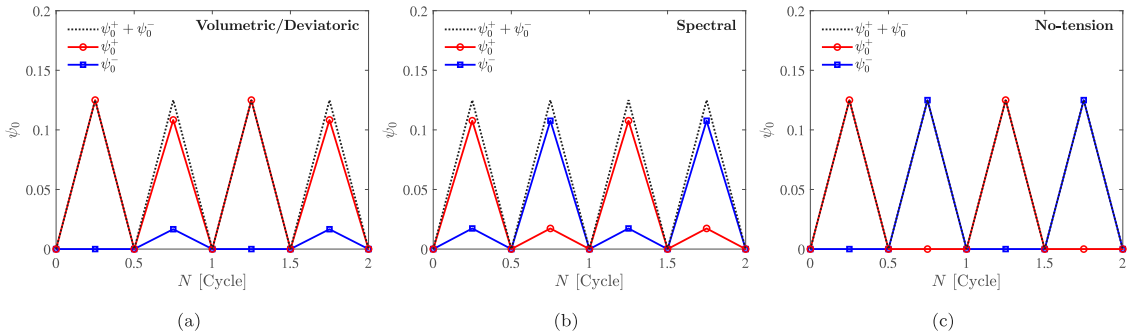

Fig. 3. Sensitivity of fatigue driving force, recall $\alpha = g(\phi)\psi_0^+$, to the choice of strain energy density decomposition; tensile ψ_0^+ and compressive ψ_0^- components for a fully-reversed cyclic loading ($R = -1$) considering the (a) `Volumetric/deviatoric`, (b) `Spectral`, and (c) `No-tension` splits.

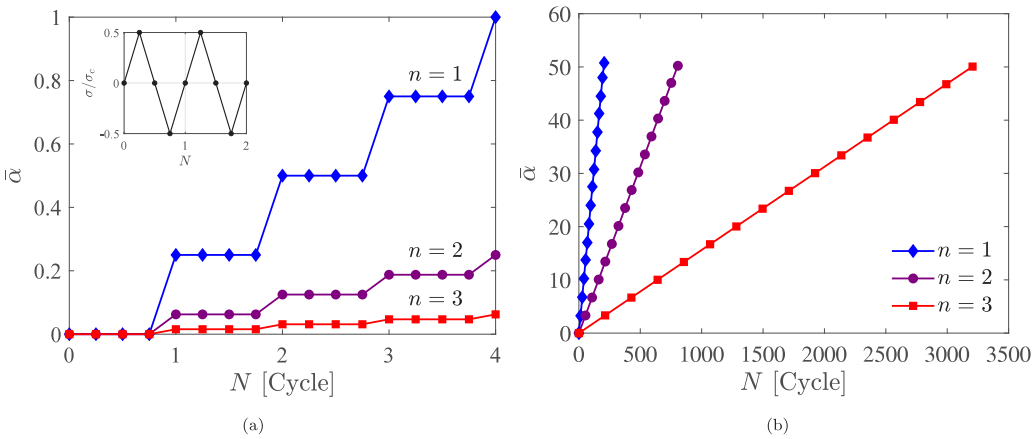

Fig. 4. Cyclic evolution of the fatigue history variable $\bar{\alpha}$ for different values of the power exponent n: (a) detail of the first cycles, showing how the `No-tension` split appropriately accumulates damage only within one half-cycle per cycle, and (b) evolution over numerous cycles, showing the influence of the exponential parameter n.

Finally, the consistent tangent stiffness matrices are obtained by differentiating the residuals with respect to the incremental nodal variables as follows

$$\begin{aligned}
\mathbf{K}^u_{ij} &= \frac{\partial \mathbf{r}^u_i}{\partial \mathbf{u}_j} = \int_\Omega \big[g(\phi) + k\big](\mathbf{B}^u_i)^{\mathsf{T}} \boldsymbol{\mathcal{L}}_0 \, \mathbf{B}^u_j \, \mathrm{d}V \\
\mathbf{K}^\phi_{ij} &= \frac{\partial r^\phi_i}{\partial \phi_j} = \int_\Omega \left\{ \left(g''(\phi)\,\mathcal{H} + f(\bar{\alpha}) \frac{G_c}{4 c_w \ell} w''(\phi) \right) N_i N_j \right. \\
&\qquad \left. + f(\bar{\alpha}) \frac{G_c \ell}{2 c_w} (\mathbf{B}_i)^{\mathsf{T}} \mathbf{B}_j \right\} \mathrm{d}V
\end{aligned} \tag{38}$$

We then solve the global linearised FE system of equations,

$$\begin{bmatrix} \mathbf{K}^u & 0 \\ 0 & \mathbf{K}^\phi \end{bmatrix} \begin{Bmatrix} \mathbf{u} \\ \boldsymbol{\phi} \end{Bmatrix} = \begin{Bmatrix} \mathbf{r}^u \\ \mathbf{r}^\phi \end{Bmatrix} \tag{39}$$

by using a quasi-Newton method. Specifically, we employ the Broyden–Fletcher–Goldfarb–Shanno (BFGS) algorithm [39,40], which provides a robust monolithic solution scheme, enabling accurate and efficient fatigue crack growth estimations. Note that, a requirement of the BFGS algorithm is that the stiffness matrix must be symmetric and positive-definite.

4. Results

4.1. Smooth bar subjected to symmetric uniaxial tension–compression loading

We first gain insight into the model characteristics by considering a smooth bar subjected to uniaxial cyclic loading with a load ratio of $R = -1$. A model material is assumed with the following properties: Young's modulus $E = 1$ MPa, Poisson's ratio $\nu = 0.3$, tensile strength $\sigma_c = 1$ MPa, endurance limit $\sigma_e = 0.2$ MPa, critical energy release rate $G_c = 1$ kJ/m^2 and fatigue material parameter $\bar{\alpha}_0 = 100$. The boundary value problem can be solved in a semi-analytical fashion, by considering the homogeneous solution to Eq. (23). A piece-wise cyclic linear variation of the remote stress (or strain) is assumed. Under 1D conditions, the length scale and the strength are related via (28), and this relation renders magnitudes of $\ell = 0.3750$ mm and $\ell = 0.1055$ mm for `AT1` and `AT2`, respectively. Unless otherwise stated, in the remainder of this paper the `AT1` model, $\kappa = 0.5$, the f_2 fatigue degradation function (29)c and the `No-tension` split (17) are used. While all the numerical studies conducted deal with constant amplitude loading, we emphasise that the model can handle any arbitrary choice of loading history and thus capture load sequence effects.

4.1.1. Overview of material behaviour

Fig. 3 illustrates the evolution of the elastic strain energy density along with its active (tensile) and inactive (compressive) parts for a constant remote stress amplitude of $\sigma_a/\sigma_c = 0.5$, upon the assumption of a fatigue power exponent of $n = 1$. It can be clearly seen that the `No-tension` split appropriately decomposes the strain energy density such that it results in a vanishing compressive part during tension and a vanishing tensile part during compression, which is not the case for the `Volumetric/deviatoric` and the `Spectral` splits. The consistency of the `No-tension` split is also showcased in Fig. 4, where the cyclic evolution of the fatigue history variable $\bar{\alpha}$ is shown. It can be seen that the accumulation of fatigue effects takes place only during the reversal (peak to valley) part of each cycle, and that the growth rate of $\bar{\alpha}$ decreases with increasing the power exponent n.

Further insight into the evolution of the model behaviour can be gained by comparing the differences between load-controlled and displacement-controlled numerical experiments. To this end, we use

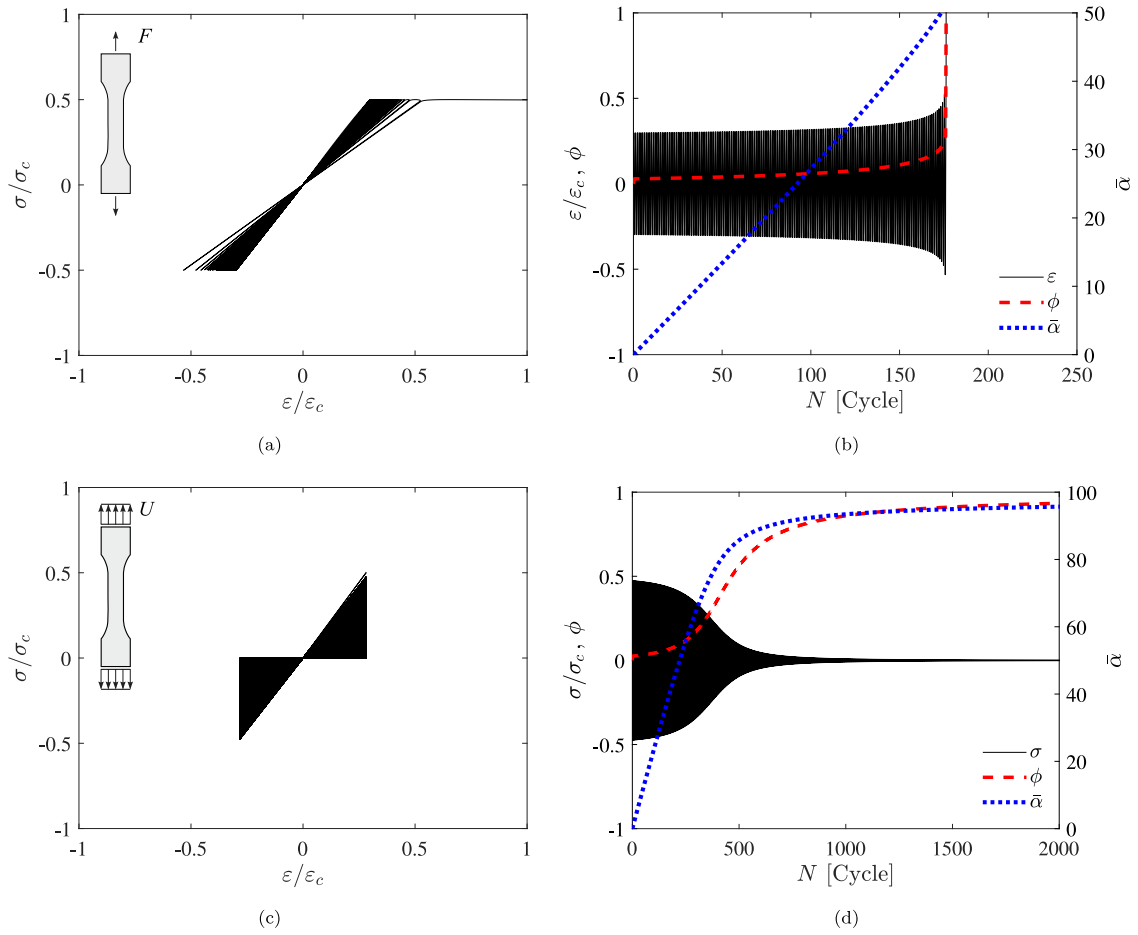

Fig. 5. Uniaxial tension–compression response under load-controlled, (a) and (b), and displacement-controlled conditions, (c) and (d). Stress versus strain curves are shown in (a) and (c), while (b) and (d) show the evolution of relevant variables ($\bar{\alpha}, \phi$, cyclic stress/strain) as a function of the number of cycles N. The number of cycles considered results in nearly overlapping curves (black regions). Calculations obtained using AT2, $n = 1$, $\kappa = 0.5$ and the No-tension split.

the AT2 phase field model and conduct simulations: (i) applying a remote stress amplitude of $\sigma_a/\sigma_c = 0.5$ (load-control), and (ii) applying a remote strain amplitude of $\varepsilon_a/\varepsilon_c = 0.5$ (displacement-control). The results obtained are given in Figs. 5(a)–(b) for load-controlled loading and in 5(c)–(d) for displacement-controlled loading. These figures illustrate both material stress–strain behaviour and the evolution with the number of cycles (N) of relevant variables ($\bar{\alpha}, \phi$, cyclic stress/strain). As shown in Fig. 5b, for the load-controlled case the phase field evolves gradually in the beginning and increases rapidly towards the end, when the strain reaches its critical value at ε_c. However, this is not the case for the displacement-controlled loading where the phase field is observed to asymptotically approach its upper limit $\phi \to 1$ (see Fig. 5d). Accordingly, a threshold for failure (e.g., $\phi = 0.95$) must be imposed when considering displacement-control conditions. This variation of ϕ in time affects the cyclic evolution of the fatigue history variable $\bar{\alpha}$ as well as the cyclic stress, owing to the phase field degradation function (25), which is present in the definitions of $\boldsymbol{\sigma}$ (12) and α (30). We proceed to gain further insight by investigating the role of the phase field fracture constitutive model (AT1 vs AT2) and the load amplitude ($\varepsilon_a/\varepsilon_c = 0.15$ vs $\varepsilon_a/\varepsilon_c = 0.5$). The results obtained are shown in Fig. 6. For the strain amplitude $\varepsilon_a/\varepsilon_c = 0.15$, the resulting stresses are below the assumed material endurance limit ($\sigma_e/\sigma_c = 0.2$) and as a result the monotonic response of the bar and its critical strength (strain) are not affected by fatigue (see Fig. 6a). On the other hand, when the load amplitude exceeds the endurance limit ($\varepsilon_a/\varepsilon_c = 0.5$, Fig. 6b), the monotonic response of the bar exhibits a significant drop in the critical strength and strain of the bar. This is observed for both AT1 and AT2 models, being more significant in the former.

4.1.2. Parametric study

Subsequently, a parametric study is conducted to investigate the influence of the fatigue model/material parameters. The calculations evaluating the sensitivity to $\bar{\alpha}_0$ and α_e are respectively shown in Fig. 7a and Fig. 7b, in terms of the remote stress amplitude versus the number of cycles to failure (S–N curves). The AT1 model is used, the stress amplitude is normalised by the material strength, and the arrows correspond to the so-called fatigue runout phenomenon — samples that do not fail in the duration of the test. First, as can be seen in Fig. 7a, the results reveal a longer fatigue life for higher values of $\bar{\alpha}_0$, in agreement with expectations. Second, Fig. 7b showcases how decreasing the threshold parameter α_e leads to a decrease in the stress amplitude at which the fatigue life is practically infinite (the endurance limit). For both $\bar{\alpha}_0$ and α_e, changes in their values do not lead to noticeable variations in the slope of the S–N curves.

Finally, the parametric study concludes with the investigation of the role of the power exponent n. The results are shown in Fig. 8. The S–N curves show a clear dependence on the magnitude of n (see Fig. 8a), with larger n values delivering fatigue responses that are more susceptible to changes in the stress amplitude. In other words, this parameter n provides additional modelling flexibility and enables capturing the S–N curve slope m^* of any material. As shown in Fig. 8b, there exists a linear relationship between n and m. Based on this finding we list in Table 1, for different phase field models and fatigue degradation functions, the coefficients of this linear relationship,

$$n = C_1\ m + C_2 \tag{40}$$

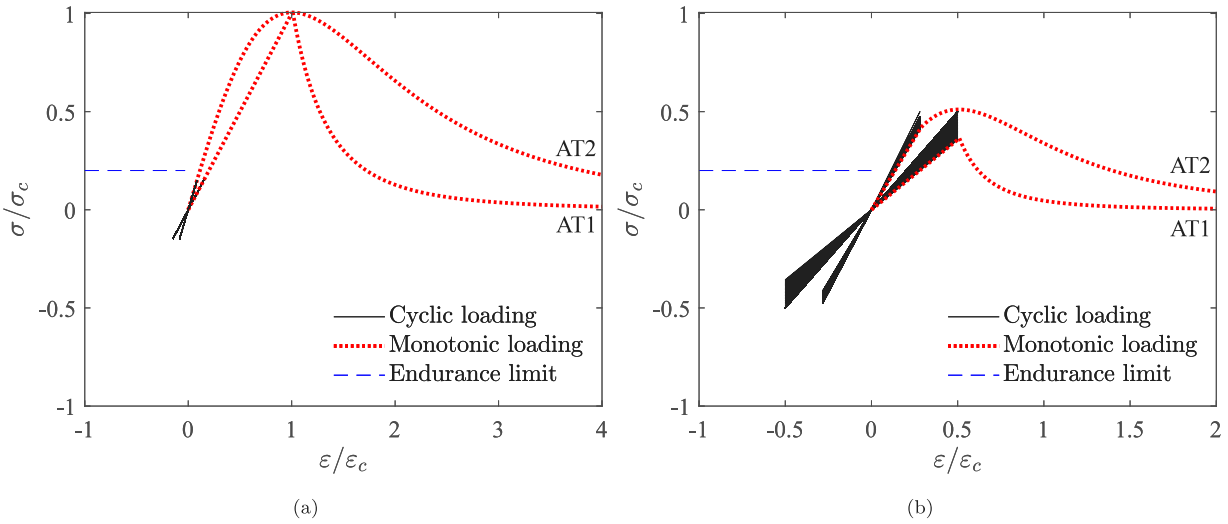

Fig. 6. Uniaxial cyclic and monotonic response of the `AT1` and `AT2` damage models, for different initially-applied remote strain amplitudes: (a) $\varepsilon_a/\varepsilon_c = 0.15$ and (b) $\varepsilon_a/\varepsilon_c = 0.5$. The number of cycles considered results in nearly overlapping curves (black regions). Calculations obtained using $n = 1$, $\kappa = 0.5$ and the `No-tension` split.

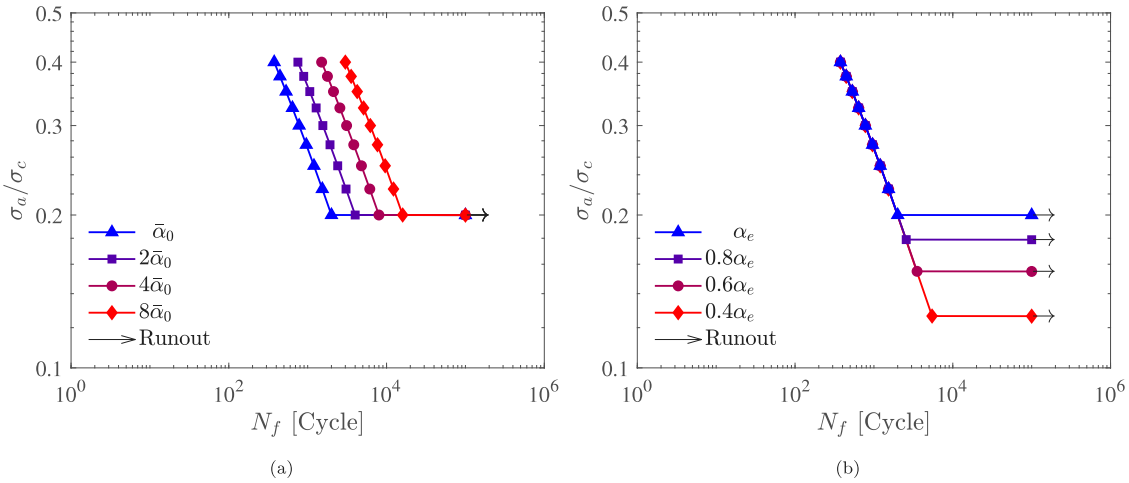

Fig. 7. Parametric study. S–N curve sensitivity to: (a) the fatigue susceptibility parameter $\bar{\alpha}_0$, and (b) the endurance parameter α_e. Calculations obtained using `AT1`, $n = 1$, $\kappa = 0.5$ and the `No-tension` split.

Table 1
Coefficients for the linear relationship between the power exponent n and the S–N slope, see Eq. (40).

	f_0		f_1		f_2	
	C_1	C_2	C_1	C_2	C_1	C_2
AT1	0.50	−0.56	0.50	−0.63	0.50	−0.13
AT2	0.50	−0.55	0.49	−0.61	0.49	−0.12

where $m = -(m^*)^{-1}$. It is also worth noticing that, for higher stress amplitudes, the S–N curve deviates from such linear behaviour, demonstrating a damage-driven failure, as also reported by Carrara et al. [28].

4.1.3. Load ratio effect

We shall now investigate the ability of the proposed model to capture the mean stress effect on S–N curve behaviour. To this end, two load-controlled scenarios are considered: (i) a varying R for a fixed stress amplitude σ_a, and (ii) a varying R for a fixed maximum stress $\sigma_{\max}$. These loading scenarios are of particular interest because experimental observations report opposite trends in terms of R vs number of cycles behaviour, with fixed σ_a experiments showing a longer fatigue life for decreasing R while the opposite is observed for fixed $\sigma_{\max}$ tests [51,52]. The results obtained are given in Fig. 9, together with a subplot depicting the loading conditions for the cases of $\sigma_a/\sigma_c = 0.4$ and $\sigma_{\max}/\sigma_c = 0.4$. A significant influence of the load ratio R on the fatigue life and the endurance limit is observed, for both loading scenarios. Consider first the fixed stress amplitude case, Fig. 9a. For a given σ_a, the fatigue life decreases significantly with increasing the load ratio R, in agreement with experimental observations [52]. It can also be observed that, for higher load ratios, the S–N curve exhibits non-linear behaviour with a notable drop in the fatigue life. This can be explained by the fact that, for higher load ratios, the maximum value of the cyclic stress observed in the subplot reaches the material critical strength σ_c, suggesting that the failure is governed by static damage rather than fatigue (see also Fig. 8a). Next, consider the constant $\sigma_{\max}$ results in Fig. 9b. Contrarily to what is observed in the constant σ_a case, and in agreement with experiments (see Ref. [51] and the experimental comparison below), fatigue lives increase with increasing R. Thus, the generalised model presented is able to adequately capture the sensitivity to the load ratio R under both constant stress amplitude and constant maximum stress.

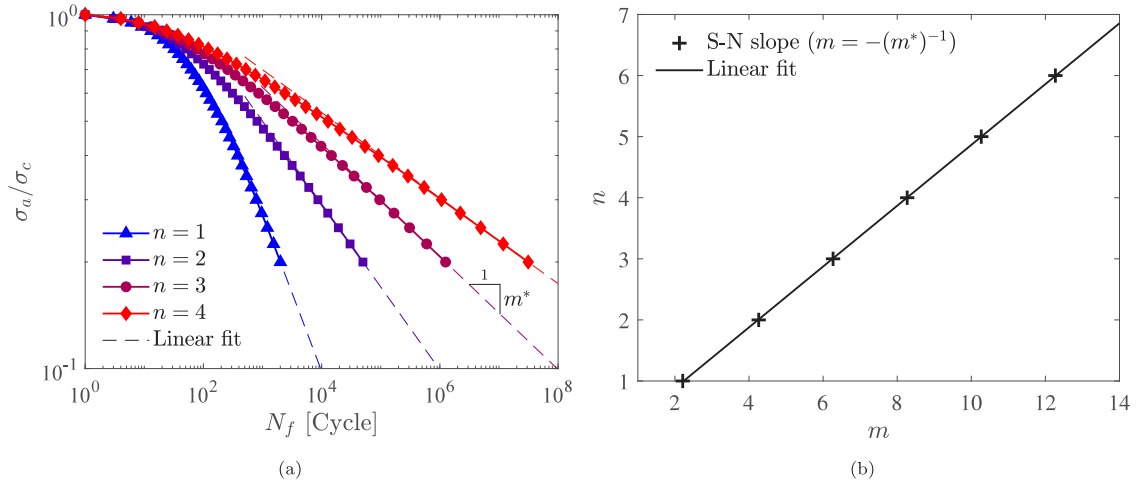

Fig. 8. Parametric study. Sensitivity to the power exponent n in terms of the (a) S–N curve behaviour and (b) its linear behaviour with the S–N slope. Calculations obtained using `AT1`, $\kappa = 0.5$ and the `No-tension` split.

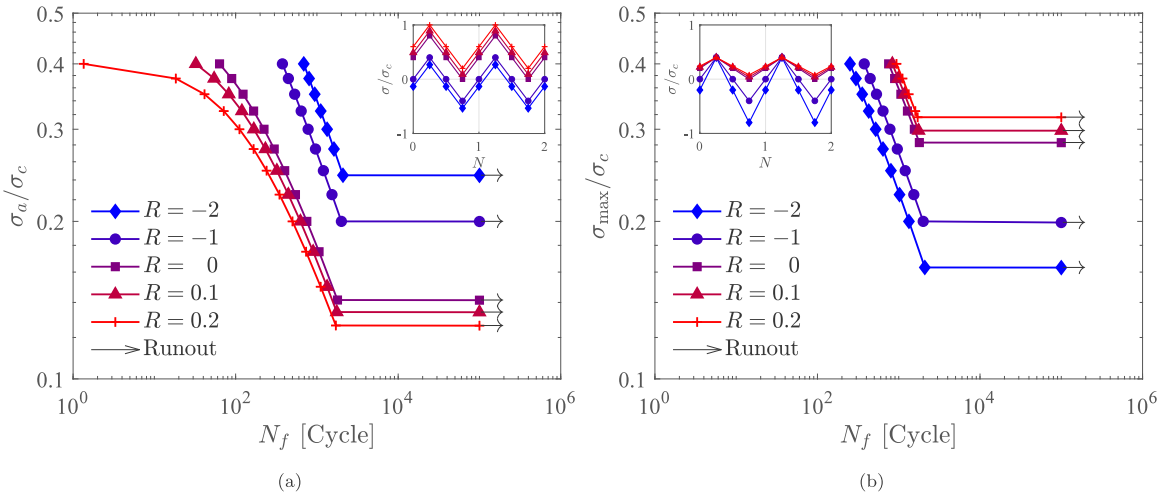

Fig. 9. Load ratio (R) effect, predictions obtained with (a) a fixed stress amplitude σ_a, and (b) a fixed maximum stress $\sigma_{\max}$. The subplots illustrate the loading conditions, for the specific cases of $\sigma_a/\sigma_c = 0.4$ and $\sigma_{\max}/\sigma_c = 0.4$. Calculations obtained using `AT1`, $n = 1$, $\kappa = 0.5$ and the `No-tension` split.

4.2. Comparison with experimental S–N curves

We proceed now to compare model predictions with S–N curves obtained from uniaxial tension–compression fatigue experiments on cylindrical bars, considering both smooth and notched samples. The experimental data are taken from Ref. [51] and correspond to two types of low-alloy steels, an AISI 4340 steel with tensile strength of 1,793 MPa, and a 300M steel with tensile strength of 2,000 MPa. The experiments were carried out in laboratory air under constant maximum stress amplitudes at various stress ratios R. As is common among steels, both materials are assumed to have a Young's modulus of $E = 210$ GPa and a Poisson's ratio of $\nu = 0.3$. The toughnesses values are taken to be equal to $G_c = 20$ kJ/m^2 and $G_c = 13$ kJ/m^2 for AISI 4340 and 300M, respectively, based on plane strain fracture toughness measurements reported in Ref. [1]. Results for the unnotched samples can be obtained semi-analytically, considering the homogeneous solution to (23). For the notched samples, finite element calculations are conducted, where axial symmetry is exploited to consider only one planar section of the sample. In addition, only the upper half of the domain is modelled due to vertical symmetry (see Fig. 10). The finite element domain is discretised using 4-node bilinear axisymmetric quadrilateral elements with full integration, with the mesh being refined ahead of the notch tip, where the characteristic element size is 10 times smaller than the phase field length scale ℓ (see Fig. 10b). Under 1D conditions, the length scale and the strength are related via (28), and this relation renders magnitudes of $\ell = 0.318$ mm and $\ell = 0.315$ mm for AISI 4340 and 300M, respectively. For the 300M notched samples, the notch radii magnitudes considered are $\rho = 1.016$, 0.368, and 0.107 mm, with the bar gross diameter being $D = 12.7$ mm and the net diameter $d = 6.35$ mm. From these, the following stress concentration factors (SCF) are obtained: $K_t = 2$, 3, and 5. For the case of AISI 4340, the notch radii magnitudes read $\rho = 0.762$ and 0.254 mm. The following diameters are considered: $D = 7.62$ mm, $D = 6.86$ mm, and $d = 5.59$ mm, which correspond to SCF values of $K_t = 2$ and 3. The samples are subjected to a piece-wise cyclic linear force-controlled loading with a load ratio of $R = -1$. The endurance limit is estimated from the S–N curve itself at the stress level below which infinite life is expected; the magnitudes of $\sigma_e = 530$ MPa and $\sigma_e = 650$ MPa are assumed for AISI 4340 and 300M, respectively. The slope of the S–N curve and its intercept with the $\log N$ axis are, respectively, linked to the fatigue parameters n and $\bar{\alpha}_0$ (see Fig. 8 and Appendix B). Thanks to this feature, the fatigue parameters n and $\bar{\alpha}_0$ can now be estimated so as to provide the best fit to the experiments of unnotched (smooth) samples subjected to fully-reversed cyclic loading ($R = -1$); the magnitudes of $\bar{\alpha}_0 = 5.0 \times 10^{-4}$, $n = 10$ and $\bar{\alpha}_0 = 1.7 \times 10^{1}$, $n = 6$, respectively, provided a good agreement with the experiments on AISI 4340 and 300M. Accordingly, any other effects

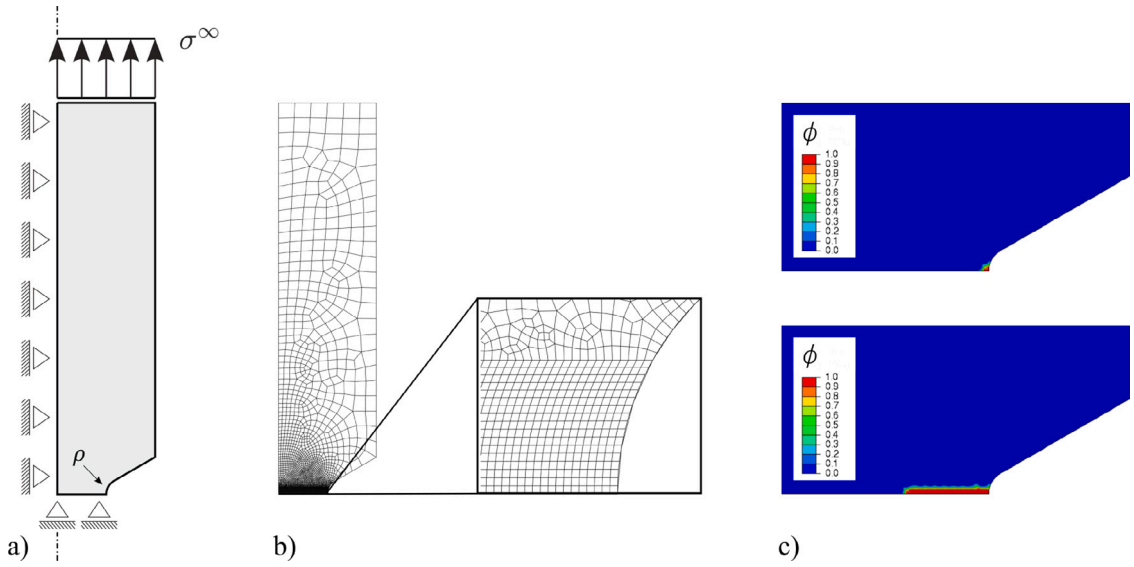

Fig. 10. Notched cylindrical bar (60° V-Groove): (a) geometry and boundary conditions, (b) finite element mesh, including a detailed view of the mesh ahead of the notch tip, and (c) representative phase field contours showing crack initiation and growth (up to the unstable failure event) for 300M steel with $K_t = 5$ and $\sigma_{\max}^{\text{nom}} = 300$ MPa.

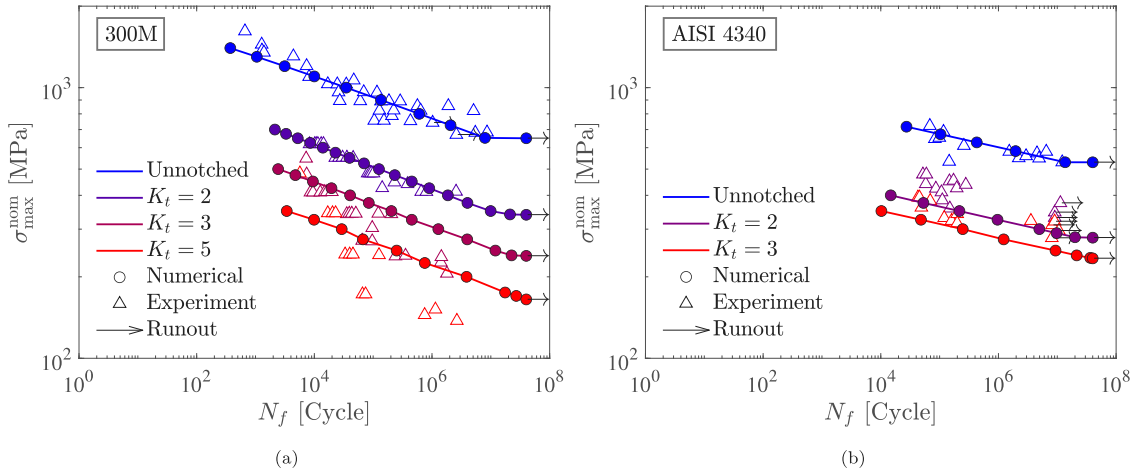

Fig. 11. Experimental validation. Numerical and experimental [51] S–N curves obtained from smooth and notched cylindrical bars for two types of steel: (a) 300M, and (b) AISI 4340. The model is shown to be able to predict the role of stress raisers (as quantified by the stress concentration factor K_t) in reducing fatigue lives.

(e.g. the role of notch radius or the sensitivity to the loading ratio) are predicted as a natural outcome of the model, without any additional fitting.

The experimental and numerical results obtained are shown in Fig. 11. It can be seen that the *Virtual* S–N curves predicted are in good agreement with the measured data. In both experiments and simulations, the results demonstrate a strong sensitivity to the notch radius, with the fatigue life decreasing by reducing the radius. Smaller radii result in higher stress concentrations at the notch tip, leading to an earlier initiation of the fatigue crack, as expected. It is also worth noting that the agreement with experiments of 300M steel becomes less satisfactory at smaller notch radii ($K_t = 5$), as the slope of the experimental S–N curve exhibits a change. This change in slope for the case of $K_t = 5$ could be related to plastic phenomena such as the reverse yielding effect [53].

Also, as shown for the AISI 4340 experiments, the model readily captures the influence of stress concentrations on the endurance limit. Overall, the model is shown to be able to reliably predict the fatigue lives and endurance limit of samples containing different notches (stress concentrators) without the need for fitting.

Building upon the 300M results, we use the model to gain further insight into the material fatigue behaviour. First, as shown in Fig. 12a, the number of cycles to initiation and failure is plotted as a function of maximum nominal stress $\sigma_{\max}^{\text{nom}}$ and the stress concentration factor K_t. The results reveal that the differences between crack nucleation and final failure increase as the notch becomes sharper. This is the result of the stronger localisation of stress, strain and damage in sharper defects. Then, we investigate the interplay between length scales by varying the phase field length scale parameter ℓ, for a fixed notch radius ρ - see Fig. 12b. Specifically, we choose to consider a value of ℓ twice as high (i.e., $2\ell = 0.63$ mm). The results show that the fatigue resistance decreases with increasing ℓ. This is in agreement with expectations as, according to Eq. (28), a higher value of ℓ will lead to a decrease in material strength and thus a shorter time to crack nucleation. It is worth noting that the values of ℓ considered are on the order of the notch radius. However, the results do not scale with ℓ/ρ, suggesting the influence of other length scales in the problem. This can be seen by considering the results for $K_t = 2$ and 2ℓ and the ones for $K_t = 3$ and ℓ, which respectively give $\rho/\ell = 1.168$ and $\rho/\ell = 1.613$, yet appear to fall on top of each other. A dimensional analysis could be carried out to establish the calculations needed to understand the interplay between the various length scales of the problem.

Finally, we validate model predictions of the load ratio effect against experiments on the two steels considered above (300M and

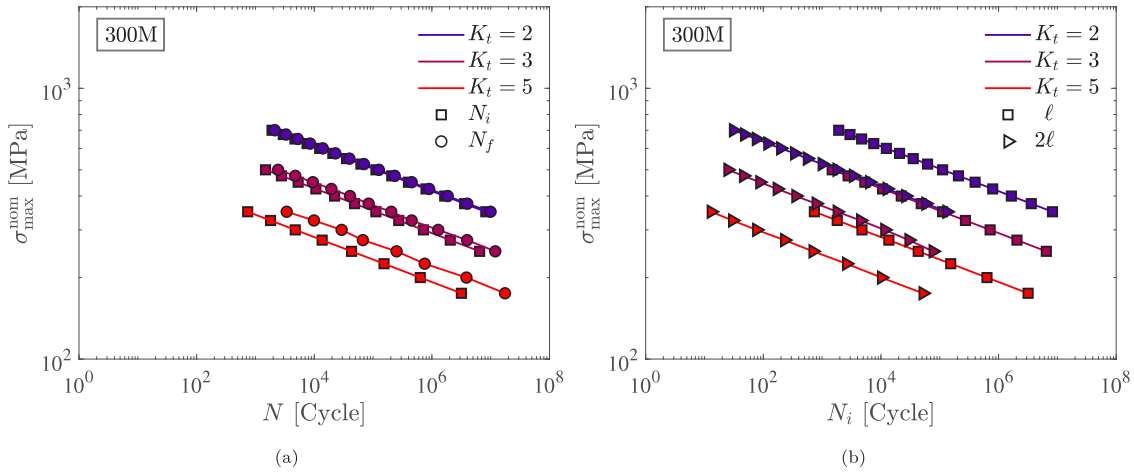

Fig. 12. S–N curves behaviour predicted for notched cylindrical bars: (a) comparison between the number of cycles for crack initiation (N_i) and the number of cycles to failure (N_f), and (b) interplay between the phase field length scale ℓ and the notch radius ρ. Results are obtained for the parameters relevant to 300M steel.

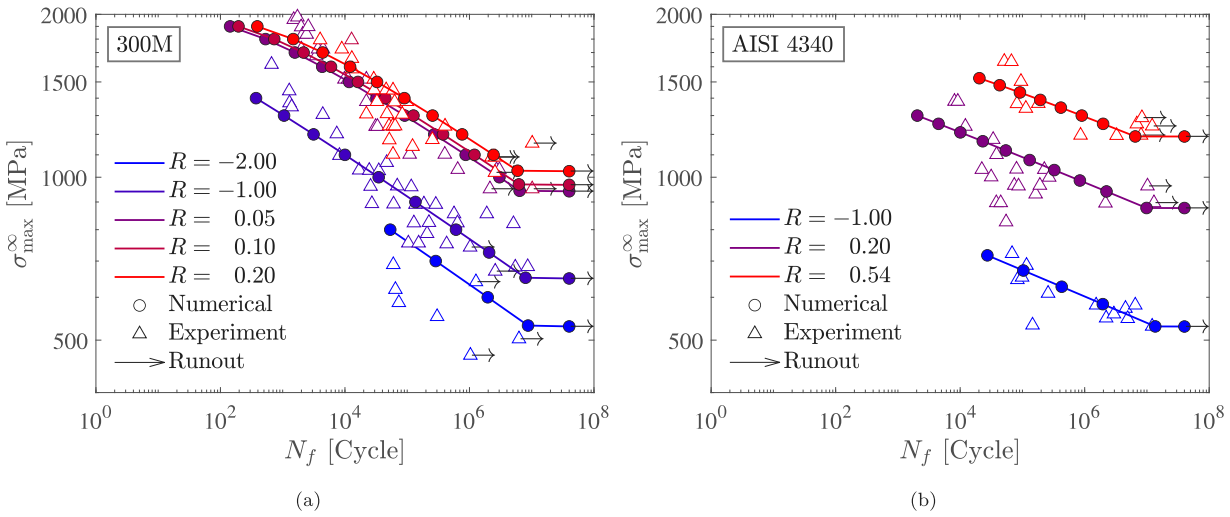

Fig. 13. Experimental validation. Numerical and experimental [51] S–N curves obtained from smooth cylindrical bars at various load ratios R for two types of steel: (a) 300M, and (b) AISI 4340. The model is shown to be able to predict the role of the load ratio in varying the fatigue resistance of the material.

AISI 4340). The model parameters are those considered before. In this regard, it should be noted that κ is taken to be equal to 0.55 and 0.5 for AISI 4340 and 300M, respectively, based on estimations reported in [52]. However, similar results would be obtained considering the simpler Smith–Watson–Topper (SWT) relationship, thus eliminating the need for this parameter altogether. The numerical predictions are shown together with experimental data in Fig. 13. Both numerical and experimental data reveal the same qualitative trend: for a fixed $\sigma_{\max}^{\infty}$, the number of cycles to failure N_f increases with increasing load ratio R. Moreover, for both 300M and AISI 4340 materials, the model delivers a good quantitative agreement with experiments, demonstrating the ability of the model to successfully predict the mean stress effect. Some differences are observed for the specific case of $R = -2$ and 300M, where the samples are under compression for the majority of their fatigue lives and the experimental scatter is notable.

5. Conclusions

We have formulated a generalised phase field formulation for modelling high-cycle fatigue behaviour in metallic materials. The modelling framework presented encompasses the two main phase field damage models (AT1 and AT2), different fatigue degradation functions, and a new accumulation approach that significantly accelerates calculations and allows modelling: (i) different S–N curve slopes, (ii) the fatigue endurance limit, and (iii) the mean stress effect (load/stress ratio). The theoretical framework presented is numerically implemented using the finite element method and the resulting system of equations is solved in a monolithic manner, by using a robust and efficient quasi-Newton (BFGS) algorithm. Total-life analyses are conducted to investigate the performance of the modelling abilities of the proposed framework. The influence on fatigue damage accumulation of various strain energy decomposition approaches (volumetric/deviatoric, spectral, no-tension) is investigated. Also, *Virtual* S–N curves are obtained for various stress/load ratios and for both notched and smooth samples. Key findings include:

- The model adequately captures the sensitivity of fatigue life to the presence of stress raisers (such as notches), with both fatigue life and endurance limit decreasing with increasing stress concentration.
- The mean stress effect (load ratio, R) on the fatigue response is adequately captured. In agreement with experimental observations, the model predicts an increase in fatigue life and endurance limit with decreasing R for a fixed stress amplitude σ_a, while the opposite is true for a fixed maximum stress $\sigma_{\max}$.
- The agreement with experiments is both qualitative and quantitative, with the model providing a good agreement with fatigue

lives and endurance limit data for 300M and AISI 4340 steels. Moreover, the role of stress raisers and load ratio on the fatigue response of these two materials is naturally captured.

The modelling framework presented provides a platform to efficiently predict the service lives of components undergoing high-cycle fatigue. Potential avenues for future work could be directed towards the development of a generalised model that could also consider low- and mid-cycle fatigue, plasticity effects and Paris law behaviour.

Declaration of competing interest

The authors declare that they have no known competing financial interests or personal relationships that could have appeared to influence the work reported in this paper.

Data availability

Data will be made available on request.

Acknowledgements

A. Golahmar acknowledges financial support from Vattenfall Vindkraft A/S and Innovation Fund Denmark (grant 0153-00018B). E. Martínez-Pañeda acknowledges financial support from UKRI's Future Leaders Fellowship programme, UK [grant MR/V024124/1].

Appendix A. Comparison with existing phase field fatigue models

Considering the following approximation for $\Delta\bar{\alpha}$ as suggested in Ref. [28, Eq. (45)]

$$\Delta\bar{\alpha} = |\alpha_{n+1} - \alpha_n|\, H\left(\frac{\alpha_{n+1} - \alpha_n}{t_{n+1} - t_n}\right) \tag{A.1}$$

where the subscripts $_n$ and $_{n+1}$ refer to the time increments $t = t_n$ and $t = t_{n+1}$, respectively. The Heaviside function $H(\square) = 0$ when $\Delta\alpha/\Delta t < 0$ (unloading). We now proceed to calculate the total increase of the fatigue history variable $\bar{\alpha}$ considering a fully-reversed cyclic loading ($R = -1$) of a bar, using the `Spectral` decomposition split (16) and 8 load steps per cycle (see Fig. A.14)

$$\begin{aligned}&\text{Inc. 0–4:}\quad \bar{\alpha}_4 = \bar{\alpha}_3 = \alpha_2 = \bar{\alpha}_1 + |\alpha_2 - \alpha_1| = \alpha_2\\ &\text{Inc. 4–8:}\quad \bar{\alpha}_8 = \bar{\alpha}_7 = \bar{\alpha}_6 = \bar{\alpha}_5 + |\alpha_6 - \alpha_5| = \underbrace{\alpha_2 + \alpha_6}_{\alpha_{\max}+\alpha_{\min}}\end{aligned} \tag{A.2}$$

which demonstrates that the accumulation of fatigue damage at the end of each cycle can be described by the values of α obtained at the peak α_2 and valley α_6 during one reversal (see also Fig. 2). Thus, Eq. (A.1), could be reformulated as

$$\Delta\bar{\alpha} = \frac{\alpha_{\max}^n - \mathrm{sgn}(R)\,\alpha_{\min}^n}{\alpha_n^n} \tag{A.3}$$

where the stress ratio R and its sign $\mathrm{sgn}(R)$ can be computed for each material point, on the fly, within each cycle. For a specific choice of $n = 1$ and $\alpha_n = 1$, Eq. (A.3) recovers Eq. (A.1), at the end of each cycle, for any arbitrary stress ratio R when using the `No-tension` split (and for $R \geq 0$ and $R = -1$ when using the other splits). In addition, for constant amplitude cases, one could accelerate the calculation of $\Delta\bar{\alpha}$ by using only one increment per cycle and applying a constant (representative) load with the maximum value of the amplitude as its magnitude. Thus, Eq. (A.3) can be altered as

$$\Delta\bar{\alpha} = \left(\frac{\alpha_{\max}}{\alpha_n}\right)^n \left(1 - \mathrm{sgn}(R)|R|^{2n}\right) \tag{A.4}$$

which yields identical analytical results to Eqs. (A.1) and (A.3) for a fixed stress ratio $R \geq 0$ when using the `No-tension` and `Volumetric-deviatoric` splits. Finally, for a specific choice of $n = 1$, $\alpha_n = 1$, $R = -1$ and $\alpha_e = 0$, our new accumulation approach (32) recovers analytically Eq. (A.1) when using the `No-tension` split.

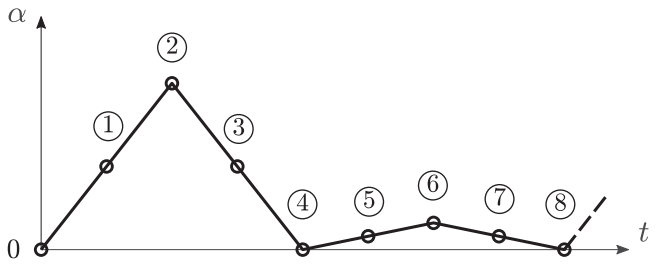

Fig. A.14. Schematic variation of α for a fully-reversed cyclic loaded ($R = -1$) bar using the `Spectral` split.

Appendix B. Estimation of the fatigue material parameter $\bar{\alpha}_0$

Considering a typical S–N curve obtained from a fatigue experiment and described mathematically by the Basquin relationship $\sigma_\square = C^*\left(N_\square\right)^{m^*}$ where $(N_\square, \sigma_\square)$ corresponds to the data set $\square$ of the fitted curve. As illustrated in Fig. 8, the slope of the S–N curve m^* is linked to the power exponent n, with the fitting parameters presented in Table 1 for different choices of phase field damage model and fatigue degradation function. We now proceed to estimate the fatigue material parameter $\bar{\alpha}_0$, by considering the homogeneous solution to (23) and assuming an *undamaged* strain energy density for $\alpha = \psi_0^+(\epsilon)$. Then, considering the `AT1` damage model, the f_2 fatigue degradation function, and the fact that $f(\bar{\alpha}) = 1$ for $\sigma = \sigma_c$ (static loading), then

$$\left(\frac{\sigma_\square}{\sigma_c}\right)^2 = f(\bar{\alpha}) = \left(1 - \frac{N_\square}{\bar{\alpha}_0}\left(\frac{\alpha_{\max}}{\alpha_c}\right)^n\right)^2 = \left(1 - \frac{N_\square}{\bar{\alpha}_0}\left(\frac{\sigma_\square}{\sigma_c}\right)^{2n}\right)^2 \tag{B.1}$$

which results in

$$\bar{\alpha}_0 = \frac{N_\square\left(\frac{\sigma_\square}{\sigma_c}\right)^{2n}}{1 - \left(\frac{\sigma_\square}{\sigma_c}\right)} \tag{B.2}$$

for which a good estimation can be obtained by using low stress magnitudes for $\sigma_\square$ (and consequently higher fatigue lives for $N_\square$), where the S–N curve is not deviating from linearity.

References

[1] Stephens RI, Fatemi A, Stephens RR, Fuchs HO. Metal fatigue in engineering. 2nd ed. John Wiley & Sons; 2000.
[2] Suresh S. Fatigue of materials. 2nd ed. Cambridge University Press; 1998.
[3] Wöhler A. Über die festigkeitsversuche mit eisen und stahl. Ernst & Korn; 1870.
[4] Griffith AA. The phenomena of rupture and flow in solids. Phil Trans A 1920;221:163–98.
[5] Francfort GA, Marigo J-J. Revisiting brittle fracture as an energy minimization problem. J Mech Phys Solids 1998;46:1319–42.
[6] Bourdin B, Francfort GA, Marigo JJ. The variational approach to fracture. Springer Netherlands; 2008.
[7] Ambati M, Gerasimov T, Lorenzis LD. Phase-field modeling of ductile fracture. Comput Mech 2015;55:1017–40.
[8] Borden MJ, Hughes TJR, Landis CM, Anvari A, Lee IJ. A phase-field formulation for fracture in ductile materials: Finite deformation balance law derivation, plastic degradation, and stress triaxiality effects. Comput Methods Appl Mech Engrg 2016;312:130–66.
[9] Isfandbod M, Martínez-Pañeda E. A mechanism-based multi-trap phase field model for hydrogen assisted fracture. Int J Plast 2021;144:103044.
[10] Borden MJ, Verhoosel CV, Scott MA, Hughes TJR, Landis CM. A phase-field description of dynamic brittle fracture. Comput Methods Appl Mech Engrg 2012;217–220:77–95.
[11] Geelen RJM, Liu Y, Hu T, Tupek MR, Dolbow JE. A phase-field formulation for dynamic cohesive fracture. Comput Methods Appl Mech Engrg 2019;348:680–711.
[12] Molnár G, Gravouil A, Seghir R, Réthoré J. An open-source abaqus implementation of the phase-field method to study the effect of plasticity on the instantaneous fracture toughness in dynamic crack propagation. Comput Methods Appl Mech Engrg 2020;365:113004.

[13] Alessi R, Freddi F. Failure and complex crack patterns in hybrid laminates: A phase-field approach. Composites B 2019;179:107256.
[14] Mandal TK, Nguyen VP, Wu J-Y. A length scale insensitive anisotropic phase field fracture model for hyperelastic composites. Int J Mech Sci 2020;188:105941.
[15] Quintanas-Corominas A, Turon A, Reinoso J, Casoni E, Paggi M, Mayugo JA. A phase field approach enhanced with a cohesive zone model for modeling delamination induced by matrix cracking. Comput Methods Appl Mech Engrg 2020;358:112618.
[16] Hirshikesh, Natarajan S, Annabattula RK, Martínez-Pañeda E. Phase field modelling of crack propagation in functionally graded materials. Composites B 2019;169:239–48.
[17] Kumar PKAV, Dean A, Reinoso J, Lenarda P, Paggi M. Phase field modeling of fracture in functionally graded materials: G -convergence and mechanical insight on the effect of grading. Thin-Walled Struct 2021;159:107234.
[18] Martínez-Pañeda E, Golahmar A, Niordson CF. A phase field formulation for hydrogen assisted cracking. Comput Methods Appl Mech Engrg 2018;342:742–61.
[19] Duda FP, Ciarbonetti A, Toro S, Huespe AE. A phase-field model for solute-assisted brittle fracture in elastic–plastic solids. Int J Plast 2018;102:16–40.
[20] Wu J-Y, Mandal TK, Nguyen VP. A phase-field regularized cohesive zone model for hydrogen assisted cracking. Comput Methods Appl Mech Engrg 2020;358:112614.
[21] Wu J-Y, Nguyen VP, Nguyen CT, Sutula D, Sinaie S, Bordas S. Phase-field modelling of fracture. Adv Appl Mech 2020;53:1–183.
[22] Kristensen PK, Niordson CF, Martínez-Pañeda E. An assessment of phase field fracture: crack initiation and growth. Phil Trans R Soc A 2021;379:20210021.
[23] Lo YS, Borden MJ, Ravi-Chandar K, Landis CM. A phase-field model for fatigue crack growth. J Mech Phys Solids 2019;132:103684.
[24] Boldrini JL, de Moraes EAB, Chiarelli LR, Fumes FG, Bittencourt ML. A non-isothermal thermodynamically consistent phase field framework for structural damage and fatigue. Comput Methods Appl Mech Engrg 2016;312:395–427.
[25] Loew PJ, Peters B, Beex LA. Fatigue phase-field damage modeling of rubber using viscous dissipation: Crack nucleation and propagation. Mech Mater 2020;142:103282.
[26] Schreiber C, Kuhn C, Müller R, Zohdi T. A phase field modeling approach of cyclic fatigue crack growth. Int J Fract 2020;225.
[27] Alessi R, Vidoli S, Lorenzis LD. A phenomenological approach to fatigue with a variational phase-field model: The one-dimensional case. Eng Fract Mech 2018;190:53–73.
[28] Carrara P, Ambati M, Alessi R, Lorenzis LD. A framework to model the fatigue behavior of brittle materials based on a variational phase-field approach. Comput Methods Appl Mech Engrg 2020;361:112731.
[29] Seiler M, Linse T, Hantschke P, Kästner M. An efficient phase-field model for fatigue fracture in ductile materials. Eng Fract Mech 2020;224.
[30] Simoes M, Martínez-Pañeda E. Phase field modelling of fracture and fatigue in shape memory alloys. Comput Methods Appl Mech Engrg 2021;373:113504.
[31] Simoes M, Braithwaite C, Makaya A, Martínez-Pañeda E. Modelling fatigue crack growth in shape memory alloys. Fatigue Fract Eng Mater Struct 2022;45:1243–57.
[32] Ai W, Wu B, Martínez-Pañeda E. A coupled phase field formulation for modelling fatigue cracking in lithium-ion battery electrode particles. J Power Sources 2022;544:231805.
[33] Hasan MM, Baxevanis T. A phase-field model for low-cycle fatigue of brittle materials. Int J Fatigue 2021;150:106297.
[34] Golahmar A, Kristensen PK, Niordson CF, Martínez-Pañeda E. A phase field model for hydrogen-assisted fatigue. Int J Fatigue 2022;154:106521.
[35] Seleš K, Aldakheel F, Tonković Z, Sorić J, Wriggers P. A general phase-field model for fatigue failure in brittle and ductile solids. Comput Mech 2021;67.
[36] Ulloa J, Wambacq J, Alessi R, Degrande G, François S. Phase-field modeling of fatigue coupled to cyclic plasticity in an energetic formulation. Comput Methods Appl Mech Engrg 2021;373:113473.
[37] Khalil Z, Elghazouli AY, Martínez-Pañeda E. A generalised phase field model for fatigue crack growth in elastic–plastic solids with an efficient monolithic solver. Comput Methods Appl Mech Engrg 2022;388:114286.
[38] Pham K, Amor H, Marigo JJ, Maurini C. Gradient damage models and their use to approximate brittle fracture. Int J Damage Mech 2011;20:618–52.
[39] Wu J-Y, Huang Y, Nguyen VP. On the bfgs monolithic algorithm for the unified phase field damage theory. Comput Methods Appl Mech Engrg 2020;360:112704.
[40] Kristensen PK, Martínez-Pañeda E. Phase field fracture modelling using quasi-newton methods and a new adaptive step scheme. Theor Appl Fract Mech 2020;107:102446.
[41] Provatas N, Elder K. Phase-field methods in materials science and engineering. John Wiley & Sons; 2011.
[42] Cui C, Ma R, Martínez-Pañeda E. A phase field formulation for dissolution-driven stress corrosion cracking. J Mech Phys Solids 2021;147:104254.
[43] Ambati M, Gerasimov T, Lorenzis LD. A review on phase-field models of brittle fracture and a new fast hybrid formulation. Comput Mech 2015;55:383–405.
[44] Miehe C, Welshinger F, Hofacker M. Thermodynamically consistent phase-field models of fracture: Variational principles and multi-field fe implementations. Internat J Numer Methods Engrg 2010;83:1273–311.
[45] Freddi F, Royer-Carfagni G. Regularized variational theories of fracture: A unified approach. J Mech Phys Solids 2010;58:1154–74.
[46] Amor H, Marigo JJ, Maurini C. Regularized formulation of the variational brittle fracture with unilateral contact: Numerical experiments. J Mech Phys Solids 2009;57:1209–29.
[47] Miehe C, Hofacker M, Welschinger F. A phase field model for rate-independent crack propagation: Robust algorithmic implementation based on operator splits. Comput Methods Appl Mech Engrg 2010;199:2765–78.
[48] Tanné E, Li T, Bourdin B, Marigo JJ, Maurini C. Crack nucleation in variational phase-field models of brittle fracture. J Mech Phys Solids 2018;110:80–99.
[49] Walker K. The effect of stress ratio during crack propagation and fatigue for 2024-t3 and 7075-t6 aluminum, effects of environment and complex load history on fatigue life. In: ASTM STP, vol. 462. 1970.
[50] Smith KN, Watson P, Topper TH. Stress- strain function for the fatigue of metals. J Mater, ASTM 1970;5:767–78.
[51] MIL-HDBK-5H. Military handbook: Metallic materials and elements for aerospace vehicle structures. U.S. Department of Defense; 1998.
[52] Dowling NE, Calhoun CA, Arcari A. Mean stress effects in stress-life fatigue and the walker equation. Fatigue Fract Eng Mater Struct 2009;32:163–79.
[53] McClung RC. Crack closure and plastic zone sizes in fatigue. Fatigue Fract Eng Mater Struct 1991;14(4):455–68.

[P2]

P. K. Kristensen, A. Golahmar, E. Martínez-Pañeda, and C. F. Niordson. Accelerated high-cycle phase field fatigue predictions. European Journal of Mechanics / A Solids 100 (2023), p. 104991.

European Journal of Mechanics / A Solids 100 (2023) 104991

Contents lists available at ScienceDirect

European Journal of Mechanics / A Solids

journal homepage: www.elsevier.com/locate/ejmsol

Accelerated high-cycle phase field fatigue predictions

Philip K. Kristensen [a], Alireza Golahmar [a,b], Emilio Martínez-Pañeda [b], Christian F. Niordson [a,*]

[a] Department of Civil and Mechanical Engineering, Technical University of Denmark, DK-2800 Kgs. Lyngby, Denmark
[b] Department of Civil and Environmental Engineering, Imperial College London, London SW7 2AZ, UK

ARTICLE INFO

Keywords:
Fatigue
Phase field fracture
Fracture mechanics
Finite element analysis

ABSTRACT

Phase field fracture models have seen widespread application in the last decade. Among these applications, its use to model the evolution of fatigue cracks has attracted particular interest, as fatigue damage behaviour can be predicted for arbitrary loading histories, dimensions and complexity of the cracking phenomena at play. However, while cycle-by-cycle calculations are remarkably flexible, they are also computationally expensive, hindering the applicability of phase field fatigue models for technologically-relevant problems. In this work, a computational framework for accelerating phase field fatigue calculations is presented. Two novel acceleration strategies are proposed, which can be used in tandem and together with other existing acceleration schemes from the literature. The computational performance of the proposed methods is documented through a series of 2D and 3D boundary value problems, highlighting the robustness and efficiency of the framework even in complex fatigue problems. The observed reduction in computation time using both of the proposed methods in tandem is shown to reach a speed-up factor of 32, with a scaling trend enabling even greater reductions in problems with more load cycles.

1. Introduction

The phase field fracture model has received substantial attention in the last decade — and for good reason. The original model, proposed by Bourdin et al. (2000) as a regularization of the variational fracture formulation by Francfort and Marigo (1998), is flexible and simple to implement numerically. It can readily capture complex cracking phenomena such as crack branching (Borden et al., 2012), coalescence (Kristensen et al., 2020b), complex crack trajectories (Hirshikesh et al., 2019) and crack nucleation from non-sharp defects (Tanné et al., 2018). Moreover, it can naturally capture the crack size effect (Tanné et al., 2018; Kristensen et al., 2021) and be readily extended to accommodate specific failure surfaces (Navidtehrani et al., 2022; Lorenzis and Maurini, 2022). The model has proven to be extremely versatile and thus has been used in a vast number of applications, both within complex fracture problems such as cohesive fracture (Wu, 2017; Feng and Li, 2022), micromechanical damage (Guillén-Hernández et al., 2020; Tan and Martínez-Pañeda, 2021), and ductile fracture (Aldakheel et al., 2018; Alessi et al., 2018), but also in multi-physics applications ranging from thermal shocks (Bourdin et al., 2014) and moisture effects (Ye and Zhang, 2022) to hydrogen embrittlement (Martínez-Pañeda et al., 2018; Duda et al., 2018; Anand et al., 2019; Kristensen et al., 2020a) and Lithium-ion battery degradation (Klinsmann et al., 2016; Boyce et al., 2022; Ai et al., 2022).

Among the many problems attracting phase field developments, fatigue is arguably one of the most important ones, from both scientific and technological perspectives. Using phase field as a framework for fatigue models is an attractive prospect (Alessi and Ulloa, 2023), as fatigue remains a longstanding challenge in solid mechanics and a sufficiently flexible phase field fatigue model could readily encompass the aforementioned phase field models and applications. An example of such a flexible framework is found in the work by Carrara et al. (2020), where a history variable is introduced to introduce a dependence of the fracture energy on the loading history of the material. The model naturally recovers the Paris Law and S–N curve behaviour and has proven an attractive platform from which to develop phase field fatigue models for various applications (Loew et al., 2020; Golahmar et al., 2022; Simoes and Martínez-Pañeda, 2021; Simoes et al., 2022). Aside from Carrara et al. (2020), there have been several other notable works, both of a cycle-by-cycle nature (Seiler et al., 2020; Mesgarnejad et al., 2019; Song et al., 2022) and more practical approaches, which take the Paris behaviour as an input (Lo et al., 2019).

Two known drawbacks associated with phase field fracture are the computational cost associated with the need for a sufficiently fine mesh to resolve the phase field length scale (Kristensen et al., 2021), and the inefficiency of the solution due to the non-convexity of the balance equations (Gerasimov and De Lorenzis, 2016). Significant efforts have been extended towards remedying both issues.

* Corresponding author.
E-mail address: cfni@dtu.dk (C.F. Niordson).

https://doi.org/10.1016/j.euromechsol.2023.104991
Received 18 January 2023; Received in revised form 1 April 2023; Accepted 2 April 2023
Available online 4 April 2023

Strategies to ease meshing requirements include adaptive mesh refinement (Heister et al., 2015; Klinsmann et al., 2015; Freddi and Mingazzi, 2022, 2023), specialized element formulations (Olesch et al., 2021) and the use of a combined finite element-finite volume approach (Sargado et al., 2021). Similarly, a wealth of improvements have also been proposed for the solution strategy, including (residual) control algorithms (Ambati et al., 2016; Seleš et al., 2019), quasi-Newton methods (Kristensen and Martínez-Pañeda, 2020; Wu et al., 2020), line search algorithms (Gerasimov and De Lorenzis, 2016; Lampron et al., 2021; Börjesson et al., 2022), and multigrid approaches (Jodlbauer et al., 2020). The computational costs of phase field fracture become particularly demanding when performing cycle-by-cycle computations of fatigue, hindering high cycle fatigue analyses. A common strategy to minimize the costs of computing high cycle fatigue is the use of so-called *cycle jumping*, where the cycle-by-cycle solution is extrapolated to skip the computation of several load cycles (Cojocaru and Karlsson, 2006). Loew et al. (2020) introduced such a scheme for phase field fatigue by locally extrapolating the fatigue history variable.

This paper seeks to introduce alternative means of accelerating cycle-by-cycle phase field fatigue computations. Two methods are proposed which are mutually compatible and individually provide substantial computational performance improvements. Furthermore, neither methods prevent the use of existing cycle jump strategies, which can be included for additional performance improvements. The first computational acceleration method proposed is a modification to existing staggered solution strategies commonly adopted in the phase field literature (Miehe et al., 2010a; Ambati et al., 2014; Seleš et al., 2019), so that the tangent stiffness matrices are not updated in each load step, but rather stored in factorized form such that subsequent increments and iterations are solved with a significant reduced computational cost. This approach, henceforth referred to as *Modified Newton (MN)*, is especially suitable for high-cycle fatigue, where very small changes to the overall system are observed between individual load increments. The second method proposed, referred to as *Constant Load Accumulation (CLA)*, is suitable for problems where only one step of the loading cycle contributes significantly to the fatigue accumulation. For systems where this assumption is valid, the fatigue accumulation rule can be adjusted to permit the simplification of the loading curve to a single load increment per cycle, significantly reducing the total number of increments in the simulation. As shall be shown, for high-cycle problems this approach can be extended to capture multiple load cycles in a single increment with negligible loss of accuracy for even greater computational performance improvement.

The manuscript is organized as follows. Section 2 formulates the phase field fatigue framework used for the cycle-by-cycle computations. The details of the numerical aspects of the finite element solution and the proposed methods are given in Section 3. Subsequently, a series of numerical examples are analyzed in Section 4 to illustrate the capabilities of the proposed method. Concluding remarks end the paper in Section 5.

2. A phase field model for fatigue

This section introduces the specific phase field fatigue model adopted, which is based on the work by Carrara et al. (2020). This choice is grounded on its flexibility, simplicity of implementation and suitability to be used in conjunction with other acceleration schemes (such as those by Loew et al. (2020)). Furthermore, the fatigue acceleration strategies presented here can be readily incorporated into a wide range of phase field fatigue models and, as such, the specific choice phase field model is of secondary importance.

2.1. Basic theory

Consider a solid domain $\Omega \in \mathbb{R}^n$ with boundary $\partial\Omega \in \mathbb{R}^{n-1}$. In a small deformations context, we consider a displacement field $\mathbf{u} \in \mathbb{R}$ and a phase field $\phi \in [0;1]$, for which a value of 0 denotes intact material and a value of 1 denotes broken material with vanishing stiffness. Then, the standard so-called AT2 phase field fracture model (Bourdin et al., 2000) can be formulated from the minimization of the following energy functional:

$$\mathcal{E}(\boldsymbol{\varepsilon}(\mathbf{u}),\phi,\nabla\phi) = \int_\Omega \left[\psi(\boldsymbol{\varepsilon}(\mathbf{u}),\phi) + \frac{G_c}{2}\left(\frac{\phi^2}{\ell} + \ell\nabla\phi\cdot\nabla\phi\right)\right] \mathrm{d}V \tag{1}$$

where G_c is the critical energy release rate or material toughness, ℓ denotes the phase field length scale, and $\psi(\boldsymbol{\varepsilon}(\mathbf{u}),\phi)$ is the strain energy density, which for a linear elastic solid may be expressed as;

$$\psi(\boldsymbol{\varepsilon}(\mathbf{u}),\phi) = (1-\phi)^2\psi_0(\mathbf{u}) = (1-\phi)^2\frac{1}{2}\boldsymbol{\varepsilon}:\mathbf{C}_0:\boldsymbol{\varepsilon}. \tag{2}$$

Here, $\mathbf{C}_0$ is the linear elastic stiffness tensor of the material and $\boldsymbol{\varepsilon}$ is the infinitesimal strain tensor, given by $\boldsymbol{\varepsilon} = (\nabla\mathbf{u} + \nabla\mathbf{u}^T)/2$. The phase field variable, ϕ, is seen to degrade the material stiffness.

2.2. Extension to fatigue

To extend the above fracture framework to account for fatigue damage, Carrara and co-workers (Carrara et al., 2020) proposed introducing a degradation function $f(\bar{\alpha})$, which reduces the material toughness, as a function of an accumulated fatigue history variable $\bar{\alpha}$. Several options are available for both the formulation of the degradation function and the accumulated fatigue history variable. Here, as in Seleš et al. (2021), the accumulated fatigue history variable at time step $n+1$ is introduced as the cumulative positive increments of undegraded elastic strain energy density:

$$\bar{\alpha}_{n+1} = \bar{\alpha}_n + |\psi_{0,n+1} - \psi_{0,n}|H(\psi_{0,n+1} - \psi_{0,n}), \tag{3}$$

where H is the Heaviside function. Also following Carrara et al. (2020), we use the asymptotic fatigue degradation function:

$$f(\bar{\alpha}) = \begin{cases} 0 & \text{if } \bar{\alpha} \le \alpha_T \\ \left(\dfrac{2\alpha_T}{\bar{\alpha}+\alpha_T}\right)^2 & \text{else .} \end{cases} \tag{4}$$

where the threshold parameter α_T introduces a lower limit below which accumulated fatigue does not influence the material toughness. This threshold is here chosen as $\alpha_T = G_c/12\ell$.

2.3. Principle of virtual power

Let us first define the Cauchy stress tensor $\boldsymbol{\sigma}$ in terms of the strain energy density ψ,

$$\boldsymbol{\sigma} = \frac{\partial\psi}{\partial\boldsymbol{\varepsilon}} = (1-\phi)^2\boldsymbol{\sigma}_0 = (1-\phi)^2\mathbf{C}_0:\boldsymbol{\varepsilon}. \tag{5}$$

Then, the internal energy of the system can be expressed as

$$\mathcal{W} = \int_\Omega (1-\phi)^2\boldsymbol{\sigma}_0:\boldsymbol{\varepsilon}\,\mathrm{d}V + \int_\Omega\int_0^t f(\bar{\alpha}(\tau))\frac{G_c}{\ell}\left(\phi\dot{\phi} + \ell^2\nabla\phi\cdot\nabla\dot{\phi}\right)\mathrm{d}\tau\,\mathrm{d}V. \tag{6}$$

Alternatively, the above may be expressed in terms of internal power density as

$$\dot{\mathcal{W}} = \int_\Omega \left[(1-\phi)^2\boldsymbol{\sigma}_0:\dot{\boldsymbol{\varepsilon}} + \frac{\partial\psi}{\partial\phi}\dot{\phi} + f(\bar{\alpha}(t))\frac{G_c}{\ell}\left(\phi\dot{\phi} + \ell^2\nabla\phi\cdot\nabla\dot{\phi}\right)\right]\mathrm{d}V. \tag{7}$$

The external power depends only on the external mechanical loading

$$\dot{\mathcal{F}} = \int_\Omega \mathbf{b}\cdot\dot{\mathbf{u}}\,\mathrm{d}V + \int_{\partial\Omega_t}\mathbf{t}\cdot\dot{\mathbf{u}}\,\mathrm{d}S, \tag{8}$$

where $\partial\Omega_t$ denotes the part of the boundary where mechanical tractions $\mathbf{t}$ are applied and $\mathbf{b}$ are the body forces. Here, the external contributions due to the phase field variable and its work-conjugate are omitted, as

only problems with homogeneous phase field boundary conditions are considered. The balance of virtual power requires

$$\dot{\mathcal{W}} - \dot{\mathcal{F}} = 0, \tag{9}$$

which, after applying integration by parts, may be expressed as:

$$\begin{aligned}&\int_\Omega -\left[(1-\phi)^2\nabla\cdot\boldsymbol{\sigma}_0 + \mathbf{b}\right]\cdot\dot{\mathbf{u}}\,\mathrm{d}V + \int_\Omega \left\{\frac{\partial\psi}{\partial\phi} - \frac{G_c}{\ell}\left[f(\bar{\alpha})\left(\ell^2\nabla^2\phi - \phi\right)\right.\right.\\ &\left.\left. + \ \ell^2\nabla f(\bar{\alpha})\cdot\nabla\phi\right]\right\}\dot{\phi}\,\mathrm{d}V + G_c\ell\int_{\partial\Omega} f(\bar{\alpha})\nabla\phi\cdot\mathbf{n}\dot{\phi}\,\mathrm{d}S\\ &+ \int_{\partial\Omega_t}\left[(1-\phi)^2\boldsymbol{\sigma}\cdot\mathbf{n} - \mathbf{t}\right]\cdot\dot{\mathbf{u}}\,\mathrm{d}S = 0\end{aligned} \tag{10}$$

The above must hold for arbitrary, kinematically admissible, variations of the velocities $\dot{\mathbf{u}}$ and phase field increments $\dot{\phi}$, which by standard arguments implies the following local balance equations and accompanying boundary conditions:

$$\nabla\cdot\left[(1-\phi)^2\boldsymbol{\sigma}_0\right] + \mathbf{b} = 0 \quad \text{in } \Omega \tag{11}$$

$$-2(1-\phi)\psi_0 + f(\bar{\alpha})\frac{G_c}{\ell}\left(\phi - \ell^2\nabla^2\phi\right) - G_c\ell\nabla f(\bar{\alpha})\cdot\nabla\phi = 0 \quad \text{in } \Omega \tag{12}$$

$$(1-\phi)^2\boldsymbol{\sigma}_0\cdot\mathbf{n} = \mathbf{t} \quad \text{on } \partial\Omega \tag{13}$$

$$\nabla\phi\cdot\mathbf{n} = 0 \quad \text{on } \partial\Omega \tag{14}$$

2.4. Strain energy split to adequately handle compression behaviour

In its original formulation, the phase field fracture model predicts a symmetric behaviour under tension and compression. That is, crack growth is equally driven by compressive and tensile stresses and, since the degradation of the material stiffness is similarly isotropic, the crack faces are allowed to interpenetrate and while carrying no compressive loads. A common strategy to mitigate this is to decompose the strain energy density into active and passive parts such that:

$$\psi = (1-\phi)^2\psi_0^+(\mathbf{u}) + \psi_0^-(\mathbf{u}) \tag{15}$$

where only the active part of the strain energy density (ψ_0^+) contributes to crack growth and only the active part of the stiffness is degraded by the phase field variable. Several suggestions have been made for defining the active and passive parts of the strain energy density, with the two most popular being the volumetric/deviatoric split by Amor et al. (2009) and the spectral split by Miehe et al. (2010b). The volumetric/deviatoric split is given by

$$\begin{aligned}\psi_0^+ &= \frac{1}{2}K\langle\mathrm{tr}\boldsymbol{\varepsilon}\rangle_+^2 + \mu(\boldsymbol{\varepsilon}_{dev}:\boldsymbol{\varepsilon}_{dev})\\ \psi_0^- &= \frac{1}{2}K\langle\mathrm{tr}\boldsymbol{\varepsilon}\rangle_-^2,\end{aligned} \tag{16}$$

where $\langle\ \rangle_\pm$ denotes the two signed Macaulay brackets, $\boldsymbol{\varepsilon}_{dev}$ is the deviatoric part of the strain tensor, K is the bulk modulus and μ is the shear modulus or second Lamé parameter. On the other side, the spectral split is based on a spectral decomposition of the strain tensor: $\boldsymbol{\varepsilon}_\pm = \sum_{a=1}^3\langle\varepsilon_I\rangle_\pm\mathbf{n}_I\otimes\mathbf{n}_I$, where ε_I are the principal strains and $\mathbf{n}_I$ denote the principal strain directions (with $I = 1,2,3$). The, the spectral strain energy decomposition is defined as

$$\psi_0^\pm = \frac{1}{2}\lambda\langle\mathrm{tr}\boldsymbol{\varepsilon}\rangle_\pm^2 + \mu\mathrm{tr}\left(\boldsymbol{\varepsilon}_\pm^2\right), \tag{17}$$

with λ denoting the first Lamé parameter and tr being the trace operator.

A significant improvement to the numerical performance of these splits was introduced with the so-called hybrid scheme by Ambati and co-workers (Ambati et al., 2014), where only the active part of the strain energy contributes to crack growth, but the stiffness is isotropically degraded by damage, with the caveat that degradation only applies if the stress state is predominantly tensile. An alternative strain energy decomposition, which has been shown to be particularly effective for fatigue modelling (Golahmar et al., 2023), is the so-called no-tension split by Freddi and Royer-Carfagni (2010). The no-tension split, first intended for masonry-like materials, filters out contributions from compressive strains more effectively than other approaches. Using λ and μ to denote the Lamé parameters, E and ν respectively being Young's modulus and Poisson's ratio, and taking $\varepsilon_1, \varepsilon_2, \varepsilon_3$ as the principal strains, with ε_1 being the largest, the strain energy decomposition is given as (Lo et al., 2019) Eq. (18) in Box I.

Unless otherwise stated, this no-tension split by Freddi and Royer-Carfagni (2010) is the one adopted in the numerical experiments reported in this manuscript.

3. Finite element implementation

This section provides details of the numerical implementation of the phase field fatigue model presented in Section 2. The finite element method is used and the solution of the resulting system of equations is discussed, together with the fatigue acceleration methods presented in this work: the Modified Newton (MN) and the Constant Load Accumulation (CLA) solution strategies. The implementation is carried out using the Ferrite.jl finite element library (Carlsson et al., 2021).[1]

3.1. Crack irreversibility

Enforcing damage irreversibility is of critical importance when considering non-monotonic loading. For simplicity, we shall here make use of the so-called history field $\mathcal{H}$ approach pioneered by Miehe et al. (2010a). Accordingly, the history field is defined as the maximum active strain energy density experienced in a point during the loading history

$$\mathcal{H} = \max_{\tau\in[0,t]}\psi_0^+(\tau) \tag{19}$$

and it replaces the active undegraded strain energy density ψ_0^+ as the crack driving force in the phase field equation (12). While this approach is convenient and tends to ease the convergence of the phase field equations, it has also been the target of sensible objections (Linse et al., 2017; Strobl and Seelig, 2020), especially regarding its influence on crack nucleation from non-sharp defects and its non-variational nature. The latter issue is of little relevance here, as the fatigue extension of phase field is not variationally consistent in the form adopted here. A more critical aspect in the case of fatigue is that for variable amplitude loading, only the locally maximal loads will be retained as a crack driving force throughout cycles that also include lower loads. However, this scenario is not relevant to this work, as the numerical examples deal with constant amplitude loading and pre-existing sharp defects.

Another method of enforcing irreversibility of fully formed cracks is the so-called crack-set method by Bourdin et al. (2000), where nodes in which the phase field exceeds a given threshold are added to a set of nodes subject to a $\phi = 1$ Dirichlet condition. Anecdotally, we find that this method seems to ease some convergence issues which have been observed to occur at the original crack tip after some degree of crack growth in high-cycle fatigue simulations, regardless of whether the degraded or undegraded strain energy is used to obtain the fatigue variable. As a result, this work uses both the history variable approach and the crack set method in tandem, with the threshold value for nodes to be added to the crack set chosen as 0.95.

3.2. Solution strategy

The governing Eqs. (11)–(14) can be reformulated in a numerically convenient decoupled form as

$$\begin{aligned}&\int_\Omega\left[(1-\phi)^2\boldsymbol{\sigma}_0:\delta\boldsymbol{\varepsilon} - \mathbf{b}\cdot\delta\mathbf{u}\right]\mathrm{d}V + \int_{\partial\Omega_t}\mathbf{t}\cdot\delta\mathbf{u}\,\mathrm{d}A = 0\\ &\int_\Omega\left[-2(1-\phi)\psi_0^+\delta\phi + f(\bar{\alpha})G_c\left(\frac{\phi}{\ell}\delta\phi + \ell\nabla\phi\cdot\nabla\delta\phi\right)\right]\mathrm{d}V = 0\end{aligned} \tag{20}$$

[1] The Julia implementation developed is openly shared with the community and made available to download at www.empaneda.com/codes.

$$
\begin{array}{llll}
\text{if} & \varepsilon_3 > 0 & \text{then} & \left\{ \begin{array}{l} \psi_0^+ = \frac{\lambda}{2}\left(\varepsilon_1+\varepsilon_2+\varepsilon_3\right)^2 + \mu\left(\varepsilon_1^2+\varepsilon_2^2+\varepsilon_3^2\right) \\ \psi_0^- = 0 \end{array} \right. \\
\text{elseif} & \varepsilon_2 + \nu\varepsilon_3 > 0 & \text{then} & \left\{ \begin{array}{l} \psi_0^+ = \frac{\lambda}{2}\left(\varepsilon_1+\varepsilon_2+2\nu\varepsilon_3\right)^2 + \mu\left[\left(\varepsilon_1+\nu\varepsilon_3\right)^2+\left(\varepsilon_2+\nu\varepsilon_3\right)^2\right] \\ \psi_0^- = \frac{E}{2}\varepsilon_3^2 \end{array} \right. \\
\text{elseif} & (1-\nu)\varepsilon_1 + \nu(\varepsilon_2+\varepsilon_3) > 0 & \text{then} & \left\{ \begin{array}{l} \psi_0^+ = \frac{\lambda}{2}\left[(1-\nu)\varepsilon_1+\nu\varepsilon_2+\nu\varepsilon_3\right]^2 \\ \psi_0^- = \frac{E}{2(1-\nu^2)}\left(\varepsilon_2^2+\varepsilon_3^2+2\nu\varepsilon_2\varepsilon_3\right) \end{array} \right. \\
 & & \text{else} & \left\{ \begin{array}{l} \psi_0^+ = 0 \\ \psi_0^- = \frac{\lambda}{2}\left(\varepsilon_1+\varepsilon_2+\varepsilon_3\right)^2 + \mu\left(\varepsilon_1^2+\varepsilon_2^2+\varepsilon_3^2\right) \end{array} \right.
\end{array}
\tag{18}
$$

Box I.

The weak form Eqs. (20) are then discretized using standard bilinear elements to form the system of equations:

$$
\begin{bmatrix} \mathbf{K}^{\mathbf{uu}} & \mathbf{K}^{\mathbf{u}\phi} \\ \mathbf{K}^{\phi\mathbf{u}} & \mathbf{K}^{\phi\phi} \end{bmatrix} \begin{Bmatrix} \mathbf{u} \\ \boldsymbol{\phi} \end{Bmatrix} = \begin{Bmatrix} \mathbf{r}^{\mathbf{u}} \\ \mathbf{r}^{\phi} \end{Bmatrix} \tag{21}
$$

where $\mathbf{K}$ and $\mathbf{r}$ are stiffness matrices and residuals vectors, respectively. The phase field equations are non-convex with respect to the variables $\mathbf{u}$ and ϕ simultaneously. As a result, the full coupled system is notoriously difficult to solve in a stable and efficient manner (unless unconventional schemes, such as quasi-Newton methods, are used (Kristensen and Martínez-Pañeda, 2020; Wu et al., 2020)). However, the equations are convex with respect to the primary variables individually. Therefore, a common strategy is to solve the system in a decoupled fashion, using alternate minimization. In the following, common staggered schemes are briefly introduced, followed by the proposed modified Newton approach for accelerated fatigue computations.

3.2.1. Standard alternate minimization techniques

Solving the phase field equations by a sequence of alternate minimization of the two decoupled subproblems was popularized by Miehe et al. (2010a). The scheme which was then proposed involves solving each of the subproblems independently until individual convergence is achieved before moving on to the next load increment. This is now commonly referred to as a single-pass scheme and introduces significant sensitivity to the size of the load increments. As was shown by Kristensen and Martínez-Pañeda (2020), this approach may be highly inefficient for fatigue computations. Alternatively, one can use so-called multi-pass schemes where the alternate minimization is repeated until some global convergence criterion is reached. Examples of such convergence criteria can be found in Refs. Ambati et al. (2014) and Seleš et al. (2019). Here, we adopt the same residual-based multi-pass approach as found in Lampron et al. (2021), also adopting the tolerances $\texttt{TOL}_{\texttt{in}} = 10^{-5}$ and $\texttt{TOL}_{\texttt{out}} = 10^{-4}$. The scheme is provided in Algorithm 1 and only differs from the single-pass algorithm by the presence of the `while` loop.

Algorithm 1 Multi-pass alternate minimization

Increment $n+1$
Initialize: $\phi_0 = \phi_n$, $\mathbf{u}_0 = \mathbf{u}_n$, $k = 0$
while $||R_\phi(\mathbf{u}_{k+1}, \phi_{k+1})||_\infty \leq \texttt{TOL}_{\texttt{out}}$ **do**
  Find ϕ_{k+1} such that $||R_\phi\left(\mathbf{u}_k, \phi_{k+1}\right)||_\infty \leq \texttt{TOL}_{\texttt{in}}$
  Find $\mathbf{u}_{k+1}$ such that $||R_{\mathbf{u}}\left(\mathbf{u}_{k+1}, \phi_{k+1}\right)||_\infty \leq \texttt{TOL}_{\texttt{in}}$
  $k \leftarrow 1$
end while
$\phi_{n+1} = \phi_k$, $\mathbf{u}_{n+1} = \mathbf{u}_k$

3.2.2. Modified Newton approach for accelerated fatigue computations

In order to accelerate high cycle fatigue computations, a simple modified Newton approach is introduced. In high cycle fatigue computations, it is generally reasonable to expect that changes to the solution variables will be small between individual load increments. Consequently, changes to the tangent stiffness matrices of the system are also expected to be small. As Newton–Raphson based methods do not require the tangent stiffness matrix to be exact, we here propose to modify the multi-pass staggered algorithm given in Algorithm 1, such that the tangent stiffness is only updated and factorized on an as-needed basis. In this implementation, the tangent stiffness matrices for the two subproblems are updated and factorized if any of the following conditions are met:

- Start of analysis
- One of the subproblems fails to converge in n_i inner Newton iterations.
- A number of load increments n_c have passed without updating the stiffness matrices.

The parameters n_i and n_c may be chosen differently. While we have not attempted a systematic study of optimal values, which will depend on the size of the boundary value problem and the total number of cycles to failure, the results obtained (see Section 4) suggest that choosing n_c to have a higher magnitude in the damage sub-problem will likely result in an improved performance.

3.3. Accelerating calculations by accumulating fatigue damage under a constant load

Another technique for accelerating cycle-by-cycle fatigue computations can be achieved by changing the way in which fatigue is accumulated. Here, henceforth referred to as the Constant Load Accumulation (CLA) acceleration strategy. In the current fatigue model, fatigue is accumulated by positive increments of active strain energy. The load ratio R is here loosely defined in term of applied displacement $\bar{u}$ as

$$
R = \frac{\bar{u}_{min}}{\bar{u}_{max}}. \tag{22}
$$

In the case where $R \geq 0$, the load cycle can be resolved using only two load increments per cycle (loading and unloading). However, only one of these increments actually contributes to fatigue. In the case where $R < 0$, four increments per cycle are required (tensile loading, unloading, compressive loading and unloading). If the compressive loading stage does not contribute significantly to fatigue, only the tensile loading increment is relevant, as illustrated by the dashed blue

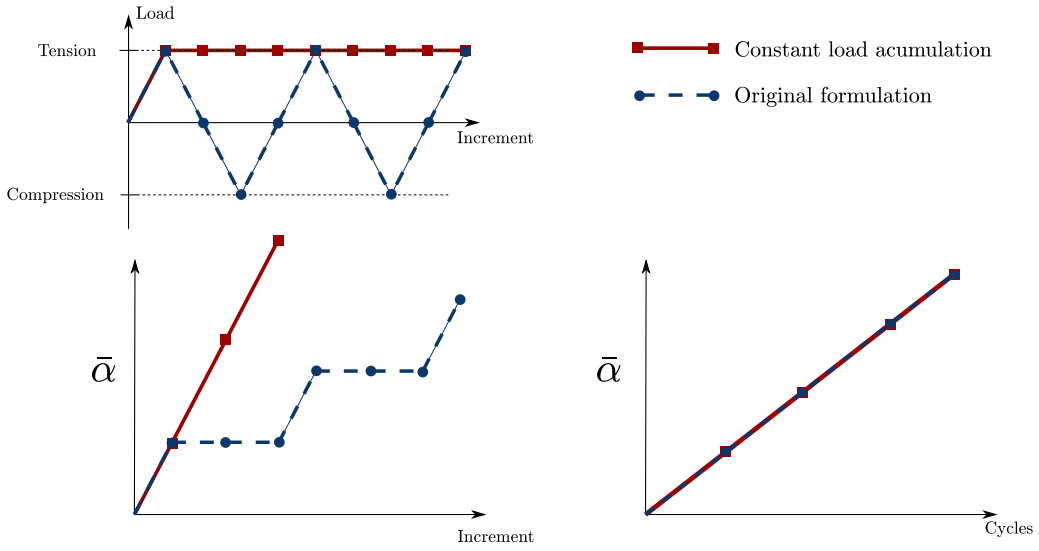

Fig. 1. Illustration of loading pattern and fatigue accumulation for the original formulation on the left and the proposed constant load accumulation scheme of the right. As illustrated, the former requires at least four increments per load cycle, while the latter requires only one.

curves in Fig. 1. Note that these considerations are only intended for high-cycle fatigue where material response is usually well within the linear regime and no effects such as compressive plasticity would be expected to occur to a significant degree. It should also be noted that there are loading conditions where multiple points in the load cycle can be relevant, such as non-proportional loading.

For problems which are sufficiently simple such that only one increment of the load cycle is significant, considerable acceleration of the computation can be achieved by changing the fatigue accumulation from Eq. (3) to

$$\bar{\alpha}_{n+1} = \bar{\alpha}_n + \psi^+_{0,n+1}, \tag{23}$$

and combining this with the application of a constant load $\bar{u} = \bar{u}_{max}$ and the counting of one cycle per increment. The approach is illustrated by solid red lines in Fig. 1. We note for completeness that formally, to account for cases where $R > 0$, the formulation should be amended to

$$\bar{\alpha}_{n+1} = \bar{\alpha}_n + \psi^+_{0,n+1}\left[1 - R^2 H(R)\right], \tag{24}$$

although such cases will not be considered here.

4. Numerical experiments

We shall now present the results of our numerical experiments, aiming at benchmarking the performance of the two novel acceleration strategies proposed here: the Modified Newton (MN) method presented in Section 3.2.2 and the constant load accumulation (CLA) scheme described in Section 3.3. For all the case studies considered, the material parameters are chosen as Young's modulus $E = 210$ GPa, Poisson's ratio $\nu = 0.3$, and toughness $G_c = 2.7\,\mathrm{kJ/m^2}$. First, the growth of fatigue cracks in a Single Edge Notched Tension (SENT) specimen (Section 4.1) is investigated to compare acceleration schemes and quantify gains relative to the reference solution system. Then, more complex cracking patterns are simulated by addressing the nucleation and growth of cracks in an asymmetric three point bending sample containing multiple holes (Section 4.2). Here, one of the objectives is to compare the crack trajectories obtained with different strain energy decomposition approaches. Finally, in Section 4.3, the robustness of the model and its ability to simulate fatigue cracking in large scale 3D problems is demonstrated.

4.1. Fatigue crack growth on a Single Edge Notched Tension (SENT) specimen

The geometry and boundary conditions of the Single Edge Notched Tension (SENT) sample considered in the first case study are shown in Fig. 2(a). The no-tension strain energy density decomposition given in Eq. (18) is used and the initial crack is initialized as a Dirichlet condition on the phase field. The Dirichlet boundary condition is applied on two rows of elements so as to define a constant width for the initial crack.

The specimen is discretized using approximately 32,000 bilinear quadrilateral elements with a refined zone in the crack growth region. In this refined zone, the characteristic element length equals 0.003 mm, more than five times smaller than the phase field length scale, chosen here as $\ell = 0.016$ mm. The specimen is subjected to an alternating applied displacement $\bar{u}$. The fatigue loading is repeated for 120.000 cycles with a maximum applied displacement $\bar{u}_{max} = 0.0002$ mm. Calculations are obtained for four scenarios. First, results are obtained for the standard fatigue accumulation given in Eq. (3) and the multipass staggered algorithm from Algorithm 1. These are considered to be the baseline conditions, not including any of the acceleration strategies proposed in this work. A second scenario constitutes the case where fatigue crack growth is simulated using the Modified Newton (MN) scheme presented in Section 3.2.2. Conversely, the third scenario employs only the Constant Load Acceleration (CLA) scheme described in Section 3.3. Finally, a fourth scenario is considered where both MN and CLA approaches are used in tandem. The MN parameters are chosen as $n_i = 25$ and $n_c = 100$ and the load ratio is always considered to be equal to $R = 0$. All computations are performed with a single core of a CPU of the model Xeon E5-2650 v4.

The finite element predictions of crack extension versus number of cycles are given in Fig. 3. Here, crack extension is measured as the distance between the original crack tip and the furthest point with $\phi = 0.95$. The results reveal that the acceleration schemes do not inherently introduce any deviation in crack extension when compared to the baseline. This is always the case for the modified Newton Method, and holds true for the CLA scheme when there is no compressive contribution to fatigue.

As shown in Table 1, the computational performance of the different modelling strategies is measured by a number of factors. The first measure of performance is the actual computation time (in hours). However, one should note that although noise in this indicator has been

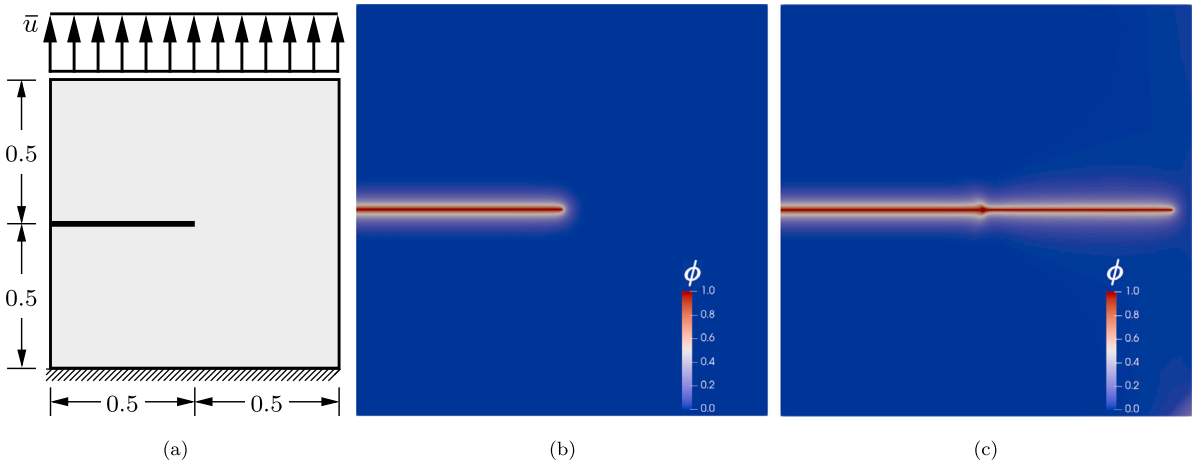

Fig. 2. Fatigue crack growth in a Single Edge Notched Tension (SENT): (a) geometry (with dimensions in mm) and boundary conditions, (b) initial crack contour, and (c) final stage of the fatigue crack propagation.

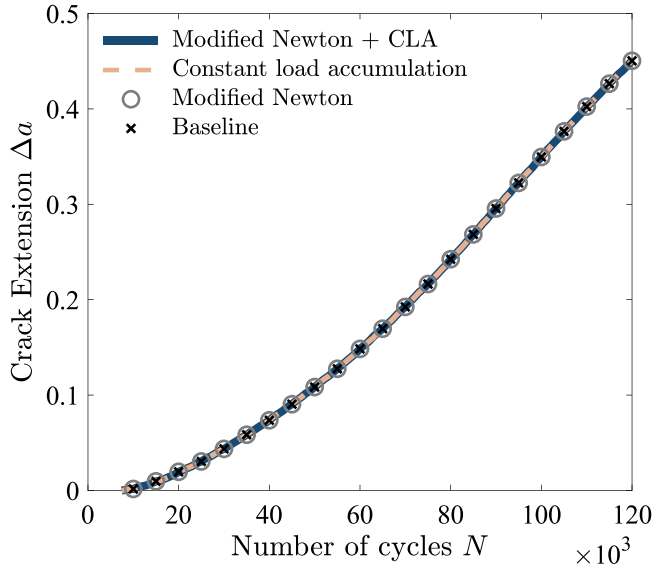

Fig. 3. Predictions of crack extension Δa versus number of cycles N for the SENT case study. The figure shows results obtained with the reference (baseline) conditions, and the two acceleration scheme presented here (Modified Newton, NM; Constant load accumulation, CLA), independently and in tandem.

minimized by the absence of parallel computing and the use of identical CPU types, individual measures of computation time should not be taken as an exact quantification of performance. A more objective measure is the second performance indicator considered, the total number of matrix factorizations, where one factorization here denotes a factorization of both the displacement and the damage subproblems. In addition, Table 1 also provides with the total number of iterations used on the phase field and displacement subproblems. The results reveal that while the use of a constant load accumulation acceleration strategy significantly reduces the computation time by reducing the necessary number of load increments, bringing a similar reduction in iterations and factorizations, the use of the Modified Newton approach presents a trade-off between a reduction in matrix factorizations and an increase in necessary iterations, especially on the displacement problem. However, with the choice of parameters for the modified Newton approach of $n_i = 25$ and $n_c = 100$, this strategy requires roughly 100 times less matrix factorizations than the baseline result in exchange for only 4 times more iterations on the displacement problem. Also, we emphasize

Table 1
Performance details for the SENT case study, comparing baseline results with the use of the Modified Newton (MN) approach, constant load accumulation (CLA) and a combination thereof.

Solutions strategy	MN + CLA	CLA	MN	Baseline
Computation time [h]	13.0	32.7	40.1	96.5
Matrix factorizations	1191	120 032	2379	240 032
Total iterations ϕ	120 205	120 032	240 114	240 032
Total iterations $\mathbf{u}$	276 812	120 032	973 678	240 032

that the iterations on the displacement problem are very cheap when using the MN approach as they only require rebuilding the residuals and trivially finding the solution with the existing factorized stiffness matrix. The results obtained show that both the Modified Newton (MN) and the constant load accumulation (CLA) accumulation strategies can provide substantial performance gains (independently or in tandem) without loss of accuracy. Moreover, these methods are compatible with existing cycle jump schemes such as those presented in Loew et al. (2020) and Seleš et al. (2021).

4.1.1. Additional acceleration with multiple cycles per increment

With the use of the constant load accumulation scheme, the choice of counting one cycle per increment is somewhat arbitrary as the update to the accumulated fatigue variable $\bar{\alpha}$ from increment n to increment $n+1$ can be readily modified to

$$\bar{\alpha}_{n+1} = \bar{\alpha}_n + \mathcal{N}\psi_{0,n+1}, \tag{25}$$

where the number of cycles per increment $\mathcal{N}$ can be chosen smaller or greater than one. While a small degree of error is expected to arise as a result of the discrete sampling of the cycle history that will result from considering $\mathcal{N} > 1$ ("cycle-jumping"), we here show that this error is negligible for simulations involving varying numbers of cycles to failure. To this end, calculations are conducted for the SENT geometry considering three values for the maximum applied displacement, namely $\bar{u}_{max} = 0.00016$ mm, $\bar{u}_{max} = 0.00020$ mm, and $\bar{u}_{max} = 0.00025$ mm, and corresponding characteristic number of cycles equal to 60,000, 120,000 and 240,000, respectively. The number of cycles per increment $\mathcal{N}$ is varied in the range from 1 to 32 to investigate its influence on the accuracy of the solution. In all cases, this enhanced CLA approach is used in conjunction with the Modified Newton method. Results are provided for all three cases in Fig. 4. It can be observed that the accumulated error is small, with deviations in final crack extension from the reference $\mathcal{N} = 1$ being in all cases below 3%. Moreover, for a given value of $\mathcal{N}$, the deviation in the

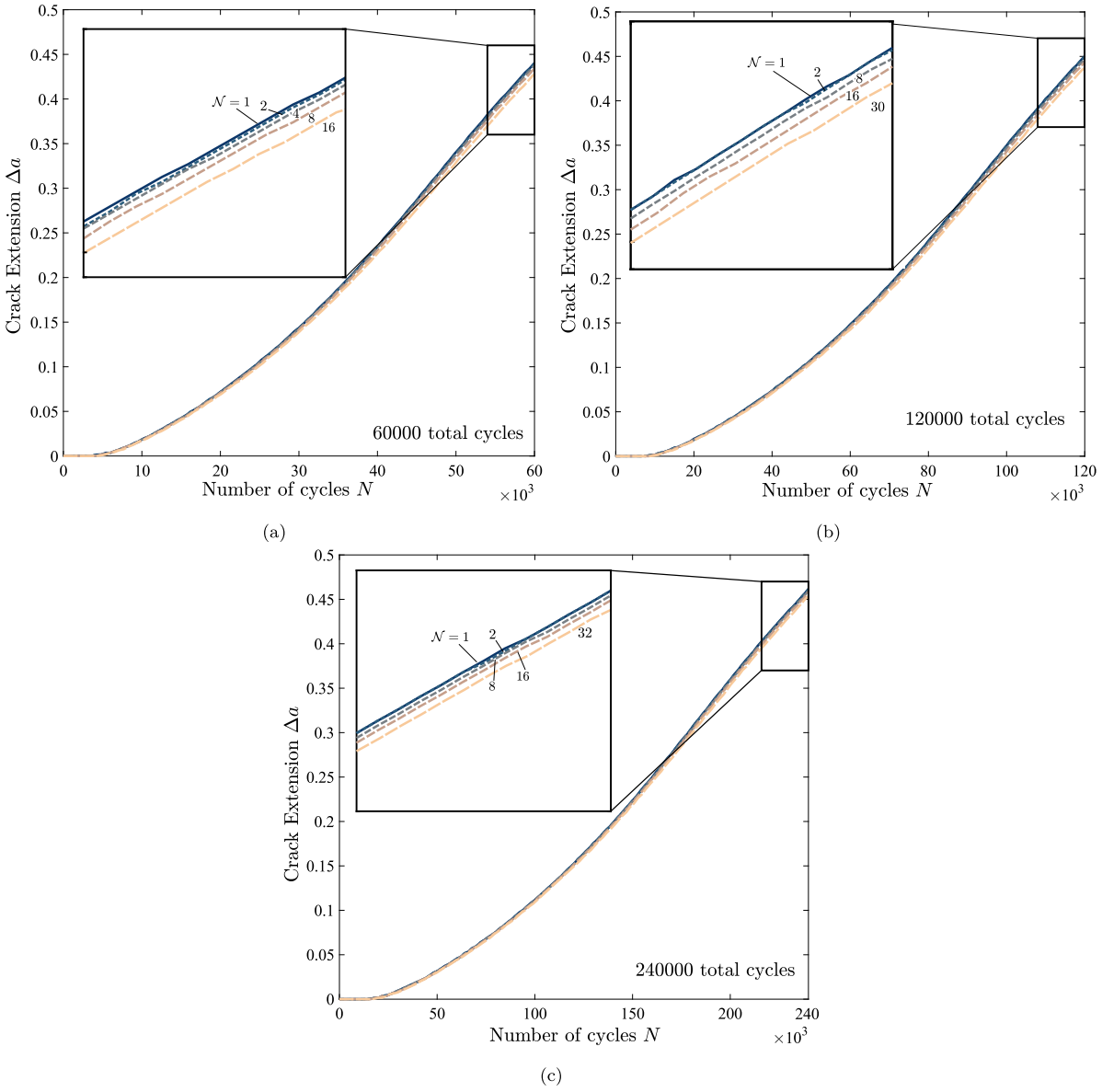

Fig. 4. Predictions of crack extension Δa versus number of cycles N for the SENT case study considering selected values of $\mathcal{N}$ (number of cycles per increment) and the following characteristic number of cycles: (a) 60,000 cycles, (b) 120,000 cycles, and (c) 240,000 cycles.

estimated crack extension at the end of the characteristic number of cycles decreases with increasing characteristic number of cycles. For high-cycle fatigue problems of engineering relevance, where the total number of cycles may be in the order of millions, a high value of $\mathcal{N}$ can be used with insignificant error. Performance tables similar to Table 1 are provided in Appendix. These show that, while computation times do not scale linearly with $\mathcal{N}$, they do monotonically decrease in the range investigated. Relative to the baseline cases in Table 1, the corresponding computation with the Modified Newton method and the constant load accumulation technique with $\mathcal{N} = 16$, is 32 times faster than the baseline case.

4.2. Asymmetric three point bending

The second case study aims at applying the fatigue acceleration schemes to a boundary value problem exhibiting more complex crack growth. As shown in Fig. 5, a plane strain beam containing an array of holes is subjected to three point bending loading conditions. An initial crack is located asymmetric to the loading pins and the holes, inducing mixed-mode cracking. This paradigmatic boundary value problem has been previously investigated in the context of static loading (see, e.g., Refs. Molnár and Gravouil (2017) and Hirshikesh et al. (2019)).

The domain is discretized using roughly 128,000 linear quadrilateral elements, with a characteristic element size $h_e = 0.01$ mm, five times smaller than the phase field length scale. The applied displacement is $\bar{u} = 0.003$ mm, which is cycled for 90,000 load cycles. As is typical for three point bending experiments, the load ratio is assumed to be $R = 0$. Both the modified Newton and the constant load accumulation scheme are exploited to capture the fatigue history in an efficient manner. The computation is carried out using different strain energy density decompositions to the differences in crack trajectory predictions. The obtained crack paths at the end of the analysis are shown in Fig. 6.

We note that in all cases the crack path differs from those observed under monotonic loading; see, e.g., Refs. Molnár and Gravouil (2017) and Mandal et al. (2019). This deviation is explained by the accumulation of fatigue near the holes which leads to the nucleation of new secondary cracks prior to the intersection of the primary crack with the

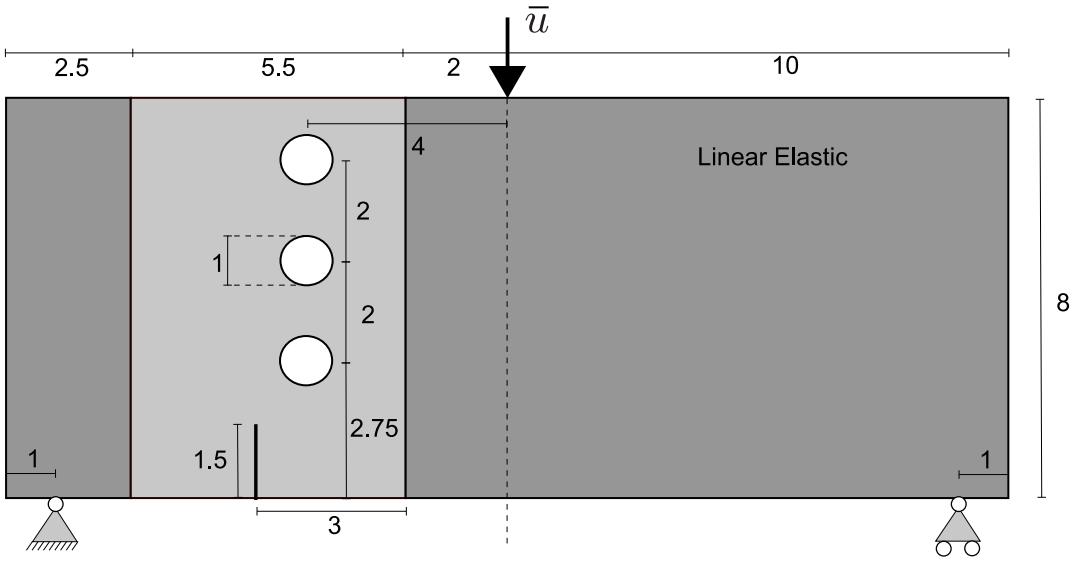

Fig. 5. Sketch of the asymmetric three point bending problem, including dimensions (in mm) and boundary conditions. Only the light grey region is subject to fatigue damage.

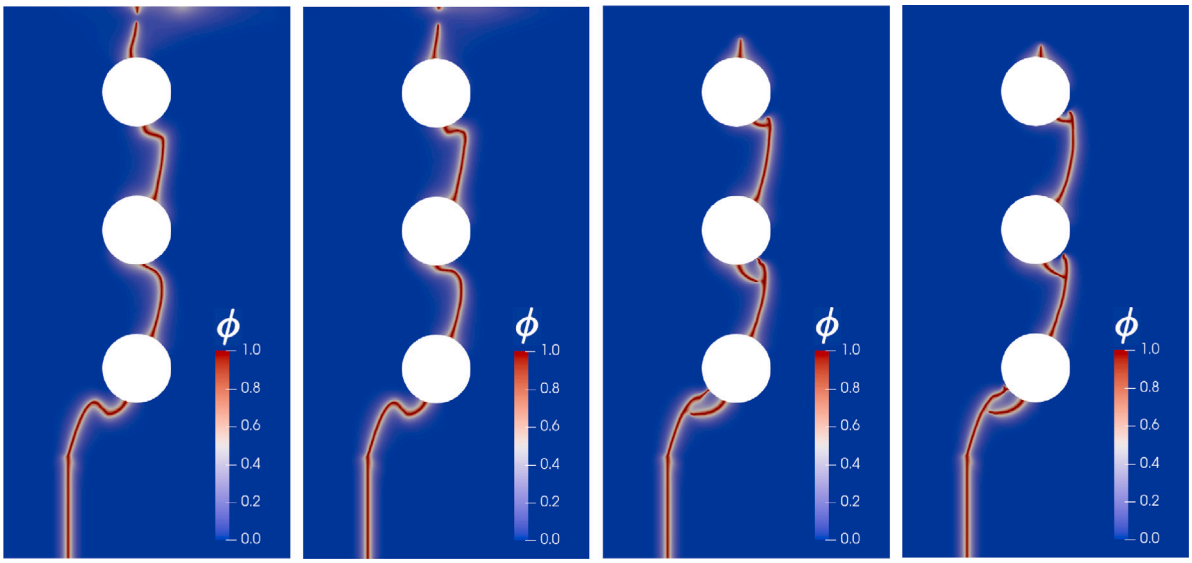

(a) Isotropic (b) Vol/Dev (c) Spectral (d) No-tension

Fig. 6. Asymmetric three point bending: Contours of the phase field crack growth after 90,000 fatigue cycles using (a) no strain decomposition. (b) The volumetric/deviatoric strain decomposition of Amor et al. (2009). (c) The spectral decomposition of Miehe et al. (2010b). (d) The no-tension split of Freddi and Royer-Carfagni (2010).

Table 2
Performance details for the asymmetric three point bending case study as a function of the strain energy decomposition.

Strain decomposition	Isotropic	Volumetric/deviatoric	Spectral	No-tension	No-tension[a]
Computation time [h]	44.9	44.4	60.3	75.5	399.0
Matrix factorizations	1249	1278	1341	1295	180 130
Total iterations ϕ	91 355	91 400	91 742	91 624	180 130
Total iterations $\mathbf{u}$	314 292	328 948	400 795	426 645	180 130

[a]Without acceleration schemes.

holes. If an endurance limit were to be introduced in the phase field fatigue formulation, these secondary cracks could be eliminated and the monotonic loading crack path might be recovered. We also remark that the issues with nucleation of cracks from non-sharp defects highlighted by Strobl and Seelig (2020), which stems from the use of the history field approach for crack irreversibility, are not of significance for this phase field fatigue model. Performance measures for the four computations are provided in Table 2.

The spectral and the no-tension split exhibit a more complex crack pattern and also require significantly more iterations on the displacement problem. However, in all cases, the proposed solution strategy offers a large reduction in the number of matrix factorizations required, in exchange for a modest increase in the number of iterations needed on the displacement problem. The results of this case study show that this performance improvement prevails even for complex crack growth studies. In the case of the No-tension split, which took the longest to

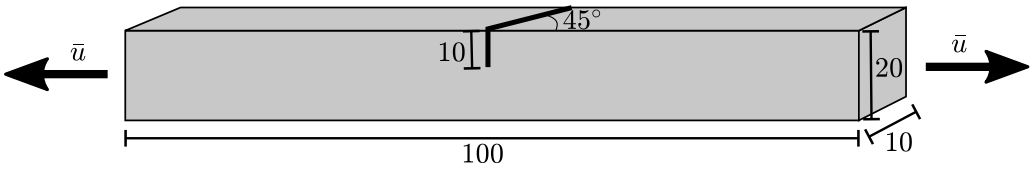

Fig. 7. Sketch of the three-dimensional beam undergoing uniaxial tension and containing a tilted edge crack, including the sample dimensions (in mm) and boundary conditions.

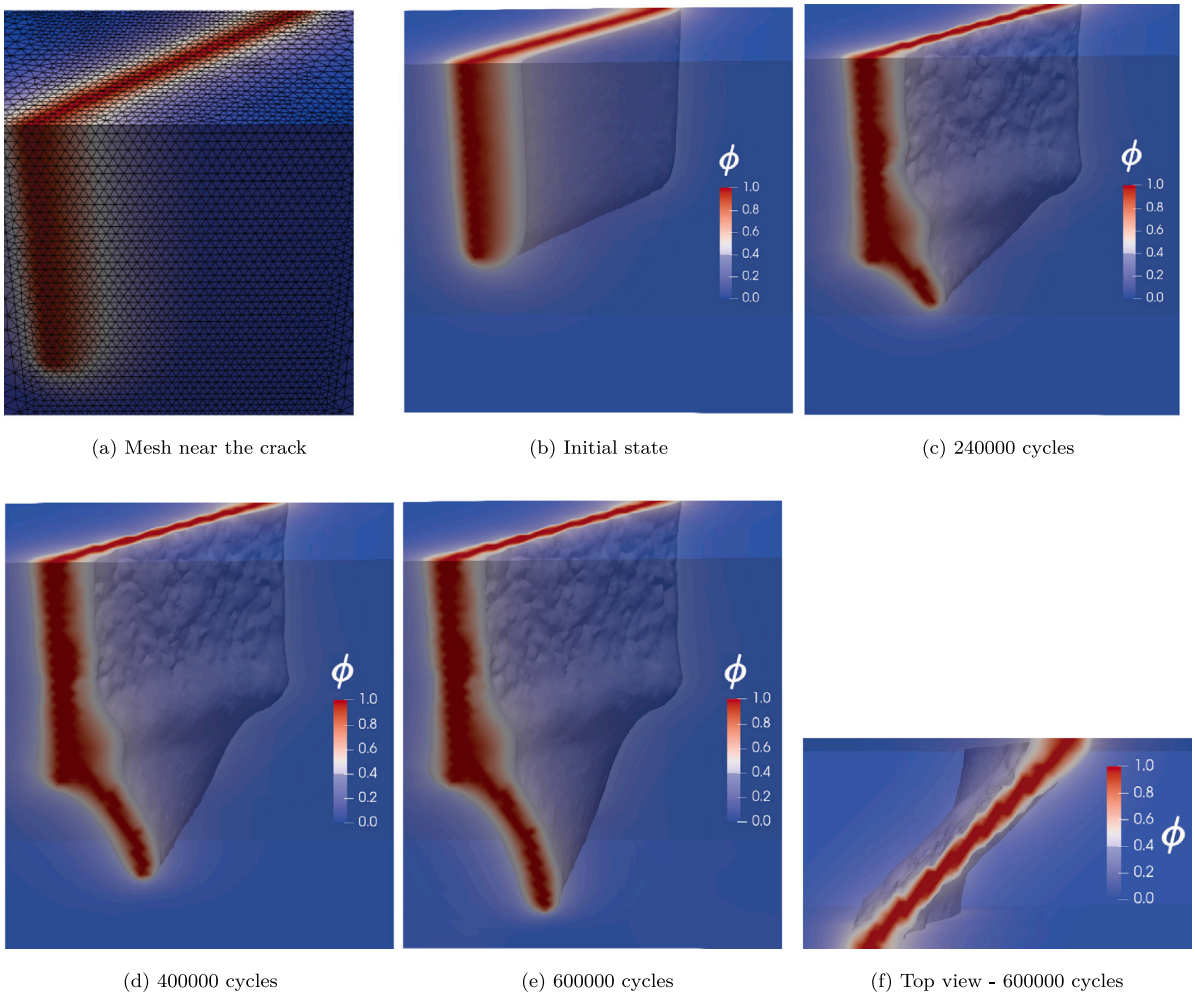

(a) Mesh near the crack (b) Initial state (c) 240000 cycles

(d) 400000 cycles (e) 600000 cycles (f) Top view - 600000 cycles

Fig. 8. Contours of the 3D tension problem. The crack rotates to be perpendicular to the overall maximal principal stress.

compute with the modified Newton approach, it is still more than five times faster than when computed with a standard Newton method and without constant load accumulation. It can be expected that in the absence of these acceleration schemes, computation time is roughly independent of the strain decomposition as only one iteration per field per increment is required even in this most advanced case. Thus, the acceleration is roughly a factor of 9 for the isotropic and volumetric/deviatoric splits. . As it was the case for the SENT specimen, a more optimal performance can most likely be achieved by differentiating how often the stiffness is updated for the two subproblems, as the damage subproblem can be updated far less frequently without paying the price of a significant number of additional iterations.

4.3. 3D beam under tension with a tilted edge crack

As a final benchmark, we consider the uniaxial tension of a three-dimensional beam with an edge crack. The induced complex crack behaviour, the crack is rotated 45° relative to the beam cross section, as sketched in Fig. 7.

The beam is subjected to cyclic tension by means of a displacement boundary condition applied on both ends. The load amplitude is $\bar{u} = 1$ mm and a total of 600 000 cycles are computed combining the Modified Newton approach with $n_i = 25$ and $n_c = 50$ with the constant load accumulation scheme with $\mathcal{N} = 4$ cycles per increment (see Section 4.1.1). The computational domain is meshed using approximately 196,000 linear tetrahedral elements, with a characteristic length near the crack $h_e = 0.35$ mm. The phase field length scale is here chosen to be equal to $\ell = 1.2$ mm. The results obtained are shown in Fig. 8 in terms of the phase field contours, showing the crack growth pattern.

The results obtained reveal the expected crack growth behaviour, with the crack rotating to position itself perpendicular to the overall maximum principal stress. The proposed methods accelerate the computation significantly, with a total of only 150,000 load increments needed to capture 600,000 cycles during which only 2978 matrix factorizations are performed. In the absence of the Modified

Newton approach and Constant Load Accumulation (CLA) acceleration strategies, a minimum of 1,200,000 increments would be required, with 1,200,000 matrix factorizations and 1,200,000 iterations on each subproblem. Combining the two acceleration schemes proposed here, the computation is achieved using only about 172,000 iterations for the displacement problem and 160,000 for the phase field problem. Furthermore, the majority of these iterations take significantly less time than in the baseline case, as only a few of them require matrix factorization. The number of matrix factorizations, which is the quantity expected to dominate the computation time for large problems, is reduced by a factor of over 400 in total. For a problem with a million cycles, a larger number of cycles per increment $\mathcal{N}$ can be employed for even greater computational improvement without loss of accuracy. Endowed with the acceleration strategies presented in this work, phase field fatigue is shown to be a technologically-relevant tool capable of delivering complex fatigue crack growth predictions in 3D over a hundred thousand cycles.

5. Concluding remarks

We have presented two compelling yet simple methods for accelerating phase field fatigue computations: (i) a Modified Newton (MN) approach, which is shown capable of drastically reducing the number of matrix factorizations necessary in the solution of a high cycle fatigue problem, and (ii) a constant load accumulation (CLA) approach that significantly reduces the number of load increments needed by considering only those relevant to the evolution of the fatigue variable. Three case studies are investigated to explore the performance benefits of these two acceleration strategies, individually and in tandem. Fatigue crack growth is predicted in 2D and 3D scenarios and compared with the baseline model. The results showed that computation times can be reduced by orders of magnitude when using MN and CLA and that these techniques remain robust even in the case of complex crack patterns and three-dimensional crack growth. The acceleration schemes presented enable predicting complex cracking patterns in 3D for over a hundred thousand cycles, endowing phase field fatigue models with the ability of delivering predictions for scales relevant to engineering practice. Moreover, the proposed methods are compatible other accelerations methods such as the cycle jump scheme presented in Loew et al. (2020), which unlocks the potential for even greater performance benefits.

Declaration of competing interest

The authors declare that they have no known competing financial interests or personal relationships that could have appeared to influence the work reported in this paper.

Data availability

Data will be made available on request

Acknowledgements

The authors gratefully acknowledge financial support from the Danish Offshore Technology Centre (DHRTC) under the “Structural Integrity and Lifetime Evaluation” programme as well as. Furthermore, this project would not have been possible without the expertise and resources of the DTU Computing Center (DTU Computing Center, 2021). Emilio Martínez-Pañeda additionally acknowledges financial support from UKRI’s Future Leaders Fellowship programme [grant MR/V024124/1]. A. Golahmar acknowledges financial support from Vattenfall Vindkraft A/S and Innovation Fund Denmark (grant 0153-00018B).

Table 3
Performance details for the SENT specimen at a characteristic number of cycles of 60 000. Computations utilize the proposed modified Newton approach and the constant load accumulation scheme with N cycles per increment.

$\mathcal{N}$	1	2	4	8	16
Computation time [h]	8.7	6.8	4.0	2.2	1.2
Matrix factorizations	606	333	298	294	290
Total iterations ϕ	60 314	30 491	15 600	8131	4528
Total iterations $\mathbf{u}$	234 934	210 754	126 138	71 018	39 680
Crack extension deviation [%]	–	0.19	−0.64	−1.36	−2.9

Table 4
Performance details for the SENT specimen at a characteristic number of cycles of 120,000. Computations utilize the proposed modified Newton approach and the constant load accumulation scheme with N cycles per increment.

$\mathcal{N}$	1	2	8	16	30
Computation time [h]	13.0	9.3	5.3	3.0	1.3
Matrix factorizations	1191	609	293	297	293
Total iterations ϕ	120 205	60 312	15 634	8271	4778
Total iterations $\mathbf{u}$	276 812	227 920	127 541	70 568	40 896
Crack extension deviation [%]	–	0.19	−0.89	−1.51	−2.85

Table 5
Performance details for the SENT specimen at a characteristic number of cycles of 240 000. Computations utilize the proposed modified Newton approach and the constant load accumulation scheme with N cycles per increment.

$\mathcal{N}$	1	2	8	16	32
Computation time [h]	20.6	12.4	7.0	4.0	2.2
Matrix factorizations	2378	1191	320	290	298
Total iterations ϕ	240 150	120 227	30 501	15 614	8186
Total iterations $\mathbf{u}$	357 149	266 701	216 611	127 401	70 764
Crack extension deviation [%]	–	0.00	−0.43	−0.83	−1.74

Appendix. Performance data for the SENT specimen with multiple cycles per increment

We here provide additional performance data for the computations addressed in Section 4.1.1. Specifically, the performance data for the analysis with a characteristic number of cycles equal to 60,000 is given in Table 3, the data pertaining to the analysis for 120,000 cycles is given in Table 4, and the results for the 240,000 cycles case is provided in Table 5. Consistent with the main text, a matrix factorization denotes a factorization of the tangent stiffness matrix of both the damage and the displacement subproblems. The crack extension at the end of the total number of cycles for a given number of cycles per increment $\mathcal{N}$ is denoted a_N. Crack extension deviation is here measure relative to the $\mathcal{N} = 1$ case such that the relative deviation Δa_N is given by:

$$\Delta a_N = \frac{a_N - a_1}{a_1}. \tag{26}$$

References

Ai, W., Wu, B., Martínez-Pañeda, E., 2022. A coupled phase field formulation for modelling fatigue cracking in lithium-ion battery electrode particles. J. Power Sources 544, 231805.

Aldakheel, F., Wriggers, P., Miehe, C., 2018. A modified gurson-type plasticity model at finite strains: formulation, numerical analysis and phase-field coupling. Comput. Mech. 62 (4), 815–833.

Alessi, R., Ambati, M., Gerasimov, T., Vidoli, S., Lorenzis, L.D., 2018. Comparison of phase-field models of fracture coupled with plasticity. Comput. Methods Appl. Sci. 46, 1–21.

Alessi, R., Ulloa, J., 2023. Endowing Griffith’s fracture theory with the ability to describe fatigue cracks. Eng. Fract. Mech. 109048.

Ambati, M., Gerasimov, T., De Lorenzis, L., 2014. A review on phase-field models of brittle fracture and a new fast hybrid formulation. Comput. Mech. 55 (2), 383–405.

Ambati, M., Kruse, R., De Lorenzis, L., 2016. A phase-field model for ductile fracture at finite strains and its experimental verification. Comput. Mech. 57 (1), 149–167.

Amor, H., Marigo, J.J., Maurini, C., 2009. Regularized formulation of the variational brittle fracture with unilateral contact: Numerical experiments. J. Mech. Phys. Solids 57 (8), 1209–1229.
Anand, L., Mao, Y., Talamini, B., 2019. On modeling fracture of ferritic steels due to hydrogen embrittlement. J. Mech. Phys. Solids 122, 280–314.
Borden, M.J., Verhoosel, C.V., Scott, M.A., Hughes, T.J., Landis, C.M., 2012. A phase-field description of dynamic brittle fracture. Comput. Methods Appl. Mech. Engrg. 217–220, 77–95.
Börjesson, E., Remmers, J.J., Fagerström, M., 2022. A generalised path-following solver for robust analysis of material failure. Comput. Mech..
Bourdin, B., Francfort, G.A., Marigo, J.J., 2000. Numerical experiments in revisited brittle fracture. J. Mech. Phys. Solids 48 (4), 1–23.
Bourdin, B., Marigo, J.-J., Maurini, C., Sicsic, P., 2014. Morphogenesis and propagation of complex cracks induced by thermal shocks. Phys. Rev. Lett. 112 (1), 14301.
Boyce, A.M., Martínez-Pañeda, E., Wade, A., Zhang, Y.S., Bailey, J.J., Heenan, T.M., Brett, D.J., Shearing, P.R., 2022. Cracking predictions of lithium-ion battery electrodes by X-ray computed tomography and modelling. J. Power Sources 526, 231119.
Carlsson, K., Ekre, F., Contributors, 2021. Ferrite.jl. URL https://github.com/Ferrite-FEM/Ferrite.jl.
Carrara, P., Ambati, M., Alessi, R., De Lorenzis, L., 2020. A framework to model the fatigue behavior of brittle materials based on a variational phase-field approach. Comput. Methods Appl. Mech. Engrg. 361, 112731.
Cojocaru, D., Karlsson, A.M., 2006. A simple numerical method of cycle jumps for cyclically loaded structures. Int. J. Fatigue 28 (12), 1677–1689.
DTU Computing Center, 2021. DTU Computing Center resources.
Duda, F.P., Ciarbonetti, A., Toro, S., Huespe, A.E., 2018. A phase-field model for solute-assisted brittle fracture in elastic-plastic solids. Int. J. Plast. 102 (November 2017), 16–40.
Feng, Y., Li, J., 2022. Phase-field cohesive fracture theory: A unified framework for dissipative systems based on variational inequality of virtual works. J. Mech. Phys. Solids 159, 104737.
Francfort, G.A., Marigo, J.J., 1998. Revisiting brittle fracture as an energy minimization problem. J. Mech. Phys. Solids 46 (8), 1319–1342.
Freddi, F., Mingazzi, L., 2022. Mesh refinement procedures for the phase field approach to brittle fracture. Comput. Methods Appl. Mech. Engrg. 388, 114214.
Freddi, F., Mingazzi, L., 2023. Adaptive mesh refinement for the phase field method: A FEniCS implementation. Appl. Eng. Sci. 14, 100127.
Freddi, F., Royer-Carfagni, G., 2010. Regularized variational theories of fracture: A unified approach. J. Mech. Phys. Solids 58 (8), 1154–1174.
Gerasimov, T., De Lorenzis, L., 2016. A line search assisted monolithic approach for phase-field computing of brittle fracture. Comput. Methods Appl. Mech. Engrg. 312, 276–303.
Golahmar, A., Kristensen, P.K., Niordson, C.F., Martínez-Pañeda, E., 2022. A phase field model for hydrogen-assisted fatigue. Int. J. Fatigue 154, 106521.
Golahmar, A., Niordson, C.F., Martínez-Pañeda, E., 2023. A phase field model for high-cycle fatigue: Total-life analysis. Int. J. Fatigue 170, 107558.
Guillén-Hernández, T., Quintana-Corominas, A., García, I.G., Reinoso, J., Paggi, M., Turón, A., 2020. In-situ strength effects in long fibre reinforced composites: A micro-mechanical analysis using the phase field approach of fracture. Theor. Appl. Fract. Mech. 108, 102621.
Heister, T., Wheeler, M.F., Wick, T., 2015. A primal-dual active set method and predictor-corrector mesh adaptivity for computing fracture propagation using a phase-field approach. Comput. Methods Appl. Mech. Engrg. 290, 466–495.
Hirshikesh, Natarajan, S., Annabattula, R.K., Martínez-Pañeda, E., 2019. Phase field modelling of crack propagation in functionally graded materials. Composites B 169, 239–248.
Jodlbauer, D., Langer, U., Wick, T., 2020. Matrix-free multigrid solvers for phase-field fracture problems. Comput. Methods Appl. Mech. Engrg. 372, 113431.
Klinsmann, M., Rosato, D., Kamlah, M., McMeeking, R.M., 2015. An assessment of the phase field formulation for crack growth. Comput. Methods Appl. Mech. Engrg. 294, 313–330.
Klinsmann, M., Rosato, D., Kamlah, M., McMeeking, R.M., 2016. Modeling crack growth during Li insertion in storage particles using a fracture phase field approach. J. Mech. Phys. Solids 92, 313–344.
Kristensen, P.K., Martínez-Pañeda, E., 2020. Phase field fracture modelling using quasi-Newton methods and a new adaptive step scheme. Theor. Appl. Fract. Mech. 107, 102446.
Kristensen, P.K., Niordson, C.F., Martínez-Pañeda, E., 2020a. A phase field model for elastic-gradient-plastic solids undergoing hydrogen embrittlement. J. Mech. Phys. Solids 143, 104093.
Kristensen, P.K., Niordson, C.F., Martínez-Pañeda, E., 2020b. Applications of phase field fracture in modelling hydrogen assisted failures. Theor. Appl. Fract. Mech. 110.
Kristensen, P.K., Niordson, C.F., Martínez-Pañeda, E., 2021. An assessment of phase field fracture: Crack initiation and growth. Phil. Trans. R. Soc. A 379 (2203).
Lampron, O., Therriault, D., Lévesque, M., 2021. An efficient and robust monolithic approach to phase-field brittle fracture using a modified Newton method. Comput. Methods Appl. Mech. Engrg. 306.
Linse, T., Hennig, P., Kästner, M., de Borst, R., 2017. A convergence study of phase-field models for brittle fracture. Eng. Fract. Mech. 184, 307–318.
Lo, Y.S., Borden, M.J., Ravi-Chandar, K., Landis, C.M., 2019. A phase-field model for fatigue crack growth. J. Mech. Phys. Solids 132, 103684.
Loew, P.J., Poh, L.H., Peters, B., Beex, L.A., 2020. Accelerating fatigue simulations of a phase-field damage model for rubber. Comput. Methods Appl. Mech. Engrg. 370, 113247.
Lorenzis, L.D., Maurini, C., 2022. Nucleation under multi-axial loading in variational phase-field models of brittle fracture. Int. J. Fract. 237, 61–81.
Mandal, T.K., Nguyen, V.P., Wu, J.Y., 2019. Length scale and mesh bias sensitivity of phase-field models for brittle and cohesive fracture. Eng. Fract. Mech. 217, 106532.
Martínez-Pañeda, E., Golahmar, A., Niordson, C.F., 2018. A phase field formulation for hydrogen assisted cracking. Comput. Methods Appl. Mech. Engrg. 342, 742–761.
Mesgarnejad, A., Imanian, A., Karma, A., 2019. Phase-field models for fatigue crack growth. Theor. Appl. Fract. Mech. 103, 102282.
Miehe, C., Hofacker, M., Welschinger, F., 2010a. A phase field model for rate-independent crack propagation: Robust algorithmic implementation based on operator splits. Comput. Methods Appl. Mech. Engrg. 199 (45–48), 2765–2778.
Miehe, C., Welschinger, F., Hofacker, M., 2010b. Thermodynamically consistent phase-field models of fracture: Variational principles and multi-field FE implementations. Internat. J. Numer. Methods Engrg. 83, 1273–1311.
Molnár, G., Gravouil, A., 2017. 2D and 3D Abaqus implementation of a robust staggered phase-field solution for modeling brittle fracture. Finite Elem. Anal. Des. 130, 27–38.
Navidtehrani, Y., Betegón, C., Martínez-Pañeda, E., 2022. A general framework for decomposing the phase field fracture driving force, particularised to a drucker–prager failure surface. Theor. Appl. Fract. Mech. 121, 103555.
Olesch, D., Kuhn, C., Schlüter, A., Müller, R., 2021. Adaptive numerical integration of exponential finite elements for a phase field fracture model. Comput. Mech. 67 (3), 811–821.
Sargado, J.M., Keilegavlen, E., Berre, I., Nordbotten, J.M., 2021. A combined finite element–finite volume framework for phase-field fracture. Comput. Methods Appl. Mech. Engrg. 373, 113474.
Seiler, M., Linse, T., Hantschke, P., Kästner, M., 2020. An efficient phase-field model for fatigue fracture in ductile materials. Eng. Fract. Mech. 224, 106807.
Seleš, K., Aldakheel, F., Tonković, Z., Sorić, J., Wriggers, P., 2021. A general phase-field model for fatigue failure in brittle and ductile solids. Comput. Mech. 67 (5), 1431–1452.
Seleš, K., Lesičar, T., Tonković, Z., Sorić, J., 2019. A residual control staggered solution scheme for the phase-field modeling of brittle fracture. Eng. Fract. Mech. 205, 370–386.
Simoes, M., Braithwaite, C., Makaya, A., Martínez-Pañeda, E., 2022. Modelling fatigue crack growth in shape memory alloys. Fatigue Fract. Eng. Mater. Struct. 45 (4), 1243–1257.
Simoes, M., Martínez-Pañeda, E., 2021. Phase field modelling of fracture and fatigue in shape memory alloys. Comput. Methods Appl. Mech. Engrg. 373, 113504.
Song, J., Zhao, L.G., Qi, H., Li, S., Shi, D., Huang, J., Su, Y., Zhang, K., 2022. Coupling of phase field and viscoplasticity for modelling cyclic softening and crack growth under fatigue. Eur. J. Mech. A Solids 92, 104472.
Strobl, M., Seelig, T., 2020. Phase field modeling of hertzian indentation fracture. J. Mech. Phys. Solids 143.
Tan, W., Martínez-Pañeda, E., 2021. Phase field predictions of microscopic fracture and R-curve behaviour of fibre-reinforced composites. Compos. Sci. Technol. 202, 108539.
Tanné, E., Li, T., Bourdin, B., Marigo, J.J., Maurini, C., 2018. Crack nucleation in variational phase-field models of brittle fracture. J. Mech. Phys. Solids 110, 80–99.
Wu, J.-Y., 2017. A unified phase-field theory for the mechanics of damage and quasi-brittle failure. J. Mech. Phys. Solids 103, 72–99.
Wu, J.-y.Y., Huang, Y., Phu, V., Nguyen, V.P., 2020. On the BFGS monolithic algorithm for the unified phase field damage theory. Comput. Methods Appl. Mech. Engrg. 360, 112704.
Ye, J.Y., Zhang, L.W., 2022. Damage evolution of polymer-matrix multiphase composites under coupled moisture effects. Comput. Methods Appl. Mech. Engrg. 388, 114213.

[P3]

A. Golahmar, C. F. Niordson, and E. Martínez-Pañeda. A phase field model for fatigue crack growth analysis. To be submitted.

A phase field model for fatigue crack growth analysis

Alireza Golahmar[a,c], Christian F. Niordson[a], Emilio Martínez-Pañeda[b,*]

[a] *Department of Mechanical Engineering, Technical University of Denmark, DK-2800 Kgs. Lyngby, Denmark*
[b] *Department of Civil and Environmental Engineering, Imperial College London, London SW7 2AZ, UK*
[c] *Vattenfall Offshore Wind, Copenhagen, Denmark*

Abstract

We present an enhanced phase field formulation for predicting fatigue crack growth behavior. Our model offers a comprehensive solution, capable of accurately capturing both fatigue crack initiation and growth under arbitrary loading scenarios and specimen geometries. To achieve this, we employ a highly efficient quasi-Newton monolithic solution scheme, complemented by an accelerated fatigue simulation strategy. Through extensive numerical experiments, we successfully identify and map the three distinct regions of fatigue crack growth (FCG) and establish a strong correlation between the Paris law and the S-N curves. One of the key strengths of our model lies in its effective incorporation of the transition flaw size effect. By integrating strength- and toughness-driven mechanisms, our approach excels in both static and fatigue fracture analyses. When compared to laboratory experiments, our model consistently delivers precise predictions of virtual FCG rate curves, as well as successfully replicates the complex crack path trajectories under mixed-mode fracture.

Keywords:
Phase field, Finite element method, Fatigue, S-N curves, Paris law, Transition flaw size effect

1. Introduction

Material fracture caused by fatigue loading is widely considered as the primary cause for failure in engineering components [1]. Given its intricate nature, devising numerical techniques for accurately predicting fatigue cracking has been an extensive area of research for years. The process of fatigue generally comprises two distinct stages: the initiation of a crack and its subsequent growth. The initiation stage involves irreversible microscopic deterioration phenomena such as micro-void formation at imperfections in the material. This initiates the development of micro-cracks, a process which is fundamentally random and is influenced by the material's micro-structural configuration

*Corresponding authors.
Email address: e.martinez-paneda@imperial.ac.uk (Emilio Martínez-Pañeda)

[2]. As the loading persists, damage accumulates within the material, prompting the micro-cracks to coalesce into larger fatigue (macro-) cracks. One or several of these macro-cracks grow through the material, initially in a stable fashion, until they reach a critical size. At this stage, they become unstable, leading to the total failure of the component. The endurance or fatigue resistance of a material is typically characterized by the number of cycles it can withstand before failure. This can be ascertained using traditional empirical approaches, methodologies based on fracture mechanics, or material models accounting for fatigue damage.

Empirical approaches, which rely on the application of data derived from a wide array of experimental tests, have played a crucial role in the advancement of this field. This progress is largely credited to Wöhler [3], who pioneered the stress-life or S-N curve method, a technique now broadly employed. The S-N curve describes the relationship between the constant stress (or strain) amplitude of a cyclic load and the total number of cycles a component can endure prior to final failure. This relationship is often presented graphically and can be mathematically expressed via the Basquin power law [4]. When it comes to total life analyses, two primary categories emerge. The first, known as high-cycle fatigue (HCF), subjects the material to low cyclic stress amplitudes, leading to mainly elastic behavior. In this scenario, failure tends to occur after an extensive number of cycles, often surpassing 10^6 cycles. The second category, conversely, deals with stresses of a magnitude significant enough to induce plasticity, resulting in failure within a considerably smaller number of load cycles, typically fewer than 10^4 cycles. This regime is identified as low-cycle fatigue (LCF). While the empirical stress-life approaches provide valuable insights, they come with inherent limitations when efforts are made to generalize them across a wide spectrum of materials, geometries, and loading scenarios. Methods based on fracture mechanics often employ the Paris law, a principle introduced by Paris and Erdogan [5] to describe the steady growth of a fatigue crack as a function of the stress intensity factor. However, it is important to clarify that this relationship holds validity only within the Paris regime and does not apply to the phases of crack initiation and failure, also known as slow and rapid crack growth regimes respectively. In order to overcome this limitation, the Paris law has been continuously enhanced and expanded. These extensive enhancements have led to the development of the widely adopted NASGRO equation [6]. This comprehensive formula successfully replicates various fundamental aspects of fatigue behavior, inclusive of the slow, steady, and rapid crack growth.

The phase field fracture model, widely recognized for its utility in exploring complex crack phenomena, leverages a variational approach rooted in Griffith's thermodynamic framework, first proposed in 1921. Griffith's theory suggests that a crack will propagate when the material exceeds its critical

energy release rate. Building on this principle, Francfort and Marigo [7] incorporated Griffith's energy postulation into their variational formulations. To further enhance the regularization, Bourdin et al. [8, 9] introduced a scalar damage variable, later called the phase field, which smoothly transitions between an intact and a fractured state of the material. The phase field fracture model has seen widespread adoption since its inception, chiefly attributed to its remarkable capability to effectively model intricate fracture features, including the initiation of cracks at multiple locations and the merging of diverse flaws, across a range of geometries and dimensions, all without relying on arbitrary criteria. There has been substantial focus on the improvement of solution schemes [10–12] and the refinement of discretization strategies [13, 14]. These advancements have been pivotal in promoting broader acceptance of the model. Owing to its firm mathematical foundation and its uncomplicated implementation and customization potential, this model has found extensive usage in a variety of applications. These include, but are not limited to, ductile damage [15–18], dynamic fracture [19–23], mixed-mode fracture [24], Herzian indentation fracture [25], interface fracture [26], composites delamination [27–31], fracture in shells [32], ceramics [33, 34], elastomers [35], shape memory alloys [36], functionally graded materials [37, 38], thermal shocks [39], Lithium ion batteries [40–42], and hydrogen embrittlement [43–46], among others. A comprehensive overview can be found in Ref. [47].

Over recent years, there have been endeavors to incorporate fatigue damage into phase field fracture models. Lo et al. [48] presented a methodology that added a viscous term to the standard phase field model for brittle materials. This addition, along with a revised J-integral, resulted in fatigue crack growth behavior in line with the Paris law. A common practice is to incorporate an additional variable symbolizing the fatigue history into the model. The designation of this variable usually includes a dissipative element in the phase field microforce equilibrium, which facilitates crack growth [49–51]. Alternatively, it can take the form of a fatigue degradation function that effectively reduces the material's resistance to fracture. Consequently, an extra equation is required to specify the evolution of the fatigue history variable. Boldrini et al. [49] developed this equation utilizing thermodynamic principles, while Loew et al. [50] proposed one rooted in micro-crack growth behavior. Seiler et al. [52] used the local strain approach, invoking Neuber's rule to incorporate plasticity, whereas [51] employed Miner's rule to specify fatigue damage accumulation. Alessi et al. [53] advocated using the accumulated strain at each cycle's loading stage as the driving factor for fatigue damage. Various other studies [36, 54–58] employed the accumulation of the tensile parts of the strain energy density (or elastoplastic energy density in [57, 58]) at the loading (unloading in [56]) stages only as their primary approach.

In the authors' previous research [59, 60], novel strategies for accumulating fatigue damage were introduced. These strategies enable the evolution of fatigue damage to occur within a single reversal per cycle (from peak to valley), drastically reducing computational costs and providing accurate descriptions of fatigue accumulation with just a single increment for multiple load cycles. Consequently, for loading scenarios with constant amplitudes, the internal increments of load cycles can be substituted by applying constant loads, representative of the maximum amplitudes. Importantly, the new accumulation strategies allow for modelling different S-N curve slopes, fatigue endurance limits, and the load ratio effect [59]. The authors conducted total-life analyses to evaluate the performance and potential of this novel modelling framework. In the present study, the authors delve deeper into the model's capabilities. Comprehensive fatigue crack growth (FCG) analyses are conducted, and the feasibility of integrating the S-N and Paris approaches for brittle solids within our model is explored. The framework includes two widely utilized phase field fracture models (`AT1` and `AT2`). A crucial aspect of the numerical implementation is the adoption of a quasi-Newton monolithic solution scheme [61, 62], which plays a vital role in minimizing the computational expense of cycle-by-cycle fatigue calculations. Additionally, the newly introduced accumulation strategy [60] further accelerates computations by allowing the integration of multiple load cycles within a single increment. The manuscript is structured as follows: Section 2 presents the theoretical foundations of the phase field fatigue framework. Subsequently, in Section 3, details of the finite element implementation are provided. In Section 4, several boundary value problems are addressed to assess the model's performance. Finally, concluding remarks are presented in Section 5.

2. A phase field model for fatigue damage

The section introduces a framework that outlines the behavior of a solid object occupying any given volume $\Omega \subset \mathbb{R}^{\delta}$ ($\delta \in [1, 2, 3]$), with an external boundary $\partial\Omega \subset \mathbb{R}^{\delta-1}$, and an outward normal vector $\mathbf{n}$. The framework is constructed by applying the fundamental concepts of rate-independent systems, which are expressed through an equilibrium of energy and a dissipation inequality. Additionally, the framework incorporates specific assumptions, including small deformations, negligible impact of inertia and constant temperature conditions.

2.1. Field variables and kinematics

The displacement $\mathbf{u}$ and the phase field ϕ are the main variables of the problem, and the strain tensor $\boldsymbol{\varepsilon}$ is given as:

$$\boldsymbol{\varepsilon} = \frac{1}{2}\left(\nabla^{\intercal}\mathbf{u} + \nabla\mathbf{u}\right) \tag{1}$$

The phase field variable, denoted as $\phi \in [0;1]$, can be interpreted as a measure of damage. It exhibits a monotonic increase ($\dot{\phi} \geqslant 0$) with a value of $\phi = 1$ signifies the presence of a crack and $\phi = 0$ represents an undamaged material point. The phase field variable ϕ possesses a smooth and continuous nature, enabling the representation of discrete cracks in a diffused or smeared manner. The extent of this smearing is controlled by a length scale parameter ℓ. Moreover, it offers an effective approach to approximating the fracture energy across a discontinuous surface Γ [9]. To incorporate time and history-dependent situations into the rate-independent fracture description, a cumulative history variable $\bar{\alpha}$ is introduced, satisfying $\dot{\bar{\alpha}} \geqslant 0$ at the current time τ. Furthermore, a fatigue degradation function $f(\bar{\alpha})$ is incorporated to capture the influence of cyclic loading on fracture characteristics. Thus, the formulation of fracture energy can be expressed as follows:

$$\Psi^{s} = \int_{0}^{t}\int_{\Omega} f(\bar{\alpha}(\tau))\, G_c\, \dot{\gamma}_{\ell}(\phi, \nabla\phi)\, \mathrm{d}V\mathrm{d}\tau \tag{2}$$

where G_c signifies the material toughness or critical energy release rate, while γ_{ℓ} refers to the functional that describes the density of the crack surfaces.

2.2. Principle of virtual power. Balance of forces

To derive the equilibrium equations of the problem, the principle of virtual power is employed. For the displacement $\mathbf{u}$, the external boundary is divided into two distinct parts: $\partial\Omega_u$ and $\partial\Omega_h$, where the displacement and traction $\mathbf{h}$ can be prescribed. A body force field per unit volume $\mathbf{b}$ can also be specified. For the phase field variable ϕ, a crack surface Γ and a microtraction $\mathfrak{f}$ can be prescribed on $\partial\Omega_{\mathfrak{f}}$. Consequently, the external and internal virtual powers can be given as:

$$\begin{aligned}
\dot{\mathcal{W}}_{\text{ext}} &= \int_{\partial\Omega}\left\{\mathbf{h}\cdot\dot{\mathbf{u}} + \mathfrak{f}\dot{\phi}\right\}\mathrm{d}S + \int_{\Omega}\mathbf{b}\cdot\dot{\mathbf{u}}\,\mathrm{d}V \\
\dot{\mathcal{W}}_{\text{int}} &= \int_{\Omega}\left\{\boldsymbol{\sigma} : \nabla\dot{\mathbf{u}} + \omega\dot{\phi} + \boldsymbol{\xi}\cdot\nabla\dot{\phi}\right\}\,\mathrm{d}V
\end{aligned} \tag{3}$$

where $\boldsymbol{\sigma}$ denotes the stress tensor, and ω and $\boldsymbol{\xi}$ the phase field micro-stress variables. By applying the fundamental lemma of calculus of variations and Gauss' divergence theorem to the principle of

virtual power ($\dot{\mathcal{W}}\text{int} - \dot{\mathcal{W}}\text{ext} = 0$), we obtain a set of local force balances (in Ω)

$$\begin{aligned} \nabla \cdot \boldsymbol{\sigma} + \mathbf{b} &= \mathbf{0} \\ \nabla \cdot \boldsymbol{\xi} - \omega &= 0 \end{aligned} \tag{4}$$

and a set of boundary conditions (on $\partial\Omega$)

$$\begin{aligned} \mathbf{h} &= \boldsymbol{\sigma} \cdot \mathbf{n} \\ \mathfrak{f} &= \boldsymbol{\xi} \cdot \mathbf{n} \end{aligned} \tag{5}$$

2.3. Free-energy imbalance

By considering the Helmholtz free energy per unit volume $\psi\left(\boldsymbol{\varepsilon}, \phi, \nabla\phi\right)$ and the external work $\mathcal{W}_{\text{ext}}$, the first two laws of thermodynamics can be combined (also known as the Clausius–Duhem inequality)

$$\int_{\Omega} \dot{\psi} \, \mathrm{d}V - \int_{\partial\Omega} \dot{\mathcal{W}}_{\text{ext}} \, \mathrm{d}S \leqslant 0 \,, \tag{6}$$

which by inserting Eqs. (3) and (5) and utilizing the divergence theorem the local free-energy inequality can be obtained

$$\left(\boldsymbol{\sigma} - \frac{\partial\psi}{\partial\boldsymbol{\varepsilon}}\right) : \dot{\boldsymbol{\varepsilon}} + \left(\omega - \frac{\partial\psi}{\partial\phi}\right)\dot{\phi} + \left(\xi - \frac{\partial\psi}{\partial\nabla\phi}\right) \cdot \nabla\dot{\phi} \geqslant 0 \tag{7}$$

for which we introduce a free energy function ψ, which is the combination of the elastic strain energy density ψ^e and the fracture surface energy density ψ^s as

$$\psi(\boldsymbol{\varepsilon}, \phi, \nabla\phi \,|\, \bar{\alpha}) = \psi^e(\boldsymbol{\varepsilon}, \phi) + \psi^s(\phi, \nabla\phi \,|\, \bar{\alpha}) \tag{8}$$

2.4. Constitutive theory

Expanding upon the given definition of free energy (8), we will now formulate a constitutive theory that considers the interconnection between deformation, fracture, and fatigue characteristics.

2.4.1. Elasticity

The strain energy density ψ^e is defined as a function of the strains $\boldsymbol{\varepsilon}$, the isotropic linear elastic stiffness tensor $\boldsymbol{\mathcal{L}}_0$, and a degradation function $g(\phi)$ associated with the phase field. The expression for ψ^e can be given as follows:

$$\psi^e(\boldsymbol{\varepsilon}, \phi) = g(\phi)\psi_0^e(\boldsymbol{\varepsilon}) \quad \text{with} \quad \psi_0^e(\boldsymbol{\varepsilon}) = \frac{1}{2}\boldsymbol{\varepsilon}^{\mathsf{T}} : \boldsymbol{\mathcal{L}}_0 : \boldsymbol{\varepsilon} \tag{9}$$

where ψ_0^e corresponds to the strain energy density of an undamaged isotropic solid. Based on this, we can determine the stress tensor $\boldsymbol{\sigma}$ as

$$\boldsymbol{\sigma} = \frac{\partial\psi}{\partial\boldsymbol{\varepsilon}} = g(\phi)\boldsymbol{\mathcal{L}}_0 : \boldsymbol{\varepsilon} \tag{10}$$

2.4.2. Fracture surface energy

Next, we will establish the definition of the fracture surface energy density ψ^s based on Eq. (2). This energy density is determined by the phase field ϕ, its gradient $\nabla\phi$, and a fatigue degradation function $f(\bar{\alpha})$, which will be discussed in detail later. The expression for ψ^s can be written as follows:

$$\psi^s(\phi, \nabla\phi \,|\, \bar{\alpha}) = f(\bar{\alpha})\, G_c\, \gamma_\ell(\phi, \nabla\phi) \tag{11}$$

where the crack surface density functional γ_ℓ is specified as:

$$\gamma_\ell(\phi, \nabla\phi) = \frac{1}{4c_w}\left(\frac{w(\phi)}{\ell} + \ell|\nabla\phi|^2\right) \quad \text{with} \quad c_w = \int_0^1 \sqrt{w(\zeta)}\,\mathrm{d}\zeta \tag{12}$$

where $w(\phi)$ represents the geometric crack function, which will be introduced and defined in the subsequent discussion, and c_w denotes a scaling factor.

2.4.3. Strain energy decomposition

In order to address the issue of crack initiation and growth under compression, the strain energy density can be separated into two components: active (associated with tension) and inactive (related to compression).

$$\psi^e\left(\boldsymbol{\varepsilon}, \phi\right) = g(\phi)\, \psi_0^+(\boldsymbol{\varepsilon}) + \psi_0^-(\boldsymbol{\varepsilon}) \tag{13}$$

where the phase field evolution only affects the active (tensile) part of the strain energy density. Various decomposition splits have been suggested in existing literature, with the volumetric-deviatoric split introduced by Amor et al. [63] and the spectral decomposition by Miehe et al. [10] being the most widely adopted. In this work, we will employ the No-tension split proposed by Freddi et al. [64], which has demonstrated notable effectiveness in fatigue modelling [59, 60]. The procedures for defining three-dimensional strain states are outlined in [48], while the energy split is provided as follows:

$$\psi_0^\pm(\boldsymbol{\varepsilon}) = \frac{1}{2}\lambda\,\mathrm{tr}^2(\boldsymbol{\varepsilon}_\pm) + Q\,\mathrm{tr}\left(\boldsymbol{\varepsilon}_\pm^2\right) \quad \text{with} \quad \boldsymbol{\varepsilon}_\pm = \mathrm{sym}_\pm(\boldsymbol{\varepsilon}) \tag{14}$$

where $\mathrm{sym}_\pm(\boldsymbol{\varepsilon})$ represents the symmetric part of the strain tensor, which can be either positive-definite or negative-definite. Highlighting the significance of strain energy decomposition, it should be noted that the stress-strain relationship becomes notably nonlinear, requiring increased computational resources. To tackle this challenge, the study conducted by Ambati et al. [65] proposes a solution in the form of a *hybrid* formulation.

2.4.4. Irreversibility condition

The concept of damage signifies a process that cannot be reversed, making it crucial for the phase field evolution law to adhere to the condition of $\dot{\phi} \geqslant 0$. As proposed by Miehe et al. [11], we incorporate a history variable field $\mathcal{H}$

$$\mathcal{H} = \max_{\tau \in [0,t]} \psi_0^+(\boldsymbol{\varepsilon}(x,\tau))\,, \tag{15}$$

which for a given time t aligns with the Karush-Kuhn-Tucker (KKT) conditions for both loading and unloading phases.

$$\psi_0^+ - \mathcal{H} \leqslant 0\,, \qquad \dot{\mathcal{H}} \geqslant 0\,, \qquad \dot{\mathcal{H}}(\psi_0^+ - \mathcal{H}) = 0 \tag{16}$$

2.4.5. Phase field micro-force variables

To derive the phase field micro-stress variables ω and $\boldsymbol{\xi}$, we begin by considering Eqs. (9), (11), and (15). By combining these equations, we obtain the total free energy density,

$$\psi(\boldsymbol{\varepsilon}, \phi, \nabla\phi \,|\, \bar{\alpha}) = g(\phi)\mathcal{H} + f(\bar{\alpha})\frac{G_c}{4c_w}\left(\frac{w(\phi)}{\ell} + \ell|\nabla\phi|^2\right) \tag{17}$$

which leads to the determination of the micro-stress variables

$$\omega = \frac{\partial\psi}{\partial\phi} = g'(\phi)\mathcal{H} + f(\bar{\alpha})\frac{G_c}{4c_w\ell}w'(\phi) \qquad \boldsymbol{\xi} = \frac{\partial\psi}{\partial\nabla\phi} = f(\bar{\alpha})\frac{G_c\ell}{2c_w}\nabla\phi \tag{18}$$

By integrating these constitutive relations into the phase field balance equation (4b), we derive the explicit formulation for the phase field damage evolution under cyclic loading.

$$\frac{G_c f(\bar{\alpha})}{2c_w}\left(\frac{w'(\phi)}{2\ell} - \ell\nabla^2\phi\right) - \frac{G_c\ell}{2c_w}\nabla\phi\nabla f(\bar{\alpha}) + g'(\phi)\mathcal{H} = 0 \tag{19}$$

2.4.6. Degradation and dissipation functions

Initially, our objective is to define the degradation function $g(\phi)$ for the phase field. This function governs the reduction of elastic strain energy as damage evolves and must satisfy the subsequent conditions:

$$g(0) = 1, \qquad g(1) = 0, \qquad g'(\phi) \leqslant 0 \qquad \text{for} \quad 0 \leqslant \phi \leqslant 1 \tag{20}$$

where the first two conditions act as boundaries for the intact and fully fractured states, while the last condition ensures the convergence of $\partial\psi/\partial\phi$ to a final value upon reaching a fully fractured state. In this work, we adopt the widely utilized quadratic degradation function

$$g(\phi) = (1-\phi)^2 \tag{21}$$

Additionally, we introduce the damage dissipation function $w(\phi)$, which controls the energy dissipation arising from the initiation of a new crack. It is imperative for this function to satisfy the subsequent conditions:

$$w(0) = 0, \qquad w(1) = w_1 > 0, \qquad w'(\phi) \geqslant 0 \qquad \text{for} \quad 0 \leqslant \phi \leqslant 1 \tag{22}$$

To achieve this, we utilize two widely recognized phase field damage models, namely the `AT1` model [66] and the `AT2` model [9], which have been extensively documented in the literature. These models are based on the Ambrosio and Tortorelli (AT) regularization approach [67], originally inspired by Mumford and Shah's work on image segmentation [68]. By selecting the specific functions $w(\phi) = \phi^2$ with $c_w = 1/2$ for the `AT2` model, and $w(\phi) = \phi$ with $c_w = 2/3$ for the `AT1` model, we obtain distinct expressions. The `AT1` model assumes a linear and elastic strain-stress response prior to damage initiation, whereas the `AT2` model incorporates $w'(0) = 0$. The `AT1` model lacks an inherent lower limit for the phase field variable, leading the phase field to approach negative infinity as the strain approaches 0. To resolve this issue, it is essential to establish a fracture driving force threshold, denoted as $\mathcal{H}_{\min}$, for the `AT1` model. This threshold ensures that the history field in Eq. (15) yields

$$\mathcal{H} = \max\left\{\max_{\tau\in[0,t]} \psi_0^+(\boldsymbol{\varepsilon}(\mathbf{x},\tau)),\ \mathcal{H}_{\min}\right\} \quad \text{with} \quad \mathcal{H}_{\min} = \frac{3G_c}{16\ell} \tag{23}$$

Let us now examine the uniform/homogeneous solution to Eq. (19) in order to gain a deeper understanding of the phase field length scale ℓ. As a result, in one-dimensional setting, when a sample with Young's modulus E is subjected to a uniaxial monotonic tensile stress $\sigma = g\,(\phi)\,E\varepsilon$, it will display a homogeneous stress distribution that reaches its maximum at the subsequent critical strength and strain:

$$\texttt{AT1}:\ \sigma_c = \sqrt{\frac{3EG_c}{8\ell}},\ \ \varepsilon_c = \sqrt{\frac{3G_c}{8\ell E}}\,, \qquad \texttt{AT2}:\ \sigma_c = \frac{3}{16}\sqrt{\frac{EG_c}{3\ell}},\ \ \varepsilon_c = \sqrt{\frac{G_c}{3\ell E}} \tag{24}$$

in which the parameter ℓ serves not only as a regularization parameter but also as a material characteristic that defines the strength. This unique attribute enables phase field models to anticipate the initiation of cracks and inherently consider the transition flaw size concept, as presented in Refs. [69, 70]. Throughout this paper, unless otherwise stated, we utilize the `AT1` damage model.

2.4.7. Fatigue damage

First, in line with Alessi et al. [53], the damage caused by cyclic loading is represented through the introduction of a fatigue degradation function $f(\bar{\alpha})$, which efficiently lowers the material's toughness

based on the fatigue history accumulated in the solid. In this work, we consider the fatigue degradation function that has been proposed by Seles et al. [56]:

$$f(\bar{\alpha}) = \left(1 - \frac{\bar{\alpha}}{\bar{\alpha} + \bar{\alpha}_0}\right)^2 \qquad \text{for } \bar{\alpha} \in [0, +\infty] \tag{25}$$

in which the material parameter $\bar{\alpha}_0$ is intended to be determined using fatigue test data. Moreover, it is necessary for the fatigue history variable $\bar{\alpha}$ to depict the cumulative effect of any parameter α that defines the cyclic history of the material. Following Carrara et al. [54], we uphold the fundamental energy-based nature of the model and employ the tensile (active) segment of the elastic strain energy density, as outlined in Section 2.4.3, as the fatigue history variable:

$$\alpha = g(\phi)\psi_0^+(\boldsymbol{\varepsilon}) \tag{26}$$

By employing the *degraded* strain energy density, we ensure that the value of the fatigue history variable $\bar{\alpha}$ remains unaffected by the singularity at the crack tip. Consequently, the progression of the fatigue history variable $\bar{\alpha}$ can be defined as

$$\bar{\alpha}_{t+\Delta t} = \bar{\alpha}_t + \mathcal{N}\Delta\bar{\alpha} \tag{27}$$

which enables the integration of multiple load cycles $\mathcal{N} > 1$ within a single increment. The dimensionless quantity $\Delta\bar{\alpha}$ represents the method used to account for fatigue damage accumulation. In our previous study [59], we proposed a comprehensive formula for fatigue damage accumulation, taking into account three factors: (i) the slope of the S-N curve, (ii) the material's endurance limit, and (iii) the impact of the stress ratio. We also suggested considering fatigue damage accumulation during a single reversal per cycle. The formula can be expressed as follows:

$$\Delta\bar{\alpha} = \left(\frac{\alpha_{\max}}{\alpha_n}\right)^n \left(\frac{1-R}{2}\right)^{2\eta n} H\left(\max_{\tau\in[0,t]} \alpha_{\max}\left(\frac{1-R}{2}\right)^{2\eta} - \alpha_e\right) \tag{28}$$

where the material parameter n is introduced as an exponent, which can be adjusted to align with the slope of any S-N curve. To maintain dimensional coherence, a normalization parameter $\alpha_n = 1/2\sigma_c\varepsilon_c$ is defined. The fatigue threshold variable $\alpha_e = \sigma_e^2/(2E)$ represents the point below which cyclic damage does not occur, with σ_e denoting the material's endurance stress limit. The stress ratio R is defined as the ratio of minimum principal stress $\sigma_{1,\min}$ to maximum principal stress $\sigma_{1,\max}$ within each cycle. The inclusion of R is inspired by the Walker mean stress relationship [71], widely used to improve Basquin-type laws to accommodate non-zero mean stresses. To characterize the material's susceptibility to mean stress, a material constant η is introduced, which ranges from 0 to 1.

3. Numerical implementation

In this section, we provide the details of the numerical implementation, which begin with the finite element discretization. This is followed by the formulation of the residuals and the stiffness matrices.

3.1. Finite element discretization

By employing Voigt notation and assuming a plane strain condition, the primary variables of the problem are discretized using nodal values. These variables include $\mathbf{u}_i = \{u_x, u_y\}^\mathsf{T}\, i$ and ϕ_i at node i. The discretization of these variables can be expressed as:

$$\mathbf{u} = \sum_{i=1}^{m} \boldsymbol{N}_i^u \mathbf{u}_i \qquad \text{and} \qquad \phi = \sum_{i=1}^{m} N_i \phi_i \tag{29}$$

where m represents the total number of nodes for each element. N_i denotes the shape functions associated with node i, and $\boldsymbol{N}_i^u$ represents the shape function matrix. The shape function matrix $\boldsymbol{N}_i^u$ is a diagonal matrix where the shape function N_i is placed on its diagonal elements. Accordingly, the discretization of the related gradient quantities can be expressed as follows:

$$\boldsymbol{\varepsilon} = \sum_{i=1}^{m} \boldsymbol{B}_i^u \mathbf{u}_i \qquad \text{and} \qquad \nabla\phi = \sum_{i=1}^{m} \mathbf{B}_i \phi_i \tag{30}$$

where $\boldsymbol{B}_i^u$ represents the strain-displacement matrix, while $\mathbf{B}_i$ is a vector that consists of the spatial derivatives of the shape functions.

3.2. Residuals and stiffness matrices

By employing the finite element discretization described in (29) and (30), and taking into account that (3) must hold for any admissible variations of the virtual quantities $\delta\square$, the corresponding residuals can be derived as follows:

$$\begin{aligned} \mathbf{r}_i^u &= \int_\Omega \big[g(\phi) + k\big] (\boldsymbol{B}_i^u)^\mathsf{T} \boldsymbol{\sigma_0}\, \mathrm{d}V - \int_\Omega (\boldsymbol{N}_i^u)^\mathsf{T} \mathbf{b}\, \mathrm{d}V - \int_{\partial\Omega_h} (\boldsymbol{N}_i^u)^\mathsf{T} \mathbf{h}\, \mathrm{d}S \\ r_i^\phi &= \int_\Omega \left\{ g'(\phi) N_i\, \mathcal{H} + f(\bar{\alpha}) \frac{G_c}{4c_w} \left(\frac{w'(\phi)}{\ell} N_i + 2\ell (\mathbf{B}_i)^\mathsf{T} \nabla\phi \right) \right\} \mathrm{d}V - \int_{\partial\Omega_\mathfrak{f}} N_i\, \mathfrak{f}\, \mathrm{d}S \end{aligned} \tag{31}$$

To calculate the consistent tangent stiffness matrices, the residuals can be differentiated with respect to the nodal variables, resulting in the following expression:

$$\begin{aligned} \boldsymbol{K}_{ij}^u &= \frac{\partial \mathbf{r}_i^u}{\partial \mathbf{u}_j} = \int_\Omega \big[g(\phi) + k\big] (\boldsymbol{B}_i^u)^\mathsf{T} \boldsymbol{\mathcal{L}}_0\, \boldsymbol{B}_j^u\, \mathrm{d}V \\ \boldsymbol{K}_{ij}^\phi &= \frac{\partial r_i^\phi}{\partial \phi_j} = \int_\Omega \left\{ \left(g''(\phi)\, \mathcal{H} + f(\bar{\alpha}) \frac{G_c}{4c_w \ell} w''(\phi) \right) N_i N_j + f(\bar{\alpha}) \frac{G_c \ell}{2c_w} (\mathbf{B}_i)^\mathsf{T} \mathbf{B}_j \right\} \mathrm{d}V \end{aligned} \tag{32}$$

We then employ an efficient quasi-Newton monolithic solution strategy [61, 62] to solve the resulting finite element system of equations

$$\begin{bmatrix} \boldsymbol{K}^u & 0 \\ 0 & \boldsymbol{K}^\phi \end{bmatrix} \begin{Bmatrix} \mathbf{u} \\ \boldsymbol{\phi} \end{Bmatrix} = \begin{Bmatrix} \mathbf{r}^u \\ \mathbf{r}^\phi \end{Bmatrix} \tag{33}$$

4. Results

In this section, we present the outcomes of numerical experiments conducted to evaluate the performance of our phase field fatigue model. Initially, a boundary layer formulation is utilized to gain insights into fatigue crack growth (FCG) under the assumption of small-scale yielding (Section 4.1). By conducting a parametric study, we examine the impact of fatigue model and material parameters on the FCG rate curves, establishing a relationship between S-N curves and FCG rate curves. Subsequently, we compare the model's predictions with experimental data obtained from compact tension (CT) tests (Section 4.2). Additionally, we explore the model's capability to predict the transition flaw size effect by analyzing a finite plate containing an internal crack of varying length (Section 4.3). Finally, we verify the model's predictions against experimental data on curvilinear crack path trajectories conducted on single edge notched samples containing a circular hole (Section 4.4).

4.1. Boundary Layer model

First, we investigate the fatigue crack growth behavior under small-scale yielding conditions using a boundary layer formulation. Our approach involves analyzing a circular region of a body that contains a crack. To simulate this, we apply a remote K_I field to the upper half of the domain, taking advantage of symmetry (as depicted in Fig. 1). The remote K_I field is elastic and is generated by prescribing the displacements of the outer region nodes based on the Williams expansion [72]. In the polar coordinate system (r, θ) centered at the crack tip, the displacements of the nodes are described by their horizontal and vertical components

$$\begin{aligned} u_x(r,\theta) &= K_I \frac{1+\nu}{E} \sqrt{\frac{r}{2\pi}} \cos\left(\frac{\theta}{2}\right) \left[3 - 4\nu - \cos(\theta)\right] \\ u_y(r,\theta) &= K_I \frac{1+\nu}{E} \sqrt{\frac{r}{2\pi}} \sin\left(\frac{\theta}{2}\right) \left[3 - 4\nu - \cos(\theta)\right] \end{aligned} \tag{34}$$

in which we define the stress intensity factor K_I as a sinusoidal function to capture the cyclic loading conditions

$$K_{\mathrm{I}} = K_{\mathrm{m}} + \frac{\Delta K}{2} \sin(2\pi f\, t) \quad \text{with} \quad K_{\mathrm{m}} = \frac{\Delta K}{2} + \frac{R\,\Delta K}{1-R} \tag{35}$$

where $f = 1$ Hz denote the load frequency, t represent the test time, K_{m} indicate the average value of the load, $\Delta K = K_{\max} - K_{\min}$ signify the load range, and $R = K_{\min}/K_{\max}$ denote the load ratio. To discretize the circular area, we utilize 4,572 bilinear quadrilateral plane strain elements with full integration. To guarantee adequate resolution of the fracture process zone, the mesh undergoes refinement in the area of crack propagation, ensuring that the characteristic element length h is small enough ($h < \ell/5.4$ [43]). The assumed material properties read $E = 210$ GPa, $\nu = 0.3$, $G_c = 16$ kJ/m^2, $\ell = 0.0048$ mm, $\sigma_e = 650$ MPa. In accordance with the definitions provided by [69, 70], we establish a reference stress intensity factor K_0 and a fracture process zone length L_f:

$$K_0 = \sqrt{\frac{G_c E}{(1-\nu^2)}} \quad \text{and} \quad L_f = \frac{G_c\,(1-\nu^2)}{E} \tag{36}$$

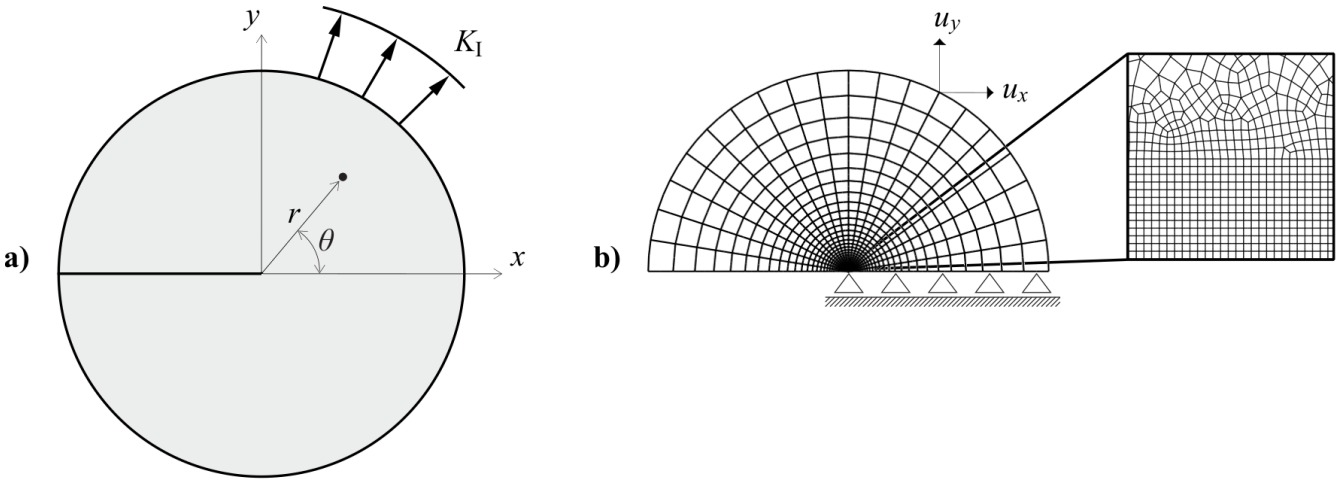

Figure 1: Boundary layer model. (a) Geometry and loading conditions, and (b) finite element mesh, featuring details of the mesh near the crack tip.

4.1.1. Parametric study

A sensitivity analysis is first performed to determine the effect of fatigue material/model parameters, detailed in Section 2.4.7. The investigation initiates with an analysis of the significance of the power exponent n. The results, illustrated in Fig. 2a, are represented as normalized fatigue crack extension against the number of load cycles. These calculations are executed for a load range of $\Delta K/K_0 = 0.1$. From the results, it is evident that with a fixed number of cycles, an increase in the power exponent corresponds to smaller fatigue crack extension. Fig. 2a reveals that the curves can be fitted with a straight line to calculate the slope, which symbolizes the crack growth rates. Fatigue crack growth rates (FCGR) for different stress intensity factor ranges ΔK and power exponent values

n are shown in Fig. 2b, which are displayed on a logarithmic scale. The linear trend within the Paris regime, a region where the crack growth maintains its stability, is evident in these findings. On surpassing this region, the crack growth rate escalates noticeably, signifying an unstable crack progression. Interestingly, a distinct association is perceived between the quantity of n and the slope

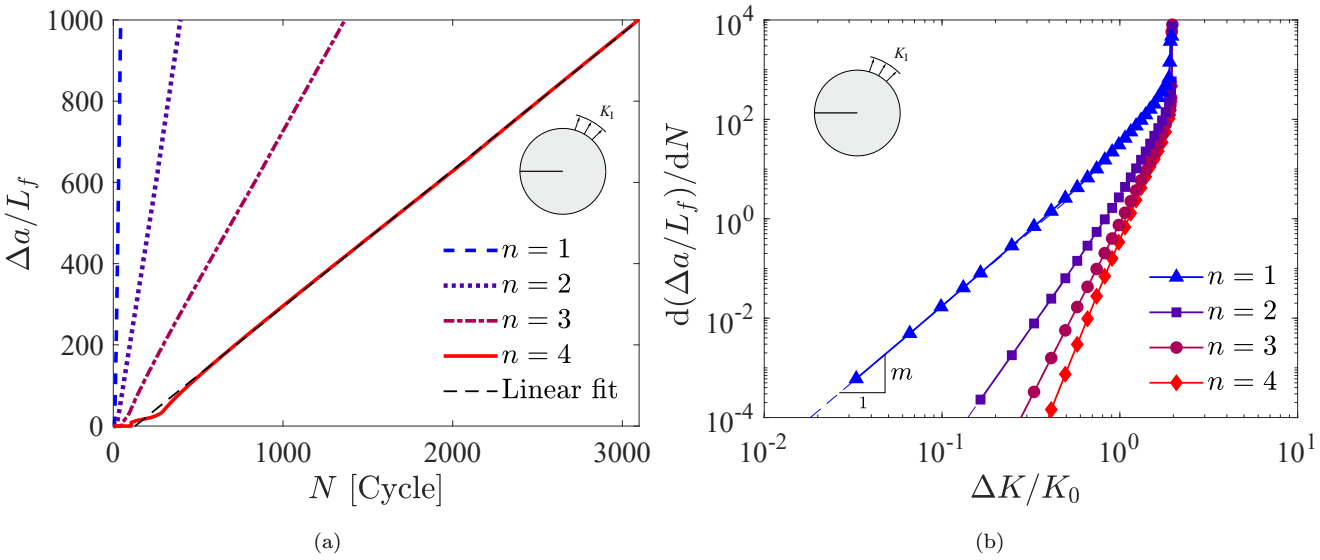

(a) (b)

Figure 2: Boundary layer model. Influence of the power exponent n on (a) crack extension (b) the FCGR curve.

m of the curves in the Paris region. With higher n values, the FCGR shows a heightened sensitivity to changes in the stress intensity factor range. Comparable to the S-N curve presented in Ref. [59], the power exponent n provides modelling adaptability to precisely determine the slope m of the Paris curve for various materials. Additionally, our model's capacity to link the S-N and FCGR curves will be proven later. It is vital to highlight that changes in the power exponent n do not affect the final fracture, as all curves meet at the critical stress intensity factor K_{Ic} of the material.

The results of parametric study, evaluating the effects of α_e and $\bar{\alpha}_0$ on the FCGR curves, are depicted in Figs. 3a and 3b. Fig. 3a illustrates that lowering the threshold parameter α_e, defined in Eq. (28), to include a material's stress endurance limit, results in a smaller nucleation/threshold area. This reduction is reflected by a decrease in the material's threshold stress intensity factor K_{th}, signifying a low (or negligible) crack growth rate. Moreover, Fig. 3b demonstrates that a rise in $\bar{\alpha}_0$ corresponds to increased FCGRs, notably within the Paris region, without any substantial influence on the other two exterior regions. Importantly, despite variations in their respective values, the slopes of the curves in the Paris region remain relatively steady for both α_e and $\bar{\alpha}_0$.

We conclude our sensitivity analyses by exploring the effect of the load ratio on the FCGR curve's characteristics in our model. As illustrated in Fig. 4, the load ratio R significantly influences all

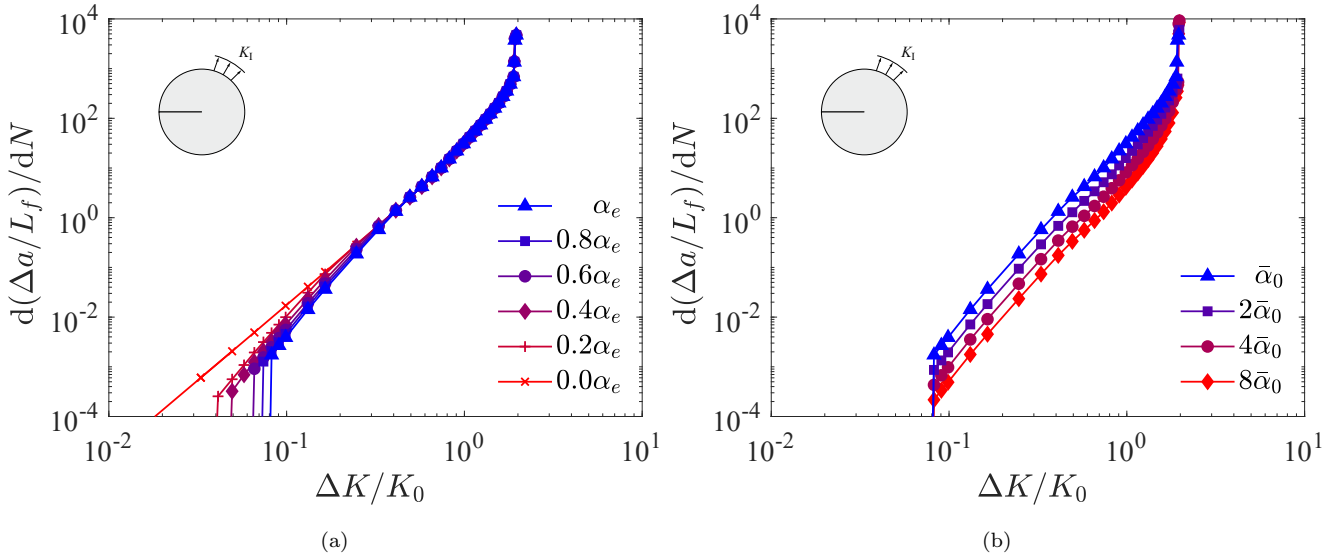

(a) (b)

Figure 3: Boundary later model. Sensitivity of the FCGR curve with respect to: (a) the threshold α_e, and (b) fatigue model parameter $\bar{\alpha}_0$.

three regions of the FCGR curves. This is in line with experimental observations [6, 73], wherein a notable rise in FCGR for a specified ΔK is observed as the load ratio R increases. Additionally, both the critical stress intensity factor K_{Ic} and the threshold stress intensity factor K_{th} of the material decrease as R rises. This reduction can be ascribed to the fact that higher load ratios result in an increased maximum value of the applied cyclic load $K_{\max} = \Delta K/(1-R)$.

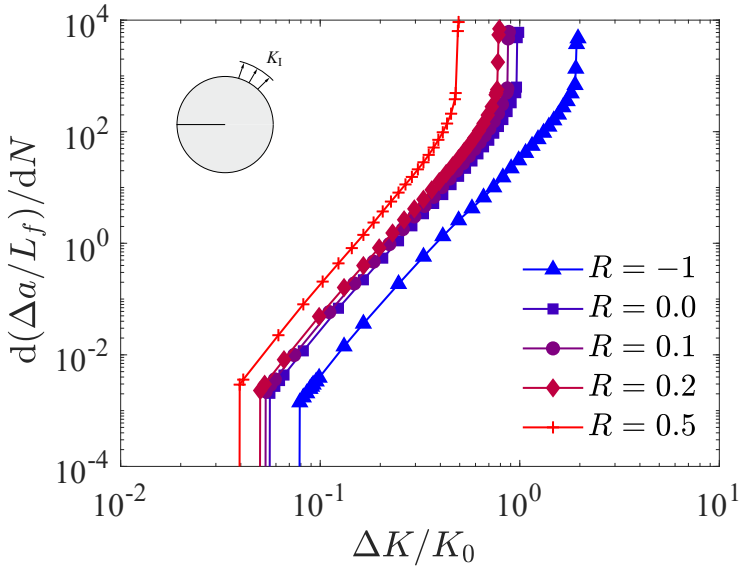

Figure 4: Boundary layer model. Influence of the load ratio R on the FCGR curve.

4.1.2. A link between S-N curve and Paris law

We then explore how our model bridges the S-N and Paris approaches for brittle materials. To start, we conduct uniaxial fatigue simulations on a smooth bar. A semi-analytical approach, focusing on the homogeneous solution to Eq. (19), is adopted to address this issue. The bar experiences a completely reversed cycle of remote stress variation. We consider three distinct values for the power exponent: $n = 1$, 2, and 3, which correspond to S-N slope values of $-1/m \simeq 3$, 5, and 7 respectively, as referenced in Ref. [59, Eq. (40) and Table 1]. The slope of the S-N curve and its intersection with the $\log N$ (or $\log \sigma$) axis equate to the fatigue parameters n and $\bar{\alpha}_0$, explained in detail in [59]. For our analysis, we propose a theoretical S-N curve, intersecting with the $\log \sigma$ axis at the material's strength σ_c, as specified by Eq. (24). Hence, assuming $n = 1$ and data ($\sigma^{\infty}_{\max}/\sigma_c = 1/3$) from our proposed S-N curve, we approximate $\bar{\alpha}_0$ as 3/2. The results, shown in Fig. 5a, represent the (normalized) remote stress amplitude versus the number of load cycles to failure, depicted on a log-log plot. The calculated S-N curves display linear behavior, adhering to a Basquin relationship, proposed by Andersons et al. [74].

$$\frac{\sigma_{\max}}{\sigma_c} = (N)^{-\frac{1}{m}} \ , \tag{37}$$

with the curves converge at the material's strength value on the $\log \sigma_{\max}$ axis. Subsequently, we carry out fatigue crack growth (FCG) simulations using our boundary layer formulation, maintaining the same fatigue material parameters as those in our smooth bar. Fig. 5b showcases the numerical results alongside the analytical outcomes derived from a Paris relationship, introduced in [74]

$$\frac{\mathrm{d}a}{\mathrm{d}N} = \mathcal{C}\left(\frac{K_I}{K_{Ic}}\right)^m \quad \text{with} \quad \mathcal{C} = \left(\frac{m}{m-2}\right) r_c \quad \text{and} \quad r_c = \frac{1}{2\pi}\left(\frac{K_{Ic}}{\sigma_c}\right)^2 , \tag{38}$$

where the Paris pre-factor $\mathcal{C}$ and the exponent m are both connected to the S-N curve parameters (Basquin law), as specified in Eq. (37). Our results emphasize a robust link between two crucial fatigue phenomena. The exponents of the Basquin law and the Paris law are interrelated, with the latter seeming to be the inverse of the former. The calculated FCGR curves exhibit a linear pattern, with the fitted curves yielding Paris pre-factor values that remarkably align with the analytical findings. This insight implies the feasibility of predicting a brittle solid's FCG behavior using S-N data, and conversely. With the introduction of our phase field fatigue model, we can integrate these typically independently addressed phenomena. This could potentially simplify analysis and design methodologies while also reducing the amount of testing required for fatigue damage characterization of brittle materials.

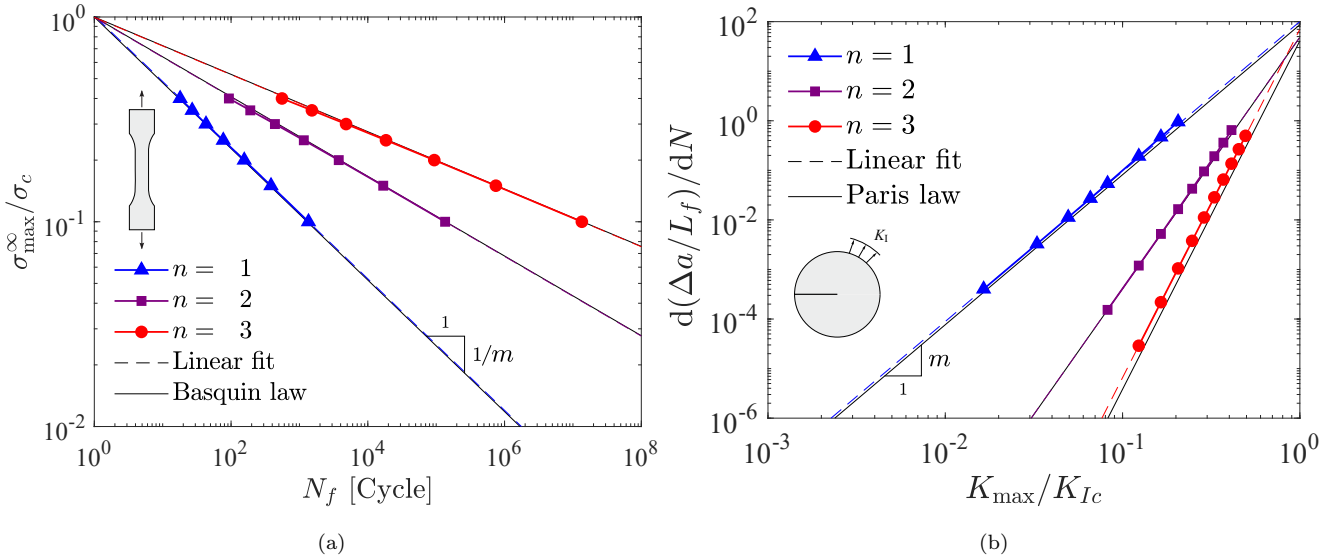

Figure 5: A connection between fundamental fatigue phenomena: (a) S-N curve and (b) Paris law. Results have been obtained for $R = -1$ and $\alpha_e = 0$.

4.2. Compact-Tension test

To further validate the accuracy of the proposed model in predicting fatigue crack growth (FCG) rates, we utilize the widely accepted compact tension (CT) test. The configuration of the CT test, displayed in Fig. 6, aligns with the experimental setup detailed by Mehmanparast et al. [75]. The FCG experiments were part of the SLIC (Structural Life-cycle Industry Collaboration) joint industry project, aimed at deepening our understanding of fatigue in butt-welded thick steel plates, a vital component in the production of offshore wind turbine foundations. The material chosen for the FCG tests is S355G8+M (EN-10225:1) structural steel, often employed in offshore monopiles for its superior weldability and resilience against harsh offshore conditions. Our analysis specifically concentrates on the experimental data derived from the parent material, also known as the base metal (BM), in an inert environment. As it is common with S355 steels, the assumed material properties read $E = 210$ GPa, $\nu = 0.3$, and $G_c = 48$ kJ/m^2. We conduct a set of numerical simulations on half of the domain, leveraging its symmetry. The specimens undergo cyclic load variations with the maximum load $P_{\max}$ and the load ratio R (refer to Table 1). The computational domains comprise around 15,750 - 17,000 bilinear quadrilateral plane strain elements with full integration. To ensure adequate resolution of the fracture process zone during crack propagation, a mesh refinement is employed in the specific region. This refinement incorporates a small value of $\ell = 0.3$ mm as the length scale parameter for the phase field.

The determination of the change in stress intensity factor, based on the assumptions of Linear

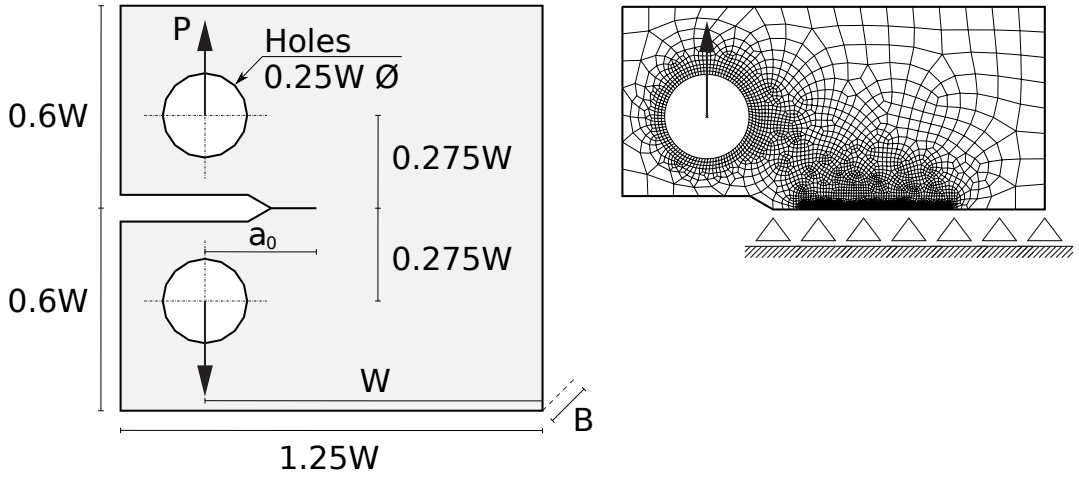

Figure 6: Compact tension (CT) test. Geometry, boundary conditions and finite element mesh.

Test ID	W [mm]	B [mm]	a_0 [mm]	$P_{\max}$ [kN]	R
A1	49.9	16.0	16.5	9.0	0.1
A2	49.9	16.0	14.8	6.7	0.1
B1	50.0	15.9	14.7	10.0	0.1
B2	50.0	15.9	14.5	10.0	0.1

Table 1: Compact tension (CT) test dimensions and loading conditions.

Elastic Fracture Mechanics (LEFM), can be referenced in the work of Tada et al. [76]

$$\Delta K = \frac{\Delta P}{B\sqrt{W}} \frac{(2+\beta)}{(1-\beta)^{3/2}} \left(0.886 + 4.64\beta - 13.32\beta^2 + 14.72\beta^3 - 5.6\beta^4\right) \tag{39}$$

with $\beta = a/W$. The fatigue parameters, $n = 1.0$ and $\bar{\alpha}_0 = 89.2$, are derived from the basic design S-N curve for structural steels, according to the slope, intercept, and fatigue limit outlined in the DNV-GL standard [77]. Our study primarily targets category C[1], associated with non-welded classifications in an inert environment. The S-N curve characteristic to this category exhibits a slope of $m = 3.0$, an intercept of 12.592 (on the $\log N$ axis), and a fatigue limit of $\sigma_e = 73.10$ MPa. It is important to underscore that the S-N curve generated from lab-based fatigue tests on smooth/polished S355 steel samples indicates a higher m value, as detailed in Refs. [78, 79]. Experimental and numerical results are displayed in Fig. 7 on a log scale, presenting the fatigue crack growth (FCG) rates ($\mathrm{d}a/\mathrm{d}N$) in relation to the stress intensity factor range ΔK. We used a 7-point incremental polynomial method,

[1]Manually gas cut material or material with machine gas cut edges with shallow and regular drag lines.

as advised by the ASTM standard [80], to determine the FCG rates. The graph also demonstrates the Paris law relationships proposed by the BS7910 standard [81], encompassing both the simplified and two-stage models. It is evident that the *virtual* FCG rate curves obtained align well with the recorded data. Both test and simulation data exhibit linear trends in the Paris regime. The data reveals that within the specified stress intensity factor range, the initial set of FCG data points coincide with or are beneath the 2-stage law recommended by BS7910. However, the following set of data points lies within the boundaries of the simplified and 2-stage laws, tending towards the simplified law. This deduction signifies that, for the specified stress intensity factor range, the simplified Paris-law advised by BS7910 provides a cautious estimation of the FCG behavior in an inert environment. Extending the conclusions of Mehmanparast et al. [75], it is noteworthy to mention a noticeable variation in the FCG behavior between the samples A1 and A2 from Test Centre A, as well as B1 and B2 from Test Centre B. This disparity is especially prominent in the initial phases of the FCG tests. Such discrepancies can likely be attributed to inherent material property differences, a factor that could greatly impact the early-stage FCG behavior of these specimens.

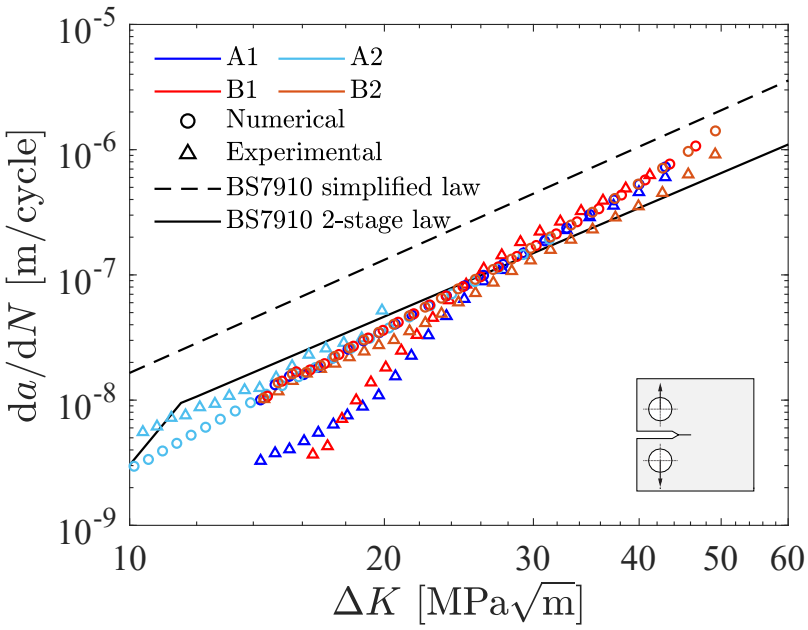

Figure 7: Virtual and experimental FCGR curves from compact tension (CT) test. The graph displays the simplified and two-stage trends suggested in BS7910 standard [81].

4.3. Transition flaw size effects

We now examine the efficacy of our model in reflecting the interaction between material and structural size effects. As highlighted in Section 2.4.6, incorporating a finite length scale ℓ^+ into our

phase field models results in a critical stress inversely proportional to the square root of ℓ. This critical stress is not found in Griffith's theory or linear elastic fracture mechanics (LEFM), which underscores the importance of ℓ as a material parameter. The use of a positive, constant ℓ is influenced by the incapacity of Griffith's theory to account for well-documented size effects. A key size effect is the concept of transition flaw size, wherein a crack smaller than the critical flaw size does not propagate, leading to failure at the material strength (or yield strength σ_y in the context of plastic design). In this regard, our objective is to showcase the natural occurrence of the transition flaw size principle within our phase field model, taking into account both monotonic and cyclic loading conditions. In

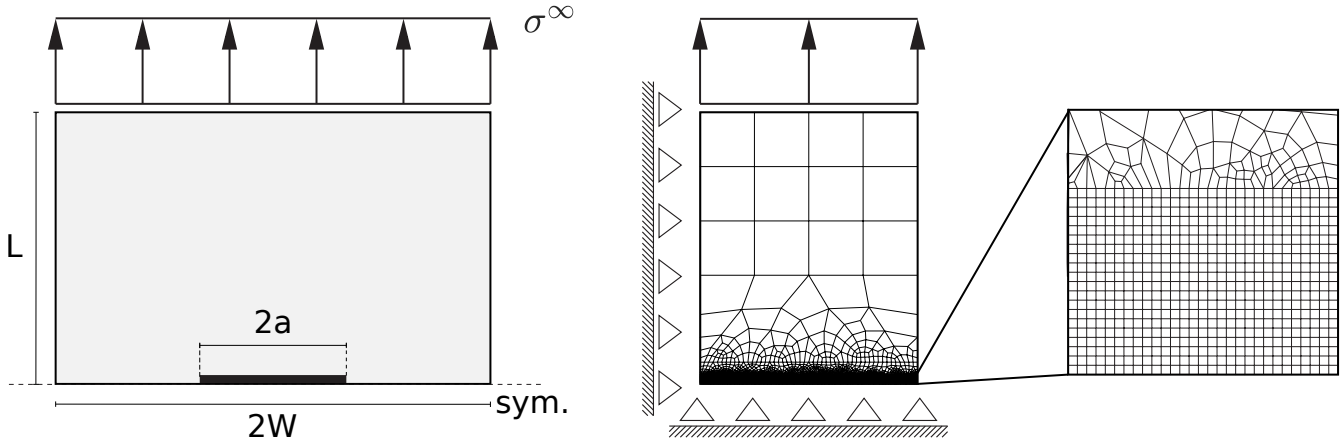

Figure 8: Internal crack of varying length in a finite plate under uniform cyclic remote stress loading. Geometry, boundary conditions and finite element mesh.

pursuit of our goal, we assess a pre-existing finite-length crack within a plate of finite width, with the plate dimensions given as $L = 4W = 4$ mm (refer to Fig. 8). This standard boundary value problem has been previously examined under static/monotonic loading conditions in Ref. [69]. We undertake a range of numerical simulations on one quarter of the domain, taking advantage of its symmetry, and the initial crack half-length a is adjusted from $0.002W$ to $0.512W$. To introduce the loading, we apply a fully-reversed cyclic remote stress fluctuation to the top edge of the plate. The material properties are assumed to be $E = 210$ GPa, $\nu = 0.3$, $G_c = 50$ kJ/m^2, $\ell = 0.02$, $\sigma_e = 250$ MPa, n=1.0, and $\bar{\alpha} = 1.0$. The plate is discretized into 12,302 bilinear quadrilateral plane stress elements with full integration. According to [76], the crack propagation threshold under the assumptions of Linear Elastic Fracture Mechanics (LEFM) can be determined by

$$\sigma^\infty = \frac{1}{Y}\sqrt{\frac{EG}{\pi a}} \qquad \text{with} \qquad Y = \left(\sec\frac{\pi a}{2W}\right)^{1/2}\left[1 - 0.025\left(\frac{a}{W}\right)^2 + 0.06\left(\frac{a}{W}\right)^4\right] \tag{40}$$

The outcomes are depicted in the Kitagawa-Takahashi diagram (see Fig. 9), expressing the amplitude of remote stress against the crack half-length. The graph displays various essential criteria,

including the strength failure limit $\sigma = \sigma_c$ (plastic failure is indicated when $\sigma_c = \sigma_y$), the Griffith (LEFM) criterion $G = G_c$, and the limit for endurance stress $\sigma = \sigma_e$. The amplitude of stress is normalized in light of material strength, as given in Eq. (24). The capacity of the model to bridge stress and toughness criteria for static and fatigue fracture is transparent. It aligns well with the Griffith criterion when evaluating larger cracks and smoothly moves to a strength-based failure as the crack size falls under the critical flaw size. Data points can be incorporated at a constant number of cycles for finite life (e.g. 10^2 and 10^4 cycles), with the higher limit pointing to static failure and the lower one indicating infinite life (cracks that do not propagate). For infinite life, a curve ($G = G_{th}$) has been fit to the results in the toughness-oriented area, enabling us to calculate a transition flaw size associated with fatigue where the curves for G_{th} and σ_e intersect (i.e. $a/W \approx 0.007$). It is worth mentioning that the flaw size estimated here is less than that for its static equivalent ($a/W \approx 0.020$), and decreases as the load cycles increase, thus bridging the gap between these two extremes.

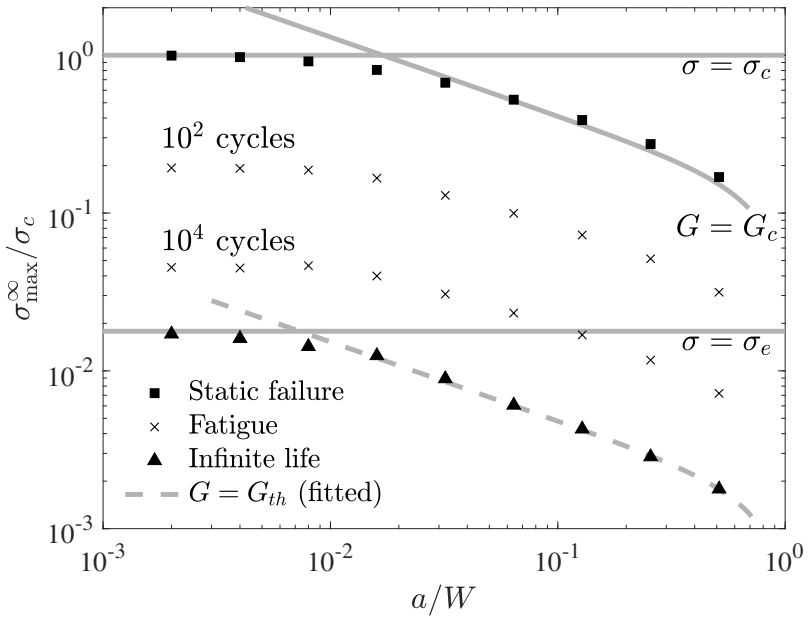

Figure 9: Transition flaw size effect (also known as Kitagawa-Takahashi diagram).

4.4. Curvilinear crack growth prediction

We now test the predictive potential of our model in projecting the path of curvilinear cracks formed under mixed-mode stress conditions. These initial experiments were performed by Chudnovsky et al. [82] on single edge notched samples of polystyrene. The dimensions of these samples (in mm) are illustrated in Figure 10. In each of these samples, a circular hole is strategically placed at different distances ($d_c = 2.5$, 3.5, 4.5, and 5.5 mm) from the center of the hole to the anticipated

trajectory of the crack. This experimental design allows for the exploration of the interaction between the hole, which serves as a stress raiser, and an incoming crack. According to Ref. [82], crack growth in the material tested involves the formation of a distinct damage zone, marked by the emergence of crazes. Importantly, the size of this damage zone is considerably less than the geometric factor of the problem, particularly the diameter of the hole. The presence of a hole affects the stress field to a distance approximately equivalent to its diameter. Consequently, a hole positioned ahead of the crack tip is expected to cause a deflection in the crack path near the hole. A summary of the test data is reported in the work by Rubinstein [83].

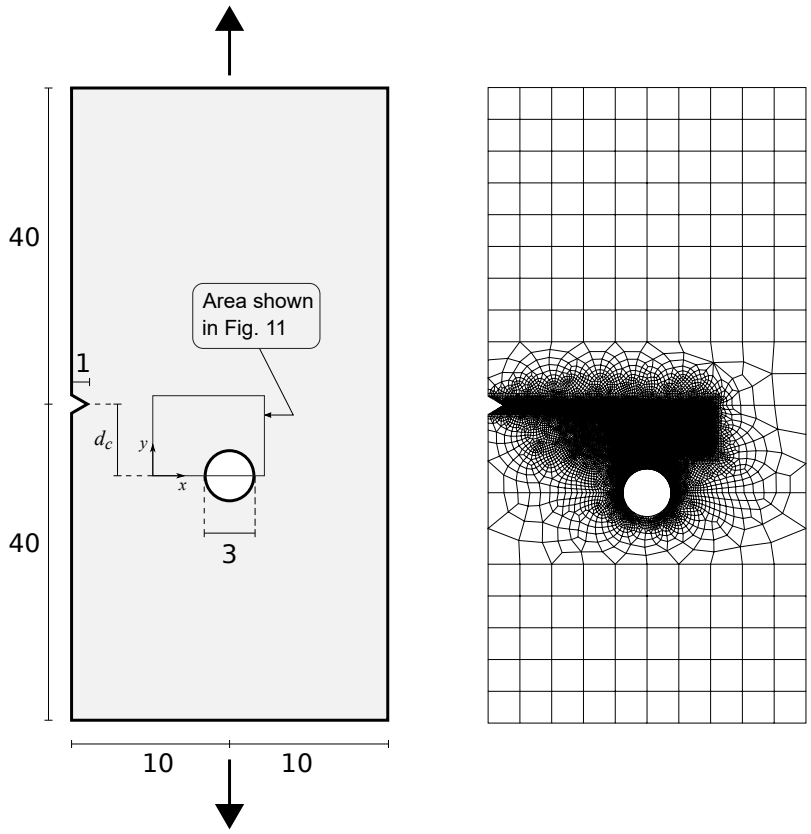

Figure 10: Notched rectangular plate with a hole. Geometry (with dimensions in mm), loading conditions and finite element mesh. d_c is the distance from the hole center to the anticipated crack path.

Simulations were performed utilizing remote stress and strain amplitudes (with a load ratio of $R = 0.1$), enabling a comparison between load-controlled and displacement-controlled numerical experiments. In the case of load-controlled tests, a maximum remote stress amplitude of 15 MPa was reported, as per [82]. When the crack tip approached the active zone (area shown Fig. 10), the load was appropriately reduced to accurately capture the hole's impact on the crack deflection. The extent of this load reduction was not detailed in Ref. [82], leading us to assume a maximum remote stress

amplitude of 10 MPa at this stage. As for the displacement-controlled tests, we assume a maximum remote strain amplitude of 0.55 mm, thereby initiating a remote stress amplitude of 15 MPa. As it is common with polystyrene, the assumed material properties read $E = 2.0$ GPa, $\nu = 0.3$, $G_c = 14$ kJ/m^2, $\sigma_e = 2/3\sigma_c = 40$ MPa, according to the data reported in Refs. [84, 85]. In addition, we assume the fatigue parameters of n=1.0 and $\bar{\alpha} = 0.1$. The computational domain is comprised of 223,838 bilinear quadrilateral plane strain elements with full integration. To ensure adequate resolution of the fracture process zone during crack propagation, a mesh refinement is employed in the active region. This refinement incorporates a small value of $\ell = 0.06$ mm as the length scale parameter. The findings derived from this analysis are depicted in Fig. 11. This figure displays four experimental crack paths and their corresponding numerical predictions, which have been normalized by the hole radius, within the effective area (refer to Fig. 10). Our results demonstrate that the model precisely interprets the impact of the hole on the incoming crack. As the vertical distance between the hole and the notch diminishes, the hole's effect intensifies, leading to a rotation of the damage zone and a subsequent alteration in its form. Observing these outcomes, three unique scenarios of crack interaction with a hole have been recognized: (i) crack attraction ($y/r = 1.67$), (ii) both attraction and repulsion ($y/r = 2.33$ and 3.00), and finally, (iii) cases where the hole does not visibly influence the crack path. It is worth highlighting that the integration of the material's fatigue limit into the analysis has effectively restrained the initial build-up of fatigue around the holes. This strategic inclusion avoids the formation of new secondary cracks before the primary crack encounters the holes. To conclude, the model's prediction of the crack path considerably aligns with the experimental findings, confirming its credibility and efficiency.

5. Conclusions

We have presented a generalized phase field formulation for modelling fatigue crack growth (FCG) behaviour. The modelling framework builds upon our previous accumulation strategy [86], which substantially accelerates fatigue simulations. Furthermore, this strategy facilitates a connection between S-N curves and FCG rate curves, providing an avenue for modelling various Paris law behaviors, fatigue threshold limits, and the effects of load ratios. The finite element (FE) method is utilized to numerically implement this theoretical framework. The resulting FE system of equations is then solved with the aid of a quasi-Newton monolithic solution scheme [61, 62]. We have also incorporated a new accumulation strategy [60], which brings additional speed to fatigue calculations by enabling the integration of multiple load cycles within a single increment (referred to as "cycle-jumping"). To

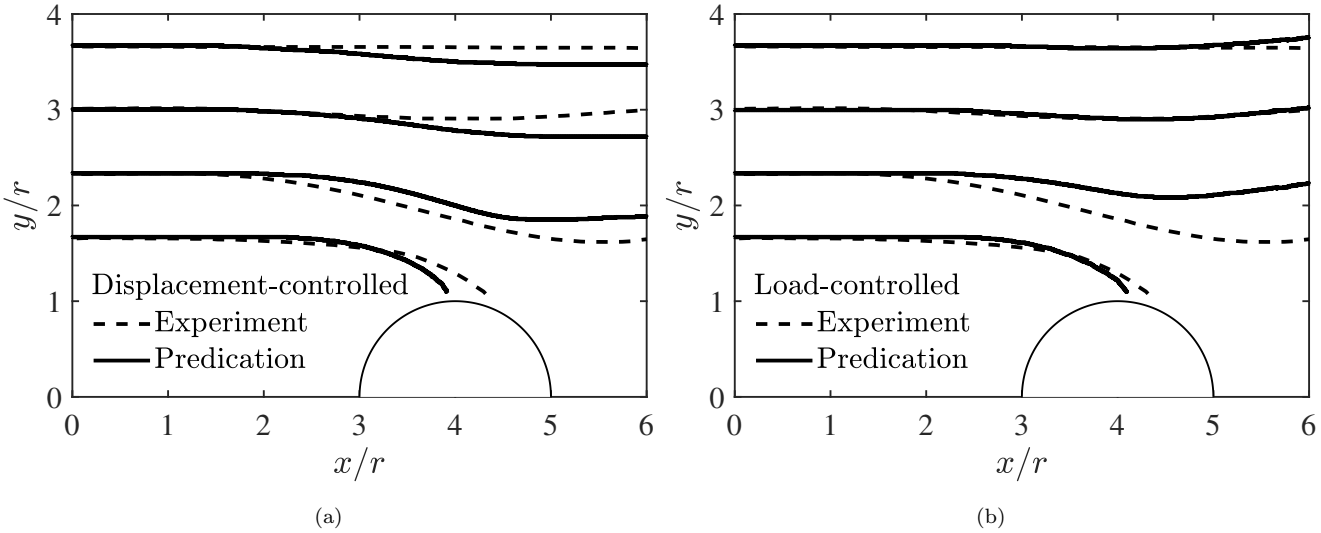

Figure 11: Virtual and experimental crack path trajectories from single edge notched polystyrene plates: (a) load-controlled, and (b) displacement-controlled tests.

assess the performance of our modelling capabilities, we conduct comprehensive FCG analyses. The key findings of this study include:

- The model is able to accurately pinpoint and differentiate the three distinct stages in the fatigue crack growth (FCG) process: the threshold region (where little to no crack growth occurs), the Paris region (characterized by steady, consistent growth), and the fracture region (noted for rapid and significant crack growth).

- The model successfully captures the load ratio R effect on the fatigue response. It predicts, in accordance with experimental observations, that a decrease in R for a fixed load range results in an increase in the FCG rate, a decrease in the material's critical stress intensity factor (K_{Ic}), and a decline in the threshold stress intensity factor (K_{th}).

- The model effectively unifies two key fatigue phenomena, establishing a robust link between the exponents of the Basquin law (S-N curves) and the Paris law of a brittle material.

- The model adeptly captures the transition flaw size effect, reconciling strength- and toughness-criteria for static and fatigue fracture. It shows remarkable consistency with the toughness-driven mechanism when dealing with large cracks (LEFM), while smoothly transitioning to a strength-driven one when the crack length reduces below the transition flaw size.

- Lastly, the model aligns remarkably well with datasets obtained from laboratory experiments. This includes the FCG rate data from compact tension (CT) tests conducted on S355G8+M

steel, and data concerning complex crack path trajectories derived from pre-cracked polystyrene samples subject to mixed-mode fracture.

6. Acknowledgements

A. Golahmar acknowledges financial support from Vattenfall Vindkraft A/S and Innovation Fund Denmark (grant 0153-00018B). E. Martínez-Pañeda acknowledges financial support from UKRI's Future Leaders Fellowship programme [grant MR/V024124/1].

References

[1] R. I. Stephens, A. Fatemi, R. R. Stephens, H. O. Fuchs, Metal Fatigue in Engineering, 2nd Edition, John Wiley & Sons, 2000.

[2] S. Suresh, Fatigue of Materials, 2nd Edition, Cambridge University Press, 1998.

[3] A. Wöhler, Über die festigkeitsversuche mit eisen und stahl, Ernst & Korn, 1870.

[4] O. H. Basquin, The exponential law of endurance tests, in: Proc ASTM, Vol. 10, 1910, pp. 625–630.

[5] P. Paris, F. Erdogan, A critical analysis of crack propagation laws, Journal of Basic Engineering 85 (1963) 528–533.

[6] S. R. Mettu, V. Shivakumar, J. M. Beek, F. Yeh, L. C. Williams, R. G. Forman, J. J. McMahon, J. C. Newman, Nasgro 3.0 - a: software for analyzing aging aircraft, Nasa Conference Publication (1999) 792–801.

[7] G. A. Francfort, J. J. Marigo, Revisiting brittle fracture as an energy minimization problem, Journal of the Mechanics and Physics of Solids 46 (1998) 1319–1342.

[8] B. Bourdin, G. A. Francfort, J. J. Marigo, Numerical experiments in revisited brittle fracture, Journal of the Mechanics and Physics of Solids 48 (2000) 797–826.

[9] B. Bourdin, G. A. Francfort, J. J. Marigo, The variational approach to fracture, Journal of Elasticity 91 (2008) 5–148.

[10] C. Miehe, F. Welshinger, M. Hofacker, Thermodynamically consistent phase-field models of fracture: Variational principles and multi-field fe implementations, International Journal for Numerical Methods in Engineering 83 (2010) 1273–1311.

[11] C. Miehe, M. Hofacker, F. Welschinger, A phase field model for rate-independent crack propagation: Robust algorithmic implementation based on operator splits, Computer Methods in Applied Mechanics and Engineering 199 (2010) 2765–2778.

[12] T. Gerasimov, L. D. Lorenzis, A line search assisted monolithic approach for phase-field computing of brittle fracture, Computer Methods in Applied Mechanics and Engineering 312 (2016) 276–303.

[13] M. J. Borden, T. J. R. Hughes, C. M. Landis, C. V. Verhoosel, A higher-order phase-field model for brittle fracture: Formulation and analysis within the isogeometric analysis framework, Computer Methods in Applied Mechanics and Engineering 273 (2014) 100–118.

[14] D. Schillinger, M. J. Borden, H. K. Stolarski, Isogeometric collocation for phase-field fracture models, Computer Methods in Applied Mechanics and Engineering 284 (2015) 583–610.

[15] M. Ambati, T. Gerasimov, L. D. Lorenzis, Phase-field modeling of ductile fracture, Computational Mechanics 55 (2015) 1017–1040.

[16] M. J. Borden, T. J. R. Hughes, C. M. Landis, A. Anvari, I. J. Lee, A phase-field formulation for fracture in ductile materials: Finite deformation balance law derivation, plastic degradation, and stress triaxiality effects, Computer Methods in Applied Mechanics and Engineering 312 (2016) 130–166.

[17] C. Miehe, F. Aldakheel, A. Raina, Phase field modeling of ductile fracture at finite strains: A variational gradient-extended plasticity-damage theory, International Journal of Plasticity 84 (2016) 1–32.

[18] R. Alessi, M. Ambati, T. Gerasimov, S. Vidoli, L. D. Lorenzis, Comparison of Phase-Field Models of Fracture Coupled with Plasticity, Springer Nature, 2018.

[19] M. J. Borden, C. V. Verhoosel, M. A. Scott, T. J. R. Hughes, C. M. Landis, A phase-field description of dynamic brittle fracture, Computer Methods in Applied Mechanics and Engineering 217-220 (2012) 77–95.

[20] A. Schlüter, A. Willenbücher, C. Kuhn, R. Müller, Phase field approximation of dynamic brittle fracture, Computational Mechanics 54 (2014).

[21] S. Zhou, T. Rabczuk, X. Zhuang, Phase field modeling of quasi-static and dynamic crack propagation: Comsol implementation and case studies, Advances in Engineering Software 122 (2018) 31–49.

[22] R. J. M. Geelen, Y. Liu, T. Hu, M. R. Tupek, J. E. Dolbow, A phase-field formulation for dynamic cohesive fracture, Computer Methods in Applied Mechanics and Engineering 348 (2019) 680–711.

[23] G. Molnár, A. Gravouil, R. Seghir, J. Réthoré, An open-source abaqus implementation of the phase-field method to study the effect of plasticity on the instantaneous fracture toughness in dynamic crack propagation, Computer Methods in Applied Mechanics and Engineering 365 (2020) 113004.

[24] J. Y. Wu, Y. Huang, V. P. Nguyen, Three-dimensional phase-field modeling of mode i + ii / iii failure in solids, Computer Methods in Applied Mechanics and Engineering 373 (2021) 113537.

[25] M. Strobl, T. Seelig, Phase field modeling of hertzian indentation fracture, Journal of the Mechanics and Physics of Solids 143 (2020) 104026.

[26] T. T. Nguyen, J. Yvonnet, Q. Z. Zhu, M. Bornert, C. Chateau, A phase-field method for computational modeling of interfacial damage interacting with crack propagation in realistic microstructures obtained by microtomography, Computer Methods in Applied Mechanics and Engineering 312 (2016).

[27] J. Reinoso, A. Arteiro, M. Paggi, P. P. Camanho, Strength prediction of notched thin ply laminates using finite fracture mechanics and the phase field approach, Composites Science and Technology 150 (2017) 205–216.

[28] V. Carollo, J. Reinoso, M. Paggi, A 3d finite strain model for intralayer and interlayer crack simulation coupling the phase field approach and cohesive zone model, Composite Structures 182 (2017) 636–651.

[29] R. Alessi, F. Freddi, Failure and complex crack patterns in hybrid laminates: A phase-field approach, Composites Part B: Engineering 179 (2019) 107256.

[30] T. K. Mandal, V. P. Nguyen, J. Y. Wu, A length scale insensitive anisotropic phase field fracture model for hyperelastic composites, International Journal of Mechanical Sciences 188 (2020) 105941.

[31] A. Quintanas-Corominas, A. Turon, J. Reinoso, E. Casoni, M. Paggi, J. A. Mayugo, A phase field approach enhanced with a cohesive zone model for modeling delamination induced by matrix cracking, Computer Methods in Applied Mechanics and Engineering 358 (2020) 112618.

[32] J. Reinoso, M. Paggi, C. Linder, Phase field modeling of brittle fracture for enhanced assumed strain shells at large deformations: formulation and finite element implementation, Computational Mechanics 59 (2017) 981–1001.

[33] V. Carollo, J. Reinoso, M. Paggi, Modeling complex crack paths in ceramic laminates: A novel variational framework combining the phase field method of fracture and the cohesive zone model, Journal of the European Ceramic Society 38 (2018) 2994–3003.

[34] W. Li, K. Shirvan, Multiphysics phase-field modeling of quasi-static cracking in urania ceramic nuclear fuel, Ceramics International 47 (2021) 793–810.

[35] A. Kumar, G. A. Francfort, O. Lopez-Pamies, Fracture and healing of elastomers: A phase-transition theory and numerical implementation, Journal of the Mechanics and Physics of Solids 112 (2018) 523–551.

[36] M. Simoes, E. Martínez-Pañeda, Phase field modelling of fracture and fatigue in shape memory alloys, Computer Methods in Applied Mechanics and Engineering 373 (2021) 113504.

[37] Hirshikesh, S. Natarajan, R. K. Annabattula, E. Martínez-Pañeda, Phase field modelling of crack propagation in functionally graded materials, Composites Part B: Engineering 169 (2019).

[38] P. K. A. V. Kumar, A. Dean, J. Reinoso, P. Lenarda, M. Paggi, Phase field modeling of fracture in functionally graded materials: G -convergence and mechanical insight on the effect of grading, Thin-Walled Structures 159 (2021) 107234.

[39] B. Bourdin, J. Marigo, C. Maurini, P. Sicsic, Morphogenesis and propagation of complex cracks induced by thermal shocks, Physical Review Letters 112 (2014) 014301.

[40] Y. Zhao, B. X. Xu, P. Stein, D. Gross, Phase-field study of electrochemical reactions at exterior and interior interfaces in li-ion battery electrode particles, Computer Methods in Applied Mechanics and Engineering 312 (2016).

[41] M. Klinsmann, D. Rosato, M. Kamlah, R. M. McMeeking, Modeling crack growth during li insertion in storage particles using a fracture phase field approach, Journal of the Mechanics and Physics of Solids 92 (2016) 313–344.

[42] A. Mesgarnejad, A. Karma, Phase field modeling of chemomechanical fracture of intercalation electrodes: Role of charging rate and dimensionality, Journal of the Mechanics and Physics of Solids 132 (2019).

[43] E. Martínez-Pañeda, A. Golahmar, C. F. Niordson, A phase field formulation for hydrogen assisted cracking, Computer Methods in Applied Mechanics and Engineering 342 (2018) 742–761.

[44] F. P. Duda, A. Ciarbonetti, S. Toro, A. E. Huespe, A phase-field model for solute-assisted brittle fracture in elastic-plastic solids, International Journal of Plasticity 102 (2018) 16–40.

[45] L. Anand, Y. Mao, B. Talamini, On modeling fracture of ferritic steels due to hydrogen embrittlement, Journal of the Mechanics and Physics of Solids 122 (2019) 280–314.

[46] J.-Y. Wu, T. K. Mandal, V. P. Nguyen, A phase-field regularized cohesive zone model for hydrogen assisted cracking, Computer Methods in Applied Mechanics and Engineering 358 (2020) 112614.

[47] J. Y. Wu, V. P. Nguyen, C. T. Nguyen, D. Sutula, S. Sinaie, S. Bordas, Phase-field modelling of fracture, Advances in Applied Mechanics 53 (2020) 1–183.

[48] Y. S. Lo, M. J. Borden, K. Ravi-Chandar, C. M. Landis, A phase-field model for fatigue crack growth, Journal of the Mechanics and Physics of Solids 132 (2019) 103684.

[49] J. L. Boldrini, E. A. B. de Moraes, L. R. Chiarelli, F. G. Fumes, M. L. Bittencourt, A non-isothermal thermodynamically consistent phase field framework for structural damage and fatigue, Computer Methods in Applied Mechanics and Engineering 312 (2016) 395–427.

[50] P. J. Loew, B. Peters, L. A. A. Beex, Fatigue phase-field damage modeling of rubber using viscous dissipation: Crack nucleation and propagation, Mechanics of Materials 142 (2020) 103282.

[51] C. Schreiber, C. Kuhn, R. Müller, T. Zohdi, A phase field modeling approach of cyclic fatigue crack growth, International Journal of Fracture 225 (2020).

[52] M. Seiler, T. Linse, P. Hantschke, M. Kästner, An efficient phase-field model for fatigue fracture in ductile materials, Engineering Fracture Mechanics 224 (2020).

[53] R. Alessi, S. Vidoli, L. D. Lorenzis, A phenomenological approach to fatigue with a variational phase-field model: The one-dimensional case, Engineering Fracture Mechanics 190 (2018) 53–73.

[54] P. Carrara, M. Ambati, R. Alessi, L. D. Lorenzis, A framework to model the fatigue behavior of brittle materials based on a variational phase-field approach, Computer Methods in Applied Mechanics and Engineering 361 (2020) 112731.

[55] M. M. Hasan, T. Baxevanis, A phase-field model for low-cycle fatigue of brittle materials, International Journal of Fatigue 150 (2021) 106297.

[56] K. Seleš, F. Aldakheel, Z. Tonković, J. Sorić, P. Wriggers, A general phase-field model for fatigue failure in brittle and ductile solids, Computational Mechanics 67 (2021).

[57] J. Ulloa, J. Wambacq, R. Alessi, G. Degrande, S. François, Phase-field modeling of fatigue coupled to cyclic plasticity in an energetic formulation, Computer Methods in Applied Mechanics and Engineering 373 (2021) 113473.

[58] Z. Khalil, A. Y. Elghazouli, E. Martínez-Pañeda, A generalised phase field model for fatigue crack growth in elastic–plastic solids with an efficient monolithic solver, Computer Methods in Applied Mechanics and Engineering 388 (2022) 114286.

[59] A. Golahmar, C. F. Niordson, E. Martínez-Pañeda, A phase field model for high-cycle fatigue: Total-life analysis, International Journal of Fatigue 170 (2023) 107558.

[60] P. K. Kristensen, A. Golahmar, E. Martínez-Pañeda, C. F. Niordson, Accelerated high-cycle phase field fatigue predictions, European Journal of Mechanics / A Solids 100 (2023) 104991.

[61] J. Y. Wu, Y. Huang, V. P. Nguyen, On the bfgs monolithic algorithm for the unified phase field damage theory, Computer Methods in Applied Mechanics and Engineering 360 (2020) 112704.

[62] P. K. Kristensen, E. Martínez-Pañeda, Phase field fracture modelling using quasi-newton methods and a new adaptive step scheme, Theoretical and Applied Fracture Mechanics 107 (2020) 102446.

[63] H. Amor, J. J. Marigo, C. Maurini, Regularized formulation of the variational brittle fracture with unilateral contact: Numerical experiments, Journal of the Mechanics and Physics of Solids 57 (2009) 1209–1229.

[64] F. Freddi, G. Royer-Carfagni, Regularized variational theories of fracture: A unified approach, Journal of the Mechanics and Physics of Solids 58 (2010) 1154–1174.

[65] M. Ambati, T. Gerasimov, L. D. Lorenzis, A review on phase-field models of brittle fracture and a new fast hybrid formulation, Computational Mechanics 55 (2015) 383–405.

[66] K. Pham, H. Amor, J. J. Marigo, C. Maurini, Gradient damage models and their use to approximate brittle fracture, International Journal of Damage Mechanics 20 (2011) 618–652.

[67] L. Ambrosio, V. M. Tortorelli, Approximation of functionals depending on jumps by elliptic functionals via gamma-convergence, Communications on Pure and Applied Mathematics 43 (1991) 999–1036.

[68] D. Mumford, J. Shah, Optimal approximations by piecewise smooth functions and associated variational problems, Communications on Pure and Applied Mathematics 42 (1989) 577–685.

[69] E. Tanné, T. Li, B. Bourdin, J.-J. Marigo, C. Maurini, Crack nucleation in variational phase-field models of brittle fracture, Journal of the Mechanics and Physics of Solids 110 (2018) 80–99.

[70] P. K. Kristensen, C. F. Niordson, E. Martínez-Pañeda, An assessment of phase field fracture: crack initiation and growth, Philosophical Transactions of the Royal Society A: Mathematical, Physical and Engineering Sciences 379 (2021) 20210021.

[71] K. Walker, The effect of stress ratio during crack propagation and fatigue for 2024-t3 and 7075-t6 aluminum, effects of environment and complex load history on fatigue life, ASTM STP 462 (1970).

[72] M. L. Williams, On the stress distribution at the base of a stationary crack, Journal of Applied Mechanics 24 (1957) 109–114.

[73] MIL-HDBK-5H, Military Handbook: Metallic Materials and Elements for Aerospace Vehicle Structures, U.S. Department of Defense, 1998.

[74] J. Andersons, M. Hojo, S. Ochiai, Model of delamination propagation in brittle-matrix composites under cyclic loading, Journal of reinforced plastics and composites 20 (5) (2001) 431–450.

[75] A. Mehmanparast, F. Brennan, I. Tavares, Fatigue crack growth rates for offshore wind monopile weldments in air and seawater: Slic inter-laboratory test results, Materials and Design 114 (2017) 494–504.

[76] H. Tada, P. C. Paris, G. R. Irwin, The stress analysis of cracks, Handbook, Del Research Corporation 34 (1973) (1973).

[77] DNV-GL Standards, Recommended Practice DNVGL-RP-C203-Fatigue Design of Offshore Steel Structures, Høvik: DNV GL AS (2016).

[78] A. M. P. de Jesus, R. Matos, B. F. C. Fontoura, C. Rebelo, L. S. da Silva, M. Veljkovic, A comparison of the fatigue behavior between s355 and s690 steel grades, Journal of constructional steel research 79 (2012) 140–150.

[79] V. Milovanović, D. Arsić, M. Milutinović, M. Živković, M. Topalović, A comparison study of fatigue behavior of s355j2+ n, s690ql and x37crmov5-1 steel, Metals 12 (7) (2022) 1199.

[80] American Society for Testing, Materials. Committee E08 on Fatigue, and Fracture, Standard test method for measurement of fatigue crack growth rates, American Society of Testing Materials, 2008.

[81] British Standards Institution, Guide on methods for assessing the acceptability of flaws in metallic structures, British Standard Institution London, UK, 1999.

[82] A. Chudnovsky, K. Chaoui, A. Moet, Curvilinear crack layer propagation, Journal of materials science letters 6 (9) (1987) 1033–1038.

[83] A. A. Rubinstein, Mechanics of the crack path formation, International Journal of Fracture 47 (1991) 291–305.

[84] A. Chudnovsky, W. L. Huang, B. Kunin, Effect of damage on fatigue crack propagation in polystyrene, Polymer Engineering & Science 30 (20) (1990) 1303–1308.

[85] R. S. Li, A. Chudnovsky, Examination of the fatigue crack growth equations, International journal of fracture 81 (1996) 343–355.

[86] A. Golahmar, P. K. Kristensen, C. F. Niordson, E. Martínez-Pañeda, A phase field model for hydrogen-assisted fatigue, International Journal of Fatigue 154 (2022) 106521.

[P4]

A. Golahmar, P. K. Kristensen, C. F. Niordson, and E. Martínez-Pañeda. A phase field model for hydrogen-assisted fatigue. International Journal of Fatigue 154 (2022), p. 106521.

International Journal of Fatigue 154 (2022) 106521

Contents lists available at ScienceDirect

International Journal of Fatigue

journal homepage: www.elsevier.com/locate/ijfatigue

A phase field model for hydrogen-assisted fatigue

Alireza Golahmar [a], Philip K. Kristensen [a], Christian F. Niordson [a], Emilio Martínez-Pañeda [b,*]

[a] Department of Mechanical Engineering, Technical University of Denmark, DK-2800 Kgs. Lyngby, Denmark
[b] Department of Civil and Environmental Engineering, Imperial College London, London SW7 2AZ, UK

ARTICLE INFO

Keywords:
Phase field
Finite element method
Fatigue
Crack growth
Hydrogen embrittlement

ABSTRACT

We present a new theoretical and numerical phase field-based formulation for predicting hydrogen-assisted fatigue. The coupled deformation-diffusion-damage model presented enables predicting fatigue crack nucleation and growth for arbitrary loading patterns and specimen geometries. The role of hydrogen in increasing fatigue crack growth rates and decreasing the number of cycles to failure is investigated. Our numerical experiments enable mapping the three loading frequency regimes and naturally recover Paris law behaviour for various hydrogen concentrations. In addition, *Virtual* S–N curves are obtained for both notched and smooth samples, exhibiting a good agreement with experiments.

1. Introduction

There is a growing interest in understanding and optimising the fatigue behaviour of metals in the presence of hydrogen (see, e.g., [1–6] and Refs. therein). Two aspects have mainly motivated these endeavours. Firstly, hydrogen-assisted cracking is a well-known concern in the transport, construction, defence and energy sectors. Hydrogen is ubiquitous and significantly reduces the ductility, strength, toughness and fatigue crack growth resistance of metallic materials, with the problem being exacerbated by the higher susceptibility of modern, high-strength alloys [7]. Secondly, hydrogen is seen as the energy carrier of the future, fostering a notable interest in the design and prognosis of infrastructure for hydrogen transportation and storage [8,9]. In the majority of these applications, susceptible components are exposed to alternating mechanical loads and thus being able to predict the synergistic effects of hydrogen and fatigue damage is of utmost importance.

Significant progress has been achieved in the development of computational models for hydrogen-assisted fracture. Dislocation-based methods [10,11], weakest-link approaches [12,13], cohesive zone models [14–16], gradient damage theories [17] and phase field fracture formulations [18–21] have been presented to predict the nucleation and subsequent growth of hydrogen-assisted cracks. Multi-physics phase field fracture models have been particularly successful, demonstrating their ability to capture complex cracking conditions, such as nucleation from multiple sites or the coalescence of numerous defects, in arbitrary geometries and dimensions [22,23]. However, the surge in modelling efforts experienced in the context of monotonic, static fracture has not been observed in fatigue. Hydrogen can influence the cyclic constitutive behaviour [24,25], reduce the number of cycles required to initiate cracks [26,27] and, most notably, accelerate fatigue crack growth [28,29]. Predicting the significant reduction in fatigue life observed in the presence of hydrogen requires capturing how hydrogen elevates crack growth rates, which is dependent on the hydrogen content, the material susceptibility to embrittlement, the diffusivity of hydrogen and the loading amplitude and frequency, among other factors. Given the complexity and higher computational demands of fatigue damage, it is not surprising that the role of hydrogen in augmenting fatigue crack growth rates has been predominantly assessed from an experimental viewpoint, with a few exceptions [30,31]. Moreover, the success of phase field formulations in predicting hydrogen-assisted static fracture has not been extended to fatigue yet.

In this work, we present the first phase field model for hydrogen-assisted fatigue. The main elements of the coupled deformation-diffusion-fatigue formulation presented are: (i) a thermodynamically-consistent extension of Fick's law of mass diffusion, (ii) a fatigue history variable and associated degradation function, (iii) a phase field description of crack-solid interface evolution, (iv) a penalty-based formulation to update environmental boundary conditions, and (v) an atomistically-inspired relation between the hydrogen content and the fracture surface energy. This novel variational framework is numerically implemented in the context of the finite element method and used to model hydrogen-assisted fatigue in several boundary value problems of particular interest. Firstly, the paradigmatic benchmark of a cracked square plate is modelled to quantify the dependency of the number of cycles to failure on the hydrogen content. Secondly, a boundary layer approach is used to gain insight into the competing

* Corresponding author.
E-mail address: e.martinez-paneda@imperial.ac.uk (E. Martínez-Pañeda).

https://doi.org/10.1016/j.ijfatigue.2021.106521
Received 28 June 2021; Received in revised form 29 July 2021; Accepted 30 August 2021
Available online 6 September 2021

role of loading frequency and hydrogen diffusivity. We show how the model captures the main experimental trends; namely, the sensitivity of fatigue crack growth rates to the loading frequency and the environment. The Paris law, and its sensitivity to hydrogen, are naturally recovered. Finally, *Virtual* S–N curves are computed for both smooth and notched samples, exhibiting a promising agreement with experimental data. The remainder of the paper is organised as follows. Section 2 presents the theoretical framework and provides details of the finite element implementation. In Section 3, the performance of the proposed modelling framework is benchmarked against several representative numerical examples as well as relevant experimental measurements. Finally, concluding remarks are given in Section 4.

2. A phase field theory for hydrogen-assisted fatigue

We present a theoretical and numerical framework for modelling hydrogen assisted fatigue. Our formulation is grounded on the phase field fracture method, which has gained notable traction in recent years. Applications include battery materials [32,33], composites [34,35], ceramics [36,37], shape memory alloys [38], functionally graded materials [39,40] and both ductile [41,42] and embrittled [43] metals. The success of phase field fracture methods is arguably twofold. First, phase field provides a robust computational framework to simulate complex cracking phenomena in arbitrary geometries and dimensions. Secondly, it provides a variational platform for Griffith's energy balance [44,45]. Thus, consider a cracked elastic solid with strain energy density $\psi(\boldsymbol{\varepsilon})$. Under prescribed displacements, the variation of the total potential energy of the solid $\mathcal{E}$ due to an incremental increase in crack area $\mathrm{d}A$ is given by

$$\frac{\mathrm{d}\mathcal{E}}{\mathrm{d}A} = \frac{\mathrm{d}\psi(\boldsymbol{\varepsilon})}{\mathrm{d}A} + \frac{\mathrm{d}W_c}{\mathrm{d}A} = 0, \tag{1}$$

where W_c is the work required to create new surfaces and $\boldsymbol{\varepsilon}$ is the strain tensor. The fracture resistance of the solid is given by the term $\mathrm{d}W_c/\mathrm{d}A$, also referred to as the material toughness or critical energy release rate G_c. A pre-existing crack will grow when the energy stored in the material is high enough to overcome G_c. Griffith's minimality principle can be formulated in a variational form as follows

$$\mathcal{E} = \int_\Omega \psi\,(\boldsymbol{\varepsilon})\,\mathrm{d}V + \int_\Gamma G_c\,\mathrm{d}\Gamma\,. \tag{2}$$

Arbitrary cracking phenomena can be predicted based on the thermodynamics of fracture, provided one can computationally track the crack surface Γ. The phase field paradigm is key to tackling the challenge of predicting the evolution of the crack surface topology. The crack-solid interface is described by means of an auxiliary variable, the phase field ϕ, which takes distinct values in each of the phases and varies smoothly in between. This implicit representation of an evolving interface has proven to be useful in modelling other complex interfacial phenomena, such as microstructural evolution [46] or corrosion [47]. In the context of fracture mechanics, the phase field ϕ resembles a damage variable, taking values of 0 in intact material points and of 1 inside the crack. Thus, upon a convenient constitutive choice for the crack surface density function γ, the Griffith functional (2) can be approximated by means of the following regularised functional:

$$\begin{aligned}\mathcal{E}_\ell &= \int_\Omega \left[g\,(\phi)\,\psi_0\,(\boldsymbol{\varepsilon}) + G_c\gamma\,(\phi,\ell)\right]\mathrm{d}V \\ &= \int_\Omega \left[(1-\phi)^2\,\psi_0\,(\boldsymbol{\varepsilon}) + G_c\left(\frac{\phi^2}{2\ell} + \frac{\ell}{2}|\nabla\phi|^2\right)\right]\mathrm{d}V\,.\end{aligned} \tag{3}$$

Here, ℓ is a length scale parameter that governs the size of the fracture process zone, ψ_0 denotes the strain energy density of the undamaged solid and $g(\phi)$ is a degradation function. It can be shown through Gamma-convergence that $\mathcal{E}_\ell$ converges to $\mathcal{E}$ when $\ell \to 0^+$ [48].

Now, let us extend this framework to incorporate fatigue damage and hydrogen embrittlement. Define a *degraded* fracture energy $\mathcal{G}_d$ that is a function of the hydrogen concentration C and a fatigue history variable $\bar{\alpha}$, such that

$$\mathcal{G}_d = f_C\,(C)\,f_{\bar{\alpha}}\,(\bar{\alpha})\,G_c \tag{4}$$

where f_C and $f_{\bar{\alpha}}$ are two suitably defined degradation functions to respectively incorporate hydrogen and fatigue damage, as described later. Replacing G_c by $\mathcal{G}_d$, taking the variation of the functional (3) with respect to $\delta\phi$, and applying Gauss' divergence theorem renders the following phase field equilibrium equation,

$$\mathcal{G}_d\left(\frac{\phi}{\ell} - \ell\nabla^2\phi\right) - 2\,(1-\phi)\,\psi_0 = 0 \tag{5}$$

Considering the homogeneous solution to (5) provides further insight into the role of the phase field length scale ℓ. Thus, in a 1D setting, consider a sample with Young's modulus E, subjected to a uniaxial stress $\sigma = g\,(\phi)\,E\varepsilon$; the homogeneous solution for the stress reaches a maximum at the following critical strength:

$$\sigma_c = \left(\frac{27E\mathcal{G}_d}{256\ell}\right)^{1/2}. \tag{6}$$

Hence, ℓ can be seen not only as a regularising parameter but also as a material property that defines the material strength. This enables phase field models to predict crack nucleation and naturally recover the transition flaw size effect [49,50].

2.1. Hydrogen degradation function

We proceed to provide constitutive definitions for the degradation functions. The dramatic drop in fracture resistance observed in metals exposed to hydrogen is captured by taking inspiration from atomistic insight. As discussed elsewhere [14,18], DFT calculations of surface energy degradation with hydrogen coverage θ exhibit a linear trend, with the slope being sensitive to the material system under consideration. Thus, a quantum mechanically informed degradation law can be defined as follows,

$$f_C = 1 - \chi\theta \qquad \text{with} \qquad \theta = \frac{C}{C + \exp\left(-\Delta g_b^0/(\mathcal{R}T)\right)} \tag{7}$$

where χ is the hydrogen damage coefficient, which is taken in this study to be $\chi = 0.89$, as this provides the best fit to the DFT calculations by Jiang and Carter in iron [18,51]. Also, the second part of (7) makes use of the Langmuir–McLean isotherm to estimate, as dictated by thermodynamic equilibrium, the hydrogen coverage θ at decohering interfaces as a function of the bulk concentration C, the universal gas constant $\mathcal{R}$, the temperature T, and the associated binding energy Δg_b^0. Here, we follow Serebrinsky et al. [14] and assume $\Delta g_b^0 = 30$ kJ/mol, as is commonly done for grain boundaries. These specific choices are based on the assumption of a hydrogen assisted fracture process governed by interface decohesion. However, we emphasise that the phase field framework for hydrogen assisted fatigue presented is general and can accommodate any mechanistic or phenomenological interpretation upon suitable choices of f_C.

2.2. Fatigue degradation function

Fatigue damage is captured by means of a degradation function $f_{\bar{\alpha}}(\bar{\alpha})$, a cumulative history variable $\bar{\alpha}$ and a fatigue threshold parameter α_T. Following the work by Carrara et al. [52], two forms of $f_{\bar{\alpha}}(\bar{\alpha})$ are considered:

$$f_{\bar{\alpha}}(\bar{\alpha}) = \begin{cases} 1 & \text{if} \quad \bar{\alpha} \le \alpha_T \\ \left(\dfrac{2\alpha_T}{\bar{\alpha} + \alpha_T}\right)^2 & \text{if} \quad \bar{\alpha} > \alpha_T \end{cases} \qquad \text{(Asymptotic)} \tag{8}$$

$$f_{\bar{\alpha}}(\bar{\alpha}) = \begin{cases} 1 & \text{if} \quad \bar{\alpha} \le \alpha_T \\ \left[1 - \kappa \log\left(\dfrac{\bar{\alpha}}{\alpha_T}\right)\right]^2 & \text{if} \quad \alpha_T \le \bar{\alpha} \le \alpha_T 10^{1/\kappa} \quad \text{(Logarithmic)} \\ 0 & \text{if} \quad \bar{\alpha} \ge \alpha_T 10^{1/\kappa} \end{cases} \tag{9}$$

where κ is a material parameter that governs the slope of the logarithmic function. For simplicity, the asymptotic function will be generally used in our numerical experiments unless otherwise stated. The fatigue history variable $\bar{\alpha}$ evolves in time t as follows,

$$\bar{\alpha}(t) = \int_0^t \mathrm{H}(\alpha\dot{\alpha})|\dot{\alpha}|\,\mathrm{d}t\,, \tag{10}$$

where $\mathrm{H}(\alpha\dot{\alpha})$ is the Heaviside function, such that $\bar{\alpha}$ only grows during loading. Finally, consistent with our energy balance, the cumulative fatigue variable is defined as $\bar{\alpha} = g(\phi)\psi_0$.

2.3. Coupled deformation-diffusion-fracture problem

The hydrogen and fatigue damage framework presented is coupled to the solution of the displacement field, as given by the balance of linear momentum:

$$\nabla \cdot \boldsymbol{\sigma} + \mathbf{b} = \mathbf{0}\,, \tag{11}$$

and mass transport,

$$\dot{C} + \nabla \cdot \mathbf{J} = 0\,. \tag{12}$$

Here, $\boldsymbol{\sigma}$ is the Cauchy stress tensor, $\mathbf{b}$ is the body force vector, and $\mathbf{J}$ is the hydrogen flux. In relation to the mechanical problem, linear elastic material behaviour is assumed, with the strain energy density given as $\psi_0 = \frac{1}{2}\boldsymbol{\varepsilon} : \boldsymbol{C} : \boldsymbol{\varepsilon}$, where $\boldsymbol{C}$ is the fourth order elasticity tensor. The hydrogen transport problem is characterised by the following definition of the chemical potential,

$$\mu = \mu_0 + \mathcal{R}T \ln\frac{\theta}{1-\theta} - \bar{V}_H \sigma_H \tag{13}$$

where μ_0 denotes the chemical potential in the standard state and $\bar{V}_H$ is the partial molar volume of hydrogen in solid solution. Our numerical examples are focused on iron-based materials and consequently $\bar{V}_H = 2000$ mm^3/mol. It must be emphasised that the hydrostatic stress σ_H lowers the chemical potential, increasing the hydrogen solubility as a result of lattice dilatation and thus attracting hydrogen to areas of high volumetric strains, such as crack tips. Finally, the hydrogen flux is related to $\nabla\mu$ through the following linear Onsager relation,

$$\mathbf{J} = -\frac{DC}{\mathcal{R}T}\nabla\mu\,, \tag{14}$$

where D is the hydrogen diffusion coefficient. The role of microstructural trapping sites in slowing diffusion can be accounted for by considering D to be the effective diffusion coefficient (as opposed to the lattice one). Also, as shown in Ref. [43] in the context of static fracture, the framework can readily be extended to capture the influence of dislocation traps, which evolve with mechanical load.

2.4. Numerical implementation

The weak forms of Eqs. (5), (11) and (12) are discretised and solved using the finite element method. In addition, the following features enrich our numerical implementation. Firstly, damage irreversibility is enforced by means of a history field that satisfies the Kuhn–Tucker conditions [53]. Secondly, damage under compressive fields is prevented by adopting a tension-compression split of the strain energy density, together with a hybrid implementation [54]. Two approaches are considered, the volumetric-deviatoric split by Amor et al. [55] and the spectral decomposition by Miehe et al. [53]; the former is generally used unless otherwise stated. Thirdly, the system of equations is solved with a staggered approach that converges to the monolithic result upon controlling the residual norm [56]. Finally, a penalty approach is adopted to implement *moving* chemical boundary conditions, by which the diffusion-environment interface evolves as dictated by the phase field crack [21,23,57].

3. Results

The predictive capabilities of the model are demonstrated through the following numerical experiments. Firstly, in Section 3.1, we validate our numerical implementation in the absence of hydrogen and extend it to demonstrate how the model can capture the role of hydrogen in accelerating crack growth rates. Secondly, in Section 3.2, we use a boundary layer formulation to gain insight into hydrogen-assisted fatigue crack growth under small scale yielding conditions. Stationary and propagating cracks are modelled to shed light on the sensitivity of the crack tip hydrogen concentration to the fatigue frequency and compute Paris law coefficients for various hydrogen contents. Also, crack growth rates versus loading frequency regimes are mapped. Thirdly, we examine the fracture and fatigue behaviour of notched components in Section 3.3, computing *Virtual* S–N curves for various hydrogenous environments. Finally, in Section 3.4 we compare model predictions with fatigue experiments on smooth samples, observing a very good agreement. Two materials are considered, with samples being exposed either to air or to high pressure hydrogen gas.

3.1. Cracked square plate subjected to fatigue in a hydrogenous environment

The case of a square plate with an initial crack subjected to uniaxial tension has become a paradigmatic benchmark in the phase field fracture community. Loading conditions and sample dimensions (in mm) are illustrated in Fig. 1a. As in Refs. [52,58], material properties read $E = 210$ GPa, $\nu = 0.3$, $G_c = 2.7$ kJ/m^2, $\ell = 0.004$ mm and $\alpha_T = 56.25$ MPa. The sample is discretised using 27,410 eight-node plane strain quadrilateral elements with reduced integration. The mesh is refined in the crack propagation region to ensure that the characteristic element length h is sufficiently small to resolve the fracture process zone ($h < \ell/5.4$ [18]). The plate is subjected to a piece-wise linear cyclic remote displacement with a load frequency of $f = 400$ Hz, a zero mean value (i.e. a load ratio of $R = -1$) and a constant range of $\Delta u = 4 \times 10^{-3}$ mm.

We proceed first to validate the model in the absence of hydrogen. The results obtained are shown in Fig. 2 in terms of crack extension Δa (in mm) versus the number of cycles N. The computations have been conducted for three choices of the strain energy density decomposition: no split, volumetric/deviatoric [55] and spectral [53]. A very good agreement is observed with the predictions of Carrara et al. [52] and Kristensen and Martínez-Pañeda [58]. The agreement is particularly good with the latter work, which uses a quasi-Newton monolithic implementation, while the work by Carrara et al. [52] employs an energy-based criterion to ensure that the staggered solution scheme iterates until reaching the monolithic solution [54]. As discussed in the literature, higher fatigue crack growth rates are predicted if no tension-compression split is considered as both tension and compression loading cycles contribute to damage.

Subsequently, the cracked square plate is exposed to a hydrogenous environment at room temperature. We assume that the plate is made of an iron-based material with diffusion coefficient $D = 0.0127$ mm^2/s. Furthermore, it is assumed that the sample has been pre-charged and is exposed to a hydrogenous environment throughout the experiment. Accordingly, a uniform hydrogen distribution is assigned as an initial condition $C(t=0) = C_0 = C_{\text{env}}\ \forall\, x$ and a constant hydrogen concentration $C(t) = C_{\text{env}}$ is prescribed at all the outer boundaries of the plate,

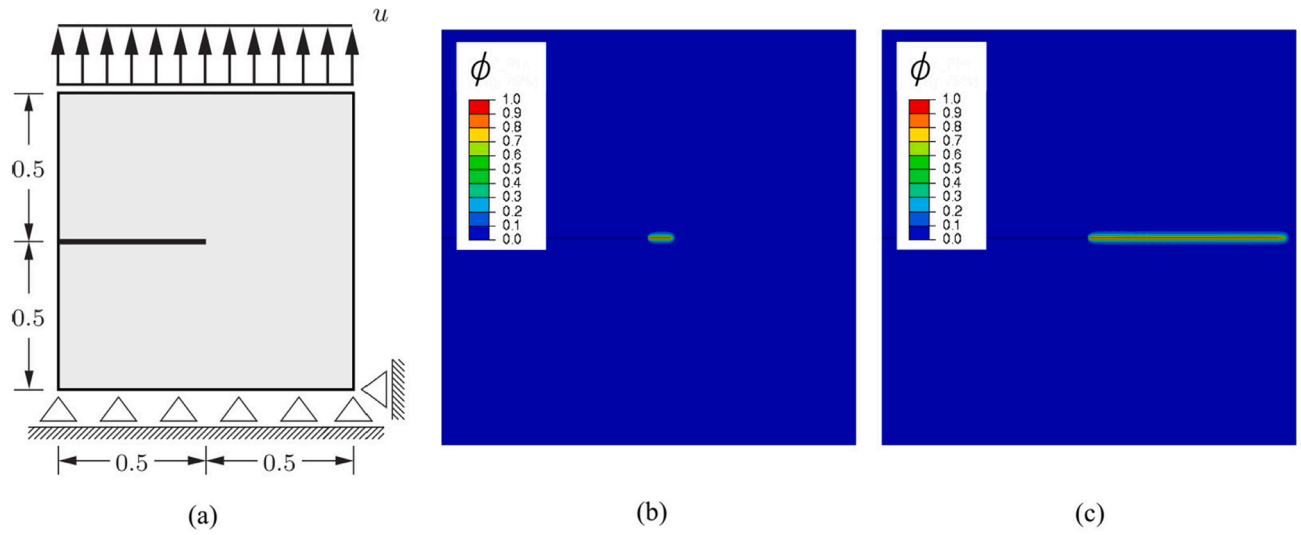

Fig. 1. Cracked square plate: (a) Loading configuration (with dimensions in mm) and phase field contours after (b) 80 and (c) 280 loading cycles.

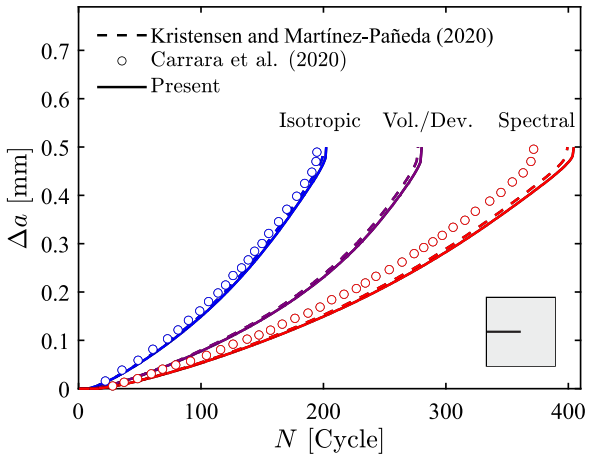

Fig. 2. Cracked square plate, validation in an inert environment: crack extension versus number of cycles and comparison with the results of Kristensen and Martínez-Pañeda [58] and Carrara et al. [52].

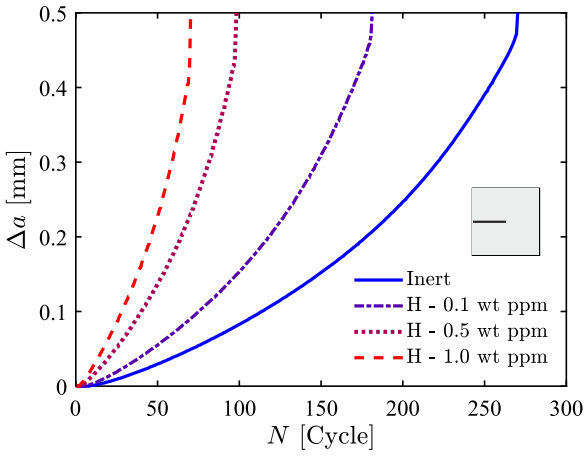

Fig. 3. Cracked square plate, influence of hydrogen: crack extension versus number of cycles for various hydrogen concentration levels.

including the crack faces.[1] The results obtained are shown in Fig. 3 for three selected values of the environmental hydrogen concentration: 0.1, 0.5 and 1 wt ppm. The results reveal that the model correctly captures the trend expected: fatigue crack growth rates increase with increasing hydrogen content (see, e.g., [9,64]).

3.2. Boundary layer model

Next, we gain insight into hydrogen-assisted fatigue under small scale yielding conditions. A boundary layer model is used to prescribe a remote K_{I} field in a circular region of a body containing a sharp crack. As shown in Fig. 4, only the upper half of the domain is considered due to its symmetry. The remote, elastic K_{I} field is applied by prescribing the displacements of the nodes in the outer region following the Williams [65] expansion. Thus, for a polar coordinate system (r,θ) centred at the crack tip, the horizontal and vertical displacements respectively read

$$\begin{aligned} u_x(r,\theta) &= K_{\mathrm{I}}\frac{1+\nu}{E}\sqrt{\frac{r}{2\pi}}\cos\left(\frac{\theta}{2}\right)\left[3-4\nu-\cos(\theta)\right] \\ u_y(r,\theta) &= K_{\mathrm{I}}\frac{1+\nu}{E}\sqrt{\frac{r}{2\pi}}\sin\left(\frac{\theta}{2}\right)\left[3-4\nu-\cos(\theta)\right] \end{aligned} \tag{15}$$

Cyclic loading conditions are attained by defining the applied stress intensity factor as the following sinusoidal function,

$$K_{\mathrm{I}} = K_{\mathrm{m}} + \frac{\Delta K}{2}\sin(2\pi f\, t)\,, \qquad \text{with} \qquad K_{\mathrm{m}} = \frac{\Delta K}{2} + \frac{R\,\Delta K}{1-R} \tag{16}$$

where f denotes the load frequency, t the test time, K_{m} the load mean value, $\Delta K = K_{\max} - K_{\min}$ the load range, and $R = K_{\min}/K_{\max}$ the load ratio. To capture the loading history with fidelity, each cycle is divided into at least 20 computational time increments. The circular domain is discretised using 4,572 quadratic plane strain quadrilateral elements with reduced integration and, as shown in Fig. 4b, the mesh is refined along the crack propagation region.

Consider first the case of a stationary crack in a solid with Young's modulus $E = 210$ GPa, Poisson's ratio $\nu = 0.3$ and diffusion coefficient $D = 0.0127\ \mathrm{mm}^2/\mathrm{s}$. The sample is assumed to be pre-charged with a uniform concentration of $C(t=0) = C_0 = 0.5$ wt ppm. The load range is chosen to be $\Delta K = 1\ \mathrm{MPa}\sqrt{\mathrm{m}}$, the load frequency equals $f = 1$ Hz,

[1] We note that, while a constant hydrogen concentration has been prescribed at the crack faces for simplicity, the use of generalised Neumann-type boundary conditions [59,60] or σ_H-dependent Dirichlet boundary conditions [61–63] is more appropriate.

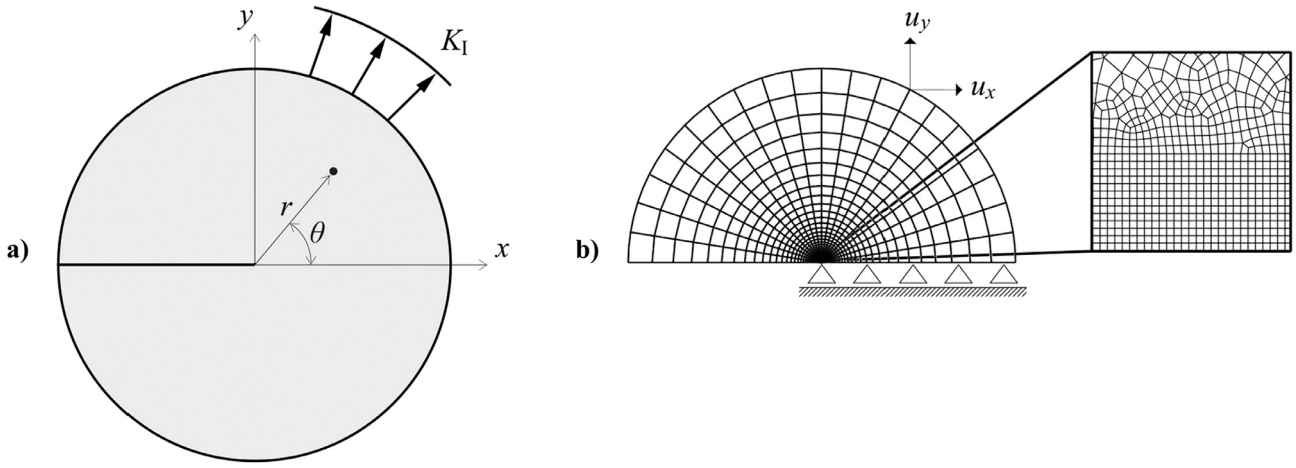

Fig. 4. Boundary layer model: (a) Geometry and boundary conditions, and (b) finite element mesh, including details of the mesh refinement ahead of the crack tip.

and the load ratio is $R = 0$. The evolution of the crack tip hydrogen distribution as a function of time t can be quantified by the following dimensionless groups, as dictated by the Buckingham Π theorem,

$$\frac{C}{C_0} = \mathcal{F}\left(\frac{f L_0^2}{D}, \quad \frac{tD}{L_0^2}, \quad \frac{E\bar{V}_H}{\mathcal{R}T}\right) \tag{17}$$

where $L_0 = (K_m/E)^2$ is a length parameter that results from the dimensional analysis and provides a measure of the gradients close to the crack tip. The first two dimensionless groups quantify the competing influence of test and diffusion times, which are denoted as the normalised frequency $\bar{f} = f L_0^2/D$ and the normalised time $\bar{t} = tD/L_0^2$, respectively.

Hydrogen diffusion is (partially) driven by gradients of hydrostatic stress, see Eq. (13), such that hydrogen atoms will accumulate in areas with high volumetric strains. Under steady state conditions, the hydrogen concentration is given as,

$$C = C_0 \exp\left(\frac{\bar{V}_H \sigma_H}{\mathcal{R}T}\right). \tag{18}$$

Accordingly, the hydrogen distribution ahead of the crack will vary during the loading cycle. Fig. 5 shows the results obtained at the maximum K_{max}, mean K_m and minimum $K_{min} = 0$ stages of the first load cycle, for a sufficiently low frequency such that conditions resemble those of steady state. In agreement with expectations, the hydrogen concentration increases with the applied load, reaching its maximum value in the vicinity of the crack tip (where σ_H is highest), and remains constant for a zero value of the hydrostatic stress at $K_{min} = 0$ ($R = 0$).

Let us now consider the more common case of transient conditions and investigate the competing role of the loading frequency and diffusion time. Fig. 6 illustrates the variation in time of the hydrogen concentration near the crack tip, at a point located at $r/L_0 \approx 0.2 \times 10^7$, as denoted by a star in Fig. 5. The results reveal that, irrespectively of the test duration, the maximum hydrogen content that can be attained ahead of the crack tip is sensitive to the loading frequency. If the diffusivity of hydrogen is sufficiently large relative to the time required to complete one cycle (low f), the amplitude of the hydrogen concentration follows that of the hydrostatic stress, as in the steady state case — see Eq. (18). Contrarily, for high loading frequencies, unloading begins before the hydrogen distribution reaches the steady state solution (18) and consequently the maximum value of C reached during the experiment is smaller than that of lower frequencies. It can be seen that, for the highest frequency ($f = 10^3$ Hz) the hydrogen concentration does not oscillate and flattens out towards a constant value that is roughly 5% lower than the maximum concentration attained at low loading frequencies (for the material properties and distance ahead of the crack

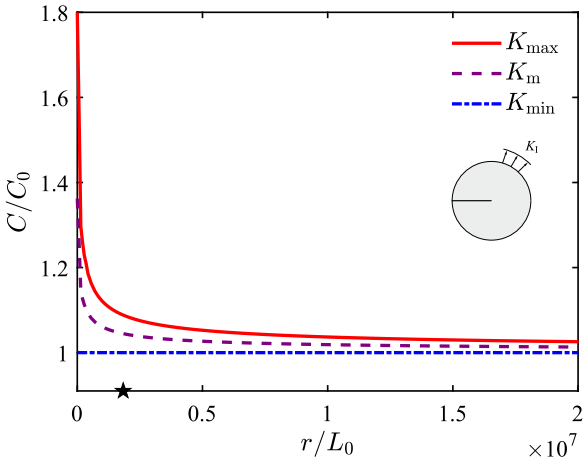

Fig. 5. Boundary layer model: Hydrogen concentration ahead of a stationary crack tip for three stages of the first load cycle. The results have been obtained under steady state conditions and with load ratio $R = 0$.

here considered). Recall that the relevant non-dimensional group $\bar{f} = f L_0^2/D$ involves the material diffusion coefficient. It follows that the present results could support the use of *beneficial* traps, which lower the material diffusivity but are not involved in the fracture process, as a viable strategy for designing materials resistant to hydrogen-assisted fatigue.

We proceed to investigate the influence of the diffusion time–frequency interplay on fatigue crack growth rates. The phase field fatigue model outlined in Section 2 is used, with material properties $G_c = 2.7\,\text{kJ/m}^2$ and $\ell = 0.0048$ mm. A reference stress intensity factor, in the absence of hydrogen, is defined as,

$$K_0 = \sqrt{\frac{G_c E}{(1-\nu^2)}} \tag{19}$$

and a fracture process zone length L_f, can be defined as [49,50]:

$$L_f = \frac{G_c\,(1-\nu^2)}{E} \tag{20}$$

Fig. 7 shows the results obtained in terms of (normalised) crack extension versus number of cycles, as a function of the environmental hydrogen concentration C_{env}. These computations have been conducted for a pre-charged solid ($C(t=0) = C_{env}$) that is exposed to a hydrogenous environment during the test ($C(t) = C_{env}$ at the boundaries). The load range equals $\Delta K/K_0 = 0.08$, while the load frequency and ratio

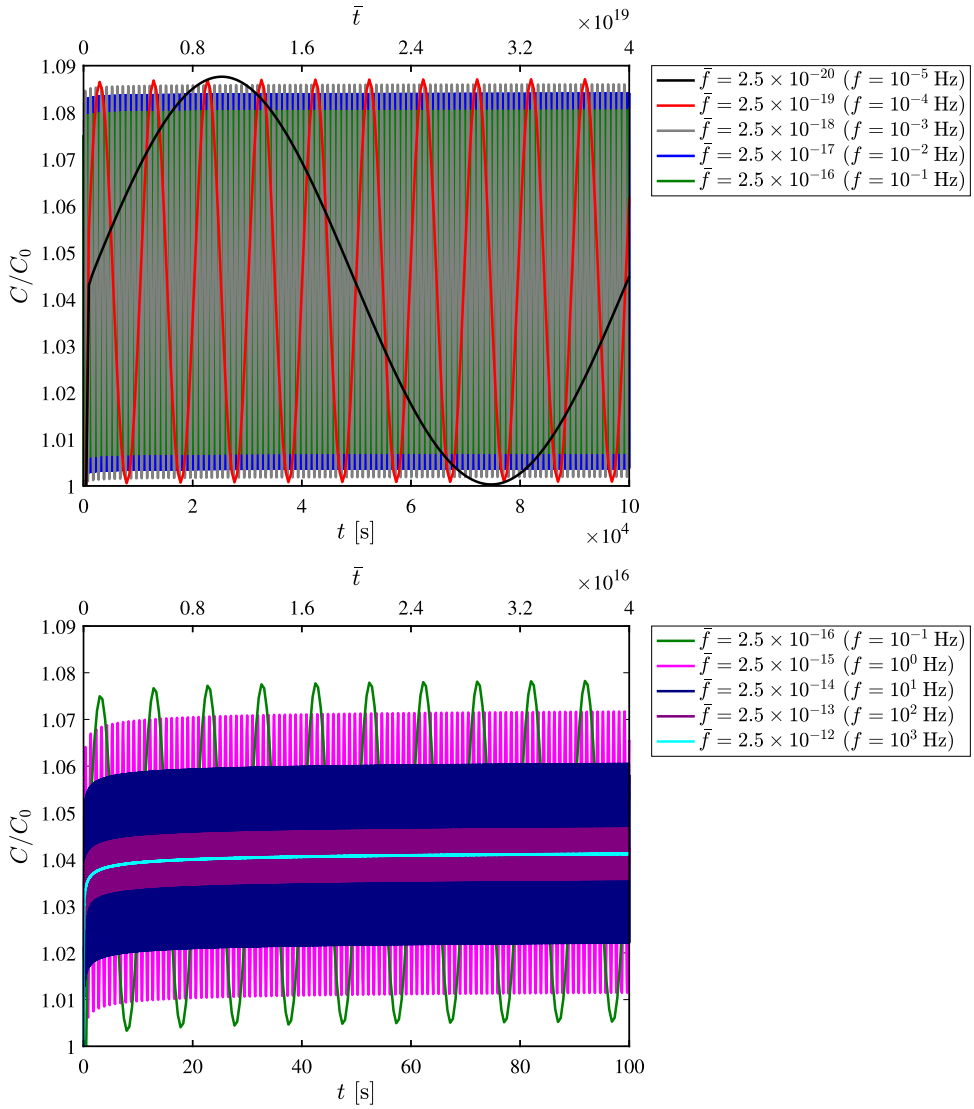

Fig. 6. Boundary layer model: Variation in time of the hydrogen concentration at a point ahead of a stationary crack tip for various loading frequencies and load ratio $R = 0$.

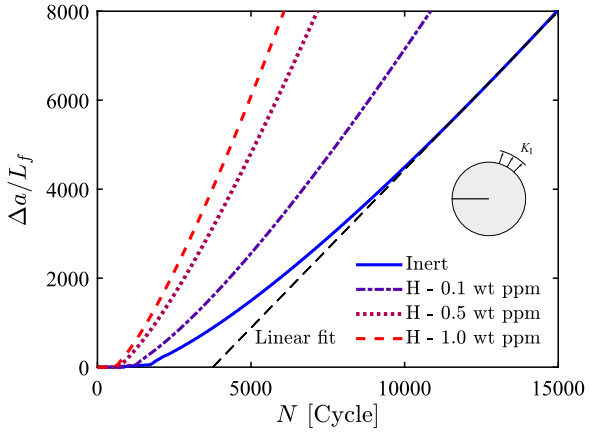

Fig. 7. Boundary layer model: Crack extension versus the number of cycles for different hydrogen concentrations. Results have been obtained for $\Delta K/K_0 = 0.08$, under a load ratio of $R = 0.1$ and load frequency $f = 1$ Hz.

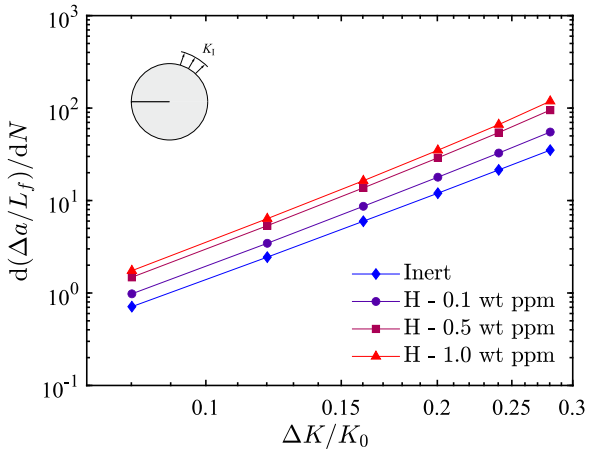

Fig. 8. Boundary layer model, Paris law behaviour: Fatigue crack growth rate versus load range for different hydrogen concentrations. Results have been obtained for a load ratio of $R = 0.1$ and load frequency $f = 1$ Hz.

equal $f = 1$ Hz and $R = 0.1$, respectively. The results shown in Fig. 7 reveal that the model is able to capture the expected trends — for a

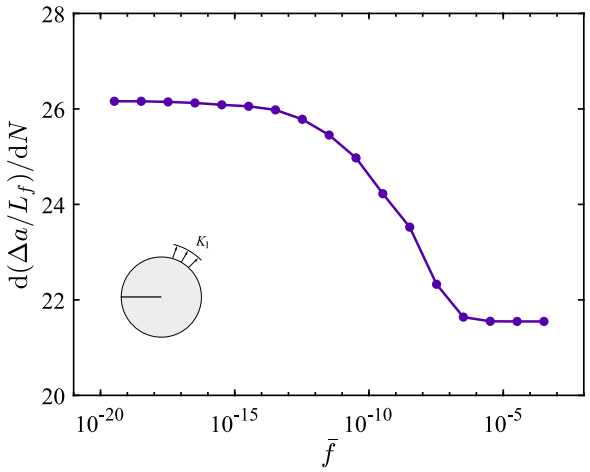

Fig. 9. Boundary layer model, mapping frequency regimes: fatigue crack growth rate versus normalised frequency $\bar{f} = fL_0^2/D$. Results have been obtained for $\Delta K/K_0 = 0.24$, under a load ratio of $R = 0$ and a hydrogen concentration of $C_0 = C_{env} = 0.1$ wt ppm.

given number of cycles, the higher the hydrogen concentration, the larger the crack extension. As depicted in Fig. 7, a linear fit can be applied to the linear part of the curve to derive the slope (crack growth rates).

The fatigue crack growth rates obtained for different ΔK and hydrogen concentrations are shown in Fig. 8, using a log–log plot. The computed curves behave linearly in the so-called Paris regime, where cracks propagate stably, as expected. By applying the well-known Paris equation $da/dN = C\Delta K^m$, one can readily observe that C increases with the hydrogen content, in agreement with the experimental trends. On the other hand, results yield a Paris exponent that appears to be less sensitive to the environment, with a magnitude ($m \approx 3.2$) that is within the range reported for metals in inert environments [66]. The present framework is capable of providing as an output (not input) the Paris law behaviour, enabling the prediction of the role of hydrogen in accelerating sub-critical crack growth rates.

Finally, Fig. 9 illustrates the sensitivity of fatigue crack growth rates to the loading frequency. Here, we consider a pre-charged sample with $C_0 = 0.1$ wt ppm exposed to a load amplitude of $\Delta K/K_0 = 0.24$ and a load ratio of $R = 0$. It is shown that the model captures another widely observed experimental trend; the fatigue behaviour of metals in the presence of hydrogen varies between two limiting cases: (i) fast tests (high f), where hydrogen does not have enough time to diffuse to the fracture process zone and the susceptibility to embrittlement diminishes, and (ii) slow tests (low f), where hydrogen atoms have sufficient time to accumulate in areas of high σ_H, magnifying embrittlement. The model readily captures the transition between these two limiting regimes.

3.3. Notched cylindrical bar

Fatigue crack growth in samples containing non-sharp defects is subsequently investigated. Consider a cylindrical bar with a notch on its surface, as sketched in Fig. 10a. Axisymmetric conditions are exploited to model one planar section of the sample only. The finite element model contains 17,003 quadratic axisymmetric quadrilateral elements with reduced integration, with the mesh being refined ahead of the notch tip, where the characteristic element size is 6 times smaller than the phase field length scale ℓ (see Fig. 10b). The assumed material properties read $E = 210$ GPa, $\nu = 0.3$, $G_c = 64$ kJ/m^2, $\ell = 0.015$ mm, $D = 0.0127$ mm^2/s, and $\alpha_T = 355.56$ MPa. The bar is pre-charged and subsequently loaded in the same environment such that all the outer boundaries of the bar, including the notch faces, are in contact with the environment during the entire numerical experiment. Three environments are considered, corresponding to hydrogen concentrations of 0.1, 0.5 and 1 wt ppm. Cyclic loading is prescribed by subjecting the bar to a piece-wise linear remote displacement with a load frequency of $f = 1$ Hz and a load ratio of $R = 0$.

The results obtained are shown in Fig. 11, in terms of the remote stress amplitude versus the number of cycles to failure, also known as S–N curves. The stress amplitude is normalised by the material strength, as given by (6). For a given stress amplitude, shorter fatigue lives are observed as the hydrogen content is increased. In all cases, the number of cycles to failure increases with decreasing stress amplitude, and the slope of the S–N curve appears to be rather insensitive to the hydrogen content.

Accurate fatigue crack growth predictions in harmful environments require suitable boundary conditions. As mentioned in Section 2, we adopt a penalty approach to implicitly enforce *moving* chemical boundary conditions, so as to capture how the newly created crack surfaces

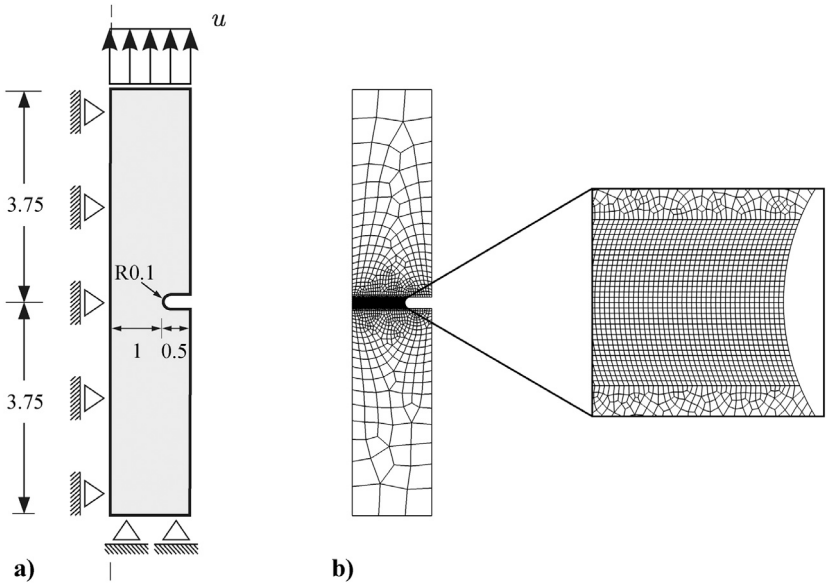

Fig. 10. Notched cylindrical bar: (a) geometry (with dimensions in mm) and boundary conditions, and (b) finite element mesh, including a detailed view of the mesh ahead of the notch tip.

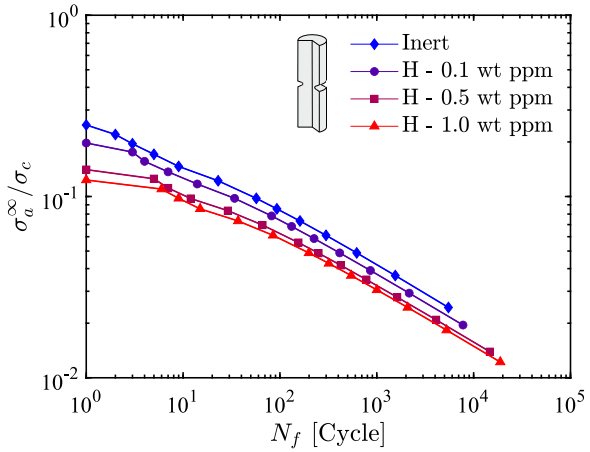

Fig. 11. Notched cylindrical bar, *Virtual* S–N curves: alternating remote stress versus number of cycles to failure for different hydrogen concentrations. The stress concentration factor equals $K_t = 3.354$.

are promptly exposed to the environment. This is illustrated in Fig. 12 by means of phase field and hydrogen concentration contours; as the crack grows, the concentration in the damaged regions equals C_{env}. Note that the contours correspond to $\sigma^\infty = \sigma_{\min} = 0$, and as a result there is no effect of σ_H on the hydrogen concentration.

3.4. Comparison with experimental S-N curves

We conclude the results section by comparing model predictions with S–N curves obtained from uniaxial tension-compression fatigue experiments on smooth samples. The tests were carried out by Matsunaga et al. [67] on two types of steels, a Cr-Mo steel (JIS-SCM435) with tensile strength of 840 MPa and a carbon steel (JIS-SM490B) with tensile strength of 530 MPa. The experiments were carried out in laboratory air and in 115 MPa hydrogen gas under constant stress amplitudes at a stress ratio of $R = -1$ and a test frequency of $f = 1$ Hz. As it is common with steels, both materials are assumed to have a Young's modulus of $E = 210$ GPa and a Poisson's ratio of $\nu = 0.3$. The toughness is assumed to be equal to $G_c = 60$ kJ/m^2 and $G_c = 27$ kJ/m^2 for JIS-SCM435 and JIS-SM490B, respectively, based on fracture toughness measurements reported in Refs. [68,69]. The boundary value problem can be solved in a semi-analytical fashion, by considering the homogeneous solution to (5). A piece-wise cyclic linear variation of the remote stress is assumed. Under 1D conditions, the length scale and the strength are related via (6), and this relation renders magnitudes of $\ell = 1.88$ mm and $\ell = 2.13$ mm for JIS-SCM435 and JIS-SM490B, respectively. The logarithmic fatigue degradation function (9) is used, together with the spectral tension-compression split [53]. The fatigue parameters α_T and κ are chosen so as to provide the best fit to the experiments in air; the magnitudes of $\alpha_T = 24$ MPa and $\kappa = 0.15$ provided the best fit to both JIS-SCM435 and JIS-SM490B data. Then, the fatigue response of samples exposed to hydrogen can be estimated by relating the H_2 pressure with the hydrogen concentration. The latter can be given as a function of the solubility S and the fugacity f_{H_2} by means of Sievert's law:

$$C = S\sqrt{f_{H_2}} \qquad \text{with} \qquad S = S_0 \exp\left(\frac{-E_s}{RT}\right), \tag{21}$$

where E_s is an activation energy. For JIS-SCM435 and JIS-SM490B, the magnitudes of S_0 and E_s are taken from Ref. [70] by considering the data reported for similar steels (AISI 4130 and AISI 1020, respectively); namely: $E_s = 27.2$ kJ/mol, $S_0 = 102$ mol/m$^3\sqrt{\text{MPa}}$ (JIS-SCM435) and $E_s = 23.54$ kJ/mol, $S_0 = 159$ mol/m$^3\sqrt{\text{MPa}}$ (JIS-SM490B). Assuming that the Abel–Noble equation is appropriate, the fugacity can be related to the hydrogen pressure p as follows,

$$f_{H_2} = p \exp\left(\frac{pb}{RT}\right) \tag{22}$$

where the Abel-Noble parameter is taken to be $b = 15.84$ cm^3/mol, rendering $f_{H_2} = 242.9$ MPa, and hydrogen concentrations of 0.00577 wt ppm (JIS-SCM435) and 0.04042 wt ppm (JIS-SM490B). The solubility dependence on the hydrostatic stress should also be accounted for; thus, we scale the hydrogen concentration according to (18) to determine the final magnitude of hydrogen uptake.

The experimental and numerical results obtained are shown in Fig. 13. Despite the scatter typically associated with these experiments, the *Virtual* S–N curves predicted are in good agreement with the measured data. In both experiments and simulations, a higher susceptibility to hydrogen-assisted fatigue is observed in the case of JIS-SM490B, a steel with a higher solubility, where hydrogen reduces the number of

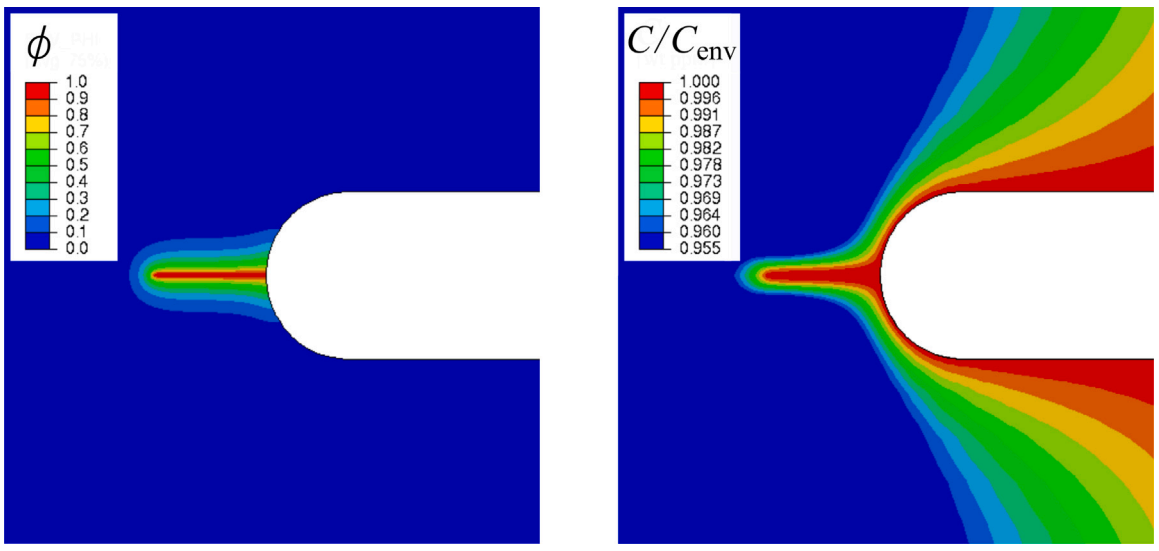

Fig. 12. Notched cylindrical bar, influence of the *moving* chemical boundary conditions: contours of the phase field ϕ (a) and hydrogen concentration (b). Results have been obtained for $C_{\text{env}} = 1$ wt ppm after 700 cycles and are plotted at $u = u_{\min} = 0$.

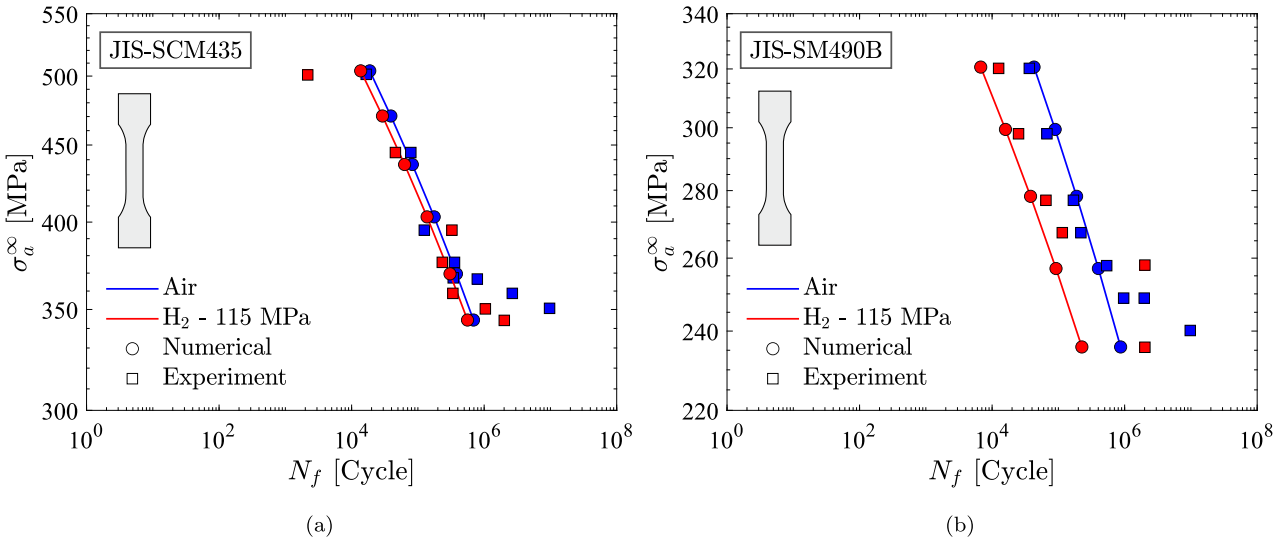

Fig. 13. S–N curves from smooth samples: numerical (present) and experimental [67] in air and at hydrogen pressure of 115 MPa. Two materials are considered: (a) JIS-SCM435, a Cr-Mo steel, and (b) JIS-SM490B, a carbon steel.

cycles to failure by almost an order of magnitude. It is also worth noting that the agreement with experiments becomes less satisfactory at low stress amplitudes, particularly in the absence of hydrogen. This is likely to be improved if a fatigue endurance limit is incorporated into the modelling. Future work will be targeted towards this extension and the investigation of the role of hydrogen in the fatigue endurance of metals.

4. Conclusions

We have presented a multi-physics phase field-based model for hydrogen-assisted fatigue. Cracking is predicted with an energy based criterion grounded on the thermodynamics of crack growth, and the role of hydrogen is incorporated through a first-principles degradation of the fracture energy. Deformation, diffusion and fatigue crack growth are coupled, with the model capturing the solubility dependence on the hydrostatic stress and the evolving environment-diffusion interface. Several findings shall be emphasised:

- The crack tip hydrogen distribution is very sensitive to the loading frequency f and the material diffusivity D. Sufficiently high f values lead to a hydrogen concentration that does not exhibit cyclic oscillations and increases in time up to a saturation value (even for a load ratio of $R = 0$).
- The model adequately captures the sensitivity of fatigue crack growth rates to hydrogen content.
- The model naturally recovers the Paris law behaviour and thus can quantify the influence of hydrogen on the Paris law parameters.
- The sensitivity of crack growth rates to loading frequency is mapped, revealing two limit states, as observed experimentally, and predicting a smooth transition in-between.
- *Virtual* S–N curves are obtained for various environments and both notched and smooth samples. Parameter-free predictions of the impact of hydrogen on the S–N curves reveal a promising agreement with experiments.

The theoretical and numerical framework presented provides a platform for addressing the long-standing challenge of predicting hydrogen-assisted fatigue failures.

Declaration of competing interest

The authors declare that they have no known competing financial interests or personal relationships that could have appeared to influence the work reported in this paper.

Acknowledgements

A. Golahmar acknowledges financial support from Vattenfall Vindkraft A/S and Innovation Fund Denmark (grant 0153-00018B). E. Martínez-Pañeda acknowledges financial support from the EPSRC, United Kingdom (grant EP/V009680/1) and from the Royal Commission for the 1851 Exhibition, United Kingdom (RF496/2018).

References

[1] Martin ML, Sofronis P, Robertson IM, Awane T, Murakami Y. A microstructural based understanding of hydrogen-enhanced fatigue of stainless steels. Int J Fatigue 2013;57:28–36.
[2] Colombo C, Fumagalli G, Bolzoni F, Gobbi G, Vergani L. Fatigue behavior of hydrogen pre-charged low alloy Cr-Mo steel. Int J Fatigue 2015;83:2–9.
[3] Yamabe J, Yoshikawa M, Matsunaga H, Matsuoka S. Hydrogen trapping and fatigue crack growth property of low-carbon steel in hydrogen-gas environment. Int J Fatigue 2017;102:202–13.
[4] Peral LB, Zafra A, Blasón S, Rodríguez C, Belzunce J. Effect of hydrogen on the fatigue crack growth rate of quenched and tempered CrMo and CrMoV steels. Int J Fatigue 2019;120:201–14.
[5] Shinko T, Hénaff G, Halm D, Benoit G, Bilotta G, Arzaghi M. Hydrogen-affected fatigue crack propagation at various loading frequencies and gaseous hydrogen pressures in commercially pure iron. Int J Fatigue 2019;121:197–207.
[6] Ogawa Y, Umakoshi K, Nakamura M, Takakuwa O, Matsunaga H. Hydrogen-assisted, intergranular, fatigue crack-growth in ferritic iron: Influences of hydrogen-gas pressure and temperature variation. Int J Fatigue 2020;140:105806.
[7] Gangloff RP. Hydrogen-assisted cracking. In: Milne I, Ritchie R, Karihaloo B, editors. Comprehensive structural integrity. vol. 6, New York, NY: Elsevier Science; 2003, p. 31–101.
[8] Murakami Y, Matsunaga H. The effect of hydrogen on fatigue properties of steels used for fuel cell system. Int J Fatigue 2006;28(11):1509–20.
[9] Gangloff RP, Somerday BP. Gaseous hydrogen embrittlement of materials in energy technologies. Cambridge: Woodhead Publishing Limited; 2012, p. 520.
[10] Martínez-Pañeda E, Niordson CF, Gangloff RP. Strain gradient plasticity-based modeling of hydrogen environment assisted cracking. Acta Mater 2016;117:321–32.
[11] Burns JT, Harris ZD, Dolph JD, Gangloff RP. Measurement and modeling of hydrogen environment-assisted cracking in a Ni-Cu-Al-Ti superalloy. Metall Mater Trans 2016;47(3):990–7.
[12] Novak P, Yuan R, Somerday BP, Sofronis P, Ritchie R. A statistical, physical-based, micro-mechanical model of hydrogen-induced intergranular fracture in steel. J Mech Phys Solids 2010;58(2):206–26.
[13] Ayas C, Deshpande VS, Fleck N. A fracture criterion for the notch strength of high strength steels in the presence of hydrogen. J Mech Phys Solids 2014;63(1):80–93.
[14] Serebrinsky S, Carter EA, Ortiz M. A quantum-mechanically informed continuum model of hydrogen embrittlement. J Mech Phys Solids 2004;52(10):2403–30.

[15] Yu H, Olsen JS, Olden V, Alvaro A, He J, Zhang Z. Continuum level simulation of the grain size and misorientation effects on hydrogen embrittlement in nickel. Eng Fail Anal 2017;81:79–93.
[16] Elmukashfi E, Tarleton E, Cocks ACF. A modelling framework for coupled hydrogen diffusion and mechanical behaviour of engineering components. Comput Mech 2020;66:189–220.
[17] Anand L, Mao Y, Talamini B. On modeling fracture of ferritic steels due to hydrogen embrittlement. J Mech Phys Solids 2019;122:280–314.
[18] Martínez-Pañeda E, Golahmar A, Niordson CF. A phase field formulation for hydrogen assisted cracking. Comput Methods Appl Mech Engrg 2018;342:742–61.
[19] Duda FP, Ciarbonetti A, Toro S, Huespe AE. A phase-field model for solute-assisted brittle fracture in elastic-plastic solids. Int J Plast 2018;102:16–40.
[20] Wu J-Y, Mandal T, Nguyen VP. A phase-field regularized cohesive zone model for hydrogen assisted cracking. Comput Methods Appl Mech Engrg 2020;358:112614.
[21] Kristensen PK, Niordson CF, Martínez-Pañeda E. A phase field model for elastic-gradient-plastic solids undergoing hydrogen embrittlement. J Mech Phys Solids 2020;143:104093.
[22] Kristensen PK, Niordson CF, Martínez-Pañeda E. Applications of phase field fracture in modelling hydrogen assisted failures. Theor Appl Fract Mech 2020;110:102837.
[23] Martínez-Pañeda E, Harris ZD, Fuentes-Alonso S, Scully JR, Burns JT. On the suitability of slow strain rate tensile testing for assessing hydrogen embrittlement susceptibility. Corros Sci 2020;163:108291.
[24] Castelluccio GM, Geller CB, McDowell DL. A rationale for modeling hydrogen effects on plastic deformation across scales in FCC metals. Int J Plast 2018;111:72–84.
[25] Hosseini ZS, Dadfarnia M, Nagao A, Kubota M, Somerday BP, Ritchie RO, et al. Modeling the hydrogen effect on the constitutive response of a low carbon steel in cyclic loading. J Appl Mech Trans ASME 2021;88(3):1–14.
[26] Esaklul KA, Wright AG, Gerberich WW. The effect of hydrogen induced surface asperities on fatigue crack closure in ultrahigh strength steel. Scr Metall 1983;17(9):1073–8.
[27] Esaklul KA, Gerberich WW. On the influence of internal hydrogen on fatigue thresholds of HSLA steel. Scr Metall 1983;17:1079–82.
[28] Fernández-Sousa R, Betegón C, Martínez-Pañeda E. Analysis of the influence of microstructural traps on hydrogen assisted fatigue. Acta Mater 2020;199:253–63.
[29] Shinko T, Halm D, Benoit G, Hénaff G. Controlling factors and mechanisms of fatigue crack growth influenced by high pressure of gaseous hydrogen in a commercially pure iron. Theor Appl Fract Mech 2021;112:102885.
[30] Moriconi C, Hénaff G, Halm D. Cohesive zone modeling of fatigue crack propagation assisted by gaseous hydrogen in metals. Int J Fatigue 2014;68:56–66.
[31] del Busto S, Betegón C, Martínez-Pañeda E. A cohesive zone framework for environmentally assisted fatigue. Eng Fract Mech 2017;185:210–26.
[32] Zhao Y, Xu BX, Stein P, Gross D. Phase-field study of electrochemical reactions at exterior and interior interfaces in Li-ion battery electrode particles. Comput Methods Appl Mech Engrg 2016;312:428–46.
[33] Mesgarnejad A, Karma A. Phase field modeling of chemomechanical fracture of intercalation electrodes: Role of charging rate and dimensionality. J Mech Phys Solids 2019;132.
[34] Quintanas-Corominas A, Turon A, Reinoso J, Casoni E, Paggi M, Mayugo J. A phase field approach enhanced with a cohesive zone model for modeling delamination induced by matrix cracking. Comput Methods Appl Mech Engrg 2020;358:112618.
[35] Tan W, Martínez-Pañeda E. Phase field predictions of microscopic fracture and R-curve behaviour of fibre-reinforced composites. Compos Sci Technol 2021;202:108539.
[36] Carollo V, Reinoso J, Paggi M. Modeling complex crack paths in ceramic laminates: A novel variational framework combining the phase field method of fracture and the cohesive zone model. J Eur Ceram Soc 2018;38(8):2994–3003.
[37] Li W, Shirvan K. Multiphysics phase-field modeling of quasi-static cracking in urania ceramic nuclear fuel. Ceram Int 2021;47:793–810.
[38] Simoes M, Martínez-Pañeda E. Phase field modelling of fracture and fatigue in Shape Memory Alloys. Comput Methods Appl Mech Engrg 2021;373:113504.
[39] Hirshikesh S, Annabattula RK, Martínez-Pañeda E. Phase field modelling of crack propagation in functionally graded materials. Composites B 2019;169:239–48.
[40] Kumar PKAV, Dean A, Reinoso J, Lenarda P, Paggi M. Phase field modeling of fracture in Functionally Graded Materials: G -convergence and mechanical insight on the effect of grading. Thin-Walled Struct 2021;159:107234.
[41] McAuliffe C, Waisman H. A unified model for metal failure capturing shear banding and fracture. Int J Plast 2015;65:131–51.
[42] Borden MJ, Hughes TJR, Landis CM, Anvari A, Lee IJ. A phase-field formulation for fracture in ductile materials: Finite deformation balance law derivation, plastic degradation, and stress triaxiality effects. Comput Methods Appl Mech Engrg 2016;312:130–66.
[43] Isfandbod M, Martínez-Pañeda E. A mechanism-based multi-trap phase field model for hydrogen assisted fracture. Int J Plast 2021;144:103044.
[44] Francfort GA, Marigo J-J. Revisiting brittle fracture as an energy minimization problem. J Mech Phys Solids 1998;46(8):1319–42.
[45] Bourdin B, Francfort GA, Marigo J-J. Numerical experiments in revisited brittle fracture. J Mech Phys Solids 2000;48(4):797–826.
[46] Provatas N, Elder K. Phase-field methods in materials science and engineering. Weinheim, Germany: John Wiley & Sons; 2011.
[47] Cui C, Ma R, Martínez-Pañeda E. A phase field formulation for dissolution-driven stress corrosion cracking. J Mech Phys Solids 2021;147:104254.
[48] Chambolle A. An approximation result for special functions with bounded deformation. J Des Math Pures Et Appl 2004;83(7):929–54.
[49] Tanné E, Li T, Bourdin B, Marigo J-J, Maurini C. Crack nucleation in variational phase-field models of brittle fracture. J Mech Phys Solids 2018;110:80–99.
[50] Kristensen PK, Niordson CF, Martínez-Pañeda E. An assessment of phase field fracture: crack initiation and growth. Phil Trans R Soc A 2021;379:20210021.
[51] Jiang DE, Carter EA. First principles assessment of ideal fracture energies of materials with mobile impurities: Implications for hydrogen embrittlement of metals. Acta Mater 2004;52(16):4801–7.
[52] Carrara P, Ambati M, Alessi R, De Lorenzis L. A framework to model the fatigue behavior of brittle materials based on a variational phase-field approach. Comput Methods Appl Mech Engrg 2020;361:112731.
[53] Miehe C, Hofacker M, Welschinger F. A phase field model for rate-independent crack propagation: Robust algorithmic implementation based on operator splits. Comput Methods Appl Mech Engrg 2010;199(45–48):2765–78.
[54] Ambati M, Gerasimov T, De Lorenzis L. A review on phase-field models of brittle fracture and a new fast hybrid formulation. Comput Mech 2015;55:383–405.
[55] Amor H, Marigo JJ, Maurini C. Regularized formulation of the variational brittle fracture with unilateral contact: Numerical experiments. J Mech Phys Solids 2009;57(8):1209–29.
[56] Seleš K, Lesičar T, Tonković Z, Sorić J. A residual control staggered solution scheme for the phase-field modeling of brittle fracture. Eng Fract Mech 2019;205:370–86.
[57] Renard Y, Poulios K. GetFEM: Automated FE modeling of multiphysics problems based on a generic weak form language. ACM Trans Math Softw 2020;47(1):1–31.
[58] Kristensen PK, Martínez-Pañeda E. Phase field fracture modelling using quasi-Newton methods and a new adaptive step scheme. Theor Appl Fract Mech 2020;107:102446.
[59] Turnbull A, Ferriss DH, Anzai H. Modelling of the hydrogen distribution at a crack tip. Mater Sci Eng A 1996;206(1):1–13.
[60] Martínez-Pañeda E, Díaz A, Wright L, Turnbull A. Generalised boundary conditions for hydrogen transport at crack tips. Corros Sci 2020;173:108698.
[61] Di Leo CV, Anand L. Hydrogen in metals: A coupled theory for species diffusion and large elastic-plastic deformations. Int J Plast 2013;43:42–69.
[62] Martínez-Pañeda E, del Busto S, Niordson CF, Betegón C. Strain gradient plasticity modeling of hydrogen diffusion to the crack tip. Int J Hydrogen Energy 2016;41(24):10265–74.
[63] Díaz A, Alegre JM, Cuesta II. Coupled hydrogen diffusion simulation using a heat transfer analogy. Int J Mech Sci 2016;115–116:360–9.
[64] Gangloff RP. Corrosion fatigue crack propagation in metals. In: NASA contractor report 4301. Tech. rep., NASA; 1990, p. 1–194, 19900015089.
[65] Williams ML. On the stress distribution at the base of a stationary crack. J Appl Mech 1957;24:109–14.
[66] Anderson TL. Fracture mechanics. Fundamentals and applications. third ed. Boca Raton: CRC Press, Taylor & Francis; 2005.
[67] Matsunaga H, Yoshikawa M, Kondo R, Yamabe J, Matsuoka S. Slow strain rate tensile and fatigue properties of Cr-Mo and carbon steels in a 115 MPa hydrogen gas atmosphere. Int J Hydrogen Energy 2015;40(16):5739–48.
[68] Matsumoto T, Kubota M, Matsuoka S, Ginet P, Furtado J, Barbier F. Threshold stress intensity factor for hydrogen-assisted cracking of CR-MO steel used as stationary storage buffer of a hydrogen refueling station. Int J Hydrogen Energy 2017;42(11):7422–8.
[69] Ogawa Y, Matsunaga H, Yamabe J, Yoshikawa M, Matsuoka S. Unified evaluation of hydrogen-induced crack growth in fatigue tests and fracture toughness tests of a carbon steel. Int J Fatigue 2017;103:223–33.
[70] San Marchi C, Somerday BP. Technical reference for hydrogen compatibility of materials. In: SANDIA report SAND2012-7321. Tech. rep., SANDIA National Labs; 2012.

DTU Construct

Section of Engineering Design and Product Development
Koppels Allé 404
288 Kongens Lyngby

www.construct.dtu.dk

ISBN: 978-87-7475-757-3